Radiative alpha capture on ^{7}Be with DRAGON at νp–process nucleosynthesis energies

Radiative alpha capture on ^{7}Be with DRAGON at νp–process nucleosynthesis energies

By
Athanasios Psaltis, B.Sc.

A Dissertation
submitted to the Department of Physics & Astronomy
and the School of Graduate Studies of McMaster University
in partial fulfillment of the requirements
for the degree of
Doctor of Philosophy

Doctor of Philosophy (2020) McMaster University
(Physics & Astronomy) Hamilton, Ontario, Canada

TITLE:	Radiative alpha capture on ^{7}Be with DRAGON at νp–process nucleosynthesis energies
AUTHOR:	Athanasios Psaltis B.Sc., (Physics) National and Kapodistrian University of Athens, Athens, Greece
SUPERVISOR:	Prof. Alan A. Chen
NUMBER OF PAGES:	xv, 166

To my family

Abstract

A possible mechanism to explain the origin of around 35 neutron–deficient stable isotopes with mass A≥75 between ^{74}Se and ^{196}Hg, known as the p–nuclei is the nucleosynthesis in the proton–rich neutrino–driven winds of core–collapse supernovae via the νp–process. However this production scenario is very sensitive to the underlying supernova dynamics and the nuclear physics input. As far as nuclear uncertainties are concerned, the breakout reaction from the pp-chains, ^{7}Be$(\alpha,\gamma)^{11}$C, has been identified as an important link which can influence the nuclear flow and therefore the efficiency of the νp–process. However its reaction rate is not well known over the relevant energy range (T_9= 1.5–3).

In this thesis we report on the direct first measurement of two resonances of the ^{7}Be$(\alpha,\gamma)^{11}$C reaction with previously unknown strengths using an intense radioactive ^{7}Be beam from ISAC and the DRAGON recoil separator in inverse kinematics. Since resonance strength measurements with low mass beams using recoil separators depend strongly on the recoil angular distribution, which can exceed the acceptance of the separator, we first performed a proof–of–principle test by measuring a known resonance of the ^{6}Li$(\alpha,\gamma)^{10}$B reaction, which also presents a similar challenge.

Our results from the ^{6}Li$(\alpha,\gamma)^{10}$B reaction are in agreement with literature, showing that DRAGON can measure resonance strengths of reactions for which the maximum momentum cone of the recoils exceeds its acceptance.

From the newly measured ^{7}Be$(\alpha,\gamma)^{11}$C resonance strengths we calculated the new reaction rate which is lower than the current recommended by 10–50% and constrained to 5–10% in the relevant temperature region. Using this new rate, we performed detailed nucleosynthesis calculations which suggest that there is no effect the production of light p–nuclei, but a production increase for CNO elements of up to an order of magnitude is observed.

Acknowledgements

The thesis you are about to read depends on the following short story:

It is August 23, 2019 and I am sitting on my room at TRIUMF House in Vancouver. Two years have passed since our first attempt to measure the $^{7}\mathrm{Be}(\alpha,\gamma)^{11}\mathrm{C}$ reaction, which unfortunately was unsuccessful due to a highly contaminated radioactive beam. The day before our group was informed that this time the radioactive beam is literally unusable for an experiment – apparently it was due to a faulty heating module – and we had already started working on an alternative experiment with a stable beam, as the main experiment of my thesis. It is almost midnight and after an emotionally intense day, I decide to fall asleep. I get my phone from the nightstand to set the alarm clock and to my surprise I see a missed call and a text from Annika Lennarz: "They have 10^9 pps ^{7}Be at the yield station. We would get at least 10^8 pps at DRAGON." This was a breakthrough! We will finally run this experiment! Ecstatic, I try to reach my supervisor Alan Chen on the phone to pass on the great news. I call on his room, but no answer. After couple of more tries and knocking on his room, we finally get to talk – the conversation was about like that:

"Alan, we have 10^9!"

"What?!"

"They fixed the beam, we have 10^9 ^{7}Be!"

"That's not a good time for a prank, Thanassis!"

"No, I'm not making fun of you, Annika called me!"

"I don't believe you! Are you sure it is 10^9?"

"Yes! We should go to TRIUMF now."

After convincing Alan that I was not joking and showing him the text messages from Annika, we quickly dressed and drove to TRIUMF with big smiles in our faces, despite the late hour. The rest is history...

First and foremost, I would like to express my deep gratitude to my supervisor Alan Chen for accepting me as a graduate student and being an amazing mentor and friend for the last five year. Alan generously provided the means to have the best education possible by attending summer schools and participating in conferences and experiments in labs around the world. I thank him for trusting a challenging project with me and letting me being in charge since the beginning, when I presented the experimental proposal at the TRIUMF Experiments Evaluation Committee, just after finishing my first year of graduate school – a daunting task I realize today. He was supportive during all the ups and downs and his patience and calmness – except once – helped me to form a similar approach for experiments and life. I appreciate his hands–off supervising approach, which gave me the freedom to learn and explore beyond my thesis project and helped me develop both as a researcher and as a person. I will miss our discussions on the history of nuclear astrophysics, quantum mechanics and his book recommendations.

I would like to thank the rest of my supervisory committee, Chris Ruiz from TRIUMF and Soo Hyun Byun from McMaster University for all their help and guidance during my graduate studies. Specifically, I thank Chris for hosting me in the summer of 2017 when I visited TRIUMF to work with the DRAGON group and for teaching me how to tame the `GEANT` simulation toolkit of DRAGON. He was always supportive and trusted my abilities. I really appreciate his experimental insight, his confidence when things are not going well and his excitement about complicated 3D plots. I thank Byun for his very detailed comments on the experimental setup and his suggestions to improve the thesis manuscript. In addition, I thank Catalin Matei from ELI–NP for serving as an external reader of this thesis and examiner for the defense.

I would like to express my appreciation to my academic brother and friend Johnson Liang for being the best office and travel mate; from sandy beaches in Hawaii to snowy mountains in the Austrian Alps and from eating ramen in Tokyo to eating ramen in Vancouver, we were together. I thank him for all the the great memories from our adventures around the world. Johnson was always supportive and optimistic and I really enjoyed our late night discussions and shenanigans. I wish him all the best for the next stage of his career. I will really miss the Friday group meetings with him and Alan, filled with science, interesting papers, Bavarian delicacies and discussions on the latest sport events.

I would also like to thank Liam Kroll, who worked for two summers in the nuclear astrophysics group as an undergraduate researcher, for getting me involved with the `MESA` code and eventually the NuGrid collaboration. I wish him all the best for his graduate studies journey.

The DRAGON group at Vancouver is part of my scientific family. My sincere thank you to Annika Lennarz for all her help and support during and after the experiments, and for her timely reminders to sleep and eat during an experiment. Special thanks are due to Devin Connolly – now at Los Alamos National Laboratory – for patiently teaching me the ins and outs of the DRAGON analysis software and introducing me to the world of `OpenSUSE` and `emacs`. I would also like to thank Matt Williams for his help during the experiments, for setting up an amazing local time–of–flight system and for quoting "Rick and Morty" – "Where are my recoils, Summer?". I really appreciate the patience of Dave Hutcheon on how to calculate γ angular distributions, Barry Davids for his deep insight on writing scientific papers and Peter Machule for keeping DRAGON healthy and safe. Finally, thank you to all the collaborators that participated in our experiments and especially the graduate students that volunteered to take the overnight shifts.

The experiments of the present thesis would not have been possible without the tremendous work and dedication of the TRIUMF beam delivery group and the ISAC operators. I owe my deep gratitude to Spencer Kiy, Jens Lassen, Friedheim Ames, Alex Gottberg, Olivier Shelbaya and Tiffany Angus for leading this effort.

Furthermore, I would like to sincerely thank Sam Jones from LANL for introducing me to the wonderful world of reaction networks, and for being an awesome host during my visit at Los Alamos. Richard Longland from North Carolina State University for carrying out the `RateMC` calculations presented in this thesis, being a great host during my visits to TUNL and providing me with valuable advice for the next step of my career. Shinya Wanajo from Sophia University and Nobuya Nishimura from Kyoto University for providing a thermodynamic neutrino–driven wind trajectory and and results from his sensitivity study, respectively.

I would like to especially acknowledge the Department of Physics and Astronomy past and present administrative stuff. The amazing Rosemary McNeice, Tina Stewart, Mara Esposto, Hope Gianicos and Cheryl Johnston. Thank you for being so helpful and supportive and I am sorry for the innumerable travel expenses reports that you

had to go through in the past five years!

I am grateful to the School of Graduate Studies (SGS) of McMaster Univeristy for organizing the Thesis Writing Boot–camp, which provide an excellent, distraction–free environment. It really helped me complete a big part of the present thesis and showed me that it is possible to get work done without procrastination just by setting up the right environment.

I would also like to thank my close friends from the Physics and Astronomy Department; Wyatt Kirkby, Tom Lai, James Lambert and Sarah Dawson (French tarot crew and Reading Group). Thank you for introducing me to the Canadian culture/politics and for the great time and discussions we had – when I was not away on a trip. Thank you to my brother–like friend Aggelos for all our interesting discussions and support since our undergraduate years in Athens. I am also indebted to my undergraduate advisor and mentor Theo Mertzimekis from University of Athens for introducing me to the field of nuclear astrophysics and for his guidance during my graduate school search.

A special thank you to my partner and best friend Carmen, and her cat Nova. Carmen is the kindest and most talented person I have ever met. She is always there for me, to support, encourage, and inspire. She is a role model both as a researcher and as a person. I look forward to your graduation in two years. Thank you for our travelling adventures, for introducing me to vector graphics and for being a great student of Greek. I love you!

Finally, I would like to express my deep gratitude to my family, my parents Iraklis and Efi and my sister Mara to whom I dedicate this thesis. I cannot overstate my appreciation for the sacrifices they made and the love and care I have received from them all my life. They have always supported my choices and encouraged me to pursue my goals.

Contents

List of Tables

List of Figures

Chapter 1

Introduction

> Non est ad astra mollis e terris.
> (There is no easy way to the stars from earth.)
> — Seneca (*Hercules Furens, 437*)

1.1 Overview

Humans have always been fascinated and curious about the cosmos and its constituents. The first attempts to understand the origin of matter come from ancient Greece[1] and the natural pre–Socratic philosophers Democritus from Abdera and his teacher Leucippus. They argued that everything is composed of indivisible entities called atoms[2] and void. Atomism, as this materialistic philosophy was named, continued to influence schools of thought through the ages and in the early 20^{th} century Einstein, Bohr, Rutherford and many other theoretical and experimental physicists managed to show the existence of atoms and turned them from philosophical entities to constituents of the physical world. The discovery of atoms eventually led to the development of nuclear and particle physics during the mid–20^{th} century.

Our ideas about the stars changed significantly over the years. Humans have always wondered why the Sun shines. The 5^{th} century B.C.E. Greek philosopher Anaxagoras first suggested that the Sun is a ball of red–hot iron not much bigger than Greece and that is the same type of object as the night time stars, but closer to

[1] Similar attempts are also recorded in ancient Indian texts of the Nyaya and Vaisheshika schools.
[2] The word "atom" originates from the Greek "*atomos*", which means "undivided".

Earth. As years passed by, our ideas about the Sun and the stars changed and in the early 20^{th} century from the work of both theoretical astrophysicists and astronomers, such as Sir Arthur Eddington and Cecilia Payne–Gaposchkin, we determined that stars are big spheres of gas, mainly composed of hydrogen and a newly discovered element called helium[3].

The interrelation between atoms and stars became apparent during the mid–20^{th} century, after the advent of quantum mechanics and when the first interactions between atoms were studied in a laboratory environment. The revolutionary theory of quantum mechanics led Bethe, Gamow, von Weizsäcker and others to the conclusion that energy can be generated in stars via reactions between nuclei. Cockcroft and Walton at the Cavendish Laboratory in the U.K., using their newly developed accelerator to bombard lithium with highly energetic protons, initiated the first nuclear reaction in a laboratory, transforming the lithium into two helium nuclei, which also led to the development of nuclear technology (energy and weapons). The idea of matter transformation dates back to the middle ages, when the alchemists were trying to turn cheap metals into gold. Shortly after Cockcroft and Walton, on the other side of the Atlantic Ocean, Lauritsen and Crane bombarded carbon with protons at the Kellogg Radiation Laboratory in Caltech.

Experimental and theoretical advancements in both nuclear physics and astrophysics during the 1950s led Cameron (1957) and Burbidge et al. (1957) independently to suggest that the chemical elements are synthesized in astrophysical environments and that could also explain the elemental abundances in the solar system, as shown in Figure 1.1. They showed that the most abundant elements in the universe, hydrogen and most of helium, were created few minutes after the Big Bang, while the rest are produced by nuclear reactions in the cores or on the surfaces of stars, during their lives and deaths. This was one of the biggest scientific triumphs of the twentieth century. Those two seminal papers officially established the field of nuclear astrophysics, which since then had some great successes, such as the direct detection of neutrinos as nuclear messengers from the sun in the 1960s by Davis and later from supernova 1987A by the Kamiokande II, IMB, and Baksan collaborations, and the recent detection of gravitational waves and the electromagnetic counterpart of a neutron star merger in 2017, that we shall discuss later in this chapter.

[3] "Helium" originates from the Greek "*helios*" which means Sun.

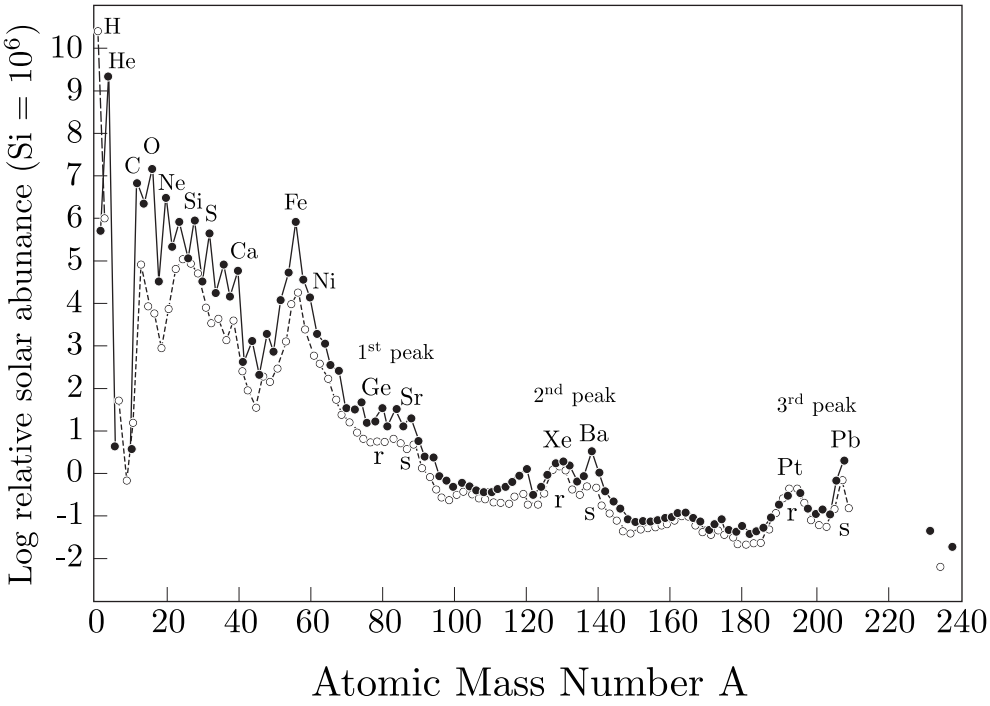

Figure 1.1: Solar elemental abundances as a function of mass number normalized to silicon. The open symbols represent odd mass number nuclei and the full symbols even ones. The three s– and r–process peaks are shown. The figure and the elemental abundances are adapted from Lodders et al. (2009).

Nowadays, nuclear astrophysics is a multidisciplinary field of study, where nuclear physics, astrophysics, astronomy, chemistry, geology, and computer science are combined to tackle the question of the origin of the elements in the cosmos and the generation of energy in the stars during their lives and deaths.

One of the long–standing puzzles in nuclear astrophysics, related to the topic of this thesis, is the production of elements heavier than iron (Fe) which, as we can see in Figure 1.1, are much less abundant than the lighter elements. According to our current understanding, the heavy elements can be produced in a core–collapse supernova explosion, the swan song of a massive star's evolution.

1.2 Massive star evolution

For the purpose of this work, we shall review the evolution of a 20 $M_\odot$ star[4], using the Modules for Experiments in Stellar Astrophysics (`MESA`)[5] software (Paxton et al., 2010, 2013, 2015, 2019). `MESA star` is an open source 1D stellar evolution module which can solve the fully coupled structure and composition equations simultaneously. For full nucleosynthesis calculations, as the ones that we shall perform in this work, the `MESA` output can be easily manipulated by post–process reaction network codes, such as NuGrid `NuPPN` (see Sections 2.3 and 6.4). More sophisticated hydrodynamics codes, such as `Fornax` (Skinner et al., 2019), can provide a more realistic description in 2D or 3D, especially during the late life stages, as we shall discuss later in this chapter.

Stars are much like all living entities: they are born, live and die in the cosmic ocean. Their formation starts in the cold interstellar medium, where massive gas clouds consisting mainly of hydrogen and helium[6], called nebulae, start to contract due to gravity. Each nebula can produce stars of different masses and their mass distribution is described by the Initial Mass Function (IMF). Low mass stars, like the Sun, are more common than the massive stars we shall study in this thesis. According to the widely used IMFs by Salpeter (1955) and Kroupa (2001), for every one star twenty times more massive than the Sun (M= 20 $M_\odot$) one thousand stars as massive as the Sun (M= 1 $M_\odot$) are formed in the Milky Way. Despite their rarity, massive stars are of extreme importance for the synthesis of elements in the cosmos.

When the newly born star can balance the gravitational contraction produced by its mass with a pressure gradient created by nuclear fusion that occurs in its hot and dense core, it enters the Zero Age Main Sequence (ZAMS) stage. Stars remain in the Main Sequence of the Hertzsprung–Russell diagram (HRD) (Figure 1.2) for most of their evolution, converting hydrogen into helium. Low–mass stars, like the Sun,

[4]The model we used (`M20.0.Z2.0e-02`) can be found in the University of Victoria Astrophysics Simulation Data Repository (ASDR) and more details about it are available on Ritter et al. (2018).

[5]The model was created using Release 3709. The software can be downloaded from the `MESA` website.

[6]In astronomy, elements heavier than helium are denoted as "metals". Each star has a specific abundance of metals, or metallicity. According to the metallicity of a star, we can group them into three populations: PopI, PopII and PopIII. PopI stars are metal–rich, meaning that they are relatively young, while PopII stars are metal–poor, hence older. PopIII is a hypothetical stellar population of the first massive stars of the universe, without any metals.

generate their energy via the *pp*–chains, while higher–mass stars (M >1.3 $M_\odot$) via the CNO cycles (Rolfs and Rodney, 1988; Iliadis, 2015).

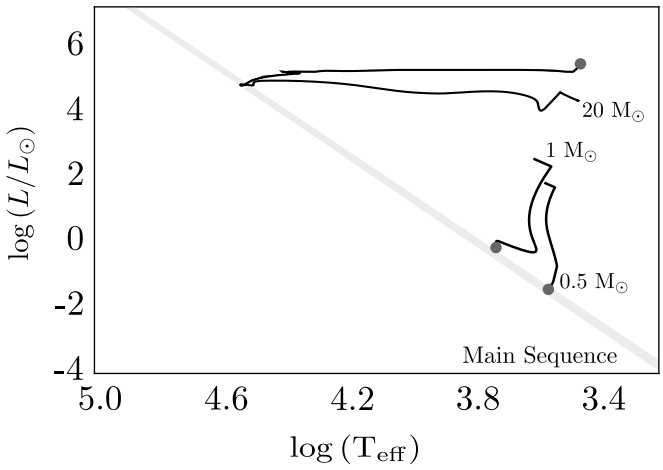

Figure 1.2: Evolutionary tracks on the Hertzsprung–Russell diagram (HRD) for three stars: 0.5 $M_\odot$ and 1 $M_\odot$ up to the ZAMS stage, and 20 $M_\odot$ just before core–collapse from `MESA` models. The grey band represents the Main Sequence, where stars spend most of their lifetime, fusing hydrogen into helium in their cores. The end of each evolutionary track calculation is indicated with a dark grey circle.

According to their mass at ZAMS, stars will undergo subsequent burning stages[7] in which both the core temperature and density will increase due to gravity (Vogt–Russell theorem). The ashes of one nuclear burning stage, will become the fuel for the next one. After the Main Sequence a 20 $M_\odot$ star[8], for example, will fuse helium into carbon and oxygen, then carbon to oxygen and neon, neon to oxygen, magnesium and silicon, oxygen to silicon and sulfur and finally silicon into iron–group elements (see Figure 1.4). As the central temperature and density rise, an equilibrium state called the Nuclear Statistical Equilibrium (NSE) develops, where all reactions between nuclear species are in equilibrium. Figure 1.3 shows the evolution of central density ρ_c and temperature T_c as the star evolves and proceeds to different burning stages.

[7]Note that our discussion is focused on single stars. However, most of the stars in the universe have one or multiple companions. Their evolution is more complicated, since it might also involve mass transfer between them, and it is beyond the scope of the present thesis. The interested reader is referred to José (2016) and references therein.

[8]We shall not discuss the effects of mass–loss, rotation, magnetic fields and metallicity in massive star evolution, since they are beyond the scope of this thesis. The interested reader is referred to the reviews by Woosley et al. (2002); Chieffi and Limongi (2013) and references therein.

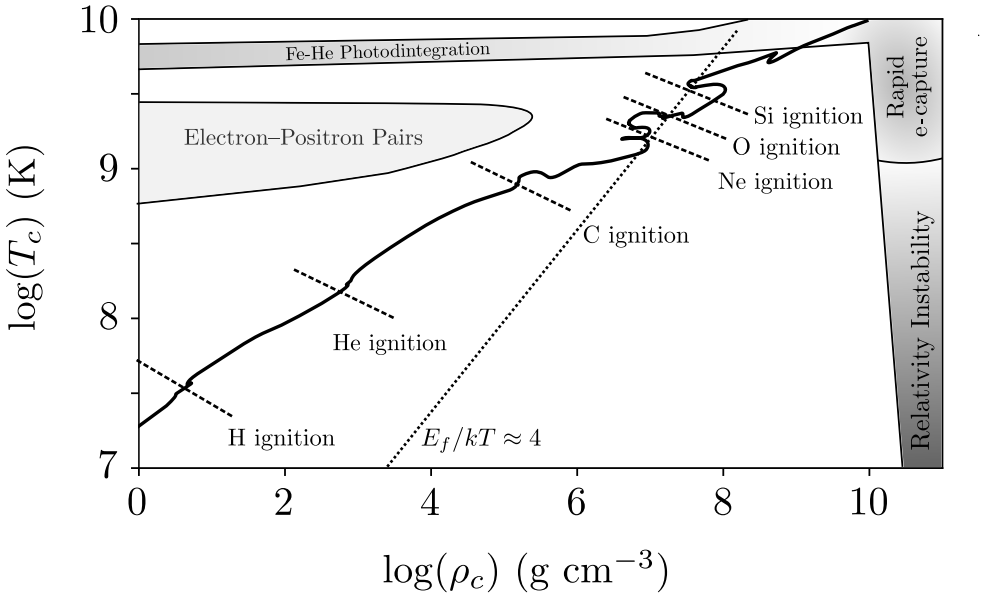

Figure 1.3: Central temperature (T_c) and density (ρ_c) profile for a 20 $M_\odot$, Z= 0.02 star using `MESA` (black solid line). The dashed lines correspond to the different stages of core burning and the diagonal dotted line the beginning of degeneracy in the electron plasma. Instability processes are indicated with grey scale.

The structure of a 20 $M_\odot$ star during its evolution up to the end of silicon burning is presented using a Kippenhahn diagram in Figure 1.5. The nuclear burning timescales decrease rapidly from $\sim 10^7$ years for core hydrogen burning to ~ 10 days for core silicon burning (see Figure 1.5 and Table 1.1). We can estimate the nuclear lifetime for each stage via $\tau_{\rm nuclear} \sim \epsilon_{\rm nuclear} {\rm M}/{\rm L}_{\rm total}$, where $\epsilon_{\rm nuclear}$ is the generated energy via nuclear reactions, M the mass of the star and $\rm L_{total}$ the total luminosity, which includes the contribution from both γ rays (L_γ) and neutrinos (L_ν). For the advanced nuclear burning stages, most of the generated energy is radiated away by neutrinos, which have very small interaction rates with the stellar plasma and for this reason they can exit the star at almost the speed of light without interacting and losing their energy. For this reason, the star will remain in the same position in the Hertzsprung–Russell diagram, since the structural change happens very quickly, as one can see in the Luminosity row of Table 1.1 for neon, oxygen and silicon burning.

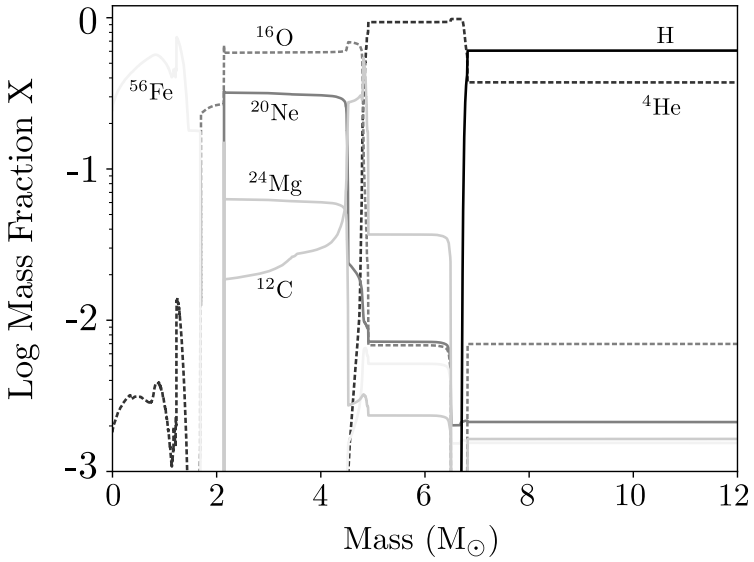

Figure 1.4: Stellar composition as a function of the enclosed mass before core collapse of the 20 $M_\odot$, Z= 0.02 `MESA` model. Some important species are shown.

Nuclear burning stops at the iron–group elements since their fusion is endothermic, and hence they cannot contribute to the luminosity of the star. The typical image of a massive star structure is that of concentric shells corresponding to the different burning phases. Early stellar evolution codes and some widely used nowadays, such as `MESA`, assume spherical symmetry (1D) to solve the equations of stellar evolution more easily. However, multi–dimensional (2D and 3D) simulations have shown that mixing in the form of convective burning is present during the different stages, especially in the oxygen and silicon layers, and that has implications for the subsequent nucleosynthesis (Janka et al., 2016).

1.3 Core–Collapse Supernovae

The core–collapse supernova (ccSN) was proposed as the last stage of massive star evolution by Baade and Zwicky (1934), well before nuclear processes in stars were well studied, as a way to explain the origin of high energy cosmic rays. After core silicon burning and NSE, the stellar core is mostly made out of iron–group elements and it is supported by degenerate electron pressure, with temperature and pressure

Table 1.1: Burning stages summary of a 20 $M_\odot$ star from Woosley et al. (2002).

Burning Stage	**Temperature (10^9 K)**	**Density ρ (g/ cm^3)**	**Luminosity $10^3 L_\odot$**	**Lifetime τ**
Hydrogen	0.04	4.53	62.6	8.13 Myr
Helium	0.20	968	102	1.17 Myr
Carbon	0.87	1.7×10^5	143	0.976 kyr
Neon	1.57	3.1×10^6	147	0.599 yr
Oxygen	1.98	5.55×10^6	147	1.25 yr
Silicon	3.34	4.26×10^6	147	11.5 d

being $T_9 \approx 10$ (T_9 is the temperature in units of 10^9 K or GK) and $\rho \approx 10^{10}$ g/cm^3 respectively (see Figure 1.3). The iron core will reach a critical mass (≈ 1.44 $M_\odot$), known as the Chandrasekhar mass limit, and after that it will start to collapse, since the electron degeneracy pressure cannot stabilize it (upper left panel in Figure 1.9). The dynamics of the collapse strongly depend on two parameters, the electron mole fraction Y_e (leptons per baryon), and the entropy per baryon s. These two quantities are determined by weak interaction processes, such as electron capture and β decay. In the early stages of the core–collapse, electron captures and photodisintegrations of iron–peak nuclei decrease the Y_e, making the material in the core more neutron–rich. In addition, electron captures remove electrons that contribute to the degenerate pressure and hence the collapse is accelerating. As the core with a radius of thousand kilometers is collapsing to an object with a radius of tens of kilometers, its density will reach $\rho \approx 10^{12}$ g/cm^3. In addition, the emitted neutrinos will be trapped, since their diffusion time becomes larger than the collapse time (Janka et al., 2007) (upper right panel in Figure 1.7). The region of the trapped neutrinos is referred to as the neutrinosphere. The core density will increase up to the nuclear density[9] ($\rho \approx 2.7 \times 10^{14}$ g/cm^3), which makes the strong nuclear force repulsive.

This results in a rebound of the core and a formation of a shock wave which will encounter material from the rest of the star, infalling at supersonic speed (middle left panel in Figure 1.7). This is commonly known as the prompt shock, and it has been shown that it cannot trigger the subsequent explosion (Janka et al., 2007). The neutrinos that are located outside the neutrinosphere will escape from the star freely,

[9]To give a perspective of the enormity of this number, it is almost 10 billion ($\approx 1 \times 10^{13}$) times more dense than the densest element, osmium.

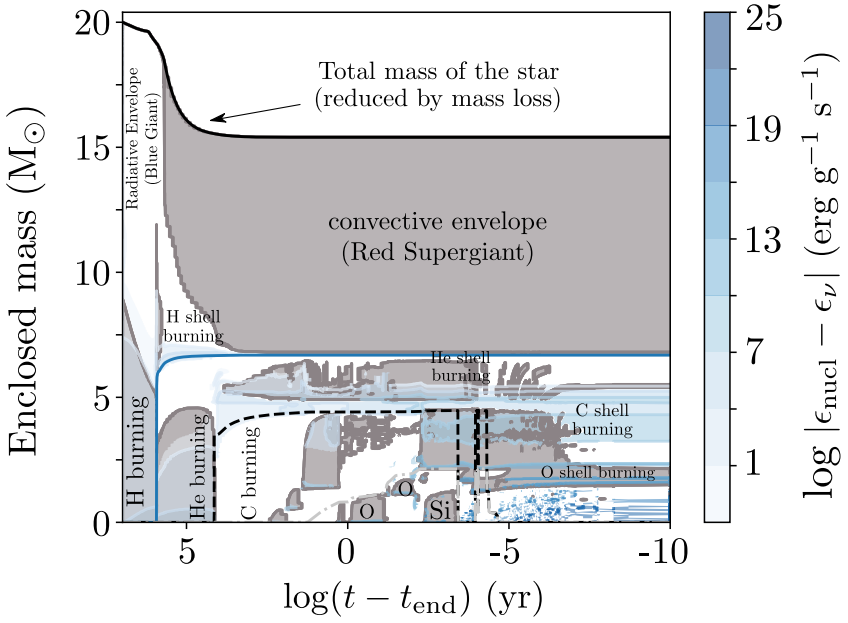

Figure 1.5: Stellar structure (Kippenhahn) diagram of a 20 $M_\odot$ star with $Z = 0.02$ from the `MESA` model. The diagram shows the evolution of the stellar structure as a function of the time left until the core collapse. The grey zones correspond to the convective zones, and the burning regions are also indicated. The blue solid line and the black dashed line represent the H–free and He–free cores respectively. The blue bands indicate the net energy generation/loss from nuclear burning and neutrino emission.

since their interaction probability is very small (middle right panel in Figure 1.7). The hot compact remnant will become a proto–neutron star (PNS) with a mass of ≈ 1.4 $M_\odot$ which grows rapidly by accreting the infalling material. It will eventually evolve into a neutron star, or collapse into a black hole, depending on the initial mass of the progenitor star[10]. The shock is weakened as it propagates outwards and stalls at around 100–200 km away from the PNS, before being able to reach the surface of the star, and turns into an accretion shock. The solution to this issue, which revives the shock and leads to a successful explosion is provided by the neutrinos streaming off the neutrinosphere (bottom left panel in Figure 1.7).

[10]Progenitor stars with 25 $M_\odot \leq M \leq 40$ $M_\odot$ usually produce a black hole (BH) by fallback and $M > 40$ $M_\odot$ a direct BH (Heger et al., 2003).

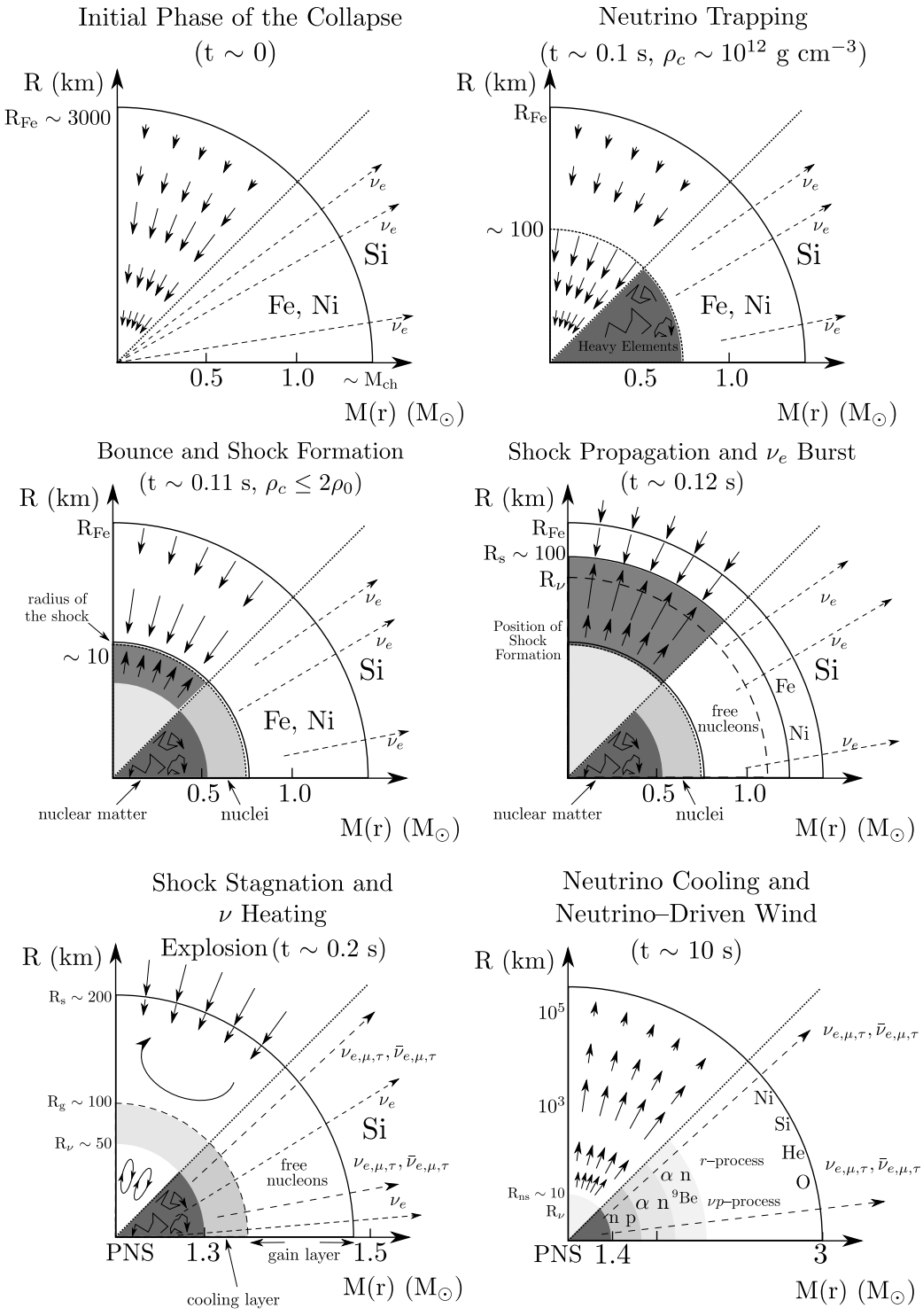

Figure 1.6: Schematic representation of the evolutionary stages of a core–collapse Supernova explosion. The figure was adapted from Janka et al. (2007). See the text for more details.

1.3.1 The Role of Neutrinos

The revival of the stalled shock that leads to a successful supernova explosion is one of the greatest puzzles in astrophysics. The importance of neutrinos for a successful ccSN explosion was already suggested by early studies from Colgate and White (1966) and Arnett (1966), since they are expected to carry the bulk of the core–collapse energy. We can calculate the gravitational binding energy released using

$$E_b \sim E_g \approx \frac{3}{5}\frac{GM_{ns}^2}{R_{ns}} \approx 3.6 \times 10^{53} \left(\frac{M_{ns}}{1.5 M_\odot}\right)^2 \left(\frac{R_{ns}}{10\ km}\right)^{-1} \text{ erg} \tag{1.1}$$

where M_{ns} and R_{ns} are the mass and radius of the neutron star, respectively. Most of this energy is carried away by neutrinos and antineutrinos. For a typical neutron star ($M_{ns} = 1.44\ M_\odot$ and R_{ns}= 12 km) $E_b = 2.8 \times 10^{53}$ erg and less than 1% of that is sufficient to power the explosion[11].

Bethe and Wilson (1985) proposed that the stalled shock is revived by the delayed neutrino–heating mechanism. Electron neutrinos (ν_e) and antineutrinos ($\bar{\nu}_e$) emerge from the hot and dense PNS and deposit some energy in the shock by getting reabsorbed by free nucleons

$$\nu_e + n \rightarrow p + e^- \tag{1.2}$$

$$\bar{\nu_e} + p \rightarrow n + e^+ \tag{1.3}$$

The stalled shock gains fresh energy from the neutrinos streaming from the neutrinosphere, and this situation is known as neutrino heating. The neutrino–induced energy deposition creates a negative entropy gradient and the heated layer becomes convectively unstable (Burrows et al., 1995). In addition, a Standing Accretion Shock Instability (SASI) increases the mass accretion between shock and neutron star and creates mushroomlike high–entropy structures (Blondin and Mezzacappa, 2007).

1.3.2 From Core–Collapse to Explosion

The energy transfer from the neutrino heating will increase the post–shock pressure and if the neutrino heating is strong enough, the shock can be ejected outward, leading

[11] The energy output of a supernova explosion is measured in units of foe (1 foe = 10^{51} erg) which is an acronym for [ten to the] fifty–one ergs.

to a successful explosion[12]. At the same time, matter is continuously accreted towards the neutron star. When the phase of mass accretion and outflow ends, neutrino–energy deposition near the PNS will launch the so–called neutrino–driven wind, which is an outflow of ejected material at supersonic velocities (Duncan et al., 1986) (lower right panel in Figure 1.9).

The equilibrium initial Y_e of the neutrino–driven wind can be calculated from an analytic model by Qian and Woosley (1996)

$$Y_e \approx \left[1 + \frac{L_{\bar{\nu_e}}}{L_{\nu_e}} \frac{\epsilon_{\bar{\nu_e}} - 2\Delta + 1.2\Delta^2/\epsilon_{\bar{\nu_e}}}{\epsilon_{\nu_e} + 2\Delta + 1.2\Delta^2/\epsilon_{\nu_e}}\right]^{-1} \tag{1.4}$$

where L_{ν_e} is the electron neutrino luminosity, $\epsilon_{\nu_e} = \langle E^2_{\nu_e}\rangle / \langle E_{\nu_e}\rangle \approx 4.1\ kT_{\nu_e}$ the ratio of the mean squared neutrino energy and the mean neutrino energy, kT_{ν_e} the neutrino temperature in MeV, with similar relations for the antineutrinos, and Δ= 1.273 MeV is the neutron–proton mass difference. Simulations have shown that supernova neutrinos show an energy hierarchy, with $E_{\nu_x} \approx E_{\bar{\nu_x}} > E_{\bar{\nu_e}} > E_{\nu_e}$, where x refers to μ and τ neutrinos and their antiparticles (Fischer et al., 2010), which suggests that the early wind should be proton–rich, $Y_e > 0.5$ (see Figure 1.7).

The value of Y_e in the wind also depends on the the neutrino and antineutrino captures on free nucleons and heavy nuclei (Qian and Woosley, 1996; McLaughlin et al., 1996), as well as on the oscillation between neutrino flavours, since they change the ν_e, $\bar{\nu_e}$ energies (Yoshida et al., 2006; Wu et al., 2015). Whether Y_e is below or above 0.5 has strong implications for nucleosythesis in neutrino–driven winds in the innermost supernova ejecta, as we shall discuss in the following section.

In terms of simulating a ccSN explosion, 1D hydrodynamic codes, like `MESA`, remove the PNS and replace it either by a piston which is driven at the innermost zone of the star (Woosley and Weaver, 1995) or by a straight energy deposition in the inner few tenths of a solar mass by means of a thermal energy bomb (Thielemann et al., 1996). State–of–the–art neutrino–driven explosions in multi–dimensional models with energy–dependent neutrino transport mechanism have been successful in both 2D, *e.g.* Buras et al. (2006); Wanajo et al. (2018), and 3D, *e.g.* Vartanyan et al. (2019) and they show that the Y_e of the neutrino–driven wind is indeed proton–rich.

[12]We can think of ccSN as a critical phenomenon, a bifurcation between steady (mass accreting) and exploding solutions of the differential equations that describe its evolution.

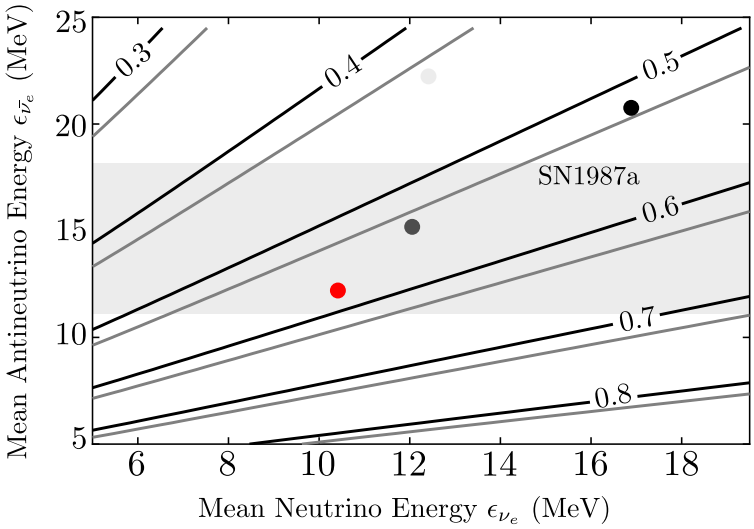

Figure 1.7: Neutrino–driven wind electron fraction Y_e from Equation 1.4 for different neutrino and antineutrino energies. Black contours correspond to $L_{\nu_e}/L_{\bar{\nu}_e} = 1$ and grey contours to $L_{\nu_e}/L_{\bar{\nu}_e} = 1.1$. The points correspond to the electron neutrino and antineutrino energies from ccSN simulations 10 s after the core bounce found in literature: Fischer et al. (2010) with red, Woosley et al. (1994) with light grey, Hüdepohl et al. (2010) with dark grey and Arcones et al. (2007) with black. The gray band corresponds to the range of electron antineutrino energies detected from SN1987A. The figure is adapted from Arcones and Montes (2011).

1.3.3 Open Questions

Despite the huge advancements in our understanding of core–collapse supernovae explosions since the 1930s, there are still many open questions regarding their nature. In the following we shall list some of them and the interested reader is referred to the references of this chapter for more details:

- Convection or SASI as the trigger of the shock expansion?
- How can self–consistent simulations match the energy output of ccSNe?
- Will the future neutrino observatories be able to detect more SN neutrinos?
- Will the Advanced LIGO detector detect gravitational waves from ccSNe (Evans and Zanolin, 2017)?

1.4 Nucleosynthesis in Core–Collapse Supernovae

Core–collapse supernovae explosions are of extreme importance for nucleosynthesis, since they can produce a wide variety of iron–peak and trans–iron elements. As the shock is moving from the PNS outwards, it encounters infalling material from different shells.

1.4.1 Explosive Burning

The shock encounters the silicon layer first, heats it to $T_9 \geq 5$ and undergoes complete explosive silicon burning, in which the ^{28}Si will be destroyed and transformed into iron–peak nuclei. At these typical temperatures reactions are in NSE, and the final abundances will be determined by the characteristics of the environment, such as temperature, density and the neutron excess (see also Section 2.3). Iron–peak nuclei with Z$\sim$N with large binding energies are produced in this scenario, *e.g.* ^{56}Ni. As the layer is expanding and cooling, reactions fall off equilibrium at a characteristic freeze–out temperature. The first reaction that drops out of equilibrium is the triple–α reaction (a two–step reaction with the first step being $^4\mathrm{He} + {}^4\mathrm{He} \rightarrow {}^8\mathrm{Be}$, immediately followed by $^8\mathrm{Be} + {}^4\mathrm{He} \rightarrow {}^{12}\mathrm{C}$), that can provide a lot of α particles. According to the density (or equivalently expansion time) of the layer when it reaches this freeze–out temperature, two distinct outcomes can occur; for highly dense layers, NSE predicts a very small amount of light nuclei (protons, neutrons and α) in the environment, and as a result the NSE abundance will not be altered (normal freeze–out). However, if the density is low at freeze–out, NSE predicts a large excess of α particles which will be captured by heavier nuclei, varying greatly the NSE abundance distribution (α–rich freeze–out).

After complete explosive silicon burning and freeze–out the shock wave will continue to encounter ^{28}Si layers, but it will heat them at a lower temperature of $T_9 \geq 4 - 5$. In these conditions, instead of NSE, two distinct quasi–equilibrium (QSE) clusters will be created, one close to ^{28}Si and one at iron–peak nuclei. The nuclear abundances will depend on the abundance of ^{28}Si, in addition to the characteristics of the environment. Not all of the ^{28}Si will be processed in this case and hence it is referred to as incomplete silicon burning (Woosley et al., 1973). Similar burning will occur as the shock wave encounters layers rich in ^{16}O (incomplete oxygen

burning), ^{20}Ne and ^{12}C (incomplete carbon/neon burning).

The other layers will be heated by the shock at temperatures $T_9 \leq 2$ for a short time, and hence they will not experience any burning. Eventually the shock will reach the stellar surface between a few hours to a day after the core–collapse.

From the explosive burning stages we discussed, some important γ ray emitters can be produced, such as ^{44}Ti and ^{56}Ni, which have been observed in supernovae remnants (see Section 1.5.3).

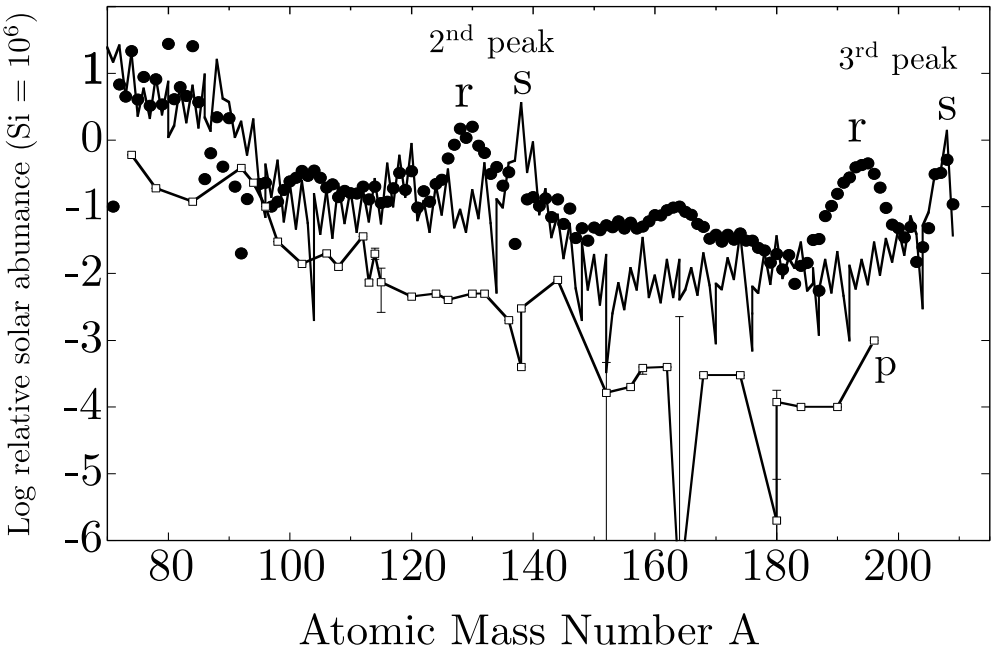

Figure 1.8: Decomposition of solar s– (solid line), r– (black circles) and p–abundances (white squares) relative to silicon. The figure is adapted from Arnould et al. (2007).

1.4.2 *s*–process

Almost half of the elements between iron (Fe) and bismuth (Bi) are synthesised by the slow neutron–capture (s-) process (Käppeler et al., 2011). The s–process path is described by radiative neutron captures – (n, γ) reactions – on stable nuclei followed by β^- decays when the path reaches an unstable, relatively long–lived nucleus (see

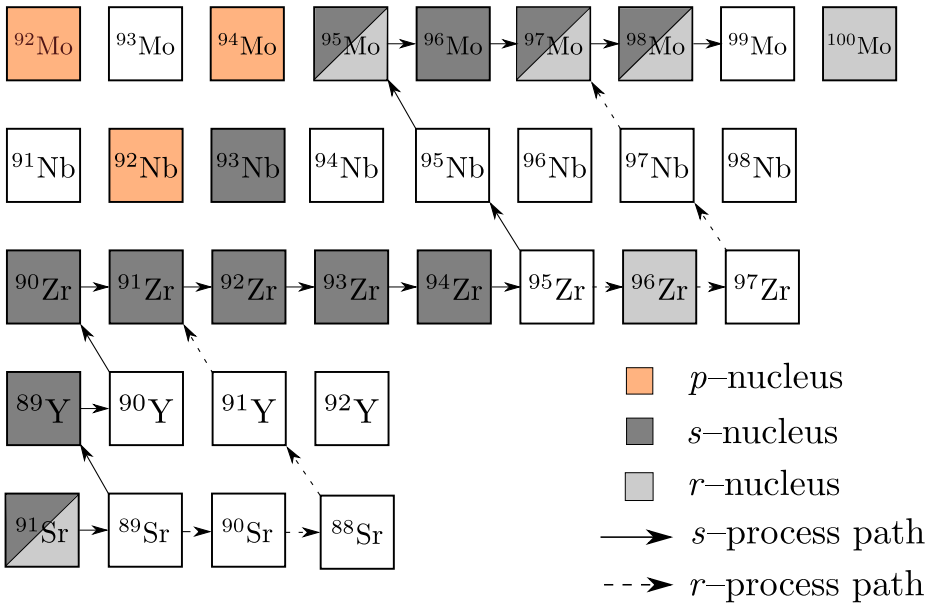

Figure 1.9: Example from the chart of nuclides illustrating the position of the light p–nuclei ^{92}Nb and ^{92,94}Mo, which are shielded from the s–process flow and the r–process decay chains.

Figure 1.9), converting an excess neutron into a proton. That way the nuclear flow heads towards heavier elements.

The s–process operates in two distinct astrophysical environments, where the neutron flux is $N_n = 10^{7-12}$ cm^{-3}, and each of those produces a specific subset of the s–nuclei:

1. Thermally pulsing low–mass (M $<$ 4 M$_\odot$) Asymptotic Giant Branch (AGB) stars produce the stable s–nuclei with A $\geq$ 90 the so–called main s–process component. The main neutron source is the ^{13}C$(\alpha, n)^{16}$O reaction with the ^{22}Ne$(\alpha, n)^{25}$Mg reaction having a small contribution during thermal pulses.

2. Massive stars (initial M$\geq$ 8–10 M$_\odot$) produce the stable s–nuclei with 60 $<$ A $<$ 90 in the weak s–process component (Pignatari et al., 2010). The neutron source is the ^{22}Ne$(\alpha, n)^{25}$Mg from the ^{18}O$(\alpha, \gamma)^{22}$Ne reaction that was produced towards the end of helium burning.

The main uncertainties of the s–process include the precise knowledge of the cross–sections of the nuclear species that act as neutron sources and poisons. The

interested reader is referred to the studies of Pignatari et al. (2010), Käppeler et al. (2011) and Reifarth et al. (2014) for an in–depth discussion.

1.4.3 *p*–process

A small group of around 35 stable neutron–deficient nuclei with A $\geq$ 74 between selenium (Se) and mercury (Hg) cannot be produced by either the *s*– or the *r*–process, which we shall describe in the next section (Figure 1.9). These are referred to as *p*–nuclei and their origin is a long–standing puzzle in nuclear astrophysics.

The fact that a distinct process produces these isotopes had been already identified from the early days of nuclear astrophysics by both Cameron (1957) and Burbidge et al. (1957). They were referred to as "excluded" nuclei, since they were "shielded" by the *s*– and the *r*–process reaction path. For this reason their solar abundances are around one to two orders of magnitude smaller than the *s*– and *r*–counterparts, as shown in Figure 1.8, and no single *p*–nucleus is the most abundant isotope of any element.

It is generally accepted that the *p*–nuclei in the solar system have been produced by more than one processes; however their synthesis mechanism is commonly referred to as *p*–process. In the following we shall focus on those operating in massive stars, but we will also mention every other proposed mechanism.

In the early models of Burbidge et al. (1957), the *p*–process was placed in the hydrogen–rich layers of core–collapse supernovae. (p, γ) and (γ, n) reactions on *s*– and *r*–nuclei would produce the *p*–nuclei at conditions of T$\approx$ 2.5 GK and $\rho \approx 100$ g/cm^3. Arnould (1976) first proposed that the *p*–nuclei are produced in the oxygen/neon burning zone as the shock passes through it. In this scenario, photodisintegration of heavy seed nuclei via (γ, n), (γ, p) and (γ, α) reactions[13] can synthesize neutron–deficient species. In the *p*–process each mass region is produced at a different peak temperature: intermediate mass *p*–nuclei (A$\approx$ 92–136) are produced at $T_9 \sim 2.5 - 3$, while the heavy *p*–nuclei (A $>$ 140) at $T_9 < 2.5$ (Rayet et al., 1990; Arnould and Goriely, 2003).

A site that has gained popularity in recent years and is now considered the dominant scenario for the production of the majority of *p*–nuclei is the thermonuclear

[13]For this reason, the *p*–process is also referred to as γ–process (Pignatari et al., 2016).

explosions of Chandrasekhar mass carbon–oxygen white dwarfs (CO WD)[14], via Type Ia supernovae (SNIa) (Travaglio et al., 2011). Galactic Chemical Evolution (GCE) models show that this site can account for the production of the p–nuclei (Travaglio et al., 2014).

Finally, some of the light p–nuclei can also be produced via the rp–process, which occurs when a neutron star accretes hydrogen and helium from a companion star and thermonuclear runaway causes a Type I X–ray burst (Schatz et al., 1998). This scenario cannot explain the solar p–abundances, because the strong gravitational field of the neutron star prohibits the ejection of the produced nuclei into the interstellar medium. Nevertheless, it has been shown that through mass–loss though radiation–driven winds some amount of material can escape (Ebisuzaki et al., 1983). This is still an open issue, since nucleosynthesis calculations show that the concentration of p–nuclei in the neutron star envelope is not high enough (José et al., 2010).

It is remarkable that despite the variety of astrophysical models, these processes can reproduce the solar abundances of most of the p–nuclei within a factor of 3 (*e.g.* see the sensitivity studies by Rapp et al. (2006) and Rauscher et al. (2016)). Nevertheless, several light species, such as ^{92,94}Mo, ^{96,98}Ru, ^{113}In and ^{115}Sn, are significantly underproduced in most models and their status as p–nuclei is under debate (Dillmann et al., 2008). Sensitivity studies have shown that the main uncertainties of the p–process arise mainly from the theoretically predicted rates of reactions on unstable nuclei and of excited state contributions, which can alter the reaction flow (Rauscher et al., 2016). Unfortunately, most of these reactions cannot be studied directly using the current radioactive ion beam (RIB) facilities.

To summarize our discussion of the p–process: it is still an open issue in nuclear astrophysics, but many different production mechanisms can explain their solar abundances.

1.4.4 ν–process

Neutrinos of all flavours that are produced during the stellar core–collapse stream through the outer layers of the star before the shock wave reaches them. Even though their cross–sections with matter are very small, their large number can excite stellar

[14]The same scenario, but with a sub–Chandrasekhar mass CO WD has been identified as the site for the pn–process which can also produce p–nuclei (Goriely et al., 2002).

mantle nuclei above particle breakup (neutron, proton or α) via charged–current and neutral–current reactions producing new nuclei. This nucleosynthesis scenario is referred to as the neutrino (ν–)process (Domogatskii and Nadezhin, 1978; Woosley et al., 1990; Heger et al., 2005).

Neutrino–induced reaction cross–sections are proportional to the square of their energy, and recalling our discussion in Section 1.3.2, the reactions relevant to the ν–process are mainly driven by μ and τ neutrinos.

The ν–process can contribute to the solar abundances of ^{7}Li via $^{4}\mathrm{He}(\nu_x, \nu'_x p/n)$, ^{11}B via $^{12}\mathrm{C}(\nu_x, \nu'_x p)$, ^{19}F via $^{20}\mathrm{Ne}(\nu_x, \nu'_x p/n)$, ^{138}La and ^{180}Ta via $^{138}\mathrm{Ba}(\nu_e, e^-)$ and $^{180}\mathrm{Hf}(\nu_e, e^-)$ reactions respectively (Langanke et al., 2019).

The models of ν–process nucleosynthesis rely heavily on the following parameters: (a) neutrino–induced cross–sections, (b) neutrino spectra and luminosities, and (c) the details of the adopted supernova model (Langanke et al., 2019), these also constitute the main uncertainties (José, 2016).

1.5 Nucleosynthesis in Neutrino–Driven Winds

Nucleosynthesis in neutrino–driven winds depends strongly on the entropy s, expansion time scale τ and the electron fraction Y_e. According to the value of the electron fraction Y_e, neutrino–driven winds of core–collapse supernovae in the innermost ejecta can be the site for two distinct nucleosynthesis processes: the νp–process, when $\mathrm{Y}_e > 0.5$ and the r–process, when $\mathrm{Y}_e < 0.5$. Recent studies of neutrino–driven wind dynamics suggest that the early wind is proton–rich for up to 20 s after the explosion, while later it transforms into slightly neutron–rich (Iliadis, 2015).

1.5.1 νp–process

The neutrino–driven wind ejects very hot ($\mathrm{T}_9 > 10$) and proton–rich material from the PNS (see Figure 1.10). The temperature is so high that the ejecta consists mainly of dissociated nucleons. As the wind is expanding and cooling down, NSE assembles these nucleons into mainly ^{56}Ni and α particles (which are synthesised via the hot pp–chain sequence (Wiescher et al., 1989)) with an excess of free protons. This is extremely important for the subsequent nucleosynthesis as we shall discuss below, because in neutron–rich NSE no free neutrons are present in the plasma (Wanajo

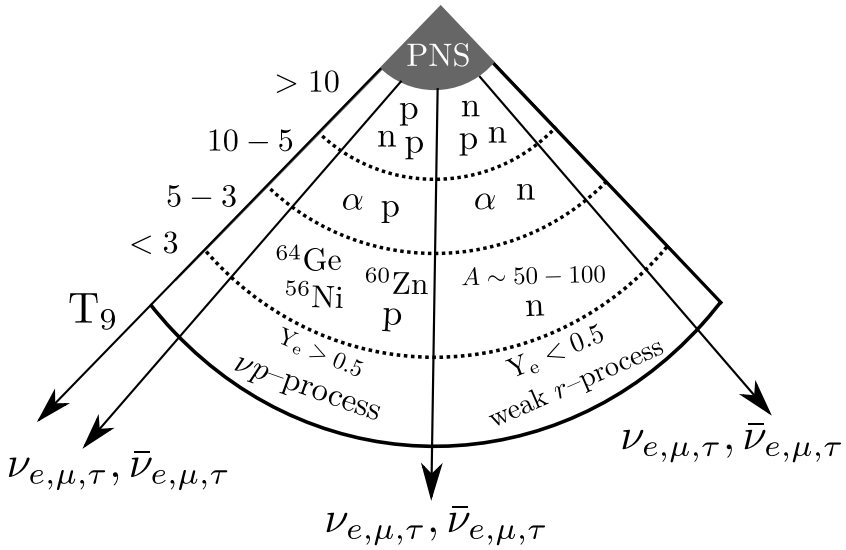

Figure 1.10: Schematic of the nucleosynthesis in a neutrino driven wind. The different stages and outcomes (νp–process and weak r–process) are shown. The figure is adapted from José and Iliadis (2011).

et al., 2011). At $T_9 < 3$–4, ^{56}Ni can rapidly capture free protons. However, the reaction flow cannot move beyond ^{64}Ge, which has a relatively long β^+ half–life of 1.06 min. This issue is solved by electron antineutrino captures on free protons via the $p(\bar{\nu}_e, e^+)n$ reaction, which produce a tiny amount of free neutrons, $10^{-11} - 10^{-12}$ of the total mass. At T_9= 3–1.5, the much faster (n, p) reaction on ^{56}Ni, followed by a sequence of radiative proton captures, *i.e.* (p, γ) reactions, bypass ^{64}Ge and similar waiting–points, such as ^{68}Se and ^{72}Kr with half–lives of 35.5 s and 17.1 s respectively. The reaction flow follows the Z = N line and up to the molybdenum region and then steers into more neutron–rich isotopes (Z < N) between molybdenum and tin. Finally, as the temperature drops below $T_9 < 1.5$, (p, γ) reactions freeze–out due to the Coulomb barrier, and the produced nuclei decay back to stability, with ^{56}Ni still being the most abundant nucleus in the plasma. This is the basic picture of the νp–process (Fröhlich et al., 2006; Pruet et al., 2006; Wanajo, 2006), which was proposed under the light of studies which suggested that the innermost ejecta of the ccSN explosion are proton–rich. It is a primary process, since the seed nuclei are directly formed from free nucleons and can create heavy elements beyond iron.

A useful measure for the strength of νp–process is the number ratio Δ_n of free neutrons created by the $p(\bar{\nu}_e, e^+)n$ reaction and seed nuclei, proposed by Pruet et al. (2006)

$$\Delta_{\rm n} \equiv \frac{\rm Y_p}{\rm Y_h} {\rm n}_{\bar{\nu}_{\rm e}} = \frac{\rm Y_p}{\rm Y_h} \int_{\rm T_9 \leq 3} \lambda_{\bar{\nu}_{\rm e}} {\rm dt} \tag{1.5}$$

where $\lambda_{\bar{\nu}_e}$ is the rate for the $p(\bar{\nu}_e, e^+)n$ reaction and $\rm Y_p$ and $\rm Y_h$ are the mass fraction of protons and seeds (nuclei with Z> 2) at $\rm T_9$=3, the onset of νp–processing.

As the number ratio Δ_n increases, the reaction flow can reach the β–stability line and cross it to the neutron–rich region. That can happen when the net number of electron antineutrino captures on free protons after the νp–process $n'_{\bar{\nu}_e}$

$$n'_{\bar{\nu}_e} = \int_{T_9 \leq 1.5} \lambda_{\bar{\nu}_e} dt \tag{1.6}$$

is not negligible compared to $n_{\bar{\nu}_e}$ (Wanajo et al., 2011).

The efficiency of νp–processing depends on a variety of parameters arising both from the supernova dynamics and from the underlying nuclear physics input. In the following we shall discuss the most important of them.

First and foremost the νp–process is dependent on the presence of neutrinos in the hot ejected material. Figures 1.11 and 1.12 show the nucleosynthesis output of a neutrino–driven wind trajectory — (T(t), ρ(t)) profile — from Wanajo et al. (2011) using the NuGrid Post–Processing Nucleosynthesis (`NuPPN`) code (see Section 6.4 for details) with the neutrino interactions (neutrino captures on free nucleons and spallations) enabled and disabled. It is evident that the neutrino interactions play a pivotal role by converting protons to neutrons, which are then absorbed by iron–group nuclei and lead to a successful νp–process; otherwise the final abundances look similar to an NSE, with a surplus of iron–group nuclei.

The next crucial ingredient for the νp–process is the electron fraction $\rm Y_e$ of the wind. Recent hydrodynamical studies with proper neutrino transport have shown that $\rm Y_e$ can lie between 0.5 and 0.6 at $\rm T_9$=3 (Wanajo et al., 2018). Sensitivity studies by Wanajo et al. (2011) and Nishimura et al. (2019) have explored a variety of $\rm Y_e$ values, ranging from 0.5 up to 0.8. Both studies suggest that the higher $\rm Y_e$ leads to a more efficient νp–process. This occurs because the Y_p/Y_h ratio is increased, leading to a higher Δ_n, even though $n_{\bar{\nu}_e}$ is the same. In the case of $\rm Y_e$ above 0.6, neutron captures compete with proton captures and the nuclear flow heads from Z = N to

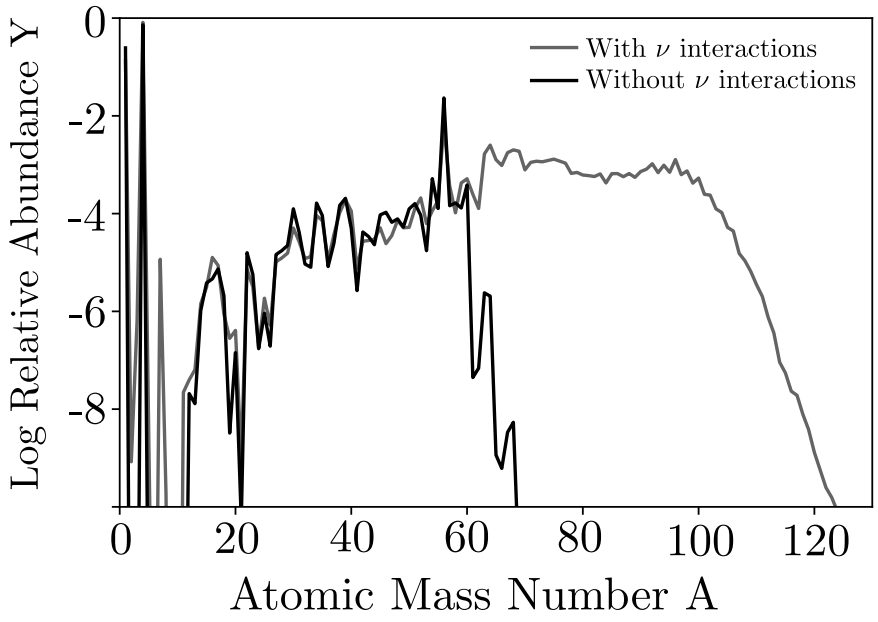

Figure 1.11: Relative abundance versus atomic mass number for two different nucleosynthesis calculations using the same hydrodynamical trajectory (Wanajo et al., 2011), but having the neutrino interactions enabled and disabled.

Z<N crossing the line of β stability at A$\sim$ 160.

Wanajo et al. (2011) also explored the effect of neutrino luminosity L_ν, which exhibits a similar effect to the Y_e (higher L_ν leads to a more efficient νp–process). This is an expected result, since according to Equation 1.4, the two quantities are related.

Concerning the nuclear physics input of the νp–process the main uncertainties arise from a handful of reactions, and the nuclear masses along its pathway. The two most important reactions that dominate in the νp–process are the bottleneck triple–α and $^{56}\mathrm{Ni}(n,p)^{56}\mathrm{Co}$. The former controls the production of α–particles, protons and the ^{56}Ni seed before the onset and during the νp–process. Therefore it controls completely the seed–to–proton ratio Δ_n. Our current knowledge of this reaction, despite its importance, is still limited and bears large experimental uncertainties. The three rates that are most commonly used in nucleosynthesis studies are those from Caughlan and Fowler (1988), Angulo et al. (1999) and Fynbo et al. (2005). In Section 3.4 we provide a detailed discussion about the importance of couple more

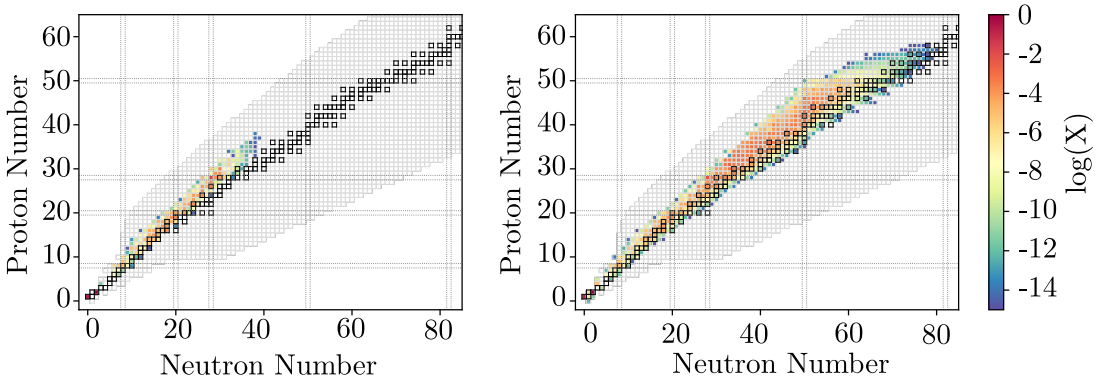

Figure 1.12: Same results as in Figure 1.11 but presented in the nuclear chart.

reactions that exhibit a similar effect as the triple–α reaction and how they can affect νp–processing, $^{7}\mathrm{Be}(\alpha,\gamma)^{11}\mathrm{C}$ and $^{10}\mathrm{B}(\alpha,p)^{13}\mathrm{C}$.

The $^{56}\mathrm{Ni}(n,p)^{56}\mathrm{Co}$ reaction is the first step in the νp–process, and for this reason its rate determines the subsequent nucleosynthesis, regardless of the detailed conditions. Specifically, a lower rate leads to a more efficient νp–process. Unfortunately, its rate, as for most of the (n,p) reactions, is based on the Hauser–Feshbach (HF) statistical model estimates (Hauser and Feshbach, 1952) which can have up to an order of magnitude uncertainty (Spyrou et al., 2014). Experimental efforts to determine its rate are underway (Gastis et al., 2017). For both reactions, a slight change in their reaction rates can have a huge impact in the efficiency of the νp–process.

Arcones et al. (2012) identified a reaction sequence after the onset of the νp–process that can delay the processing to heavier masses:

$$^{56}\mathrm{Ni}(n,p)^{56}\mathrm{Co}(p,\gamma)^{57}\mathrm{Ni}(n,p)^{58}\mathrm{Ni}(p,\gamma)\begin{cases}^{59}\mathrm{Cu}(p,\alpha)^{56}\mathrm{Ni} & \text{(NiCu cycle)}\\ ^{59}\mathrm{Cu}(p,\gamma)^{60}\mathrm{Zn} & \text{(breakout from the cycle)}\end{cases}$$

In this scenario the proton capture on ^{59}Cu is of great importance, because according to its rate it can either break–out (if $\lambda_{(p,\gamma)} > \lambda_{(p,\alpha)}$), or cycle material back to ^{56}Ni and thus delay the reaction flow to heavier nuclei (if $\lambda_{(p,\gamma)} < \lambda_{(p,\alpha)}$). For this reason it is important to study both reactions experimentally.

Finally nuclear masses can affect the equilibrium abundances within an isotonic chain, where a $(p,\gamma) \leftrightarrow (\gamma,p)$ equilibrium exists (Schatz, 2006). Many nuclear masses

on the νp–process pathway have being measured since its advent in 2006 (Weber et al., 2008; Fallis et al., 2011; Xing et al., 2018).

Despite the aforementioned uncertainties, the νp–process is considered one of the main contributors to the origin of the light p–nuclei, such as ^{92,94}Mo and ^{96,98}Ru that are underproduced in the p–process. If the wind conditions are favourable, the νp–process can synthesize neutron–deficient nuclei up to $A \sim 180$ (Wanajo et al., 2011).

Furthermore it has been suggested as a Light Element Primary Process (LEPP) to explain the missing abundances in ultra metal poor stars (UMP) as shown in Figure 1.13 (Arcones and Montes, 2011), and can also explain the presence of strontium in the extremely metal–poor star HE 1327-2326 (Frebel et al., 2005).

To summarize, it is widely accepted that the νp–process is a nucleosynthesis scenario that can produce a variety of neutron–deficient nuclei and that varies from event to event, since the conditions in the neutrino–driven wind can be different depending on the progenitor star composition and the explosion mechanism.

1.5.2 r–process

The rapid neutron–capture process (r–process) is responsible for the origin of around half the abundances of the elements heavier than iron (Horowitz et al., 2019). A high density of neutrons, $N_n = 10^{20-28}$ cm^{-3} leads to fast radiative neutron captures which lead the abundance flow far from the valley of β stability. When the flow reaches the magic neutron numbers (N = 50, 80 and 126) β^- decays and β–delayed neutron emission lead the nuclear flow back to stability.

Core–collapse supernovae explosions have been identified as the astrophysical site of the r–process since the early days of nuclear astrophysics (Cameron, 1957; Burbidge et al., 1957) and simulations during the 1990s supported that claim via the delayed neutrino–driven explosions (Meyer et al., 1992; Woosley et al., 1994). Modern ccSNe simulations with energy–dependent neutrino transport suggest that the neutrino–driven wind ejecta are slightly neutron rich ($Y_e \sim 0.4 - 0.49$) (Martínez-Pinedo et al., 2012) and can produce nuclei up to A$\approx 90 - 110$, below the second r–process peak (see Figure 1.8) by α, neutron, and proton capture reactions, as well as β decays. However the conditions are not sufficient to produce the gold–platinum peak and the actinides. This is referred to as the weak r–process mechanism (Arcones and Montes,

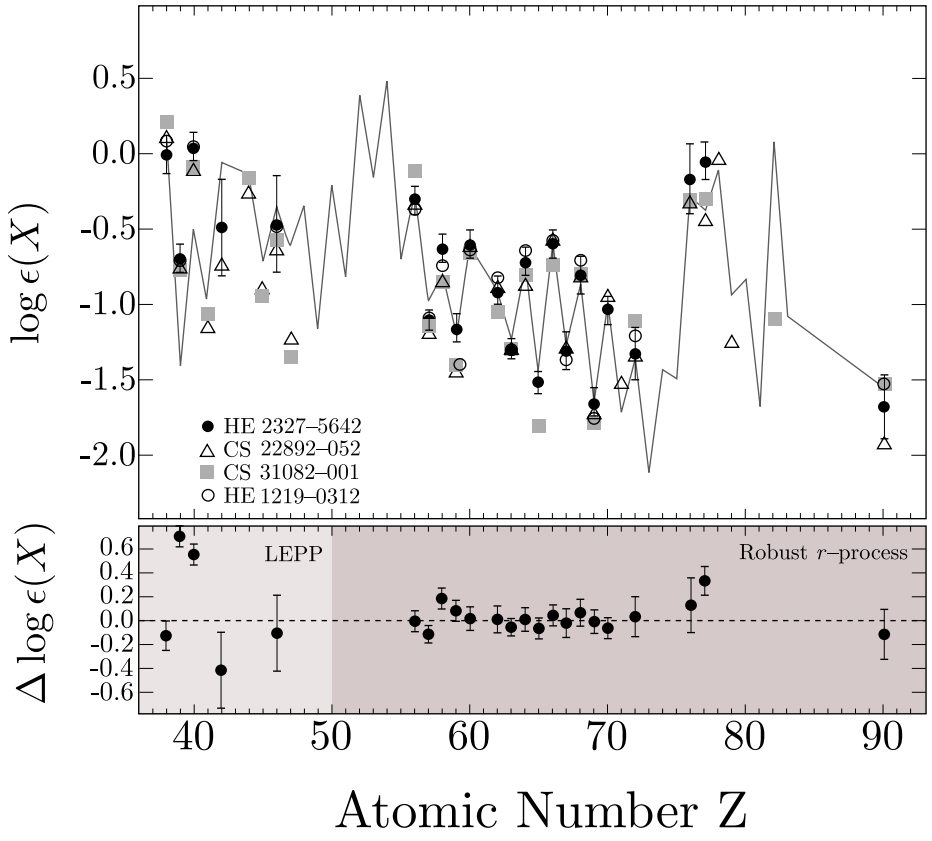

Figure 1.13: Heavy element abundances of the low–metallicity halo stars HE 2327–5642, CS 22892–052, CS 31082–001, and HE 1219–0312 (Mashonkina et al., 2010). On the top panel the solid line shows the solar r–process abundances scaled to match the Ba–Hf region. The standard spectroscopic notation is used, where $\log \epsilon(X) \equiv \log_{10}(N_X/N_H) + 12.0$, where N_X is the abundance by number. The measurements have been normalized to the $\log \epsilon$(Eu) found in HE 2327–5642. In the bottom panel the difference in $\log \epsilon(X)$ between HE 2327–5642 and the solar r–process abundances is shown. The figure is adapted from José (2016).

2011; Wanajo, 2013).

The weak r–process nuclear flow is sensitive to (α, n) reactions (Bliss et al., 2017) and neutron captures (Surman et al., 2014) which rely on reaction models, such as the Hauser–Feshbach (HF) statistical model. For this reason, experimental information, such as reaction cross–sections, is crucial to improve our understanding of this nucleosynthesis scenario.

An additional astrophysical site for the r–process, which has been confirmed by the recent observation of gravitational waves by the LIGO collaboration (Abbott et al., 2017) and its electromagnetic counterpart (Drout et al., 2017), is the merger of two neutron stars and the subsequent kilonova explosion.

1.5.3 Observations

Nucleosynthesis in core–collapse supernovae is also supported by astronomical observations. In the following we shall discuss two notable examples; the supernova 1987A (SN 1987A[15]) and the Cassiopeia A (CasA) supernova remnant (SNR).

SN 1987A was discovered on February 24, 1987 and it is thought to originate from a blue supergiant star, Sanduleak 69202 (Sk -69 202), on the outskirts of the Tarantula Nebula in the Large Magellanic Cloud (LMC), a satellite galaxy of the Milky Way. The most important discovery associated with SN1987A was the first observation of supernova neutrinos. Nineteen neutrino events were observed three hours prior the first photographic record, eleven by Hirata et al. (1987) using the Kamiokande II detector and eight by Bionta et al. (1991) using IMB (Irvine—Michigan—Brookhaven) water Cherenkov detector. This was the first observational evidence of a stellar core–collapse explosion via the neutrino–driven mechanism and the birth of extrasolar neutrino astronomy.

In addition to the neutrino observation, astronomers detected photons from the radioactive decays of ^{56}Ni and ^{44}Ti in the object's brightness as a function of time after explosion (light curve) (Matz et al., 1988; Tueller et al., 1990; Grebenev et al., 2012), which reveals some of the composition of the supernova ejecta and also confirms that they are the source of the light curve.

[15]The naming convention for supernovae includes the prefix SN followed by the year of discovery suffixed with a one or two-letter designation. For the first twenty six supernovae of a year the letters A to Z are used and afterwards pairs of lower–case letters, e.g 'be' is the 57$^{\text{th}}$.

Cassiopeia A is a supernova remnant in the namesake constellation, which is located around 3.4 kpc ($\approx 10^{17}$ km) away from Earth in the Milky Way (Reed et al., 1995) and is relatively young, since it underwent the core–collapse explosion around 300–400 years ago. It is arguably the best–studied core–collapse SNR with observations from COMPTEL (Schoenfelder et al., 1993) in γ rays, INTEGRAL (Winkler et al., 2003), NuSTAR (Harrison et al., 2013) and Chandra (Weisskopf et al., 2000) in X–rays, and Spitzer (Werner et al., 2004) in infrared. While silicon, sulfur, iron and calcium have been observed in X–rays (Hwang et al., 2004), the most notable discovery is the observation of γ rays from radioactive ^{44}Ti. Grefenstette et al. (2014) mapped the spatial distribution of ^{44}Ti in CasA and showed that it is asymmetric, with the mass clumps being predominantly in the half plane opposite to the compact remnant. This result is consistent with multi–dimensional, non–spherically–symmetric explosion simulations which suggest that more heavy elements are produced in the direction where the shock is stronger (Wongwathanarat et al., 2013).

1.6 Summary

In this chapter we have given a brief overview of the evolution of massive stars, along with the respective nucleosynthesis and we focused on the core–collapse supernovae explosions. The story we described in this chapter is a cyclic process, meaning that through these stellar winds and explosions, the newly synthesized material will enrich the interstellar medium and it will become part of the next stellar generation. In the next chapter we shall present an introduction to nuclear reaction formalism in stars and in the laboratory.

Chapter 2

Stellar Nuclear Reaction Formalism

> The fault, dear Brutus, is not in our stars
> But in ourselves, that we are underlings.
> (*Julius Caesar, Act I, Scene III, L. 140-141*)

2.1 Introduction

Thermonuclear reactions play a critical role in the generation of energy in stars and as a result they determine their evolution and produce the chemical elements during this process, as we discussed in the previous chapter. Nuclei are complicated many–body quantum systems and reactions between them require a very careful treatment. In this chapter we shall focus on the general characteristics of these reactions, both in stellar environments and in laboratories. Specifically, we shall first present the general characteristics of thermonuclear reactions and nuclear reaction networks. After that, we shall discuss the determination of experimental reaction yields and the relevant reaction kinematics for the experiment discussed in this thesis.

2.2 Thermonuclear Reaction Rate

Let us consider a stellar gas consisting of, for the sake of simplicity, two charged–particle species a and b. They can interact via a nuclear reaction, $a + b \rightarrow c^{\star} \rightarrow$

$d + e$, where d and e are the products and $c^\star$ is an intermediate, short–lived excited state of a nucleus composed of a combination of a and b (or c and d), called the compound nucleus. The rate of the aforementioned reaction is an energy–dependent or, equivalently, a velocity–dependent quantity, which can be expressed as

$$r_{ab} = n_a n_b \langle \sigma v \rangle_{ab} \tag{2.1}$$

where n_a and n_b are the concentrations, or number densities, of species a and b per unit volume (usually expressed in cm^{-3}) and $\langle \sigma v \rangle_{ab}$ is an average value of the reaction cross section σ (usually expressed in barns, where $1\ b \equiv 10^{-24}\ \mathrm{cm}^{-2}$) and the relative velocity distribution of the charged–particles a and b.

The general expression for the stellar reaction rate, including the case of identical particles, is given by

$$r_{ab} = \frac{n_a n_b \langle \sigma v \rangle_{ab}}{(1 + \delta_{ab})} \tag{2.2}$$

where δ_{ab} is the Kronecker symbol. The quantity that is most commonly used in the literature is the number of reactions per unit volume and time, expressed as $\mathrm{N}_A \langle \sigma v \rangle_{ab}$ in units of $\mathrm{cm}^3\ \mathrm{mol}^{-1}\ \mathrm{s}^{-1}$, where N_A is Avogadro's number. This occurs because in stellar model calculations, mass density ρ (expressed in $\mathrm{g\ cm}^{-3}$) and mass fraction X_i (or abundance Y_i) are commonly used instead of the number density (Rolfs and Rodney, 1988). The aforementioned quantities are related through the following expression

$$n_i = \frac{\rho N_A X_i}{A_i} = \rho N_A Y_i \tag{2.3}$$

where A_i is the atomic mass of species i in amu.

In a stellar gas the temperature is high enough to ionize completely the constituent atoms, such that they do not experience any long range electronic interactions. Any reactions are initiated from their thermal motion, and for this reason they are called *thermonuclear*. Accordingly, relative particle velocities can be described by the Maxwell–Boltzmann distribution

$$P(v)\ dv = \left(\frac{\mu}{2\pi k T}\right)^{3/2} e^{-\mu v^2/(2kT)} 4\pi v^2 dv \tag{2.4}$$

which expresses the probability that the relative velocity of charged–particles a and b lies between v and $v + dv$. $\mu = m_a m_b/(m_a + m_b)$ is the reduced mass of the system,

k is the Boltzmann constant, with a value of $k = 8.6173 \times 10^{-5}$ eV/K and T is the gas temperature expressed in Kelvin. The Maxwell–Boltzmann distribution shows the following behaviour: it increases linearly with energy E at low energies, E $\ll$ kT, reaches a maximum value at E = kT and decreases exponentially at high energies, E $\gg$ kT.

The assumption concerning the thermal motion of a stellar gas holds true for the majority of astrophysical sites, including both degenerate and non–degenerate gas, but it might need adjustments in special circumstances, such as in big bang nucleosynthesis (BBN). In that case, the Maxwell–Boltzmann distribution needs to be modified by a more generalized distribution, which also maximizes entropy, such as the Tsallis statistics, to describe the complex, fast-expanding, hot plasma after the Big Bang (Hou et al., 2017).

We can express the Maxwell–Boltzmann particle velocity distribution as an energy distribution and obtain the reaction rate in the center–of–mass energy

$$N_A\langle\sigma v\rangle_{ab} = \left(\frac{8}{\pi\mu}\right)^{1/2} (kT)^{-3/2} N_A \int_0^\infty \sigma(E) E e^{-E/kT} dE \tag{2.5}$$

Equation 2.5 is a general expression for the thermonuclear reaction rate. In principle, the only missing piece for its calculation is the energy–dependent reaction cross section, $\sigma(E)$. Once this quantity is either measured experimentally, or estimated theoretically, Equation 2.5 can be integrated numerically and then evaluated at the temperature of interest. For the majority of astrophysical environments, reaction rate calculations span a temperature window of $T_9 = 0.001 - 10$ (Angulo et al., 1999). In some cases, when the cross section has a relatively simple energy dependence, as we shall discuss below, the reaction rate can be calculated analytically. Nevertheless, in cases of complicated energy dependence, a numerical integration is necessary.

In the following, we shall examine two cross section energy dependencies that we encounter frequently in charged–particle reactions relevant for nuclear astrophysics: the smooth (non–resonant) and the strong (resonant) energy dependence. Both result in an analytic expression for the reaction rate.

2.2.1 Non–resonant Reactions

Let us recall the nuclear reaction $a + b \rightarrow d + e$. Such a reaction occurs, in a stellar or a laboratory environment, when the projectile a intrudes in the nuclear vicinity of the target b. Particle b exhibits an electric field, proportional to its charge. Projectile a's energy (velocity) is usually not high enough to overcome the Coulomb barrier of b, but quantum–mechanically there is a finite probability to penetrate through it. Gamow (1928) calculated this transmission probability to be

$$P \propto e^{-2\pi\eta} \tag{2.6}$$

where η is a dimensionless factor, called the Sommerfeld parameter and is equal to

$$\eta = \frac{Z_a Z_b e^2}{\hbar v} \tag{2.7}$$

where Z_a, Z_b are the charges of the interacting particles, e is the elementary charge, $\hbar$ is the reduced Planck constant and v is the relative velocity of the interacting particles.

The transmission probability is also known as the Gamow factor and it is a strongly increasing function with increasing energy, meaning that in stellar gases it is more probable for the particles at the high energy tail of the Maxwell–Boltzmann distribution to tunnel through the Coulomb barrier, as we shall discuss in the following.

The cross section for non–resonant charged–particle reactions can be expressed as

$$\sigma(E) = \frac{S(E)}{E} e^{-2\pi\eta} \tag{2.8}$$

where $S(E)$ is a usually slowly varying function of energy referred to as the nuclear or astrophysical S–factor and removes the strong 1/E energy dependence of the nuclear cross section. With the definition of a non–resonant charged–particle reaction cross section, we can re-write Equation 2.5 as follows

$$\begin{aligned} N_A\langle\sigma v\rangle_{ab} &= \left(\frac{8}{\pi\mu}\right)^{1/2} (kT)^{-3/2} N_A \int_0^\infty S(E) e^{-2\pi\eta} e^{-E/kT} dE \\ &= \left(\frac{8}{\pi\mu}\right)^{1/2} (kT)^{-3/2} N_A \int_0^\infty S(E) \exp\left(-\sqrt{\frac{E_G}{E}} - \frac{E}{kT}\right) dE \end{aligned} \tag{2.9}$$

where E_G is called the Gamow energy and is given by

$$E_G = 2\mu c^2 (\pi \alpha Z_a Z_b)^2 \tag{2.10}$$

with α being the fine structure constant $\alpha = e^2/(4\pi\epsilon_0 \hbar c) \simeq 1/137$, which sets the relative weakness of the electromagnetic interaction compared to the strong interaction.

The integrand of Equation 2.9 exhibits a very interesting energy dependence, which is shown in Figure 2.1 for the ^{7}Be$(\alpha,\gamma)^{11}$C reaction. Multiplying the transmission probability through the Coulomb barrier, $e^{-2\pi\eta}$, which increases with increasing energy, with the Maxwell–Boltzmann factor, which increases with decreasing energy, results in a peak which defines the energy region where it is more probable for nuclear reactions to occur in a stellar gas. The peak is referred to as the Gamow peak and its maximum value E_0 can be found from determining the maximum of the integrand of Equation 2.9 at E_0

$$E_0 = \left(\frac{\sqrt{E_G} kT}{2} \right)^{2/3} = 0.122 \left(Z_a^2 Z_b^2 \mu T_9^2 \right)^{1/3} \text{ MeV} \tag{2.11}$$

It is evident from Figure 2.1 that the Gamow peak shows a striking similarity to a Gaussian function. The Gamow peak can be then approximated fairly well by

$$\exp\left(-\sqrt{\frac{E_G}{E}} - \frac{E}{kT} \right) \approx \exp\left(-\frac{3E_0}{kT} \right) \exp\left[-\left(\frac{E - E_0}{\Delta/2} \right)^2 \right] \tag{2.12}$$

where Δ is the effective width of the Gaussian and can be obtained by matching the second derivatives of Equation 2.12

$$\Delta = \frac{4}{\sqrt{3}} \sqrt{E_0 kT} = 0.2368 \left(Z_a^2 Z_b^2 \mu T_9^5 \right)^{1/6} \tag{2.13}$$

Thermonuclear reactions typically occur in energies between $E_0 \pm \Delta/2$, which is commonly referred to as the Gamow window, but there are also some exceptions, which we shall discuss later in this chapter.

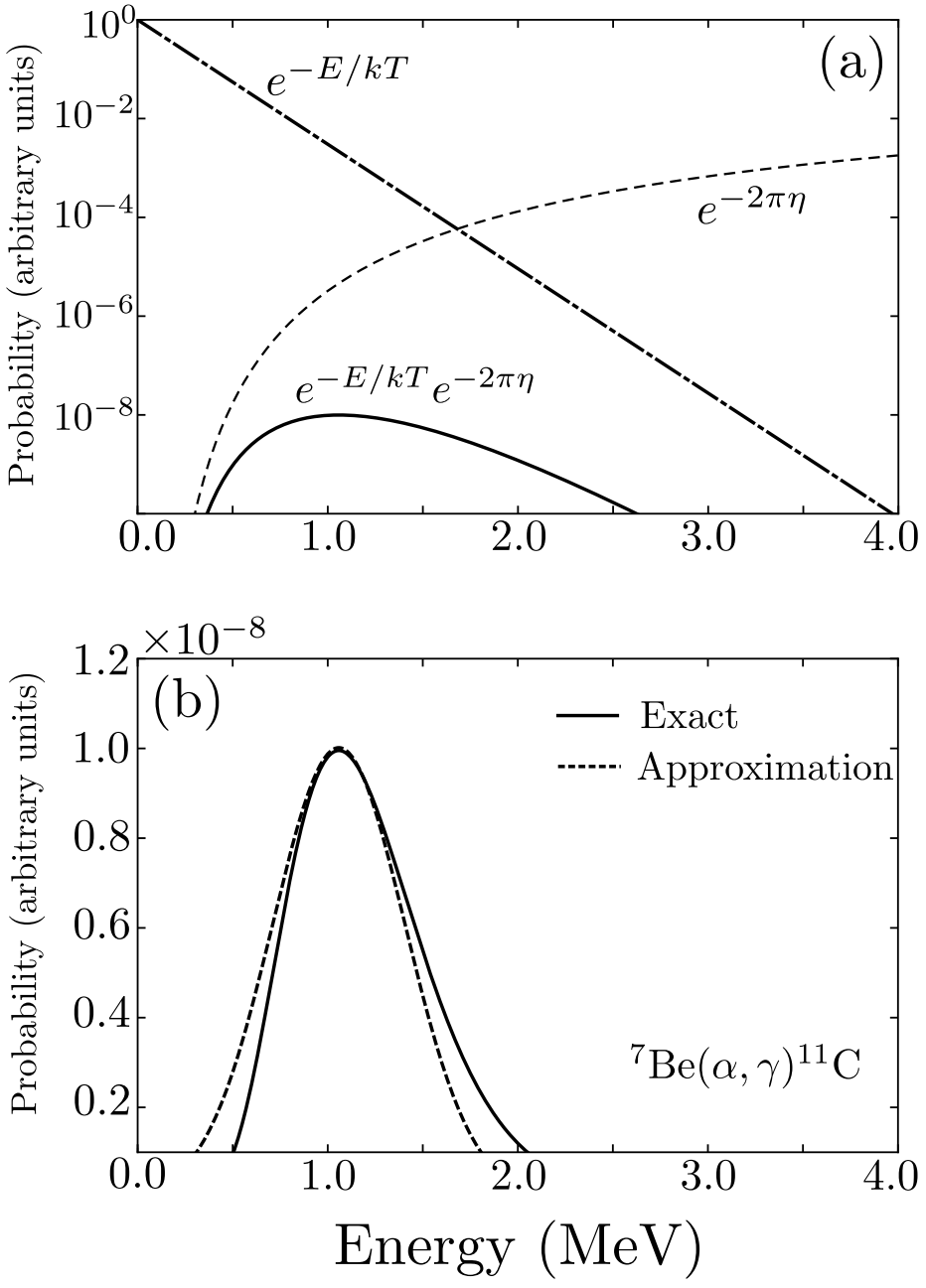

Figure 2.1: (a) Transmission probability ($e^{-2\pi\eta}$, dashed line), Maxwell–Boltzmann distribution ($e^{-E/kT}$, dashed–dotted line) and their product (Gamow peak) for the ^{7}Be$(\alpha,\gamma)^{11}$C reaction at $T_9 = 2$. (b) The Gamow peak shown in linear scale (solid line) with the Gaussian approximation (dashed line).

2.2.2 Resonant Reactions

In the following we shall calculate the rate for charged–particle reactions that are dominated by resonances of the compound nucleus, $c^{\star}$. More specifically, we will focus our discussion on resonances which have approximately constant partial widths over the total resonance width ($\Gamma(E)/E_r < 0.1$, called narrow) and in addition do not overlap significantly with other resonances (isolated). The cross section can be described by the single–level Breit–Wigner formula

$$\sigma(E) = \frac{\lambda^2}{4\pi}\frac{(2J+1)}{(2j_a+1)(2j_b+1)}(1+\delta_{ab})\frac{\Gamma_1(E)\Gamma_2(E)}{(E_r-E)^2+(\Gamma(E)/2)^2} \tag{2.14}$$

where λ is the de Broglie wavelength, which expresses the wave nature of the interacting particles, j_i are the spin of projectile and target, J and E_r are the spin and energy of the resonance respectively, Γ_i are the partial widths for entrance and exit channels and Γ is the sum of all the partial widths Γ_i, which correspond to the energetically allowed decay channels.

According to Heisenberg's uncertainty principle, the lifetime τ of any resonant state is connected with its total width Γ by $\tau\ \Gamma = \hbar$. The ratio of an individual width Γ_i and the total width Γ defines the probability that the compound nucleus will decay via the i^{th} channel. Figure 2.2 shows the cross section for a narrow and isolated resonance of the $^{7}\text{Be}(\alpha,\gamma)^{11}\text{C}$ reaction represented by a Breit–Wigner function.

Returning to Equation 2.5 and assuming a single narrow resonance, we can replace the Maxwell–Boltzmann factor and the partial widths with their values at E_r and calculate the integral analytically

$$N_A\langle\sigma v\rangle_{ab} = N_A\left(\frac{2\pi}{\mu kT}\right)^{3/2}\hbar^2\omega\gamma e^{-E_r/kT} \tag{2.15}$$

where $\omega = (2J+1)(1+\delta_{ab})/(2j_a+1)(2j_b+1)$ is the nuclear spin factor and $\omega\gamma$ is called the resonance strength

$$\omega\gamma \equiv \omega\frac{\Gamma_1\Gamma_2}{\Gamma} \propto \int_0^\infty \sigma(E)dE \tag{2.16}$$

It is proportional to the area under the resonance cross section, or the product of the total resonance width and the cross section at the resonance energy, $\Gamma\cdot\sigma(\text{E}=\text{E}_\text{r})$,

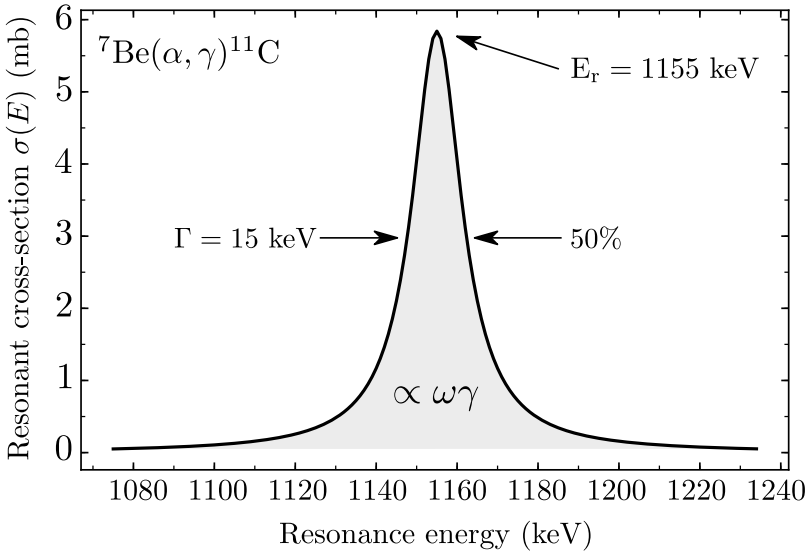

Figure 2.2: Resonant cross section, $\sigma(E)$ as a function of energy for the E_r= 1155 keV resonance of the ^{7}Be$(\alpha,\gamma)^{11}$C reaction. The resonance energy E_r and total width Γ are shown. See the text for details.

and it is measured in units of energy. The resonance strength essentially expresses the contribution of the resonance to the total reaction rate.

For a charged–particle reaction with many narrow and isolated resonances, the total reaction rate can be calculated by adding incoherently the contribution from each resonance (Equation 2.15)

$$N_A\langle\sigma v\rangle = N_A\left(\frac{2\pi}{\mu kT}\right)^{3/2}\hbar^2\sum_i(\omega\gamma)_i\ e^{-E_i/kT} \tag{2.17}$$
$$= \frac{1.5399\times10^{11}}{(\mu T_9)^{3/2}}\sum_i(\omega\gamma)_i\ e^{-11.605E_i/T_9}\ (\mathrm{cm}^3\ \mathrm{mol}^{-1}\ \mathrm{s}^{-1})$$

where $(\omega\gamma)_i$ and E_i are expressed in units of MeV.

There are a few points that need to be addressed regarding the calculation of a reaction rate dominated by resonances using Equation 2.17. The first one is that the resonance energy is an extremely important ingredient for the calculation of the reaction rate, since it enters exponentially in the above relation. For example, a

change of the resonance energy by 10 keV, which is a typical uncertainty for a charged–particle spectroscopy experiment, at kT = 129 keV ($T_9 = 1.5$, which is typical for the νp–process and explosive nucleosynthesis in general) can result in a $\sim 10\%$ change in its contribution to the total reaction rate. In the case that the aforementioned resonance dominates the total reaction rate, that change can have a significant impact. Iliadis (2019) has recently shown that the calculation of a resonance energy E_r from the reaction Q value, through

$$E_r = E_x - Q_{atomic} \tag{2.18}$$

where E_x is the excitation energy level of the product nucleus, can introduce an error on the contribution of the resonance to the reaction rate. Specifically, the use of the atomic, instead of the nuclear masses, can change E_r by a few keV. This argument is valid in our context, since in an astrophysical environment the gas is ionized, so the electron binding energy should not be taken into account.

The second point is regarding the influence of partial widths and the notion of the Gamow peak. Let us assume our general nuclear reaction, $a + b \rightarrow c^\star \rightarrow \gamma + e$, with only two channels being open, that is $\Gamma = \Gamma_1 + \Gamma_2$, and the compound nucleus emits a γ ray, so that $\Gamma_2 = \Gamma_\gamma$. It is customary in the nuclear astrophysics community to attribute great importance to all the resonances located inside the Gamow peak, usually $E_0 \pm \Delta/2$, on the premise that they all contribute significantly to the total reaction rate. In fact, this assumption is justified only when the total resonance width is dominated by the γ partial width, that is, $\Gamma_\gamma \gg \Gamma_1$ (Iliadis, 2015). The resonance strength will then depend only on the charged–particle width, remember the definition in Equation 2.16, and in that case the resonances inside the Gamow peak will contribute significantly to the total reaction rate.

On the other hand, when the γ ray partial width is much smaller than the particle width, $\Gamma_1 \gg \Gamma_\gamma$, the resonance strength depends only on the γ ray partial width. In that case, the Gamow peak argument cannot be justified, since it does not exist. Instead, the individual resonance contribution to the total reaction rate depends on the Boltzmann factor $e^{-E/kT}$, which increases rapidly with decreasing energy, meaning that the low energy resonances dominate the reaction rate.

In any case, resonant thermonuclear reaction rates are usually higher than non–resonant rates by a factor of around 10^5 (Cameron, 1957). This indicates the extreme

importance of knowing whether there are resonances in the thermonuclear energy region when considering the astrophysical importance of specific nuclear reactions. However, that does not imply that non–resonant reactions are not important. In some cases, the non–resonant contribution can be very important.

2.3 Nuclear Reaction Networks

The thermonuclear reaction rates we studied in the previous section are used to calculate the abundance evolution of nuclear species and the energy release by these reactions in an astrophysical environment. A system of first–order coupled differential equations, which describes this abundance evolution and energy generation is called a nuclear reaction network. The size of these networks can vary according to the astrophysical environment, with quiescent stellar burning being much smaller compared to explosive burning. For example, a νp–process nucleosynthesis network can include 5,000 nuclei and around 50,000 reactions. In this section we shall introduce nuclear reaction networks and in Section 6.4 we shall present the study of a νp–process nucleosynthesis network.

To begin, the abundance, or number fraction, $\mathrm{Y}_i = n_i/(\rho N_A)$, of the nuclear species i in an astrophysical environment is a dynamical quantity, dependent on the nuclear processes that occur. It is more convenient to use abundances rather than number densities n_i in reaction network calculations since the latter quantity changes with both the number of the species i and the volume of the astrophysical system (Lippuner and Roberts, 2017). Most reactions can be grouped into three functional categories, according to the number of interacting nuclei: reactions involving a single nucleus, such as decays and electron/positron captures, two (*e.g.* $^{7}\mathrm{Be}(\alpha,\gamma)^{11}\mathrm{C}$) and three (*e.g.* $^{4}\mathrm{He}(\alpha\alpha,\gamma)^{12}\mathrm{C}$ – triple–α reaction) nuclei (Hix and Thielemann, 1999). We can write a generalized abundance evolution equation for Y_i, or rate equation, as follows

$$\frac{\mathrm{dY_i}}{\mathrm{dt}} = \underbrace{\sum_j \lambda_j Y_j}_{\text{1–body reactions}} + \underbrace{\sum_{j,k} \lambda_{jk} Y_j Y_k}_{\text{2-body reactions}} + \underbrace{\sum_{j,k,l} \lambda_{jkl} Y_j Y_k Y_l}_{\text{3-body reactions}} \tag{2.19}$$

where the quantities λ_j, $\lambda_{j,k}$ and $\lambda_{j,k,l}$ are the rates of these reactions, which are

related to the thermonuclear reaction rates we calculated earlier in this chapter. For the case of a two–body reaction, we can write

$$\lambda_{ij} = \mathcal{N}^{i}_{j,k}(\rho N_A)\langle\sigma v\rangle_{ij} \tag{2.20}$$

with $\mathcal{N}^{i}_{j,k} = N_i/\prod_{m=1}^{n_m}|N_{j_m}!|$ being used for a proper counting of the number of nuclei involved in the reaction.

Figure 2.3 shows a schematic representation of the different processes that create and destroy ^{7}Be and Equation 2.19 gives us its abundance evolution

$$\frac{dY_{^7\mathrm{Be}}}{dt} = \lambda_{^3\mathrm{He},\alpha}Y_{^3\mathrm{He}}Y_{^4\mathrm{He}} + \lambda_{^6\mathrm{Li},p}Y_{^6\mathrm{Li}}Y_{^1\mathrm{H}} - \lambda_{\beta^+}Y_{^7\mathrm{Be}} - \lambda_{^7\mathrm{Be},\alpha}Y_{^7\mathrm{Be}}Y_{^4\mathrm{He}} + \cdots \tag{2.21}$$

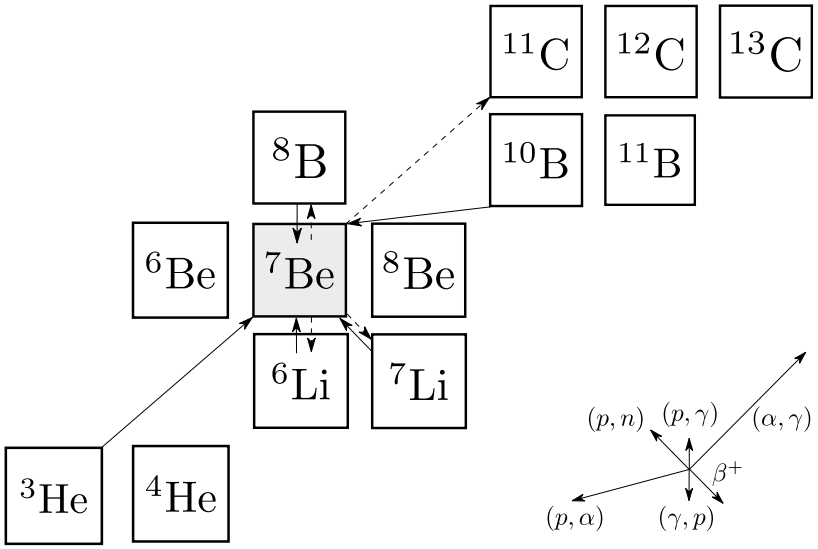

Figure 2.3: Relevant part of the chart of the nuclides showing nuclear processes that create (solid arrows) and destroy (dashed arrows) ^{7}Be.

In the special case of Nuclear Statistical Equilibrium (NSE), where all nuclides are in equilibrium via strong and electromagnetic interactions, the reaction network is greatly simplified and the abundance, Y_i, of each species can be calculated in terms

of the free protons, Y_p, and neutrons, Y_n, by applying the Saha equation

$$\frac{dY_i}{dt} = 0 \tag{2.22a}$$

$$Y_i = G_i \left(\rho N_A\right)^{A_i - 1} \frac{A_i^{3/2}}{2_i^A} \left(\frac{2\pi\hbar^2}{mkT}\right)^{\frac{3}{2}(A_i-1)} e^{B_i/kT} Y_n^{N_i} Y_p^{Z_i} \tag{2.22b}$$

where G_i and B_i is the partition function and binding energy of species i, A is its mass number, N the number of neutrons, Z the number of protons and ρ and T are the density and temperature of the environment. The unique solution of the network for (T, ρ, Y_e) can be obtained using two constraints, namely mass and charge conservation

$$\sum_i A_i Y_i = 1 \tag{2.23a}$$

$$\sum_i Z_i Y_i = Y_e \tag{2.23b}$$

The energy released by nuclear reactions in an astrophysical environment, $\epsilon_{\text{nuclear}}$, can be calculated using Equation 2.19

$$\epsilon_{nuclear} = -\sum_i N_A m_i c^2 \frac{dY_i}{dt} \text{ (MeV/g s)} \tag{2.24}$$

where $m_i c^2$ is the rest mass energy of species i in MeV.

Thermonuclear reaction networks, like the ones that we will encounter later in this thesis (Section 6.4), are known to be very stiff, meaning that their solution is numerically unstable, and as such, smaller steps of integration must be used. Stiffness in a network arises from the fact that its differential equations include very slow and very fast reactions simultaneously. For this reason, it is computational challenging to include many species in a stellar evolution hydrodynamic code since it causes a slowdown on its performance, and thus post–processing nucleosynthesis calculations are preferred (José, 2016).

Various numerical techniques can be used to solve (integrate) such networks. Reaction network codes, such as NuGrid `NuPPN` (see Section 6.4), employ mostly the backward (implicit) Euler method, "Wagoner's method" (Wagoner, 1969), Gear's

method (Gear, 1971) or the Bader–Deuflhard semi–implicit method (Bader and Deuflhard, 1983). For more details on the integration of nuclear reaction networks, we refer the reader to the work of Timmes (1999) and of Longland et al. (2014).

2.4 Laboratory Reaction Yields

The calculation of a thermonuclear reaction rate in a laboratory setting requires the knowledge of the reaction cross section, which expresses the probability that the particular interaction will occur. Nevertheless, in a nuclear astrophysics experiment, what is usually measured is the total number of reactions that occur, $\mathcal{N}_{\mathcal{R}}$, and the total number of incident beam particles, $\mathcal{N}_{\mathcal{B}}$. Their ratio

$$Y = \frac{\mathcal{N}_{\mathcal{R}}}{\mathcal{N}_{\mathcal{B}}} \tag{2.25}$$

is called the reaction yield. In fact, an experimental setup has a finite detection efficiency η and does not detect the total number of reactions, but rather a fraction of it, $\mathcal{N}_r$. The experimental yield is given by

$$Y = \frac{\mathcal{N}_r}{\mathcal{N}_{\mathcal{B}}\ \eta} \tag{2.26}$$

In Chapter 5, we shall discuss in more detail how this equation is derived and the specifics of the detection efficiency for the experimental apparatus of the present thesis.

The reaction yield can also be expressed as a relation between the reaction cross section σ and the characteristics of a target with thickness Δx and number density of active target nuclei n

$$Y = \sigma\ n\ \Delta x \tag{2.27}$$

Suppose that a beam of particles with energy E impinges on a target. We can divide the target in thin slices of thickness Δx_i and assume that both the cross section σ_i and the rate of energy loss, or stopping power ϵ_i, are constant over each slice. To calculate the total yield we will have to integrate over all the slices

$$Y = \int \sigma(x) n(x) dx = \int \sigma(x) n(x) dx \frac{dE(x)}{dx} \frac{dx}{dE(x)} \tag{2.28}$$

In fact, the beam will lose energy as it travels through the target. The stopping power can be expressed as

$$\epsilon(E) = -\frac{1}{n(x)}\frac{dE}{dx} \tag{2.29}$$

Including this in Equation 2.28, we obtain for the yield

$$Y = \int_{E-\Delta E}^{E} \frac{\sigma(E)}{\epsilon(E)} dE \tag{2.30}$$

where ΔE is the total energy loss by the beam in the target, *i.e.*, the target thickness expressed in energy units.

For the case of a narrow resonance with constant stopping power over the resonance width, we can express Equation 2.30 using our known Breit–Wigner cross section formula (Equation 2.14), and solve it analytically (Fowler et al., 1948)

$$\begin{aligned} Y(E) &= \int_{E-\Delta E}^{E} \frac{1}{\epsilon_0}\frac{\lambda^2}{4\pi}\omega\frac{\Gamma_1\Gamma_2}{(E_r-E)+(\Gamma/2)^2}dE \\ &= \frac{\lambda_r^2}{2\pi}\ \frac{\omega\gamma}{\epsilon_r}\ \frac{\Gamma}{2}\int_{E+\Delta E}^{E}\frac{dE}{(E_r-E)^2+(\Gamma/2)^2} \\ &= \frac{\lambda_r^2}{2\pi}\ \frac{\omega\gamma}{\epsilon_r}\left[\arctan\left(\frac{E-E_r}{\Gamma/2}\right)-\arctan\left(\frac{E-E_r-\Delta E}{\Gamma/2}\right)\right] \end{aligned} \tag{2.31}$$

where λ_r and ϵ_r are the de Broglie wavelength and the stopping power at the resonance energy, $\mathrm{E_r}$, respectively.

Figure 2.4 shows the corresponding yield for the resonance shown in Figure 2.2 for different target thicknesses. In the case of an infinitely thick target, that is, $\Delta E \to \infty$, or equivalently $\Delta E \gg \Gamma$, we can obtain a simple relation between the maximum reaction yield, $\mathrm{Y_{max}}$, and the resonance strength, $\omega\gamma$, by integrating Equation 2.31

$$Y_{max,\Delta E\to\infty} = \frac{\lambda_r^2}{2}\frac{\omega\gamma}{\epsilon_r} = \frac{\lambda_r^2}{2}\frac{m_a+m_b}{m_b}\frac{\omega\gamma}{\epsilon_r} \tag{2.32}$$

where in the last step we expressed the stopping power in the center–of–mass system with m_a and m_b the masses of the projectile and the target respectively.

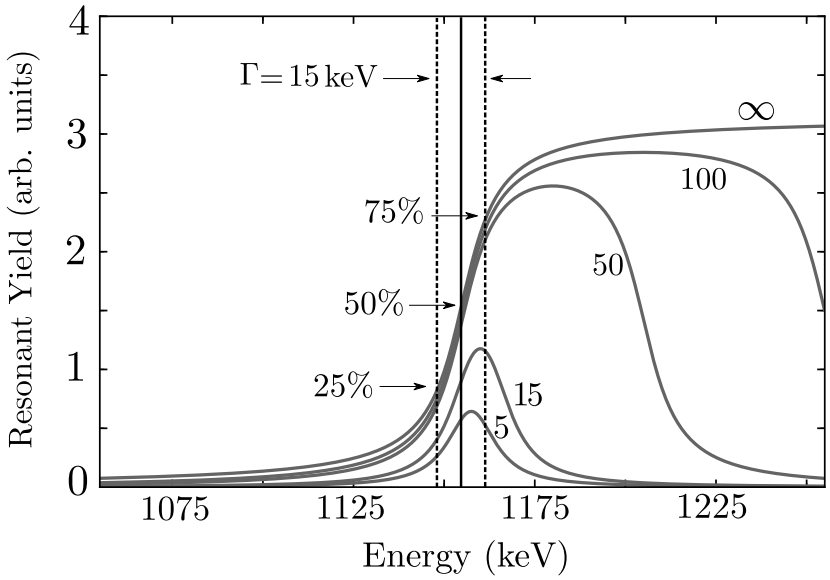

Figure 2.4: Yield from the resonance of the ^{7}Be$(\alpha,\gamma)^{11}$C reaction (E_r= 1155 keV, Γ= 15 keV) for different target thickness ΔE, ranging from 5 keV to 100 keV. The case of infinite thickness is also shown.

The resonance strength can then be determined experimentally using

$$\omega\gamma = \frac{2Y_{max,\Delta E\to\infty}\epsilon}{\lambda_r^2}\frac{m_b}{m_a+m_b} \tag{2.33}$$

The DRAGON facility at TRIUMF can measure resonance strengths of astrophysically interesting reactions using this thick target yield technique (Hutcheon et al., 2003). In Chapters 4 and 5 we shall focus on the experimental details of such measurements.

2.5 Kinematics of Radiative Capture Reactions

Let us recall the nuclear reaction $a + b \to c^\star \to d + e$[1]. If particle d is a photon, the reaction is called a radiative capture. This class of reactions is of extreme importance for astrophysics, as the reader might recall from the previous chapter (for example the ^{4}He$(\alpha\alpha,\gamma)^{12}$C – triple–$\alpha$, ^{7}Be$(\alpha,\gamma)^{11}$C reactions, and others).

[1] An equivalent way to describe this reaction is $a(b,d)e$, which is commonly used in nuclear physics.

Figure 2.5 shows the radiative capture of ^{4}He on ^{7}Be (α = ^{7}Be, b = ^{4}He and e = ^{11}C). In the resonant case, which is more important for astrophysics since the cross section is greatly enhanced, the two particles fuse into an excited state of the compound nucleus $^{11}C^{\star}$, with energy $E_x = E_r + Q_{nuclear}$, where E_r is the corresponding resonance energy and $Q_{nuclear}$ is the energy released by a reaction, given by the mass difference between reacting and product nuclei and accounting for the binding energy of the electrons. These resonant states are usually short–lived ($\tau \leq 10^{-12}$ s) and decay with the emission of one or multiple γ rays. Their total energy, according to conservation of energy, will be E_x, leaving the product nucleus in its ground state. It is worth noting that there is a small correction for the γ energies, called the recoil shift, which is caused by the energy shift of the recoil nucleus. The recoil shift can be considered negligible for γ energies between 100 keV and 15 MeV. Specifically, for the γ transitions that DRAGON detects, $E_\gamma \approx 0.1 - 10$ MeV and ΔE_{rec} is $\approx 10^{-4}$ MeV (Iliadis, 2015).

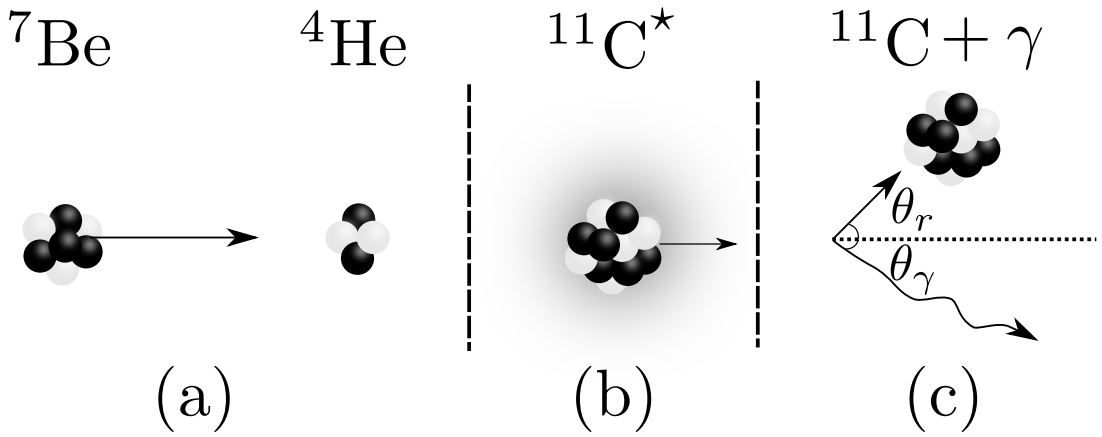

Figure 2.5: Schematic representation of a radiative α–capture on ^{7}Be in inverse kinematics in the lab system: (a) beam (^{7}Be) and target (^{4}He) particles interact, (b) the compound nucleus (^{11}C) is synthesised in an excited state and then, (c) it decays by emitting a γ ray. The recoil nucleus and the γ ray are emitted at angles θ_r and θ_γ respectively.

Radiative capture reactions are generally studied experimentally using two different methods: the forward kinematics method, where the light ion, in our example ^{4}He, impinges on a heavier ion target, ^{7}Be, and the inverse kinematics method, where

the heavy ion impinges on a usually gaseous light ion target. In the first case, one can only detect γ rays of the compound nucleus, since the target is too thick to allow the compound nucleus to escape, whereas in the latter, one can detect both prompt γ rays and the product of the reaction. Each technique has its advantages and drawbacks, which we shall discuss in Chapter 4. In this thesis, we are studying a radiative capture reaction in inverse kinematics, and for this reason, we shall focus our discussion on the specifics of that method.

Let us consider the general radiative capture reaction $a+b \rightarrow c^{\star} \rightarrow d+\gamma$ in inverse kinematics, with particle b being at rest. The product nucleus d in the framework of inverse kinematics reactions is also called the recoil nucleus. Conservation of energy and linear momentum gives the following three equations

$$m_a c^2 + E_a + m_b c^2 = m_d c^2 + E_d + E_\gamma \tag{2.34a}$$

$$\sqrt{2m_a E_a} = \frac{E_\gamma}{c}\cos\theta_\gamma + \sqrt{2m_d E_d}\cos\theta_r \tag{2.34b}$$

$$0 = \frac{E_\gamma}{c}\sin\theta_\gamma - \sqrt{2m_d E_d}\sin\theta_r \tag{2.34c}$$

where E_i and m_i denote kinetic energy and rest mass respectively. Solving the system of equations for the linear momentum of the recoil we find that

$$p_d = \sqrt{2E_a\ m_a}\left(1 \pm \frac{E_\gamma}{\sqrt{2m_a E_a\ c^2}}\right) \tag{2.35}$$

where the $\pm$ sign indicates whether the photon is emitted parallel or anti–parallel to the beam direction.

Taking now the ratio of Equations 2.34b and 2.34c for the special case of a single γ transition perpendicular to the beam direction, that is $\theta_\gamma = \pi/2$, we obtain the maximum angle for the recoil nucleus

$$\theta_{r,max} = \arctan\left(\frac{E_\gamma}{\sqrt{2m_a c^2 E_a}}\right) = \arctan\left(\frac{E+Q}{\sqrt{2\frac{m_a}{m_b}(m_a+m_b)c^2 E}}\right) \tag{2.36}$$

where E is the center–of–mass energy of the reactants.

The maximum recoil angle for the energies relevant to νp–process nucleosynthesis

for the $^{7}\mathrm{Be}(\alpha,\gamma)^{11}\mathrm{C}$ reaction is $\theta_{r,max} \sim 40 - 56$ mrad. The minimum of the above relation appears at E=Q. This behaviour is very interesting, since in the astrophysically relevant energy region, reactions with relatively smaller Q values have increasing $\theta_{r,max}$ with increasing energy, while reactions with higher Q values exhibit the opposite behaviour. This has implications for the feasibility of experimental studies in inverse kinematics, as we shall discuss below. Figure 2.6 shows the maximum laboratory recoil half–angle for some astrophysically important radiative capture reactions, including $^{7}\mathrm{Be}(\alpha,\gamma)^{11}\mathrm{C}$.

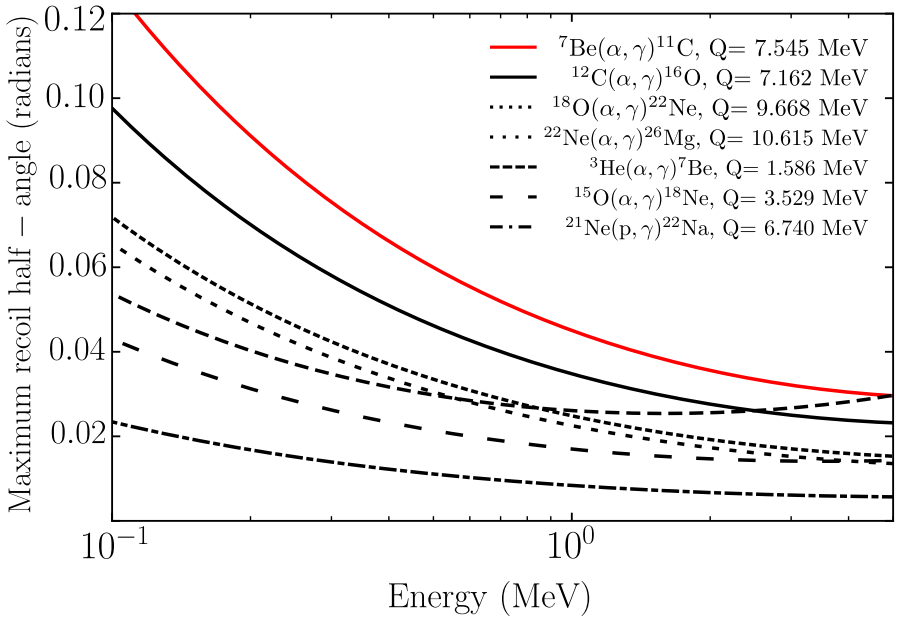

Figure 2.6: Maximum laboratory recoil momentum cone half–angle, $\theta_{r,max}$, versus center–of–mass energy for some astrophysically important reactions. See the text for details.

Recoil separators are detection systems that are designed to study radiative capture reactions in inverse kinematics and have the ability to detect both the prompt γ rays and the recoil nucleus. In addition, they have a finite geometric and energy acceptance, meaning that they can accept recoils up to a specific angle θ_r and energy E_{rec}. DRAGON, for example has a geometric acceptance of $\pm$ 21 mrad at the central energy and an energy acceptance of $\pm$ 4% at the central trajectory. In Chapter 4 we

shall explore the characteristics of DRAGON in more detail.

Thus far, we have discussed only about the maximum recoil angle $\theta_{r,max}$. In an experiment, however, the recoils have a distribution of angles that can be either higher or lower than $\theta_{r,max}$, according to the reaction. In the following, we shall demonstrate how the characteristics of a radiative capture reaction, specifically the number of γ rays emitted by the compound nucleus and their angular distribution, can affect the distribution of recoil angles and subsequently the efficiency of the detection system, η (Equation 2.19).

Figure 2.7 shows an inverse kinematics distribution of recoil angles from a resonance at E_r= 1155 keV of the ^{7}Be$(\alpha,\gamma)^{11}$C reaction for two different cases: a single transition to the ground state, and a cascade of four γ rays. It is evident from the figure that a single transition to the ground state shifts the average recoil angular distribution towards the maximum, $\theta_{r,max} \simeq 42$ mrad. Therefore, it is very important to know both the number of γ rays in the cascade, as well as their relative intensities, or branching ratios. When branching ratios of a resonance state are unknown, simulations have to be used to calculate the γ ray detection efficiency. Combining simulations with experimental γ ray information one can also determine the unknown branching ratios experimentally (Ruiz et al., 2014).

If we now consider several γ rays in a cascade, the recoil angular distribution also depends on the different nuclear level spins and the multipole mixing ratios of the γ transitions, which can become very complicated to calculate. For a formal treatment of γ angular correlations, the interested reader is referred to Ferguson (1965) and (Rose and Brink, 1967). To illustrate the aforementioned effect, Figure 2.7 shows the same resonance of the ^{7}Be$(\alpha,\gamma)^{11}$C reaction, but for three different γ angular distributions for the dominant transition: isotropic, dipole and quadrupole. The dipole angular distribution shifts the recoils towards higher angles higher, while the quadrupole tends to decrease them. For a more detailed discussion, the reader is referred to Ruiz et al. (2014).

In Section 5.1 we shall discuss how one can account for both those factors when planning experiments and analyzing experimental data on DRAGON, by performing detailed simulations of the experimental setup.

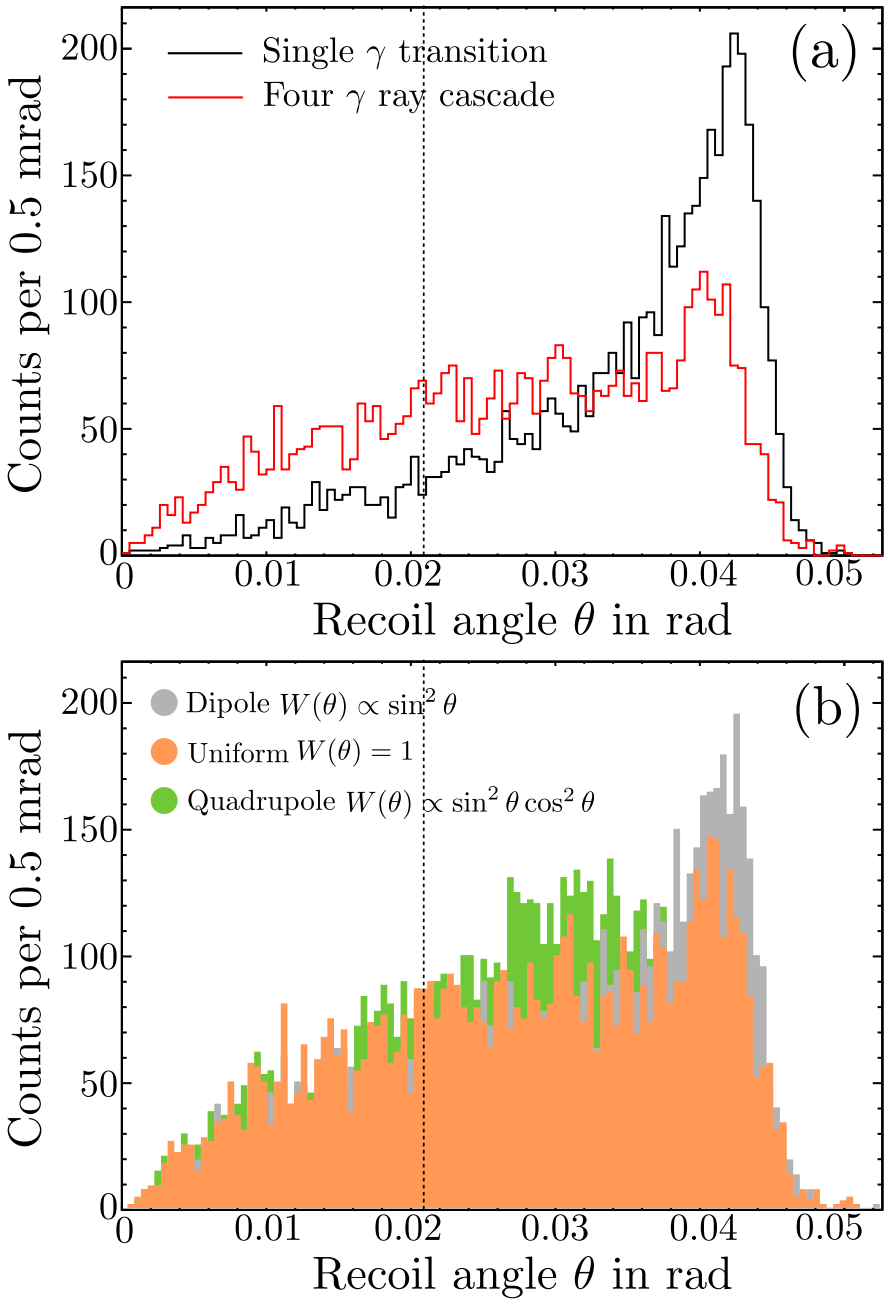

Figure 2.7: GEANT simulations for the recoil angular distributions of the E_r= 1155 keV resonance of the ^{7}Be$(\alpha,\gamma)^{11}$C reaction, by changing a) the number of γ rays emitted from the excited state and b) their angular distribution. The vertical line shows the angular acceptance of the DRAGON recoil separator ($\pm$ 21 mrad). See text for details and Section 5.1 for a discussion on the GEANT simulations.

2.6 Summary

To summarize, in this chapter we explored the theoretical considerations for a nuclear astrophysics experiment, such as the thermonuclear reaction rate and the reaction kinematics and yields. We focused our discussion on resonances of radiative capture reactions, since this is the topic of the present thesis. We shall proceed in the next chapter with an overview of our current knowledge of the $^{7}\mathrm{Be}(\alpha,\gamma)^{11}\mathrm{C}$ reaction and we shall present motivation for the present work.

Chapter 3

^{7}Be$(\alpha,\gamma)^{11}$C: Present Status

3.1 Overview

After having explored the importance of nuclear reactions for stellar evolution, energy generation and the origin of the chemical elements in the cosmos and presented the stellar reaction rate formalism in the last two chapters, the next step is to look into the reaction studied in this thesis in more detail. Prior to every nuclear astrophysics experiment the researcher must first identify the importance of a specific reaction in a certain energy range, which also reveals the astrophysical environment(s) and the nucleosynthesis process(es). After that, a detailed study of all the known experimental or theoretical knowledge with its associated uncertainty follows. In case there are unknown or very uncertain parameters that will have a significant effect on the reaction rate in the relevant energy range and subsequently in the nucleosynthesis process, then the experiment is necessary to be performed.

In this chapter we shall give an overview of the current status for the ^{7}Be$(\alpha,\gamma)^{11}$C reaction with all the relevant information for the calculation of its rate and present the open questions that motivate the present work.

The ^{7}Be$(\alpha,\gamma)^{11}$C reaction is a very interesting case because even though it involves two radioactive species, one of them is long–lived isotope ($t_{1/2}(^{7}\mathrm{Be}) = 53.12(6)$ d) and for that reason studies in forward kinematics with radioactive targets are possible, as we shall see below.

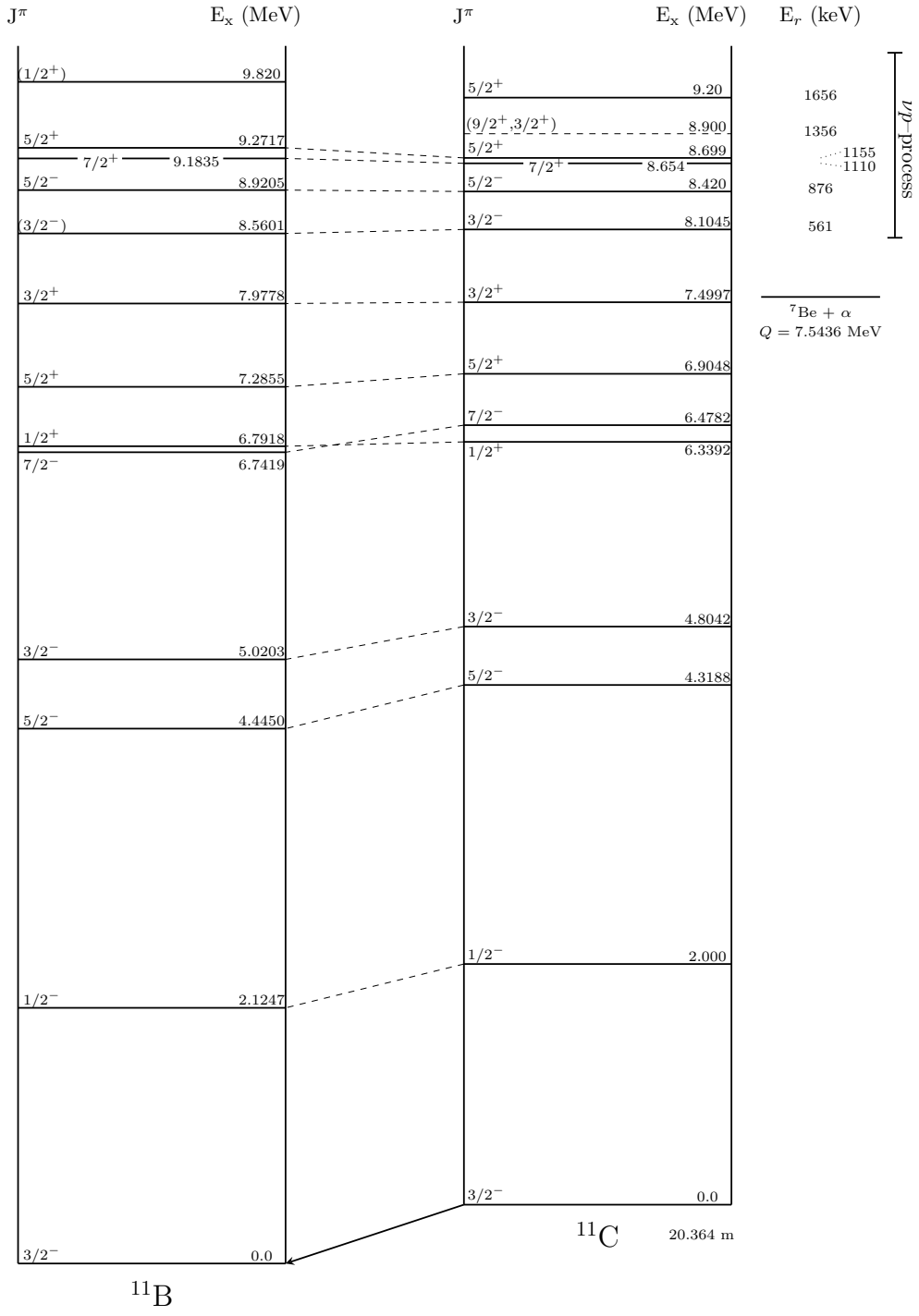

Figure 3.1: Level scheme of the mirror nuclei ^{11}C and ^{11}B adopted from Kelley et al. (2012), with the addition of the $E_x = 8.900$ MeV state from Yamaguchi et al. (2013). The dashed lines indicate isobaric analog states, and next to the ^{11}C scheme we present the α separation energy Q_α, the resonances of the ^{7}Be$(\alpha,\gamma)^{11}$C reaction, E_r, in keV and the relevant energy region for νp–process nucleosynthesis.

3.2 Previous measurements

Figure 3.1 shows the current level structure of ^{11}C and its mirror nucleus ^{11}B from the A = 11 data compilation of Kelley et al. (2012). Six resonances are located inside the relevant energy region for νp–process nucleosynthesis and a summary of their parameters are shown in Table 3.1. Recalling our discussion from Section 2.2.2, not all of these resonances contribute equally to the reaction rate, because the γ partial width is much smaller than the α–particle width ($\Gamma_\alpha \gg \Gamma_\gamma$). For this reason the most important contribution to the total reaction rate originates from the low energy resonances. In the following, we shall briefly review the experiments that studied these resonances of interest.

Table 3.1: Resonance parameters for the ^{7}Be$(\alpha,\gamma)^{11}$C reaction. Experimentally measured resonance strengths are adopted from Kelley et al. (2012). Tentative assignments and estimates are presented in parentheses.

$\mathbf{E_x}$ (MeV)	$\mathbf{E_r}$ (keV)	$\mathbf{J^\pi}$	$\mathbf{\Gamma}$	$\mathbf{\Gamma_\gamma}$ (eV)	$\boldsymbol{\omega\gamma}$ (eV)
8.1045(17)	561(2)	$3/2^-$	6^{+12}_{-2} eV	0.350(56)	0.331
8.420(2)	876(2)	$5/2^-$	12.6(38) eV	3.1(13)	3.80
8.654(4)	1110(4)	$7/2^+$	$\leq$ 5 keV		
8.699(2)	1155(2)	$5/2^+$	15(1) keV	$2.60(15) \times 10^{-4} \cdot \Gamma$	
8.900	1356	$(9/2^+)$	>8 keV	(0.48)	(1.2)
9.20(5)	1657(50)	$5/2^+$	500(80) keV		

3.2.1 The E_r = 561 & 876 keV resonances

The two lowest–lying energy resonances of the ^{7}Be$(\alpha,\gamma)^{11}$C reaction, which correspond to the E_x = 8.105 and 8.420 MeV levels in ^{11}C, were studied by Hardie et al. (1984) in forward kinematics at Argonne National Laboratory.

A singly charged ^{4}He ion beam was accelerated in the 4.5 MV Dynamitron accelerator at a maximum current of 15 μA (beam intensity of 9.4 $\times$ 10^{13} pps) and impinged on a radioactive ^{7}Be target. The target was produced using the molecular plating method by the ^{7}Li$(p,n)^7$Be reaction (Filippone and Wahlgren, 1986) with initial activity of 80 mCi and ^{7}Li:^{7}Be ratio of less than 5×10^{-3}. However, by the time of the experiment, half of the original ^{7}Be in the target had decayed into ^{7}Li,

because the target was first used for the measurement of the ^{7}Be$(p,\gamma)^{8}$B reaction by Filippone et al. (1983).

The experimental setup comprised two detectors for the γ rays from the de–excitation of the ^{11}C nucleus, a Ge(Li) detector and a NaI(Tl) detector. The detectors were placed at 55° and 90° to the beam direction respectively, and lead between target and detectors blocked the γ rays from the 478 keV line of the ^{7}Be decay. The γ ray spectra were used to determine the branching ratios of the two resonances (see Table 3.2).

The authors used two methods to calculate the resonance strengths: the first was the thick target yield formula, similar to Equation 2.32, and the second was a complementary relative method which employed the presence of ^{7}Li in the target and the fact that they were studying ^{7}Li$(\alpha,\gamma)^{11}$B reaction in the same campaign. More specifically, the relative method provided the resonance strength ratio between the resonances of interest in ^{7}Be$(\alpha,\gamma)^{11}$C and the known E_r = 660 keV (E_x = 9.272 MeV in ^{11}B) resonance of the ^{7}Li$(\alpha,\gamma)^{11}$B reaction, reported in the same work. The main advantage of this method is that both the ^{7}Li:^{7}Be ratio in the target and the detector efficiencies are more accurately known than the number of ^{7}Be atoms alone and the absolute efficiencies. Nevertheless, one has to include an extra uncertainty factor from the ^{7}Li$(\alpha,\gamma)^{11}$B resonance. The adopted values for the two resonance strengths in Table 3.1 are the weighted averages of the two methods.

Using Equation 2.16 and considering negligible γ widths, the authors compared the experimentally deduced α–particle widths (Γ_α) for the two resonances with shell–model calculations by Kurath (1973). Their results agree well for the E_r = 876 keV resonance ($\Gamma_\alpha^{\text{Exp.}} = 12.6\pm 3.8$ eV & $\Gamma_\alpha^{\text{Calc.}} = 11$ eV), but strongly disagree for the E_r = 561 keV resonance ($\Gamma_\alpha^{\text{Exp.}} = 6^{+12}_{-2}$ eV & $\Gamma_\alpha^{\text{Calc.}} = 53$ eV).

3.2.2 The E_r = 1110 & 1155 keV resonances

Wiescher et al. (1983) studied the E_r = 1110 and 1155 keV resonances, which correspond to the E_x = 8.654 and 8.699 MeV levels in ^{11}C, using the ^{10}B$(p,\gamma)^{11}$C reaction in forward kinematics employing three different linear accelerators (7 MV Super-CN Van de Graaff at Ohio State University, 1 MV Van de Graaff at the University of Toronto and 350 kV accelerator at the University of Münster), covering a wide energy range (E_x = 8 – 10.7 MeV).

Enriched ^{10}B targets of different thicknesses were irradiated using proton beams with intensities of 15–300 μA, depending on the accelerator used. γ rays of interest were detected using high resolution Ge(Li) detectors and thick lead shields were used to decrease background radiation. In all three experimental setups, more than one detector were used, allowing for angular distribution measurements. Specifically, at the University of Toronto and Ohio State the authors studied the angular distribution over seven angles using two detectors and in Münster over four angles (0°, 45°, 90° and 135°) using three detectors.

The authors observed primary γ transitions from the E_x = 8.654 and 8.699 MeV states and calculated the ratio Γ_γ/Γ for them using the cross sections from the γ ray and α–particle channels, $\sigma(p,\gamma)/\sigma(p,\alpha)$. Using their measurements, we can estimate the corresponding resonance strengths, using Equation 2.16, to be <600 eV and 6.24 eV respectively. The branching ratios for the resonance at E_r = 1155 keV were also determined and are presented in Table 3.2.

Table 3.2: γ ray branching ratios for excited states of ^{11}C nucleus adopted from Kelley et al. (2012). For the E_r= 1110 keV resonance, the branching ratios of the mirror nucleus ^{11}B are used.

E_r (keV)	**E_i (MeV)**	**E_f (MeV)**	**Branching ratio (%)**
560	8.105	0	74 ± 12
		2.000	26 ± 5
877	8.420	0	100
		4.319	< 7
1110	*8.654*	*0*	*0.9 ± 0.3*
		4.319	*86.6 ± 2.3*
		6.478	*12.5 ± 1.1*
1155	8.699	0	42 ± 10
		4.319	42 ± 10
		4.804	2.4 ± 1.5
		6.478	13.6 ± 4.6
1356	8.900		unknown
1657	9.200	0	74 ± 18
		4.319	6 ± 5
		6.478	20 ± 10

3.2.3 The $E_r = 1356$ keV resonance

The most recent study relevant to the $^7Be(\alpha,\gamma)^{11}C$ reaction was performed by Yamaguchi et al. (2013) using the low–energy radioactive ion beam facility CRIB at RIKEN, Japan. The CNS Radioactive Ion Beam separator (CRIB) (Yanagisawa et al., 2005) is a facility focused on nuclear astrophysics and nuclear structure studies and has four main components: (a) the production target, where a stable beam from the AVF cyclotron of RIKEN impinges and produces a radioactive beam in–flight (see Section 4.1), (b) a double achromatic system, which first analyzes the unstable nuclei produced according to their momentum and then focuses the beam (c) a Wien filter system, which provides a better isotone separation and purification of the radioactive ion beam and (d) the final focal plane, where the reaction of interest takes place and the produced nuclei are detected.

The $^7Be + \alpha$ resonant scattering and $^7Be(\alpha, p)$ reaction measurements were performed using the thick–target method in inverse kinematics and provided the excitation functions for $E_x = 8.7$–13.0 MeV. The ^7Be beam was produced at the production target from a cyclotron–accelerated ^7Li beam and had around 2×10^5 pps intensity at the final focal plane with almost 100% purity after the Wien filter. The reactions occurred in a 815 Torr helium gas, sufficiently thick to stop the beam. Protons and α particles from the reactions of interest were detected using two silicon detectors which provided $\Delta E - E$ particle identification. In addition, ten NaI(Tl) detectors were used to detect γ rays from the 429 keV excited state of ^7Be.

The R–matrix analysis of the data shows two small peaks in the low energy region, between 8.90 and 9.20 MeV. The first one is considered to be the known $5/2^+$ state at 9.20 MeV observed by Wiescher et al. (1983). The second one, located at around 8.90 MeV (see Table 3.1 & Figure 3.1), is regarded by the authors as a new resonance. However, they argue that this spectral feature could also originate by either the 8.655 or the 8.699 MeV state because the energy uncertainty was quite large in this energy region. Furthermore, they calculated the contribution of that new resonance to the total reaction rate. Since the state does not have an absolute spin assignment, the authors considered the cases of $J^\pi = 9/2^+$, which was the best fit of the R–matrix analysis, and $3/2^+$. The contribution of this resonance was 10% compared to the NACRE rate (see Section 3.3) in the temperature range relevant to the νp–process nucleosynthesis ($T_9 = 1.5$–3).

3.2.4 The E_r = 1657 keV resonance

The highest energy resonance inside the relevant energy window for νp–process nucleosynthesis corresponds to the E_x = 9.20 MeV state in ^{11}C. It was first observed in a $^{12}C(p,d)^{11}C$ study (Ajzenberg-Selove and Busch, 1980) and later in the studies of Wiescher et al. (1983) and Yamaguchi et al. (2013). The resonance fit of the second study yielded $J^\pi = 5/2^+$ and $\Gamma = 0.55 \pm 0.10$ MeV for its spin–parity and total width respectively. No further information is published, but since its contribution to the total reaction rate compared to the important, low–energy resonance with E_r = 877 keV at T = 2 GK is:

$$\frac{R(E_r = 1657 \text{ keV})}{R(E_r = 877 \text{ keV})} \sim e^{-\Delta E_r/172.3 \text{ keV}} \sim 10^{-2} \tag{3.1}$$

it is safe to ignore it from the following discussion.

3.3 The current ^{7}Be$(\alpha,\gamma)^{11}$C reaction rate

The current rate for the $^7Be(\alpha,\gamma)^{11}C$ reaction, which all the reaction rate libraries for nuclear astrophysics are adopting, such as STARLIB (Sallaska et al., 2013) and REACLIB (Cyburt et al., 2010), was calculated from the European Compilation of Reaction Rates for Astrophysics (NACRE and NACRE-II) (Angulo et al., 1999; Xu et al., 2013). NACRE includes contributions only from the E_r = 561 and 876 keV resonances, for which experimentally measured strengths exist, and the non–resonant contribution is adopted with the same parameters as those of the mirror $^7Li(\alpha,\gamma)^{11}B$ reaction, up to $T_9 < 0.7$ only. The sub–threshold resonance at E_x = 7.50 MeV has a large contribution at low temperatures, below $T_9 \approx 0.3$, according to Descouvemont (1995). Figure 3.2 shows the current rate, along with an older reaction rate compilation from Caughlan and Fowler (1988).

3.4 Motivation for the present study

In the study of Wanajo et al. (2011) that we already discussed in Chapter 1, the authors also examined how the uncertainties in the nuclear data inputs affect the νp–process nucleosynthesis. To determine the elemental abundances of the νp–process,

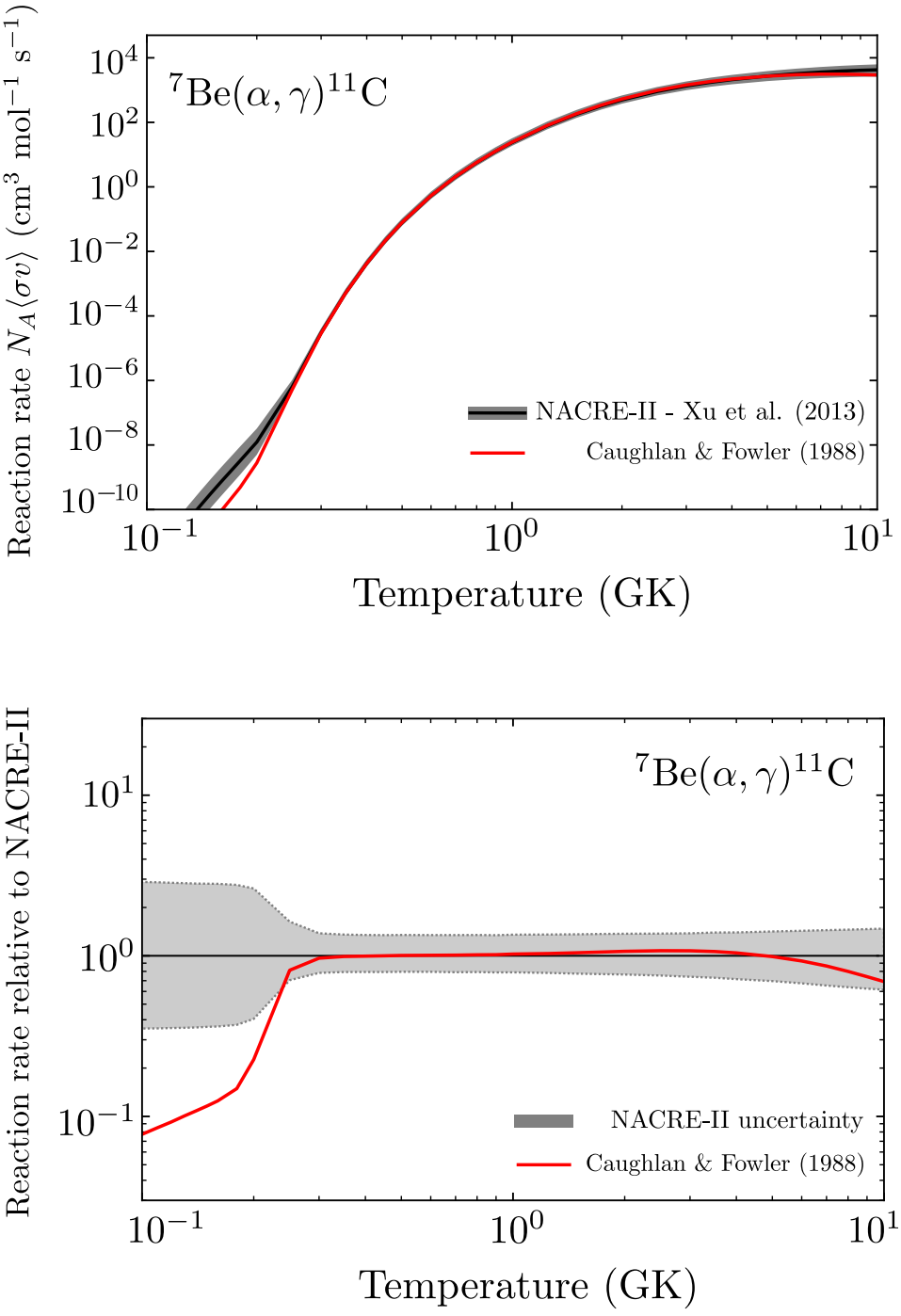

Figure 3.2: (Upper panel) The ^{7}Be$(\alpha,\gamma)^{11}$C reaction rate for T= 0.1–10 GK. The rates by Xu et al. (2013) and Caughlan and Fowler (1988) are shown. (Lower panel) Comparison between the current ^{7}Be$(\alpha,\gamma)^{11}$C reaction rate (Xu et al., 2013) and that of Caughlan and Fowler (1988) for the same temperature region.

they used an extensive reaction network of 6,300 species including all relevant reactions and their inverse and adopted reaction rates from REACLIB (Cyburt et al., 2010) and BRUSLIB (Arnould and Goriely, 2006). Nuclear masses were taken from experimental studies (Audi et al., 2003) or theoretical calculations (Goriely et al., 2005), where applicable.

When the dissociated nucleons start forming the Z = N seeds for the νp–process (Section 1.5.1), the reaction flow moves from the pp–chain region (A$<$ 12) to the CNO region (A$\geq$ 12). The authors found that there are a couple of two–body reaction sequences, namely $^{7}\mathrm{Be}(\alpha,\gamma)^{11}\mathrm{C}(\alpha,p)^{14}\mathrm{N}$ and $^{7}\mathrm{Be}(\alpha,p)^{10}\mathrm{B}(\alpha,p)^{13}\mathrm{C}$, which compete with the triple–α reaction, the main link between those regions, before ($\mathrm{T}_9 > 3$) and after ($\mathrm{T}_9 < 3$) the onset of νp–process respectively, as one can see in Figure 3.3.

The most important reaction for each of the two sequences is the $^{7}\mathrm{Be}(\alpha,\gamma)^{11}\mathrm{C}$ and the $^{10}\mathrm{B}(\alpha,p)^{13}\mathrm{C}$ respectively, since, like the triple–α reaction, they control the reaction flow. For this reason, the authors selected them to test their importance for νp–process nucleosynthesis.

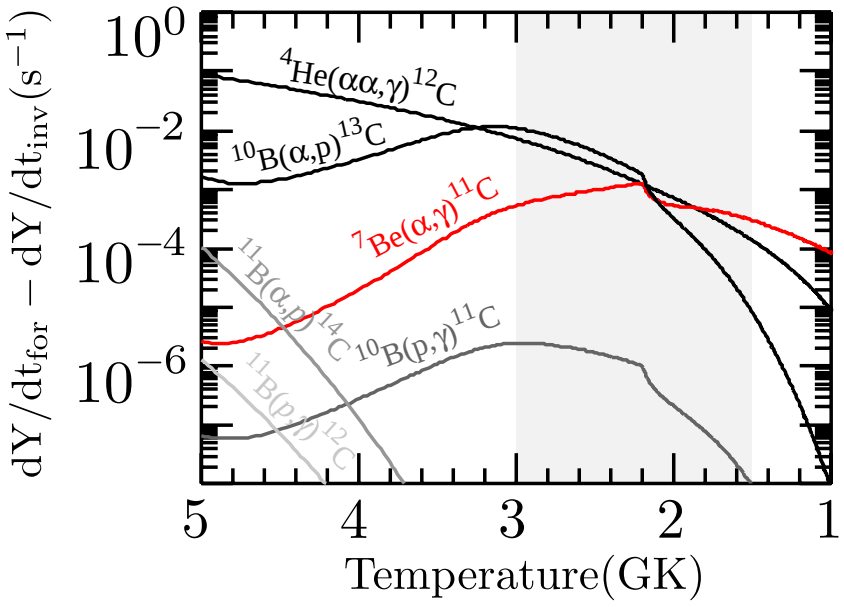

Figure 3.3: Nuclear flows for the reactions that bridge from A$<$ 12 (pp–chain region) to A$\geq$ 12 (CNO–region) as a function of temperature. The band indicates the temperature range relevant to the νp–process (T_9 = 1.5–3) and the red line shows the $^{7}\mathrm{Be}(\alpha,\gamma)^{11}\mathrm{C}$ reaction. The figure is adopted from Wanajo et al. (2011).

Figure 3.4 shows the results of the reaction network calculations for five different rates of the $^{7}\mathrm{Be}(\alpha,\gamma)^{11}\mathrm{C}$ reaction. The authors used the reaction rate from Caughlan and Fowler (1988), which was increased and decreased by a factor of 2 and 10. In nuclear astrophysics, this is commonly known as a sensitivity study. It is evident that the abundances of p–nuclei in the mass region of $A \sim 100 - 110$ are sensitive to this reaction, varying by a factor of $\approx 1.3 - 6$, as shown in Figure 3.4. More specifically, a larger rate affects the abundances more strongly than a lower one. This result can be explained by the fact that a larger rate leads to the production of more intermediate mass nuclei, which remove protons from the stellar gas, decreasing the electron fraction $\mathrm{Y_e}$, and therefore the efficiency of νp–processing, as we discussed in Section 1.5.1.

In addition to the study of Wanajo et al. (2011), Nishimura et al. (2019) recently performed a large scale Monte Carlo (MC) sensitivity study of the nuclear physics uncertainties of the νp–process. The authors explored a wide range of electron fraction, $0.55 \leq Y_e \leq 0.725$, and entropies, $11.4 \leq s \leq 184\ k_B$ baryon^{-1}, for their one–dimensional neutrino–driven wind trajectories. A total of 23 trajectories were post–processed using the MC framework `PizBuin` (Rauscher et al., 2016), and for each trajectory 10,000 nucleosynthesis calculation runs were performed. For each run, all rates were randomly varied within pre–defined factors, which for (α,γ) reactions varied between 0.1 and 2 (factor of ten decrease and factor of two increase). Important reactions that affect the final abundances were identified by using a Pearson product–moment correlation coefficient, $\mathrm{r_{cor}}$, where $0 \leq |\mathrm{r_{corr}}| \leq 1$, between the reaction rate variation and the isotopic abundance change.

Despite the fact that the authors did not report their findings on the variation of the $^{7}\mathrm{Be}(\alpha,\gamma)^{11}\mathrm{C}$ reaction rate, they mention that it has a similar impact as the triple–α reaction which is extensively discussed. Figure 3.5 shows unpublished data of the impact of the $^{7}\mathrm{Be}(\alpha,\gamma)^{11}\mathrm{C}$ reaction rate on the production of nuclides for some of the hydrodynamic trajectories. The largest effect for most of the trajectories is in the mass region $70 \leq \mathrm{A} \leq 120$, which is wider than, but consistent with, the region identified by Wanajo et al. (2011).

Considering all the above, our knowledge of the $^{7}\mathrm{Be}(\alpha,\gamma)^{11}\mathrm{C}$ reaction rate and its impact on νp–process nucleosynthesis is limited, since it does not account for the contribution of at least three resonances, *i.e.* $\mathrm{E_r} = 1110$, 1155 and 1356 keV, which

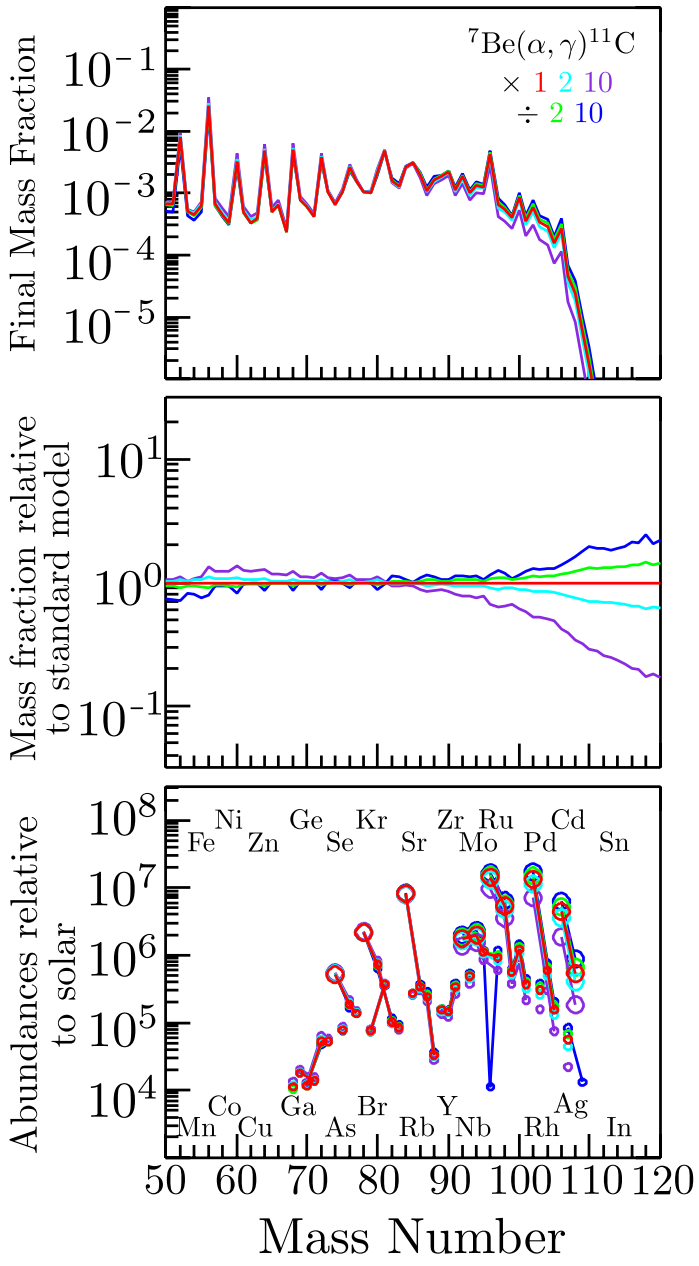

Figure 3.4: Comparison of the nucleosynthesis results for five different rates of the ^{7}Be$(\alpha,\gamma)^{11}$C reaction. The final mass fractions (upper panel) and comparison to the standard model (middle panel) are shown as a function of mass number. (Lower panel) Abundances of isotopes relative to solar values. The colour coding corresponds to different rates of the ^{7}Be$(\alpha,\gamma)^{11}$C reaction. The figure is adopted from Wanajo et al. (2011).

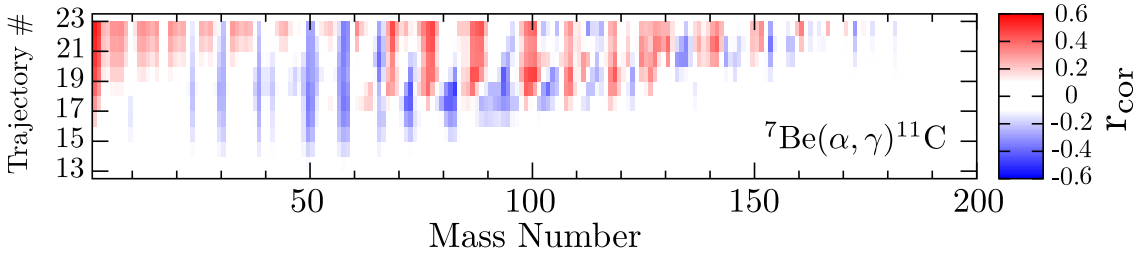

Figure 3.5: The impact of the ^{7}Be$(\alpha,\gamma)^{11}$C reaction (Xu et al., 2013) on the production of nuclides for a subset of the studied trajectories (increasing trajectory corresponds to increased Y_e) from the study by Nishimura et al. (2019). The correlation of the abundance variation of a given isotope with the variation of the rate is shown. See the text for details.

can lead to a significant change in the relevant energy region. For this reason, it is important to determine experimentally the unknown resonance strengths to improve the reaction rate for νp–process nucleosynthesis temperatures and determine its effect on the isotopic abundances. In the following chapters we shall discuss the first direct measurement of resonances with unknown strengths of the ^{7}Be$(\alpha,\gamma)^{11}$C reaction in inverse kinematics using the DRAGON recoil separator, which is the main topic of the present thesis.

3.5 Conclusions

In summary, despite the richness of experimental studies relevant to the ^{7}Be$(\alpha,\gamma)^{11}$C reaction, there are still unknown nuclear parameters that could influence the total reaction rate and subsequently its impact on nucleosynthesis in neutrino–driven winds via the νp–process. At this point, we proceed with the presentation of an experimental study to improve the ^{7}Be$(\alpha,\gamma)^{11}$C reaction rate.

Chapter 4

Experimental Methods

> It does not do to leave a live dragon
> out of your calculations,
> if you live near him.
> — J. R. R. Tolkien, The Hobbit

The experiments presented in this thesis took place at TRIUMF, Canada's particle accelerator centre in Vancouver, BC. TRIUMF is managed by a consortium of 20 member and associate member universities from across Canada. Its particle accelerators are used for both fundamental and applied research in nuclear physics and astrophysics, particle physics, molecular and materials science and life sciences. At the heart of TRIUMF lies the largest cyclotron in the world, about 18 m in diameter, which accelerates protons at 520 MeV. These protons are used for the production of radioactive ion beams (RIBs), as we shall discuss below.

This chapter is structured as follows: in Section 4.1 we will discuss about the production, separation and acceleration of both stable and radioactive beams at the ISAC–I facility of TRIUMF and in Section 4.2 we will give an overview of the DRAGON recoil separator, which was the apparatus used for the experiments of the present thesis.

4.1 The ISAC Facility

The stable and radioactive beams used at TRIUMF were produced at the Isotope Separator and Accelerator (ISAC) facility. ISAC was first built with one experimental

hall, ISAC–I (see Figure 4.1), where ion beams are accelerated up to 1.8 MeV/u. Almost a decade after its commissioning, a high energy area was built, ISAC–II, where ions with A< 150 can be accelerated up to 6 MeV/u and ions with A< 30 up to 16 MeV/u. In the near future, a new facility will be commissioned at TRIUMF, the Advanced Rare Isotope Laboratory (ARIEL), which will further improve the capabilities of the laboratory with production of neutron rich isotopes. In this chapter, we will only discuss ISAC–I, since the experiment of this thesis took place there. The interested reader can find an overview of the ISAC and ARIEL facilities in Dilling et al. (2014).

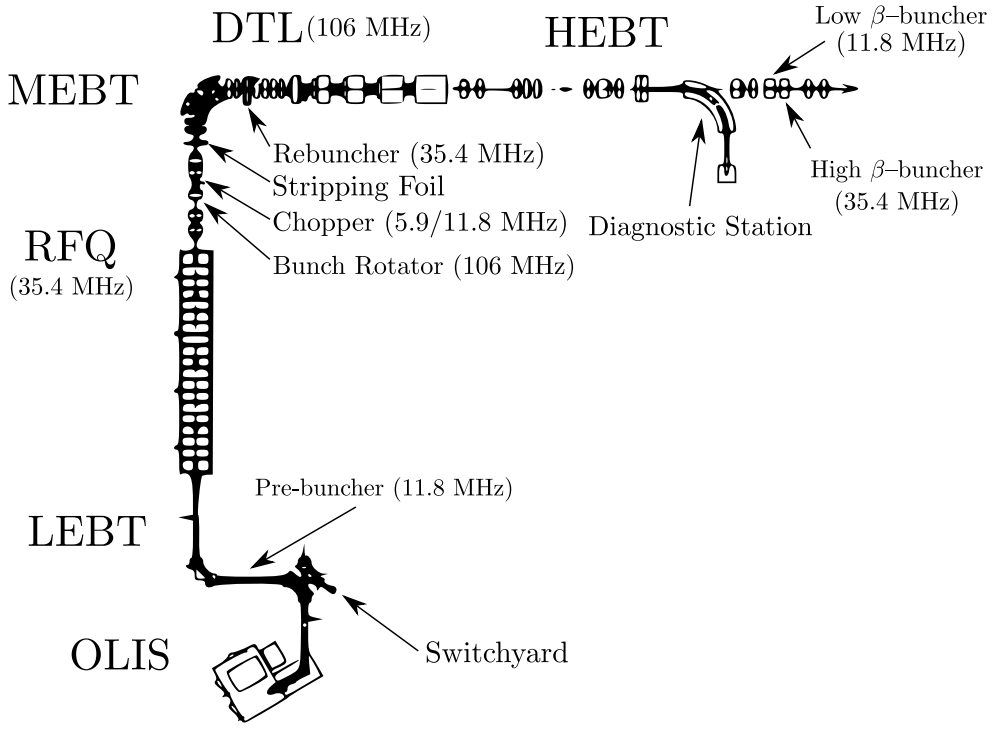

Figure 4.1: Schematic representation of the ISAC–I facility accelerators. The three main beam transport lines (LEBT, MEBT and HEBT) and the Off–Line Ion Source (OLIS) are shown. The image is adapted from Laxdal (2003).

4.1.1 Radioactive Beam Production and Separation

The ISAC facility produces radioactive ion beams (RIBs) using the Isotope Separation On–Line (ISOL) technique (Ravn, 1979). ISOL–produced beam quality is comparable

to stable beams, but their intensities are far smaller, which affects the feasibility of challenging measurements (Blackmon et al., 2006). In the following we shall give a brief overview of the ISOL beam production at ISAC: high intensity (50–100 μA) protons at 500 MeV from the cyclotron impinge on a thick heavy isotope target in one of the two target stations (denoted as East and West), creating radioactive species through spallation, fragmentation and/or fission reactions. The target module (see Figure 4.2) is kept at high temperature, up to 2300 °C, to speed up the release of the rare isotopes, which are usually short–lived with half–lives that vary from a few milliseconds to a few seconds. Target materials are chosen to optimize the production and release efficiency of the species of interest and withstand the beam power without degradation. The production targets used at ISAC operate for two to five weeks before they are replaced. The ^{7}Be beam was produced using a thick zirconium carbide (ZrC) target, manufactured at TRIUMF.

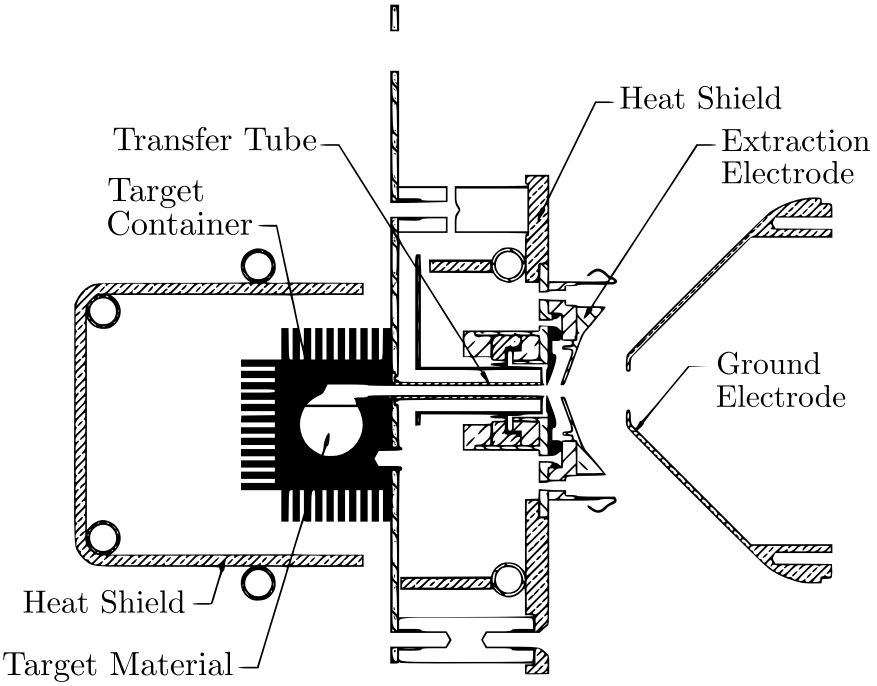

Figure 4.2: Schematic of the ISAC target/ion source module. The beam direction is into the page. The image is adapted from Sen et al. (2016).

Figure 4.3 shows a schematic of the rare isotope release from the target module to the ion source. The radioactive atoms are released from the target by two different

processes: diffusion from the target crystal to the surface and effusion until they reach the ion source, which removes an electron and thus makes them positively charged and ready to be accelerated. According to the radioactive beam of interest, ISAC can employ one of its three ion sources: the Surface Ionization Source (SIS), the Resonant Ionization Laser Ion Source (RILIS), or the Force Electron Beam Induced Arc Discharge (FEBIAD) ionization source. For the ^{7}Be ion beam RILIS was used, and the reason for this choice will become apparent in the following.

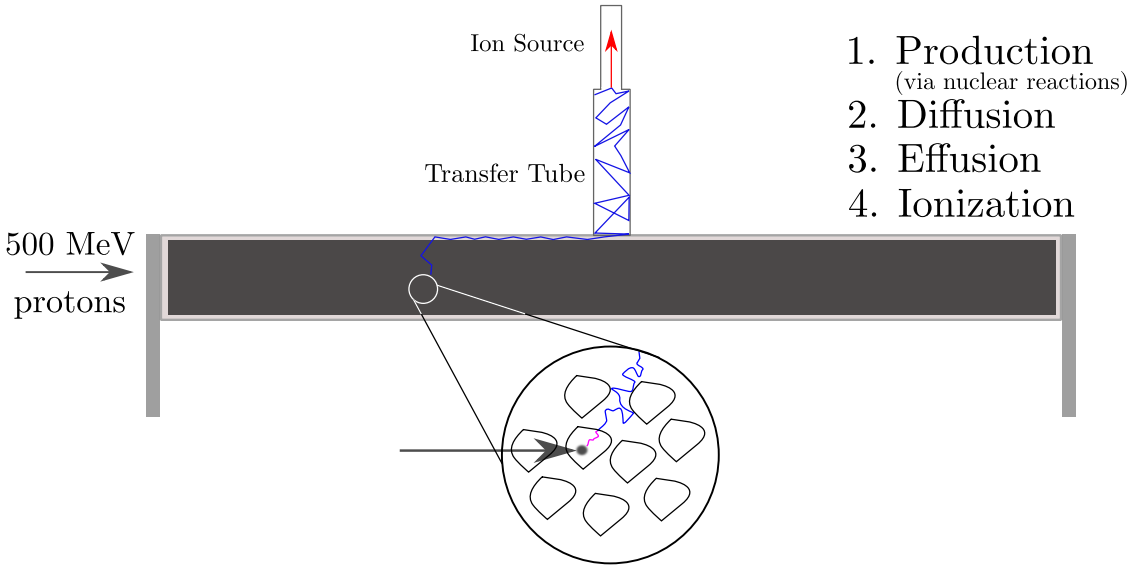

Figure 4.3: Schematic representation of the RIB production using the ISOL method. The rare isotope is produced via nuclear reactions in the target and then through diffusion and effusion reaches the ion source, where it gets ionized. The image is adapted from Ramos et al. (2018).

The TRIUMF Resonant Ionization Laser Ion Source (TRILIS) (Lassen et al., 2005) uses a tunable titanium–sapphire (Ti:Al_2O_3) laser, pulsed at 10 kHz, located 20 m away from the target to generate laser beams, which, via a series of prisms and mirrors impinge in the ion source. The laser pulse is tuned to resonantly excite the outermost electron of the beam species of interest, thereby ionizing it. This is one of the main advantages of TRILIS, since each element has a different resonant ionization energy, and that results very pure radioactive beams, almost free of isobaric contaminants. For this experiment, the main isobaric contaminant, ^{7}Li, was initially reduced using TRILIS.

After the ion source, the beam is transported through the ISAC high resolution ($M/\Delta M = 2000$) mass separator, where the beam species of interest are selected according to their mass. It is evident that nuclei of the same mass as the species of interest – isobars – can potentially get through the mass separator. For example, the resolution needed to separate ^{7}Be and ^{7}Li is $m_{^7\mathrm{Be}}/\delta(m_{^7\mathrm{Be}} - m_{^7\mathrm{Li}}) \approx 7500$, which cannot be achieved by the ISAC mass separator. For this reason, the use of TRILIS is necessary to keep the isobaric contamination at a low level.

The intensity of the radioactive ion beam produced using the ISOL technique can be calculated using (Köster, 2002)

$$\mathrm{I} = \Phi \cdot \sigma \cdot \mathrm{N} \cdot \eta_{\mathrm{target}} \cdot \eta_{\mathrm{source}} \cdot \eta_{\mathrm{separation}} \cdot \eta_{\mathrm{transport}} \tag{4.1}$$

where Φ is the flux of protons, σ is the cross section to produce the desired species, N is the number of target particles that are exposed to the proton flux, η_{target} is the efficiency of ion release from the target, η_{source} the ion source efficiency, $\eta_{\mathrm{separator}}$ the transmission through the mass separator, and $\eta_{\mathrm{transport}}$ the transport efficiency to the experimental apparatus. The beam intensity of the ^{7}Be beam was $\mathrm{I} \approx 1.15 \times 10^9$ pps, one of the highest ever achieved for that isotope. Nevertheless, stable beam intensities can be as high as 10^{12-13} pps for low mass nuclei and another 1–2 orders of magnitude higher for proton or alpha beams.

A complementary technique to ISOL, called in–flight projectile fragmentation, is also used for nuclear astrophysics experiments with radioactive ion beams. In that case, a high energy beam impinges on a light element target fragmenting it into many high energy smaller residues. The exotic nuclei of interest are separated from the primary beam and other fragments with the use of magnetic and electrostatic elements according to their mass and charge. The main advantage of this technique is that it is not sensitive to chemical properties and the half–life of the isotopes of interest. However, the purity of the radioactive ion beams produced is poorer than in ISOL and the high energy of the radioactive ion beams produced cannot be used directly for nuclear astrophysics studies. For this reason beams produced in–flight need to be slowed down and then re–accelerated to suitable energies. Notable examples of in–flight projectile fragmentation facilities are the National Superconducting Cyclotron Laboratory (NSCL) at Michigan State University in the United States and RIKEN in Japan.

4.1.2 Off–Line Ion Source

In addition to radioactive beam delivery to experiments, the ISAC facility employs the Off–Line Ion Source (OLIS) terminal to provide stable isotope beams with mass–to–charge ratio (A/q) up to 32. OLIS can be used for stable beam experiments, for accelerator commissioning, or to provide pilot beams for radioactive beam experiments. Its terminal comprises three ion sources; a microwave cusp ion source, a surface ion source or a hybrid surface–arc discharge ion source, and a multi–charge ion source (Jayamanna, 2014). We shall discuss the first two, since they provided beams for the measurements of the present thesis.

The microwave ion source (MWIS) is the most used source of the OLIS terminal. It has been operational for over two decades and it can provide singly and some doubly charge ion beams from various stable isotopes. MWIS is very robust, being able to operate for months without maintenance (Jayamanna, 2014). It consists of two vacuum chambers, one plasma chamber and one RF coupling chamber, respectively. For this thesis, the microwave ion source provided ^{12}C and ^{11}B beams for charge state distribution measurements (see Sections 5.2.5 and 5.3.3).

The Surface Ion Source (SIS) consists of an ionizing chamber and three ovens which can run in three different temperature regions simultaneously (25–600 °C, 600–1200 °C and 1200–2000 °C). Figure 4.4 shows a schematic of this ion source. SIS has the advantage of having a removable extraction system which can be easily replaced if there is an alkali contamination. It is mainly used for the production of alkali and semi–alkali isotopes from lithium to praseodymium and it produced the ^{6,7}Li beams for the experiments of this thesis (see Section 5.2).

4.1.3 Beam Transport and Acceleration

Two post–target accelerators transport the ion beam to the high energy experimental area of ISAC–I. The first one is an eight meter long Radio Frequency Quadrupole (RFQ) accelerator (Poirier et al., 2000), which is part of the Low Energy Beam Transport (LEBT) line (see Figure 4.1). The RFQ accelerates ions with mass–to–charge ratio (A/q) less than 30 from 2 keV/u to 150 keV/u using oscillating electric fields of varying strength from nineteen split ring resonators with a frequency of 35 MHz. A pre–buncher located upstream from the RFQ creates beam bunches,

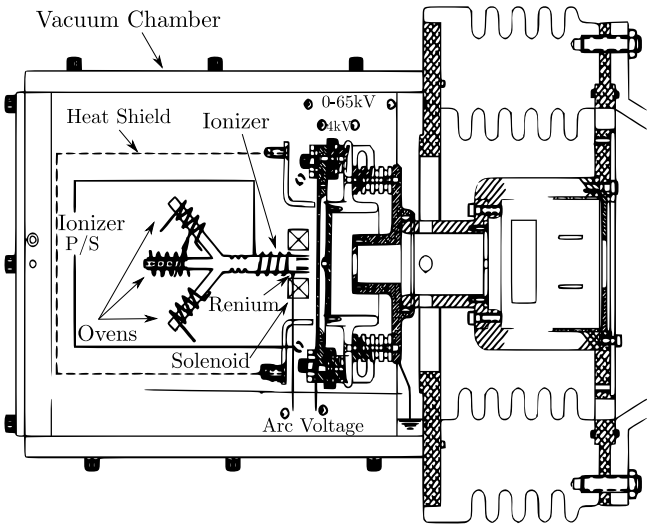

Figure 4.4: Schematic of the OLIS surface ion source, with the three heaters and the ionizer. The image is adapted from Jayamanna (2014).

which are separated by 85 ns (the RF frequency is 11.78 MHz) and it also improves the beam quality and transmission. Four electrodes in the RFQ also focus the ions towards the beam axis, and the transmission through it is usually around 80%.

The second post–target accelerator is a Drift Tube Linac (DTL) (Laxdal et al., 2001). The two accelerators, RFQ and DTL, are joined by the Medium Energy Beam Transport (MEBT) line. DTL accepts beams with A/q $\leq$ 7, which is much less than the RFQ's 30. If this condition is not satisfied, a thin carbon stripping foil of 4 μg/cm^2 between the two accelerators is used to increase the beam charge state, with a stripping efficiency $30-50\%$, and thus decrease the mass–to–charge ratio. After the stripping foil, two dipole magnets select the charge state of interest at MEBT before the beam is injected to the DTL. There, it will be accelerated to a fully variable final energy between 117 keV/u and 1.80 MeV/u. The maximum final energy that the DTL can achieve depends on A/q and can be estimated using the following relation

$$\mathrm{E} \simeq 1.95 - 0.074\ (\mathrm{A/q})\ \mathrm{MeV/u} \tag{4.2}$$

for A/q between 2 and 7 (Laxdal and Marchetto, 2014). For example, the maximum energy of a $^7\mathrm{Be}^{2+}$ (A/q = 7/2) beam is $\mathrm{E_{max}} = 1.69$ MeV/u. The beam transmission

through the DTL is usually greater than 95%.

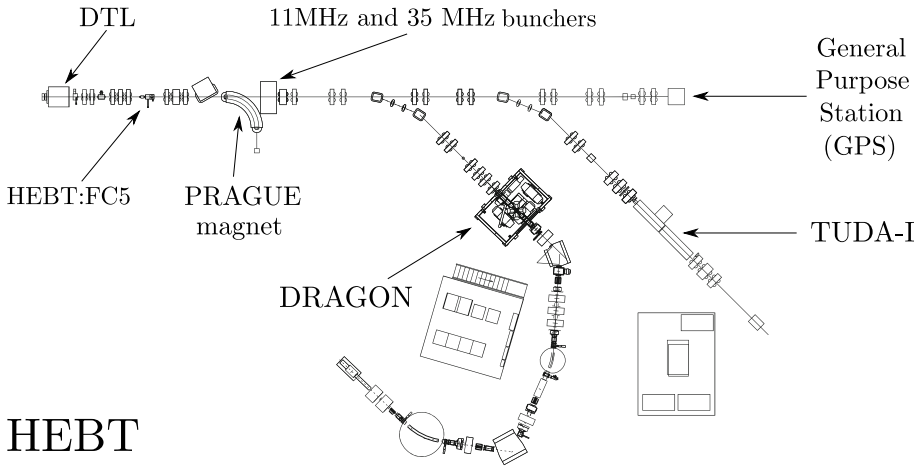

Figure 4.5: The High Energy Beam Transport (HEBT) line at ISAC–I. The image is adapted from Marchetto and Laxdal (2013).

Finally, the High Energy Beam Transport (HEBT) line (Figure 4.5) connects the DTL to two target stations at ISAC–I, DRAGON and TUDA. Downstream of the DTL, the energy of the beam is measured by the ISAC beam operators using the diagnostic Prague magnet and a subsequent buncher provides an energy spread of $\Delta E/E = 0.1 - 0.4\%$.

Specifically for the ^{7}Be beam, to ensure a high purity, an additional carbon stripping foil of 20 $\mu g/cm^2$ was placed at HEBT to select a specific charge state (4^+), which eliminates the isobaric ^{7}Li contaminant. For example, a ^{7}Be/^{7}Li (2^+) beam at 441.7 A keV with initial 1:3 composition, will result in $\sim 150 : 1$ after passing the stripping foil, according to the empirical charge state distribution of Liu et al. (2003).

4.2 The DRAGON Recoil Separator

At the HEBT line of ISAC–I lies the DRAGON (Detector of Recoils and Gammas Of Nuclear reactions) recoil separator (Hutcheon et al., 2003). DRAGON studies radiative proton and alpha capture reactions relevant for astrophysics with either stable or radioactive beams in inverse kinematics using the thick target yield technique

(see Sections 2.3 & 2.4 for more details). Even though it was designed to study reactions with beams up to A= 30, since it was commissioned, over two decades ago, it has demonstrated a unique versatility having performed experiments from A= 3, *e.g.* ^{3}He$(\alpha,\gamma)^{7}$Be in Sjue et al. (2013), to A= 76, *e.g.* ^{76}Se$(\alpha,\gamma)^{80}$Kr in Fallis et al. (2020). DRAGON has four main components: the windowless, differentially pumped, recirculated gas target, the γ ray detection system of 30 BGO detectors, the electromagnetic separator and the recoil detection system (shown in Figure 4.6). In the following we shall discuss all these components in more detail, along with the data acquisition system.

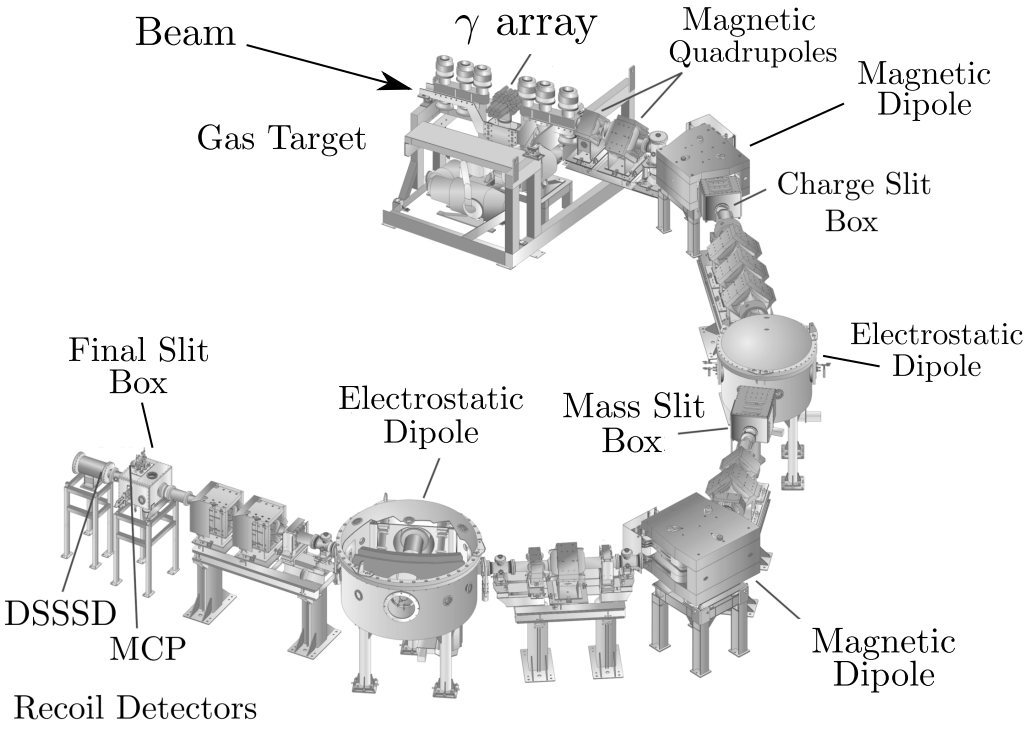

Figure 4.6: Schematic representation of the DRAGON recoil separator. The main components are shown. See the text for details.

4.2.1 Windowless Gas Target

The radiative capture reaction of interest occurs inside a trapezoidal gas chamber which can be filled with hydrogen or helium up to P $\approx$ 10 Torr, to study (p,γ)

or (α, γ) reactions, respectively (see Figure 4.7). The chamber is enclosed in an aluminum pumping box with thin walls to reduce the attenuation of the reaction prompt γ rays.

Gas targets have many advantages over solid targets, but we shall point only a few of them. First and foremost, gas targets are chemically pure, and hence no stoichiometry is needed, which introduces an additional systematic error in the reaction yield calculation. Windowless gas targets have an extra advantage of reduced unwanted background, since even thin windows can produce a significant signal, mostly from elastic scattering. In addition, windows can deteriorate the beam quality due to straggling, and can cause a significant beam energy loss (Rolfs and Rodney, 1988).

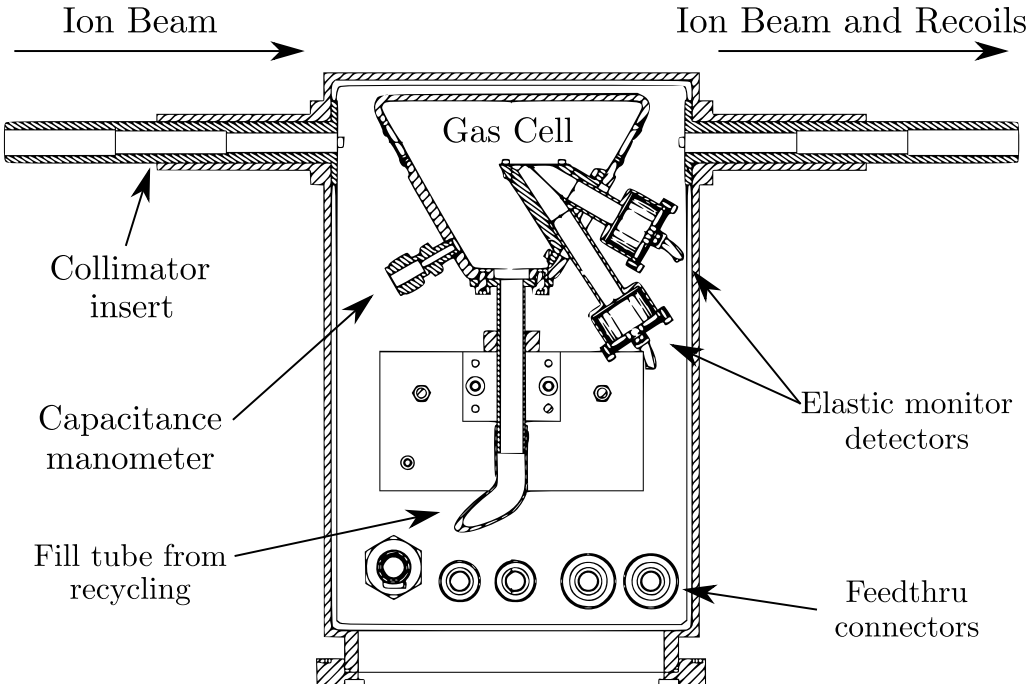

Figure 4.7: Sectional view of the DRAGON windowless gas target. The ion beam enters the target from the left, while beam and recoils exit from the right. The rest of the target module components are shown. The figure is adapted from Hutcheon et al. (2012). See the text for details.

The gas inside the DRAGON target is contained by multiple stages of differential pumping, instead of with physical windows. The first stage employs five large roots blowers (two Leybold WSU2001 with 2000 m^3/h pumping speed in parallel,

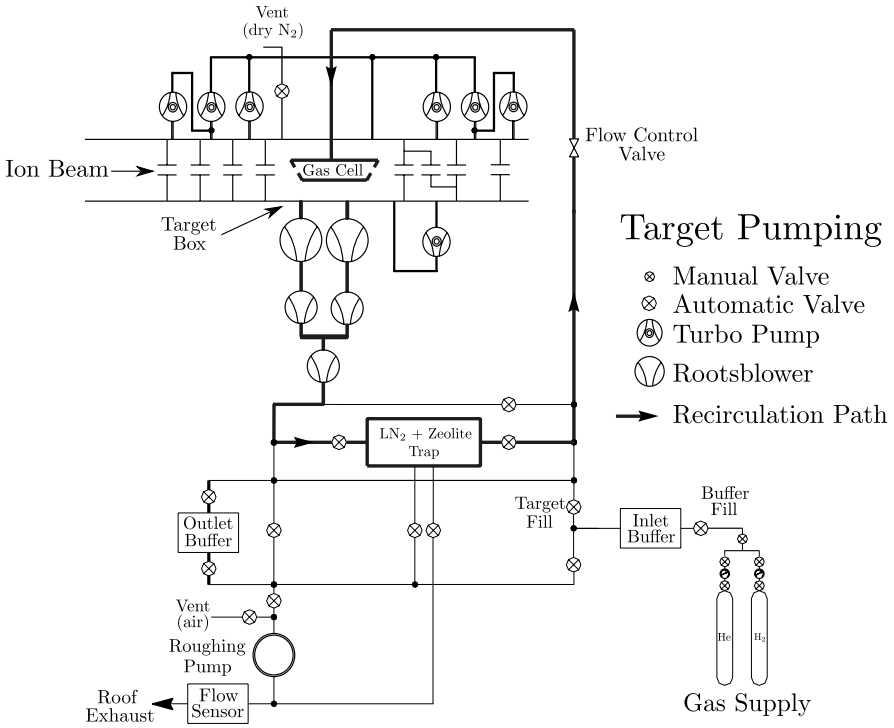

Figure 4.8: Schematic of the DRAGON pumping system. The main components are shown. The figure is adapted from Hutcheon et al. (2003).

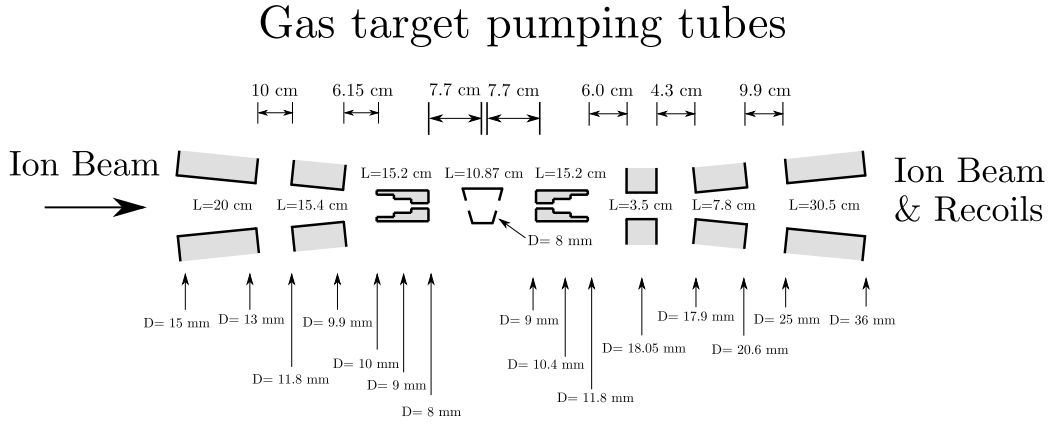

Figure 4.9: Schematic of the DRAGON gas recirculation and differential pumping system. The figure is adapted from Hutcheon et al. (2003).

two WSU201 of 200 m^3/h pumping speed in parallel and one WS500) which raise the outflow gas pressure to >40 Torr. Since the gas recirculation can introduce impurities in the target from pump–oil vapor and air leaking in the system (Rolfs and Rodney, 1988), DRAGON uses a liquid–nitrogen–cooled zeolite adsorption molecular trap in the backing line to reduce them. The pressure falls from few Torr inside the gas chamber to $\sim 1 \times 10^{-6}$ Torr outside by means of seven turbomolecular pumps (Varian V1000HT), three upstream the gas target and four downstream. For this reason, the effective length of the target is larger than its geometric 10.87 cm, $L_{eff} = 12.3(5)$ cm. According to Ruiz et al. (2014) gas target lengths between 10 and 15 cm are desirable for recoil separator gas targets, since they provide a better recoil acceptance. Figures 4.8 and 4.9 show a schematic representation of the gas recirculation and differential pumping and system respectively.

To measure a resonance strength using the thick target yield technique (see Section 2.3), the gas target needs to be sufficiently thick to contain the resonance within its limits. The gas target thickness in units of atoms $\cdot$ cm^{-2} can be calculated using the following relation

$$n = n_0 \, \nu \, \frac{P}{760} \, \frac{273}{T} \tag{4.3}$$

where $n_0 = 2.68 \times 10^{19}$ cm^{-3} is the Loschmidt constant, ν is the number of atoms per molecule (ν= 1 for helium and 2 for hydrogen). P and T are the pressure and temperature in units of Torr and Kelvin respectively. For helium gas at 8 Torr and 300 °K the target thickness is 3.17×10^{18} cm^{-2}. Nevertheless, the target density is not constant throughout the gas target, *i.e.* a step function, because of the differential pumping system. We can better describe it with a Fermi function

$$\rho_t(z) = \frac{1}{1 + e^{(|z|-R)/\alpha}} \tag{4.4}$$

where R and α are free parameters. The DRAGON density profile was measured by Carmona Gallardo (2014) using a shielded BGO detector that was moved along the length of the target measuring the yield of the $^{12}C(^3He, p\gamma)^{14}N$ reaction. Figure 4.10 shows the data from this measurement. In Chapter 5 we will discuss how the density profile can be used to estimate the reaction yield along the target.

In addition to the differential pumping system, inside the target box two silicon surface barrier (SSB) detectors at laboratory angles of 30° and 57° with respect to

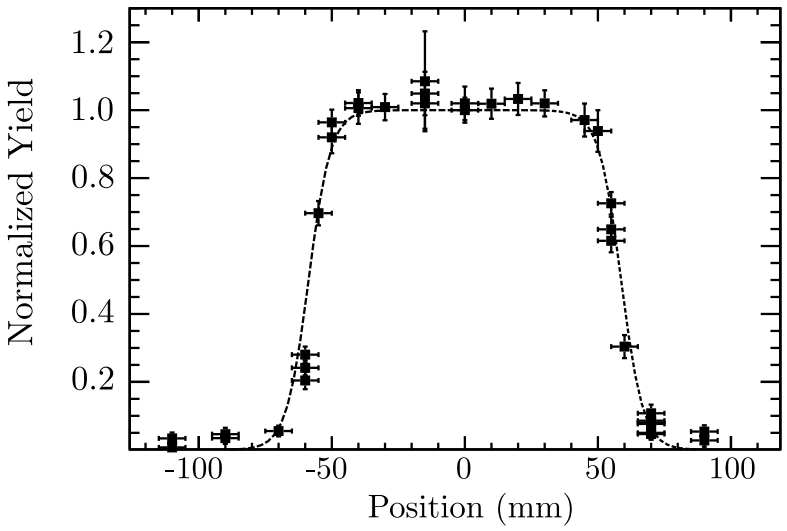

Figure 4.10: DRAGON target density as a function of position. The data are taken from Carmona Gallardo (2014).

the beam axis are used to monitor the beam intensity by detecting the elastically scattered target particles (see Figure 4.7). In Section 5.2.4 we shall discuss how we can use these measurements to extract the number of beam particles impinging on the gas target N_{beam}, using a normalization coefficient $\mathcal{R}$.

4.2.2 BGO γ ray array

An array of 30 Bismuth Germanate Oxide (BGO) crystals surrounds the windowless gas target, as shown in Figure 4.12. The crystals are hexagonal in shape, roughly 6 cm in diameter and 8 cm deep, packed in a tight geometry, covering $89-92\%$ of 4π solid angle (Ruiz et al., 2014). Each crystal is coupled to a Photo–Multiplier Tube (PMT), which converts the scintillating light into an electronic signal to be read by the DRAGON data acquisition system (DAQ). A typical applied voltage for each detector is $\sim$1700 V.

BGO ($Bi_4Ge_3O_{12}$) is a high Z, high density scintillating material and as such it has high detection efficiency. It is also relatively cheap compared to other scintillators, such as lanthanum bromide ($LaBr_3$) or barium fluoride (BaF_2), which have superior timing abilities and if they were used at DRAGON, they could further improve its

detection capabilities.

The segmented array allows for the detection of individual prompt γ rays from the radiative capture reactions inside the gas target and the tagging of the associated recoil particles, which provides an additional background reduction in the focal plane detectors. Its resolution is not a crucial aspect, since it is not the main detection system at DRAGON, and the typical value of 10% in FWHM is sufficient for most experiments.

For the present experiments the BGO array was calibrated using a radioactive ^{244}Cm/^{13}C source, which produces a strong 6.13 MeV γ ray from the ^{13}C$(\alpha, n)^{16}$O reaction – the α particles being produced from the decay of ^{244}Cm. Apart from that transition, the BGO array can also detect the first escape peak, which is located at $6.130 - 0.511 \simeq 5.6$ MeV. Figure 4.11 shows a typical spectrum that we used for the calibration of the BGO array. Furthermore, to further reduce unwanted low–energy γ rays that would increase the detector dead–time and decrease the efficiency of the array, a 1.5 MeV hardware threshold was applied.

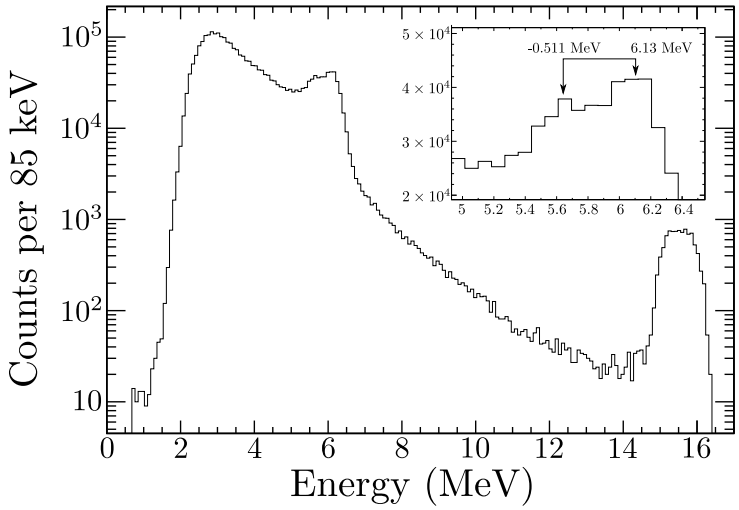

Figure 4.11: Typical calibration γ spectrum from one BGO detector using a radioactive ^{244}Cm/^{13}C source. The E_γ= 6.13 MeV transition of ^{16}O from the ^{13}C$(\alpha, n)^{16}$O reaction, along with its escape peak, is shown in the inset.

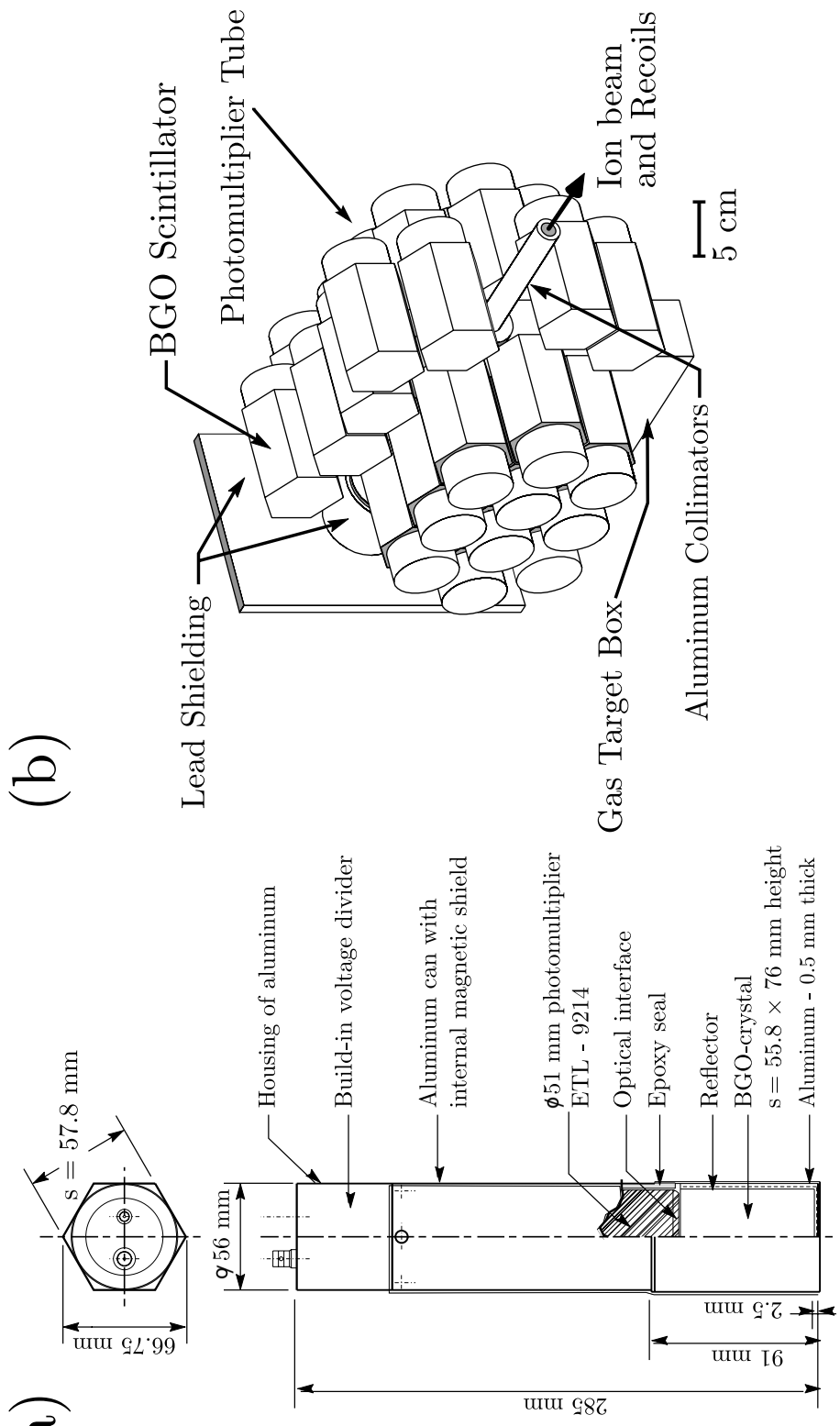

Figure 4.12: (a) Schematic of a single γ ray scintillator with its photomultiplier tube (b) The DRAGON BGO γ array, surrounding the gas target. Both figures are adapted from Hutcheon et al. (2003).

The efficiency of the γ array, $\eta_{\rm BGO}$, depends on details of the γ cascade as we have already discussed in Section 2.4, and it is typically between 45 and 60% for 1–10 MeV γ rays (Gigliotti et al., 2003). In addition, it can be calculated using `GEANT` simulations (see Section 5.3.1) and it is one of the main systematic errors in DRAGON experiments (see Section 5.3.7).

In the next chapter we shall discuss how we can accurately, up to a precision of 0.5 %, calculate the resonance energy, $\rm E_r$, of a radiative capture reaction from the spatial distribution of the highest energy prompt γ rays (γ_0) inside the gas target (Hutcheon et al., 2012).

4.2.3 Electromagnetic Mass Separator

After the beam interacts with the gas target, recoils and beam particles enter the electromagnetic mass separator with roughly the same momentum, but different energies. Since the radiative reaction cross sections for astrophysical reactions are relatively low, the number of beam particles is a factor of $\approx 10^{10-15}$ greater than the recoils. For this reason, the beam has to be suppressed by many orders of magnitude to allow for recoil detection. In particular, for a typical cross section for astrophysical reactions of 1 μb, a gas target density of 10^{17} atoms/cm^2 and a beam intensity of 10^7 pps, the ratio of recoils to unreacted beam nuclei is 1 part in 10^{13}.

The basic equation that governs the DRAGON electromagnetic mass separator is the Lorentz force law

$$\mathcal{F} = q(\mathcal{E} + v \times \mathcal{B}), \tag{4.5}$$

where $\mathcal{F}$ is the Lorentz force, v the particle velocity and $\mathcal{E}$, $\mathcal{B}$ the electric and magnetic field vectors, respectively.

The DRAGON electromagnetic mass separator consists of two magnetic (M) and two electric dipoles (E) in a M–E–M–E configuration, with bending angles $\phi = 50°$, $20°$, $75°$ and $35°$ and bending radii ρ = 100 cm, 200 cm, 81.3 cm and 250 cm, respectively (Hutcheon et al., 2003). In addition, along the separator, there are ten magnetic quadrupoles and six magnetic sextupoles for beam focusing.

After the first magnetic dipole lies a CCD camera, which serves as a beam centering monitor, especially during low–intensity radioactive beam experiments (see Figure 4.13) (Vockenhuber et al., 2008).

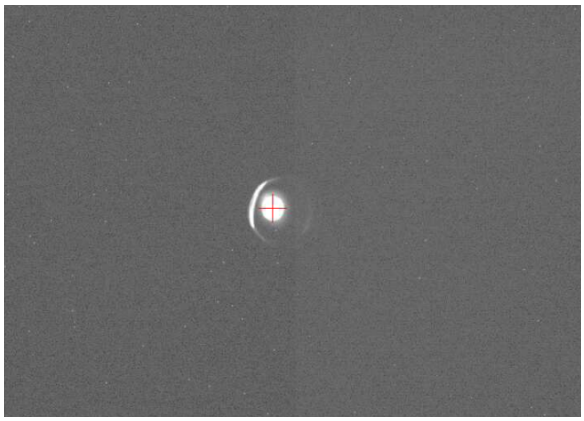

Figure 4.13: Picture of a ^{7}Be RIB taken from the DRAGON CCD camera. The ring around the beam spot is the refection of the beam projected on the pumping tubes.

DRAGON separates recoils and beam particles in two stages: first the particle cocktail is separated according to charge. Due to charge exchange inside the target, mainly originated from electron capture and loss, recoils and beam particles exit with a charge distribution, which can be either calculated theoretically, or preferably measured experimentally (see Section 5.2.5). The first magnetic dipole is used to select a single ion charge state to continue through DRAGON. Usually this charge state is the most intense, to ensure the highest recoil detection yield. Nevertheless, in some cases a different charge state is selected, in case the electric field required to bend the ions does not lie in the limits of DRAGON. This limiting factor can be remedied using the charge state booster (CSB), which is a retractable silicon nitride (SiN) stripping foil located right after the windowless gas target. The CSB extends DRAGON capabilities and is especially useful for heavy ion beams (A $>$ 40).

The radius of curvature for an ion can be calculated by equating the centripetal force to the Lorentz force acting on it as it traverses the magnetic element

$$\frac{mv^2}{\rho} = qv\mathcal{B} \Rightarrow \rho = \frac{mv}{q\mathcal{B}} \tag{4.6}$$

Recoils that do not have the aforementioned charge are deflected to slits that are located downstream of the first magnetic dipole. Subsequently, the recoils are led to the first electric dipole, which is shown in Figure 4.14. There they are separated according to their mass. Ions of different mass are steered on slits downstream of

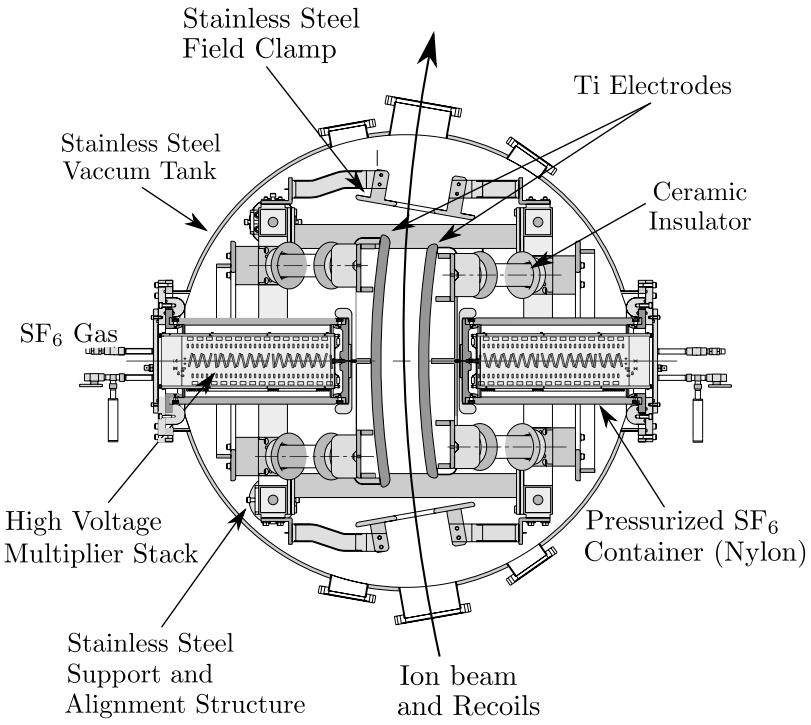

Figure 4.14: Schematic view of the DRAGON electrostatic dipole. The figure is adapted from Hutcheon et al. (2003).

the electric dipole. The electric dipole is followed by another stage of magnetic and electric dipoles, until the beam reaches the focal plane, where the heavy ion detectors are lying.

The fields in the electromagnetic elements can be used to determine the beam energy using the following relation from Hutcheon et al. (2012)

$$\frac{\mathrm{E}}{\mathrm{A}} = \mathrm{c_{MD1}} \left(\frac{\mathrm{q}\mathcal{B}}{\mathrm{A}}\right)^2 - \frac{1}{2\mathrm{uc}^2} \left(\frac{\mathrm{E}}{\mathrm{A}}\right)^2 \tag{4.7}$$

where c is the speed of light in vacuum, q is the charge state of the beam, $m = A \cdot u$ is its mass (u is the atomic mass unit – amu), $\mathrm{c_{MD1}}$= 48.15(7) MeV T^{-2} is the MD1 constant and $\mathcal{B}$ is the magnetic field in MD1 in Tesla. The mass–to–charge ratio of

the beam can be calculated using

$$\frac{A}{q} = 2468\ \frac{\mathcal{B}^2}{\mathcal{V}} \tag{4.8}$$

where $\mathcal{B}$ is the magnetic field in MD1 in Tesla and $\mathcal{V}$ is the voltage of ED1 in kV. The value obtained by the above Equation is expected to deviate less than 1% from the real A/q of the beam.

Unfortunately, despite the very high background suppression factor that DRAGON can demonstrate (Hutcheon et al., 2008), *e.g.* $> 10^{14}$ at the 90% confidence level for the ^{3}He$(\alpha,\gamma)^7$Be reaction (Sjue et al., 2013), it is not uncommon for beam ions to pass through the separator and end up at the focal plane. These unwanted ions constitute the so called "leaky beam" and are a source of systematic uncertainty.

DRAGON was designed for the study of the ^{15}O$(\alpha,\gamma)^{19}$Ne reaction, which is important for the *rp*–process (see Section 1.4.3). Its geometric acceptance is $\theta_{\max}= \pm$ 21 mrad and its energy acceptance is $\pm$4%. For reactions with larger recoil momentum cone, such as the ^{7}Be$(\alpha,\gamma)^{11}$C, extensive simulations of both the BGO array and the separator should be performed, to ensure the feasibility of the experiment, as we discussed in Section 2.4.

In the case of low–intensity or low–purity radioactive beam experiments, DRAGON can employ three auxiliary detectors, namely a pair of sodium iodine scintillators (NaI) and a high–purity germanium (HPGe) detector. They are used to detect decay radiation (γ rays) from the radioactive species of the beam, and thus monitor the beam intensity and purity during the experiment.

4.2.4 Time–Of–Flight Systems

DRAGON can identify recoils from unwanted species by means of two time–of–flight (TOF) detection systems, which are referred to as the "local" and the "separator" time–of–flight.

The local time–of–flight system is based on a timing measurement between two Micro–Channel Plate (MCP) detectors which are located 59.0(5) cm apart, close to the DRAGON focal plane (see Figure 4.15). The detectors are not blocking the beam line, but instead thin (4–5 mg/cm^2) diamond–like carbon (DLC) foils in each detector produce secondary electrons as ions traverse them (Vockenhuber et al., 2009).

The electrons are reflected by an electrostatic mirror at 45° and are detected by the MCPs via photo–multiplication, providing a timing signal. The upstream detector (MCP0) detects electrons from the downstream side, while the downstream (MCP1) is mounted backwards to detect upstream electrons. The two detectors also have different sizes, with the MCP1 being twice as large as the MCP0, to have larger acceptance for diverging recoils. This local time–of–flight has a timing resolution of 300–400 ps and its efficiency varies, according to the reaction, from $\eta_{\mathrm{MCP}} \sim 0.30 - 0.99$ (Vockenhuber et al., 2009).

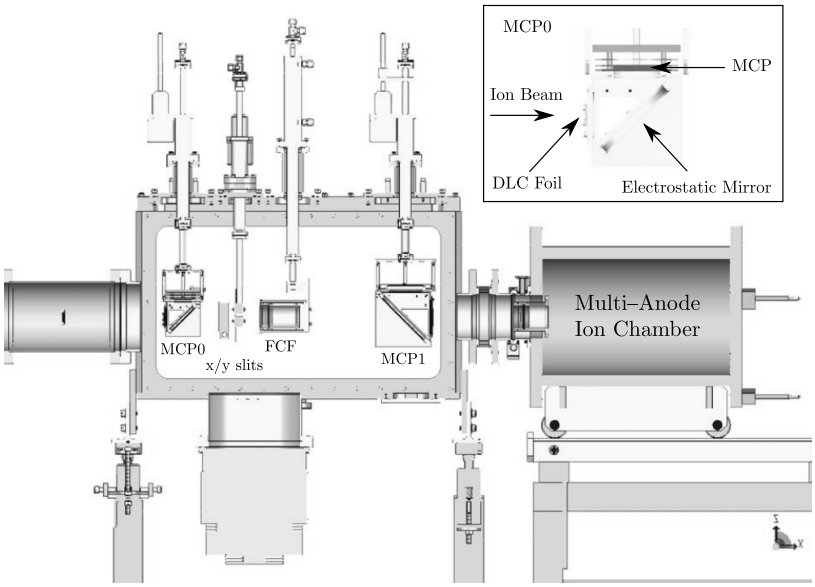

Figure 4.15: Schematic of the DRAGON local time–of–flight system with two MCP detectors. The inset shows the details of MCP0. The figure is adapted from Vockenhuber et al. (2008).

The separator time–of–flight system measures how long it takes for an ion to be transmitted through DRAGON, from the gas target to the focal plane. The start and stop signals are the detection of a γ ray event at the BGO array and a heavy particle at the focal plane, respectively. The separator time–of–flight is a very useful tool for particle identification (PID), as we shall discuss in Chapter 5, since particles with roughly equal momenta but different masses will travel through the 20.7 m length of DRAGON in different times. For example, at center–of–mass energy $\mathrm{E_{c.m.}} = 1155$ keV in the $^{7}\mathrm{Be}(\alpha,\gamma)^{11}\mathrm{C}$ reaction ($\mathrm{T_{lab}} = 3.18$ MeV) it takes 3.47 μs for a ^{11}C ion to travel through DRAGON in comparison to 2.21 μs for a ^{7}Be ion of the same momentum.

According to Ruiz et al. (2014) this system can provide 2–3 orders of magnitude further background suppression. Later in this chapter we shall describe how the separator time–of–flight system works with the Data Acquisition System (DAQ).

4.2.5 Focal Plane Detectors

The main detection system of DRAGON is located roughly 60 cm downstream from the focal plane. After been transmitted through the electromagnetic mass separator, heavy ions can be detected by either a 5 cm × 5 cm, 256 quasi–pixel Double–Sided Silicon Strip Detector (DSSSD) or a 4–anode isobutane–filled Ionization Chamber (IC).

The Double–Sided Silicon Strip Detector consists of two layers of 16 strips each, and it is oriented perpendicular to the trajectory of the heavy ions (see Figure 4.16). By reading out perpendicular strips on the front and the back of the detector, the DSSSD can provide 2D position and energy measurements. The former feature is useful for particle identification, since the recoils and the "leaky beam" have different trajectories and therefore will show up in different positions on the detector. Furthermore the DSSSD provides good energy and timing resolution; the former follows from the fact that it has a large number of charge carriers which require only 3.6 eV for an electron–hole pair. The latter can be explained by its fast pulse rise time of around 10 ns, which can be used for very accurate time–of–flight measurements, as we already discussed in the previous section. Its main disadvantage is the sensitivity to radiation damage (Ruiz et al., 2014); a particle rate of few kilohertz for few seconds can cause irreparable damage to the exposed strips. A Micron W1 model DSSSD was the heavy ion detector of choice in the present thesis, because of its high energy resolution for light ions and timing capability (Vockenhuber et al., 2008).

The ionization chamber is 25 cm in length and consists of 25 anode strips grouped in three regions, as shown in Figure 4.17. The volume of the detector can be filled with $10 - 20$ Torr of isobutane (C_4H_{10}) gas and is separated from the beam line by a thin Mylar (biaxially-oriented polyethylene terephthalate or BoPET) window. As low–energy heavy ions traverse the active volume of the detector, they ionize the isobutane gas, creating electron–ion pairs. An electric field of $\mathcal{E}$= 50 V/cm separates the electron–ion pairs which subsequently drift towards the electrode of opposite charge electrons towards the anode and ions towards the cathode creating an electrical

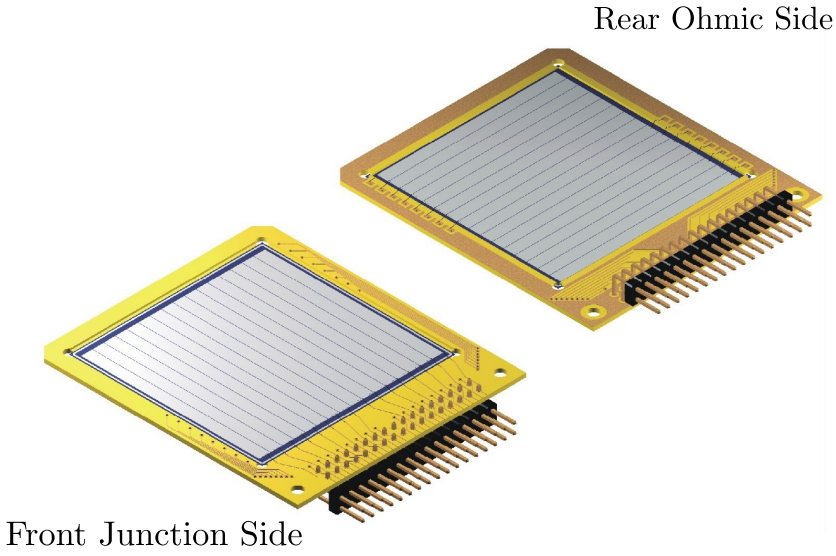

Figure 4.16: Computer–Aided Design of a Micron W1 model DSSSD detector. The two sides, front junction and rear ohmic, are shown. The figure was adapted from Micron Semiconductor Ltd.

pulse. A Frisch grid on ground potential is placed between the anode and the cathode to remove any position dependence on the ionization pulse signal and to improve the timing resolution of the detector. Furthermore, charged particles lose energy as they pass through a material and according to the Bethe formula the rate of energy loss depends on their energy (Bethe, 1950). Since DRAGON selects ions according to E/A, the ionization chamber can also be used to identify recoils from unreacted beam particles as a $\Delta E - E$ detector. The DRAGON ionization chamber is the preferred heavy ion detector used for beams with $A \geq 20$ and energies $E \leq 0.5$ MeV/u (Vockenhuber et al., 2008). Due to the very small mass and energy difference between ^{11}C and ^{11}B (the product of $^{7}Li(\alpha,\gamma)^{11}B$ reaction) the Ionization Chamber was not used in the experiments of this thesis.

Finally, a new hybrid $\Delta E - E$ detector was recently developed at TRIUMF (Burke, 2016). It consists of a DSSSD enclosed in an ionization chamber, taking advantage of the strengths of both detectors and it will improve the heavy ion detection capabilities of DRAGON, especially in reactions involving intermediate mass nuclei with heavy isobaric contamination.

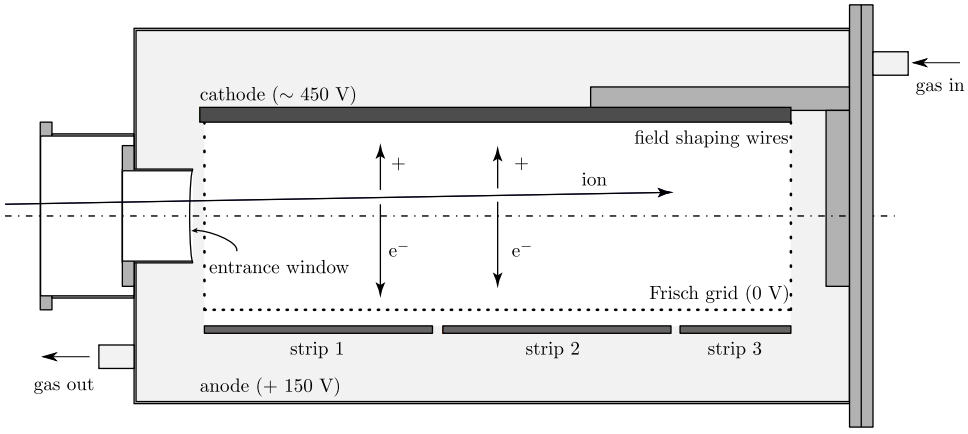

Figure 4.17: Layout of the DRAGON ionization chamber (IC). The figure was adapted from Vockenhuber et al. (2008). Note that the same setup is used for the DRAGON hybrid detector, with the addition of a DSSSD at the edge of the chamber.

4.2.6 Data Acquisition System

DRAGON employs a state–of–the–art timestamp based Data Acquisition (DAQ) system (Christian et al., 2014). It consists of two independent DAQ systems: one for the γ ray detection from the BGO array ("head") and one for the rest of the DRAGON detectors ("tail"). Each DAQ system has independent triggering and readout, and coincidence events can be identified using digital timestamps in a backend computer. The two main advantages of this DAQ system compared to its predecessor is that the coincidence requirement is no longer dependent on hardware gating, which was prone to human error or faulty modules, and it also reduces the DAQ dead time.

Each of the two DAQs employs an IO32, a general purpose VERSA Module Eurocard (VME) board designed and manufactured at TRIUMF (Olchanski, 2012). An Altera–Cyclone FPGA (Field–Programmable Gate Array) control board inside each IO32 is responsible for DRAGON trigger logic and timestamping. It contains sixteen Nuclear Instrumentation Modules (NIM), sixteen Emitter–Coupled Logic (ECL) input channels and sixteen NIM output channels. A 20 MHz quartz oscillator crystal with accuracy of 20 parts per million is also housed inside the FPGA for timing measurements.

Figure 4.18 illustrates the timestamp–based trigger logic. The trigger for the "head" DAQ contains the anode signals from 30 BGO detectors, which are split into analog and logic branches. The former branch is sent through a physical time delay to a CAEN V792 32-channel, charge-sensing ADC (Analog to Digital Converter) (or "QDC"). The latter is sent through a pair of CAEN V812 Constant Fraction Discriminators (CFD). The CFD output signals are then sent to a CAEN V1190B 64–channel, multi–hit TDC (Time to Digital Converter) and the OR outputs to IO32 ECL inputs 0 and 1 to create the system trigger. The "tail" DAQ trigger all detector signals are also split into analog and logic branches. The analog signals, after being converted through a series of amplifiers, discriminators and shapers are sent to a CAEN V785 32–channel, peak–sensing ADC and the logical to a CAEN V1190B TDC. The logical signal is then sent to ECL inputs 0–7 to create the system trigger.

In both DAQs, a signal of the system trigger and a copy of the the ISAC–I 11.78 MHz RFQ signal (see Section 4.1.3) is sent to both TDCs for the measurement of the separator time–of–flight and for additional timing reference, respectively. The RFQ signal is gated by an adjustable–width copy of the system trigger (usually three RF pulses for every event), to avoid any flooding of the TDC buffers with RF pulses.

The data acquisition and online analysis is based on the Maximum Integrated Data Acquisition System (MIDAS) (Ritt et al., 1997) software. MIDAS data files can be integrated into the ROOT data analysis framework (Antcheva et al., 2009) for online and offline analysis. Both MIDAS and ROOT are based on the `C/C++` programming languages, making the integration from one to other, very convenient. The offline analysis suite that we employ in the next chapter, `dragon::analyzer`[1], is also written in `C++`. In addition to MIDAS, TRIUMF employs the Experimental Physics and Industrial Control (EPICS) (Dalesio et al., 1991) software to control beamline elements and apparatuses, such as gas pumps and valves. Many useful data are recorded during the experiment by the DRAGON DAQ using EPICS, such as the gas target pressure and temperature, Faraday Cup measurements, and others.

Experimental data from the two DAQ systems are transferred from the "frontend" VME processor to the "backend" analysis computer once per second, for efficiency reasons. In between, "head" and "tail" events are buffered locally in the VME. This

[1]The analysis suite is available online at
`https://github.com/DRAGON-Collaboration/analyzer`.

means that coincidence events (recoil from the "tail" and associated γ ray from the "head") arrive at the analysis computer asynchronously, since other events might arrive before them. Figure 4.18 shows a flow chart of the coincidence matching algorithm. The VME buffer orders the events by their Time–Stamp Counter (TSC) value in a First In, First Out data structure (FIFO). As new events are placed in the buffer, the time difference between the earliest and latest event is calculated. If the difference is greater than a user specified value (in Figure 4.18 is the default value of 4 seconds), the queue is searched for events with timestamps of less than 10 μs. Events that satisfy this condition are sent to both the singles and the coincidence processor, while the rest are sent only to the singles processor.

Measuring the live time, which is the time over which the DAQ is available to accept new triggers, is very important for the calculation of the reaction yield and eventually the resonance strength. The real number of events is calculated from the number of recorded events and the live time. For each of the singles triggers, "head" and "tail", the live time is just the ratio between the number of acquired and accepted triggers. For coincidence events this approach cannot be employed, since coincidences are determined during the analysis. To remedy that, DRAGON calculates the busy time for each event from the TSC and records it in the data stream. Assuming a non–paralyzable dead time response, meaning that events happening during the dead time are lost, and random Poisson statistics, the number of events lost during the dead time, n_{lost}, is given by

$$n_{lost} = \lambda \sum_{i=0}^{n} \tau_i = \lambda\tau \tag{4.9}$$

where n is the number of recorded events, λ is the rate of generated events (Poisson; $\lambda = N/T$), τ_i is the busy time for the i$^{\text{th}}$ event, τ is the total busy time and T the total measurement time. The total number of generated events N is equal to

$$\begin{aligned} N &= n + n_{lost} \\ &= n + \lambda\tau \\ &= n + (N/T)\tau \\ &= \frac{n}{1 - \tau/T} \end{aligned}$$

Using the above relations, the live time, $\eta_{live} = n/N$, will be

$$\eta_{\rm live} = 1 - \tau/{\rm T} \tag{4.10}$$

Using the above, for coincidence events, τ is the total time during which the "head" or the "tail" is busy.

Nevertheless, the beam intensity and the target density can fluctuate in an experiment, meaning that Poisson statistics are not always valid. In any case, at DRAGON the difference between Poisson and non–Poisson statistics for the calculation of the live time is less than 2%. For a more detailed discussion about the DRAGON DAQ the interested reader is referred to the work of Christian et al. (2014) and the references therein.

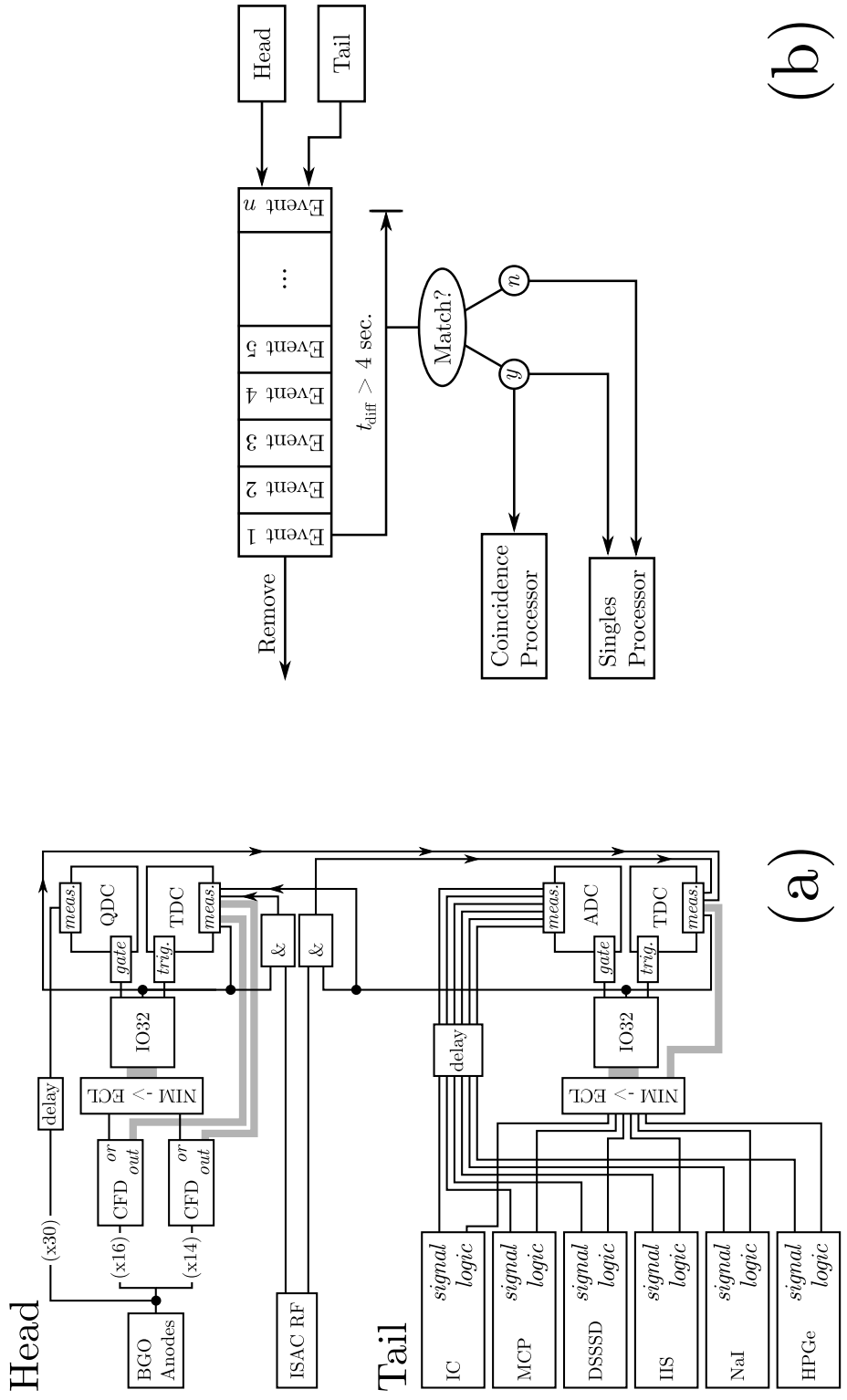

Figure 4.18: (a) Diagram of the DRAGON timestamp–based trigger logic used by the Data Acquisition System. (b) Diagram of the coincidence matching algorithm used by the Data Acquisition System. Both figures are adapted from Christian et al. (2014).

Chapter 5

Analysis and Results

> An experiment is a question which science poses to Nature
> and a measurement is the recording of Nature's answer.
> — Max Planck

5.1 GEANT Simulations of DRAGON

In Chapter 2 we discussed the challenges that arise from the study of reactions in inverse kinematics. Specifically, a limiting factor to study astrophysically interesting reactions with recoil separators, mainly in the low mass region (*i.e.* A$\leq$ 20), is the angular cone of the recoils, which arises from the reaction kinematics and can be higher than the intrinsic geometric acceptance of the separator (see Equation 2.36).

The ^{7}Be$(\alpha,\gamma)^{11}$C reaction is such a case, with the maximum angular cone of the ^{11}C recoils being $\theta_{\rm r,max} \sim 40-56$ mrad for the energies relevant to νp–process nucleosynthesis (E$_{\rm c.m.}$= 561–1356 keV). We remind the reader that the angular acceptance of DRAGON is $\theta_{\rm DRAGON} \sim \pm 21$ mrad (see also Sections 2.5 and 4.2). For this reason, the planning and data analysis of such an experimental study using DRAGON require detailed simulations of the separator, from which one can extract the recoil transmission $\eta_{\rm separator}$ and the efficiency of the BGO array $\eta_{\rm BGO}$, which are used to calculate the reaction yield, and finally the resonance strength $\omega\gamma$, as part of the recoil detection efficiency of DRAGON $\eta_{\rm DRAGON}$.

In this section we shall provide an introduction to the DRAGON GEANT simulation toolkit and present some results from the detailed simulations we performed for the

reactions studied in this thesis.

GEANT (Agostinelli et al., 2003) (GEometry ANd Tracing) is a toolkit to simulate the passage of particles through matter using Monte Carlo techniques. It incorporates the physics processes that occur in a laboratory setting, such as electromagnetic and hadronic processes. Its real advantage over other simulation packages, such as MCNP (Briesmeister, 1986), is its tracking capabilities through complex geometries. GEANT is widely used by the nuclear astrophysics community to plan experiments and interpret the corresponding data. The latest version of the code, GEANT4, is written in the C++ programming language, while the DRAGON simulation toolkit[1] is based on the previous version of the code, GEANT3 (Brun et al., 1987), which is written in the FORTRAN programming language. This toolkit has been extensively used for experimental planning, such as in the study of the $^{12}C(\alpha,\gamma)^{16}O$ reaction (Matei et al., 2006), and its results show agreement with experimental data to within 1–10% (Gigliotti, 2004).

The DRAGON GEANT toolkit can be executed in two different modes, interactive (dsinter) and batch (dsbatch). The former is mostly used to ensure that the simulation is providing reasonable outputs that agree with the experimental parameters (*e.g.* beam energy loss in the target), providing a visual representation of the separator (see Figure 5.1) and the reactions that occur, and the latter is used to simulate a large number of interactions that will provide important information about the separator, *i.e.*, its BGO efficiency and the transmission of the recoils.

The software employs hard–coded routines to specify experimental details, such as the gas target pressure (ugmate_trgt.f), beam size (beam_init.f) and the γ angular distribution of the recoils (angdist.f). All electromagnetic elements (*i.e.* electrostatic magnetic dipole voltages and fields) are calculated and tuned automatically for each reaction. The geometry of DRAGON is also included in hard–coded FORTRAN routines and the final assembly of its components is done according to a text file (dragon_2014_DSSSD.dat) which includes the positions of each element (see Figure 5.1).

Most user–defined settings for DRAGON and the reaction of interest can be found in two files: the dragon_2003.ffcards and the reaction input file (*e.g.* 7beag.dat) respectively. In the former file the user can select the number of simulated particles (to

[1]The code is available online at https://github.com/DRAGON-Collaboration/G3_DRAGON.

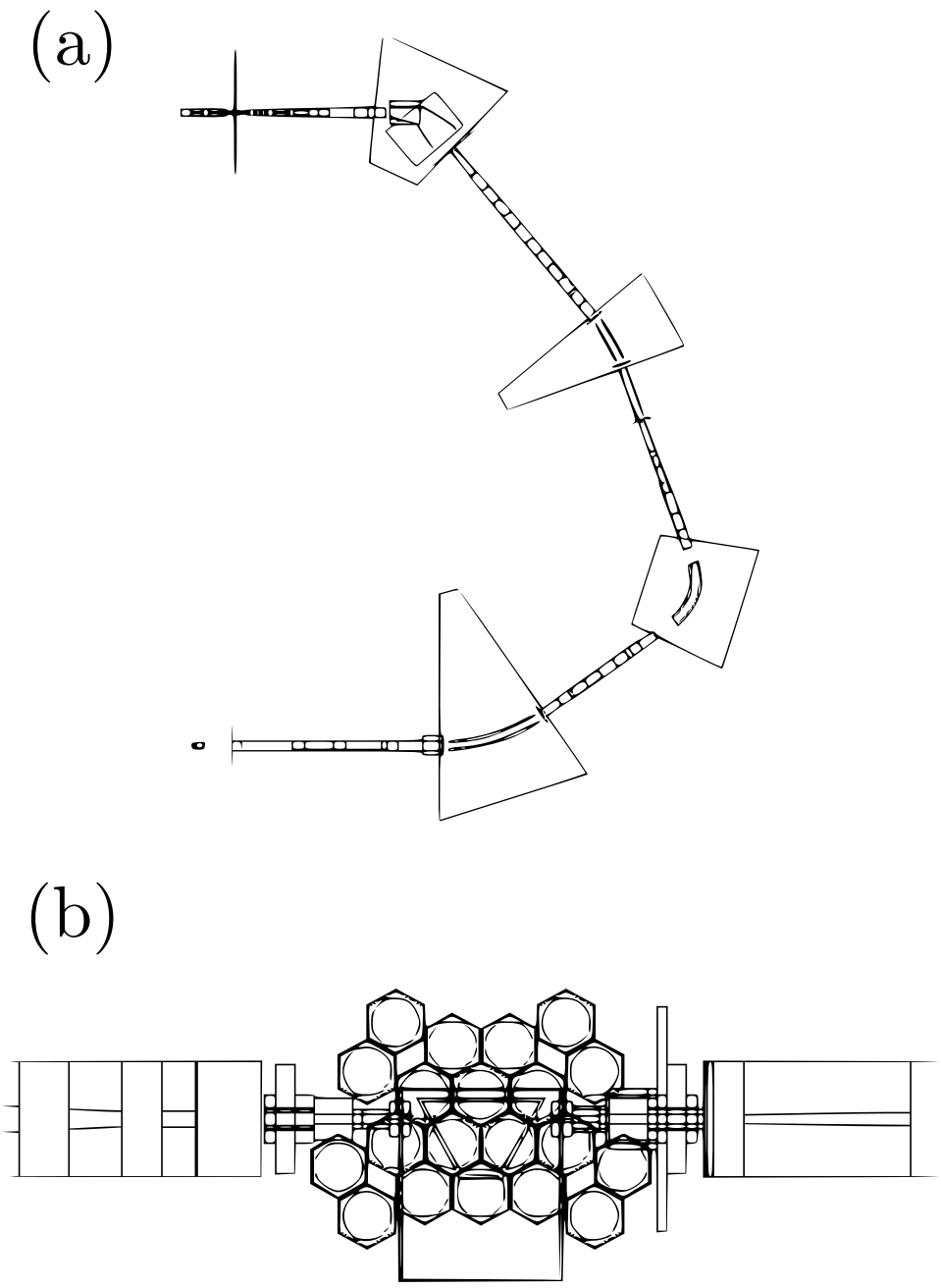

Figure 5.1: Schematic representation of DRAGON using the `GEANT` toolkit. (a) Full DRAGON layout. The beam lines and the electromagnetic elements are shown. (b) The windowless gas target surrounded by the BGO array. Both figures were adapted from the `GEANT` interactive (`dsinter`) mode. see the text for details.

be run in the `dsbatch` mode), the beam energy[2] in MeV, a possible position or angle off–set and energy mistune. The reaction input file includes all the information `GEANT` requires to perform the simulation, such as the energy, spin, lifetime, and γ branching ratios for each nuclear level and in addition the energy and width of the resonance of interest. An example of a reaction input file can be found in Appendix A.1.

The simulation output is in the form of an HBOOK/PAW file (`.hbook`), which can be converted into a `ROOT` file using the `h2root` program to be easily manipulated using `C/C++` scripts. Each `GEANT` output file includes a variety of information in the form of 1D and 2D histograms. The most relevant for experimental planning and data analysis are the ones that present the angular distribution of the recoils (`thet_r`, see an example in Figure 5.5) and the number of recoils that reach the end detector (`recdet` and `recoil_hit_endv`). Using this information and the simulated BGO spectrum which can be found in the `e0_conv` histogram (see Figure 5.3), one can easily calculate the separator transmission $\eta_{\text{separator}}$ and the BGO detection efficiency η_{BGO}. For more details the interested reader is referred to Gigliotti (2004) and Carmona Gallardo (2014).

5.1.1 $^{6}\text{Li}(\alpha,\gamma)^{10}\text{B}$

The $^{6}\text{Li}(\alpha,\gamma)^{10}\text{B}$ was selected as a benchmark reaction to test that DRAGON can measure resonance strengths for reactions in which the angular cone of the recoils exceeds its acceptance. The resonance we selected was at $E_r = 1458.5$ keV, corresponding to the $E_x = 5.920$ MeV of ^{10}B ($J^\pi = 2^+$) and had a known resonance strength $\omega\gamma = 0.228(38)$ eV (Tilley et al., 2004). In this Section we shall focus our discussion on the specifics of the `GEANT` simulations and in Section 5.2 the experimental details are presented in detail.

To better reproduce the experimental BGO position spectrum of the γ rays emitted by the ^{10}B recoils (see Figure 5.2) and extract the resonance energy E_r and strength $\omega\gamma$ via a log–likelihood analysis (see Section 5.2.7) we performed simulations varying the resonance energy (13 values, spanning from $E_r = 1457.8$ to 1469.8 keV). To ensure that the simulation best represents the conditions of the experiment, we kept the beam energy fixed at 3.675 MeV, and the target pressure we selected

[2]If no specific value for the beam energy is selected, `GEANT` calculates the beam energy so that the resonance is centered in the gas target.

reproduced the experimental energy loss. The GEANT input file included nuclear level information for the compound nucleus ^{10}B, such as lifetimes and γ branching ratios, from Tilley et al. (2004). Table 5.1 shows a summary of the GEANT simulation reaction input file.

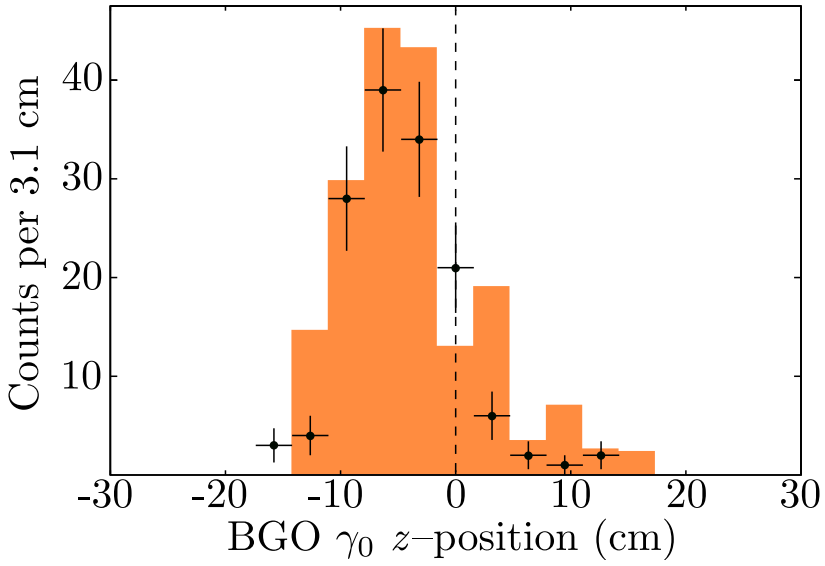

Figure 5.2: The distribution of the z position of the highest energy γ ray for a yield measurement at P=5 Torr of the ^{6}Li$(\alpha,\gamma)^{10}$B reaction. The orange histogram represents the GEANT simulation with the highest overall likelihood, and the black dots the experimental data. The centroid is at -3.85 cm from the center of the gas target.

To calculate the γ angular distribution for each transition of the level of interest, which as we discussed in Section 2.5 affects the recoil transmission through the separator and the BGO efficiency, we proceeded as follows: a spin 1 beam (^{6}Li) on a spin 0 target (^{4}He) can populate M= $0, \pm 1$ magnetic substates of ^{10}B. Using the prescription of Rose and Brink (1967), we found the statistical tensor coefficients $\rho_2(2,0) = \rho_2(2,1) = -1.195$. Then we multiplied with the geometry factors $R_2(2 \to 3) = 0.1195$ and $R_2(2 \to 1) = 0.4183$, which results in the γ angular distribution for the two transitions (see also Figure 5.6): $\mathrm{W}(\theta) = 0.86 + 0.21\sin^2(\theta)$ to the J=3 ground state and $\mathrm{W}(\theta) = 0.5 + 0.75\sin^2(\theta)$ to the J=1 first excited state, given in terms of $\sin^2\theta$. Therefore the angular distribution of the dominant ground state transition is nearly isotropic and that of the other is between isotropic and bipolar.

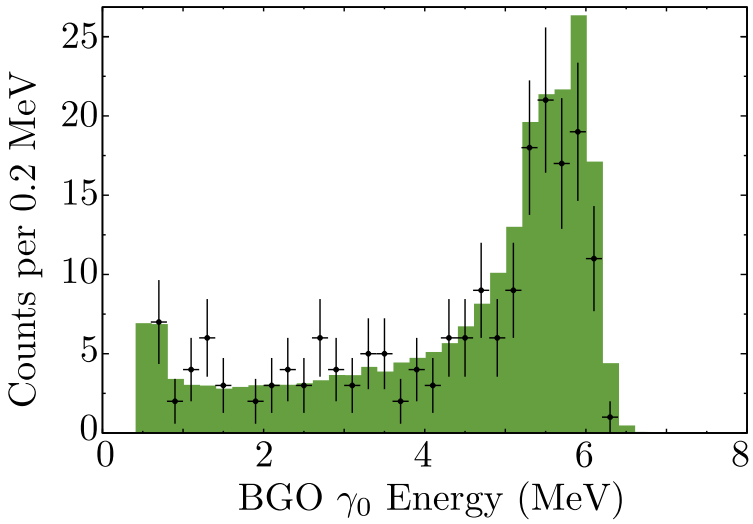

Figure 5.3: γ_0 energy plot comparison between experiment (black points) and `GEANT` simulation (green histogram) for the $^6\mathrm{Li}(\alpha,\gamma)^{10}\mathrm{B}$ reaction.

Table 5.1: Settings of the `GEANT3` simulation for the $^6\mathrm{Li}(\alpha,\gamma)^{10}\mathrm{B}$ Log–Likelihood analysis. Nuclear properties were adopted from Tilley et al. (2004). For the full input file, see Appendix A.1.

Quantity	**Used Value**
Excited state lifetime	1.13×10^{-19} s
Resonance energy	1457.8–1469.8 keV
Beam mass excess	14.0868 MeV
Recoil mass excess	12.0507 MeV
Particle (α) partial width	5.82 keV
γ partial width	0.1114 eV
γ branching ratios	82% (to the ground state)
	18% (to the first excited)
γ angular distributions	
$2 \rightarrow 3$ (ground state)	$W(\theta) = 0.86 + 0.21\sin^2(\theta)$
$2 \rightarrow 1$ (first excited)	$W(\theta) = 0.50 + 0.75\sin^2(\theta)$

In addition, we took into account the beam transmission of the beam through the gas target. In particular, during the experiment we measured an ∼86% transmission of the beam through the gas target by means of Faraday cup measurements. This implies that the beam was not centered as it was entering the gas target, given that its 2rms size, assuming a Gaussian profile, was measured by the ISAC beam operators to be 1.78 mm in both x and y. To include this piece of information in our `GEANT` simulations, we performed Monte–Carlo simulations sampling both x– and y–axis offsets for the measured beam size. Figure 5.4 shows the results of the simulated transmission. After that, we selected six points with 86% transmission to perform our log–likelihood analysis (black points in Figure 5.4, see also Section 5.2.7).

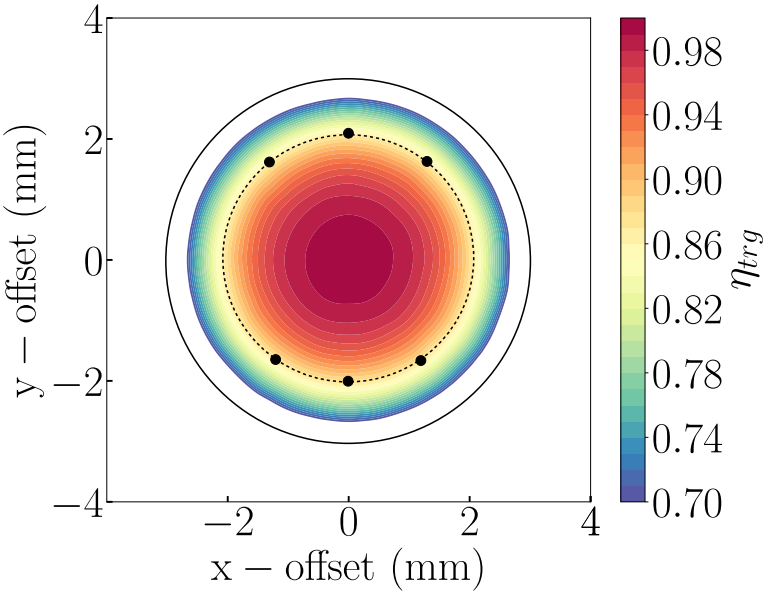

Figure 5.4: 2D plot of x– and y–beam off–set and the corresponding transmission. The black solid line shows the 6 mm diameter collimator before the gas target and the dashed line shows the measured transmission of the beam. The six black points show simulations that match the experimental beam transmission through the gas target.

5.1.2 $^{7}\mathrm{Be}(\alpha,\gamma)^{11}\mathrm{C}$

For the $^{7}\mathrm{Be}(\alpha,\gamma)^{11}\mathrm{C}$ reaction we simulated the two resonances that we measured using DRAGON (E_r= 1110 and 1155 keV). We followed a similar procedure as in the $^{6}\mathrm{Li}(\alpha,\gamma)^{10}\mathrm{B}$ case, with some differences that we shall explain below. The simulated beam energy was set to the one we measured at DRAGON, and the gas target pressure was such that it reproduced the experimental energy loss (see Section 5.3.4).

The main ingredients of the reaction input files are presented in Table 5.2 and the different γ angular distributions used are presented in Table 5.3. In contrast to the $^{6}\mathrm{Li}(\alpha,\gamma)^{10}\mathrm{B}$ reaction, the statistical tensor coefficients for the nuclear substates M= 1/2, 3/2 are not equal, and hence we had to run separate simulations for each resulting angular distribution following the prescription of Rose and Brink (1967). γ branching ratios were used from Kelley et al. (2012) (see Table 3.2) and for E_r= 1110 keV, since there are no experimental γ branching ratios, we used the ones from the mirror ^{11}B nucleus.

We performed simulations for each resonance energy within its uncertainty, ±4 and ±2 keV for the 1110 and 1155 keV resonance, respectively. The final results that we shall use in the data analysis below are the averages of these simulations. Figure 5.5 shows a typical recoil angular distribution plot from each cascade of the E_r= 1155 keV resonance.

Table 5.2: Settings of the `GEANT3` simulation for the $^{7}\mathrm{Be}(\alpha,\gamma)^{11}\mathrm{C}$ data analysis. Nuclear properties were adopted from Kelley et al. (2012). See the text for details.

Quantity	**E_r = 1110 keV**	**E_r = 1155 keV**
Excited state lifetime	1.31×10^{-19} s	4.3×10^{-20} s
Resonance energy	1106–1114 keV	1153–1157 keV
Beam mass excess	14.0868 MeV	14.0868 MeV
Recoil mass excess	12.0507 MeV	12.0507 MeV
Particle (α) partial width	5 keV	15 keV
γ branching ratios	see Table 3.2	see Table 3.2
γ angular distributions	see Table 5.3	see Table 5.3

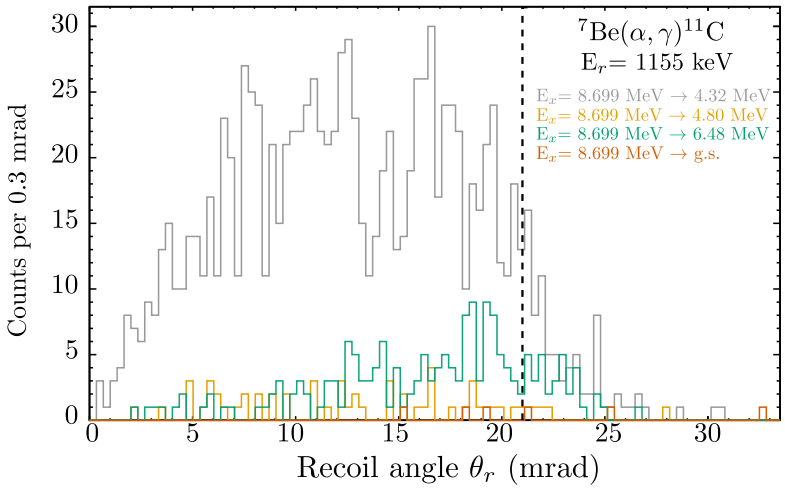

Figure 5.5: Angular distribution for recoils of the E$_r$= 1155 keV resonance that hit the DSSSD from GEANT. The contributions from different cascades are shown. The vertical dashed line defines the angular acceptance of DRAGON, $\theta = 21$ mrad.

Table 5.3: Summary of the γ angular distributions used in the GEANT simulations of DRAGON for the E$_r$ = 1110 (top) and 1155 keV (bottom) resonances of the ^{7}Be$(\alpha,\gamma)^{11}$C reaction calculated from Rose and Brink (1967).

$\mathbf{E_{final}(MeV)}$	J_f	$W(\theta)$ $(M = 1/2)$	$W(\theta)$ $(M = 3/2)$
g.s	$3/2^-$	2.02 - 1.53 $\sin^2\theta$	1.61 - 0.915 $\sin^2\theta$
4.32	$5/2^-$	0.29 - 1.07 $\sin^2\theta$	0.57 + 0.645 $\sin^2\theta$
6.48	$7/2^-$	1.95 - 1.43 $\sin^2\theta$	1.57 - 0.855 $\sin^2\theta$
g.s	$3/2^-$	0.2+1.2 $\sin^2\theta$	0.8+0.3 $\sin^2\theta$
4.80	$3/2^-$	0.2+1.2 $\sin^2\theta$	0.8+0.3 $\sin^2\theta$
4.32	$5/2^-$	1.92 - 1.38 $\sin^2\theta$	1.23 - 0.345 $\sin^2\theta$
6.48	$7/2^-$	0.71 + 0.435 $\sin^2\theta$	0.93 + 0.105 $\sin^2\theta$

5.2 Benchmark Experiment: $^{6}\mathrm{Li}(\alpha,\gamma)^{10}\mathrm{B}$

Before measuring the $^{7}\mathrm{Be}(\alpha,\gamma)^{11}\mathrm{C}$ reaction cross section, we performed a proof of principle test of the capability of DRAGON to measure resonant cross sections of radiative capture reactions in which the angular cone of the recoils exceeds its acceptance. We chose a known resonance at $\mathrm{E_r}$ = 1458.5(6) keV of the $^{6}\mathrm{Li}(\alpha,\gamma)^{10}\mathrm{B}$ reaction whose strength was originally measured in forward kinematics by Forsyth et al. (1966). The benchmark measurement was performed in inverse kinematics, using a stable ^{6}Li beam provided by the TRIUMF Off-Line Ion Source (OLIS) (Jayamanna, 2014).

5.2.1 Previous Work

The only published measurement of $^{6}\mathrm{Li}(\alpha,\gamma)^{10}\mathrm{B}$ reaction's $\mathrm{E_r}$ =1458.5(6) keV ($\mathrm{E_x}$= 5919.5(6) keV) resonance strength was performed by Forsyth et al. (1966). It was carried out at the University of Maryland Van de Graaff accelerator lab in forward kinematics, using a single–charged ^{4}He beam (E_α= 0.9–3.3 MeV and I_α = 2.5 μA) and a 96% isotopically enriched ^{6}Li target. γ rays were detected using a NaI crystal placed at 90° with respect to the beam.

The resonance strength was found to be $\omega\gamma$ = 0.228(38) eV and its width Γ = 6(1) keV in the center of mass system. Branching ratios of the γ transitions were determined to be 82(5) % and 18(5) % to the ground state and the first excited state respectively (see Figure 5.6), as opposed to a single transition to the ground state reported in a study by Meyer-Schützmeister and Hanna (1957). The reported branching ratios were used as input for the `GEANT` simulations of the BGO γ array of DRAGON (see Section 5.2.7 and Table 5.1).

5.2.2 Experimental Details

For our benchmark study, a beam of $^{6}\mathrm{Li}^{+}$ from OLIS, which was accelerated through the ISAC–I Radio–Frequency Quadrupole (RFQ) and Drift–Tube Linac (DTL) to an average energy of 0.612(1) A MeV (E_{lab}= 3.675(6) MeV, $E_{c.m.}$= 1.468(3) MeV), so that the resonance was centered in the gas target. The beam energy spread was $\Delta E/E \leq 0.3$ % throughout the experiment (Laxdal, 2003), with an average intensity

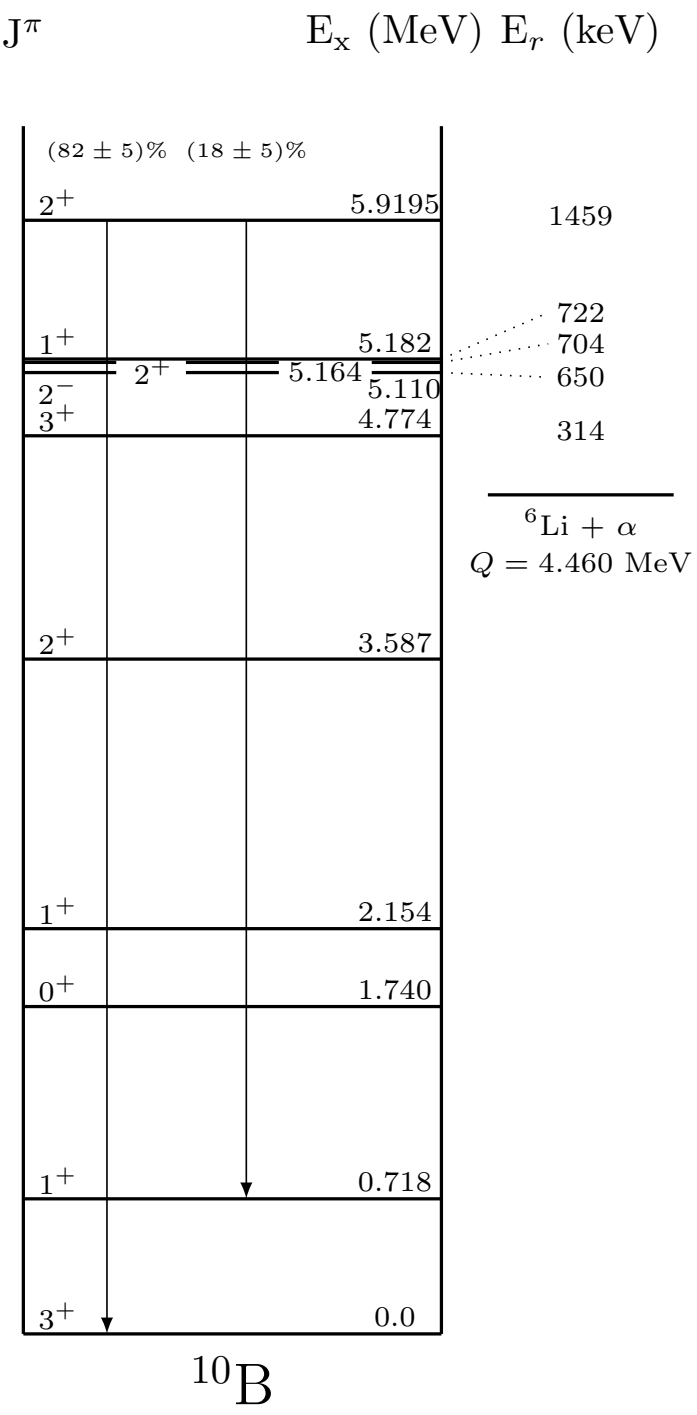

Figure 5.6: Level scheme of the ^{10}B nucleus adopted from Tilley et al. (2004). The energy levels that correspond to resonances of the $^6\mathrm{Li}(\alpha,\gamma)^{10}\mathrm{B}$ reaction and the γ decay scheme of the E_r= 1459 keV resonance are shown. The reaction Q value was taken from AME2016 (Wang et al., 2017). See the text for details.

of 1.17×10^{10} s^{-1}.

The windowless gas target pressure was maintained at P= 5.0(1) Torr, corresponding to a thickness of $1.97(4) \times 10^{18}$ atoms/cm^2. The most intense charge state of the recoils ($^{10}B^{2+}$) was tuned through the separator to a 66 μm thick, gridded Double–Sided Silicon Strip Detector (DSSSD) placed near the focal plane of DRAGON.

5.2.3 Particle Identification

To extract the resonance energy E_r and strength $\omega\gamma$ and compare it to the literature values, we first have to calculate the reaction yield, which includes identifying the recoils, determining the total number of beam particles, measuring the charge–state fraction of the recoils, and calculating the efficiency of the BGO array and the transmission of the recoils through the separator using `GEANT` simulations.

The main particle identification technique that was used in this experiment was the separator time–of–flight measurement (see also Section 4.2.4). Figure 5.7 shows a typical separator time–of–flight spectrum. The clear peak shows the recoils of interest (^{10}B). We define the "Golden Gate" as a requirement for a real coincidence event such that the separator time–of–flight, energy deposited in the DSSSD and BGO detectors lie in the experimentally expected limits. For example, the expected separator time–of–flight for the ^{10}B recoils was ∼3480 ns, which agrees very well with the peak of Figure 5.7. As we have already discussed, the beam suppression for (α, γ) reactions with DRAGON is on the order of 10^{11-12}, and hence the beam induced background in the form of "leaky beam" is negligible.

5.2.4 Beam Normalization

To determine the number of incident beam particles in the windowless gas target of DRAGON N_{beam}, we used the 57° SSB detector to collect elastically scattered α particles during each run. These measurements were normalized to beam current measurements at a Faraday cup located 2 m upstream of the target (FC4). For a time window $\Delta t \sim 240$ s, before and after each run, we were recording these measurements to calculate R_0 and R_1 respectively. The average of those two is the R for the run. The normalization coefficient $\mathcal{R}$ is given by

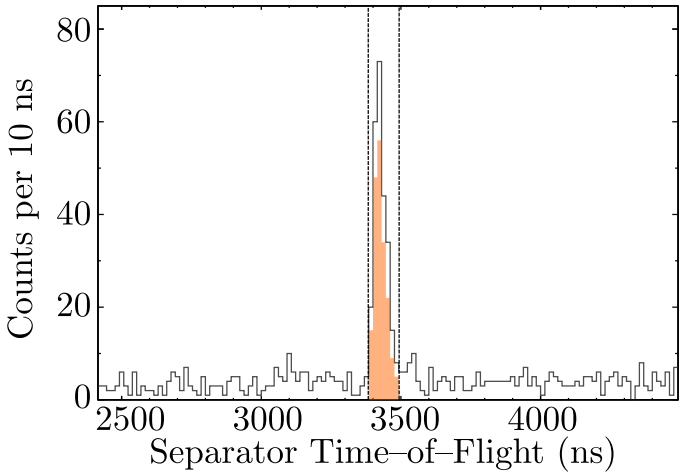

Figure 5.7: Separator time–of–flight spectrum. The orange histogram corresponds to the recoils in the "Golden Gate".

$$R = \frac{I}{|q \cdot e|} \frac{\Delta t}{N_\alpha} \frac{P}{E^2} \eta_{trg} \tag{5.1}$$

where I is the average current reading at FC4, q is the beam charge state, e is the elementary charge (e= 1.6×10^{-19} C), N_α is the number of scattered α particles detected by the surface barrier detectors in time window Δt, P is the gas target pressure in Torr, E is the beam energy in keV/u and η_{trg} is the transmission through an empty target. The normalized number of beam particles $\mathrm{N_{beam}}$, is then given by

$$\mathrm{N_{beam}} = \mathcal{R}\mathrm{N}_\alpha \frac{\mathrm{E}^2}{\mathrm{P}} \tag{5.2}$$

Figure 5.8 shows the R coefficient for a set of runs during the experiment.

5.2.5 Boron–in–Helium Charge State Distribution

In Section 4.2 we showed that DRAGON is able to transmit only one charge state through the separator after the first magnetic dipole MD1. Hence, its overall detection efficiency, η_{DRAGON}, depends on the precise measurement of the charge state distribution (CSD) of the recoils at the energy with which they exit the gas target. This piece of information will eventually be used to calculate the thick target reaction yield Y and subsequently the resonance strength $\omega\gamma$ (recall Equations 2.19 and 2.33).

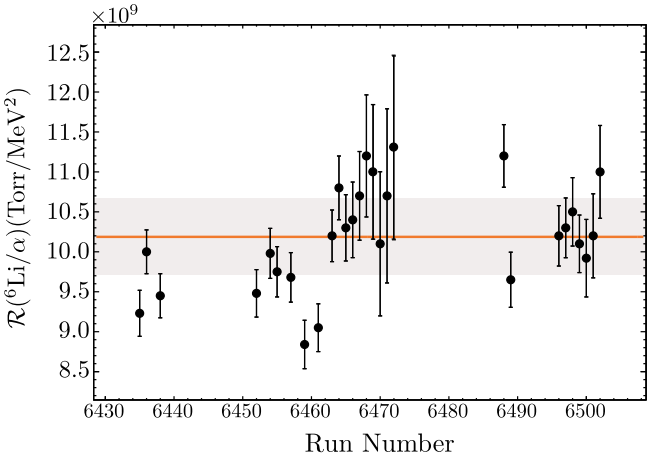

Figure 5.8: Beam normalization coefficient $\mathcal{R}$ results for the resonance of the $^6\mathrm{Li}(\alpha,\gamma)^{10}\mathrm{B}$ reaction. The orange line shows the line of best fit and the grey band the 95% confidence level. See the text for details.

In the following, we shall give a brief overview of charge–exchange processes and present how charge state distributions are measured at DRAGON.

Inside the DRAGON gas target, charge exchange is happening between the heavy ions (beam particles and recoils) and the target, mainly in the form of single electron capture or loss[3]. The charge distribution of an ion species is described by its charge state fraction, $\mathrm{F_q}$, for charge q, and it generally depends on the thickness of the gas target. Charge state distributions are normalized to unity

$$\sum_q F_q = 1 \tag{5.3}$$

The charge state of an ion species is independent of its mass, and therefore it is preferable to choose a stable and abundant isotope of the recoil element to measure the charge state distribution. In the case of the $^6\mathrm{Li}(\alpha,\gamma)^{10}\mathrm{B}$ reaction, a beam of $^{11}\mathrm{B}$ was chosen.

We assume that after the recoils exit the gas target a charge state equilibrium has been achieved, meaning that the number of ions populating charge state q is the same

[3]For hydrogen gas multiple electron capture/loss is not possible since its atom has only one electron. For helium the probability for double capture/loss for low mass projectiles (A$<$ 10) is less than 10% compared to single electron capture/loss (DuBois, 1985), and hence it is not taken into account in the calculations of the charge state distribution.

as the ones depopulating it ($dF_q/d\chi = 0$). This assumption is reasonable since the critical target thickness χ_c where this equilibrium is achieved, is usually of the order of 10^{17} atoms/cm^2 (Liu et al., 2003), which is much lower than the ones in the present study. In addition, the equilibrium charge state distribution is independent of the incident charge state, and hence we can choose the one that can easily be extracted from the ion source and accelerated to DRAGON.

There are many semi–empirical theoretical studies that estimate the equilibrium charge state distribution of ions traversing gaseous or solid targets. Such studies are of extreme importance, especially for experimental planning, since by selecting the most probable recoil charge state of the distribution, one can detect more reaction products. We shall focus our discussion on the study of Liu et al. (2003), since it was motivated by the first experiments at DRAGON. The interested reader is referred to the review of Betz (1972) and Schiwietz and Grande (2001).

At equilibrium conditions, the average or mean charge $\bar{q}$, is an important quantity which is defined by

$$\bar{q} = \sum_q q \; F_q \tag{5.4}$$

$\bar{q}$ usually is non-integer and in smooth charge state distributions it coincides with the maximum. Liu et al. (2003) showed that for light target ions, Z$<$ 13, F_q is close to a Gaussian distribution

$$F_q = \frac{1}{\sqrt{2\pi d}} \exp\left[-\frac{(q-\bar{q})^2}{2d}\right] \tag{5.5}$$

where the width of the distribution, Γ, is

$$\Gamma = 2\sqrt{2\sum_q (q-\bar{q})^2 F_q} \tag{5.6}$$

At DRAGON, the charge state distributions can be determined experimentally by measuring the current (number of particles) on Faraday cups before (FC4) and after the gas target (FC1), and comparing it to the current on a Faraday cup downstream from the first magnetic dipole, MD1 (FCCH). The mean equilibrium charge can be calculated using the following relation

$$\bar{q} = q \; \frac{I_{FC1}}{I_{FC4} \; \eta_{target}} \tag{5.7}$$

where q is the measured charge state, I_{FC1} and I_{FC4} the currents on the namesake Faraday cups and η_{target} the transmission of the beam through an empty gas target.

The charge state fraction F_q can be calculated using

$$F_q = \frac{\bar{q}}{q} \frac{I_{FCCH}}{I_{FC1}} \tag{5.8}$$

We recorded the transmission through an empty target, η_{target}, before and after the charge state distribution measurements and we adopted the average value for the calculation of F_q. The final results are presented in Table 5.4 and Figure 5.9.

Table 5.4: Summary of the boron–in–helium gas charge state distribution (CSD) measurement. The incoming ^{11}B beam charge state was $q_{in} = 2^+$. See the text for details.

$\mathbf{E_{beam}}$ **(keV/u)**	$\mathbf{P_{target}}$ **(T)**	$\boldsymbol{\eta_{target}}$	$\bar{\boldsymbol{q}}$	$\mathbf{2^+}$	$\mathbf{3^+}$	$\mathbf{4^+}$
194(1)	6.4(1)	0.92(1)	2.11(2)	0.497(7)	0.363(5)	0.011(1)
213(1)	6.8(1)	0.95(1)	2.27(3)	0.467(9)	0.438(6)	0.020(1)

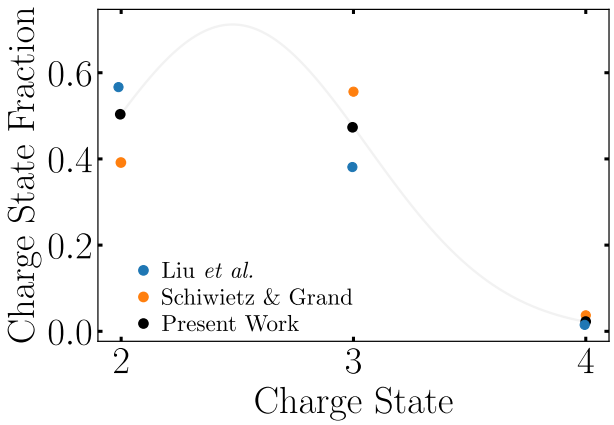

Figure 5.9: Lithium in helium charge state distribution results (CSD) for E_{beam} = 194 keV/u. The predictions of the semi–empirical formulae of Liu et al. (2003) and Schiwietz and Grande (2001) are shown. The error bars are smaller than the size of the points.

5.2.6 ^{6}Li Stopping Power in ^{4}He and Energy Loss

One of the advantages of studying reactions in inverse kinematics using recoil separators is that the stopping power ϵ, which is required for the calculation of the resonance strength (Equation 2.33), is measured directly and is not based on semi–empirical formulae, which introduce an additional uncertainty to the measurement, especially when they are extrapolated to low energies. At DRAGON, stopping powers are measured by varying both the pressure in the gas target and the magnetic field strength needed to centre the beam at a momentum dispersed angular focus in the focal plane of the first magnetic dipole. Figure 5.10 shows a typical stopping power measurement plot. Our result, $\epsilon_{\mathrm{DRAGON}} = (24.6 \pm 1.35)$ eV/ (10^{14} atoms/ cm^2), was compared to the calculation of the Stopping and Range of Ions in Matter (SRIM) (Ziegler et al., 2010), $\epsilon_{\mathrm{SRIM}} = 22.6$ eV/ (10^{14} atoms/ cm^2), and agrees to within 8.6%. We used these results to calculate the expected yield $Y_{\omega\gamma_0}$ in Equation 5.9 and compare our experimental results with `GEANT` simulations (see Section 5.2.7).

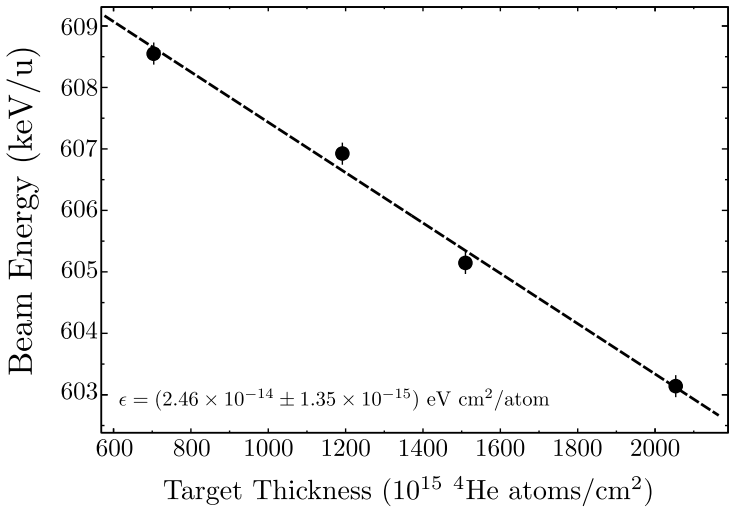

Figure 5.10: Gas target thickness versus beam energy for different values of the target pressure. The slope of the linear fit is the stopping power ϵ.

5.2.7 Log–Likelihood Analysis

The analysis of the BGO position spectrum of the γ rays emitted by the de–excitation of the ^{10}B recoils (Figure 5.2) shows that the resonance is excited upstream of the center of the gas target, indicating that the resonance energy is higher than 1458.5 keV. Therefore, we cannot use the standard method of DRAGON to determine the resonance energy from the distribution of the z position of the highest energy γ ray, since it assumes that the resonance is excited in the uniformly dense region surrounding the center of the gas target (Hutcheon et al., 2012) (see Section 5.3.5 for more details). Instead, we performed a likelihood analysis similar to the ones in Erikson et al. (2010) and Christian et al. (2018) to extract the resonance energy E_r, and its strength, $\omega\gamma$.

After performing extensive `GEANT` simulations of DRAGON (see Section 5.1.1), we scaled the generated BGO spectra according to the expected reaction yield by a factor

$$\eta \frac{Y_{\omega\gamma_0} N_{beam}}{N_{sim}}, \tag{5.9}$$

where η is the recoil detection efficiency [4], $Y_{\omega\gamma_0}$ is the reaction yield from a single–level Breit–Wigner resonance ($\Gamma = 5.82$ keV (Tilley et al., 2004)) of arbitrary strength $\omega\gamma$ (200 values spanning from 0.05 - 10 eV), N_{beam} is the number of incident beam particles normalized by the $\mathcal{R}$ coefficient (see Section 5.2.4) and $N_{sim} = 5 \times 10^4$ is the number of simulated events. The BGO array efficiency and the separator transmission are built–in the `GEANT` simulation, and thus we do not include them in the η factor.

The scaled BGO spectra are then compared to the experimental data. From these simulations we created a (E_r, $\omega\gamma$) space of 2,600 points (13×200) and for each point on this grid, we calculated the negative log–likelihood using

$$-\ln \mathcal{L} = \sum_i [\ln(n_i!) - n_i \ln(f_i)] + S, \tag{5.10}$$

where i is the number of bins in the experimental BGO spectrum, n_i is the number of events in the i^{th} bin, f_i is the number of events in the scaled simulation i^{th} bin and S the total number of events in the scaled histogram.

[4] It includes the recoil charge state fraction, the heavy ion detector efficiency, and the data acquisition dead time.

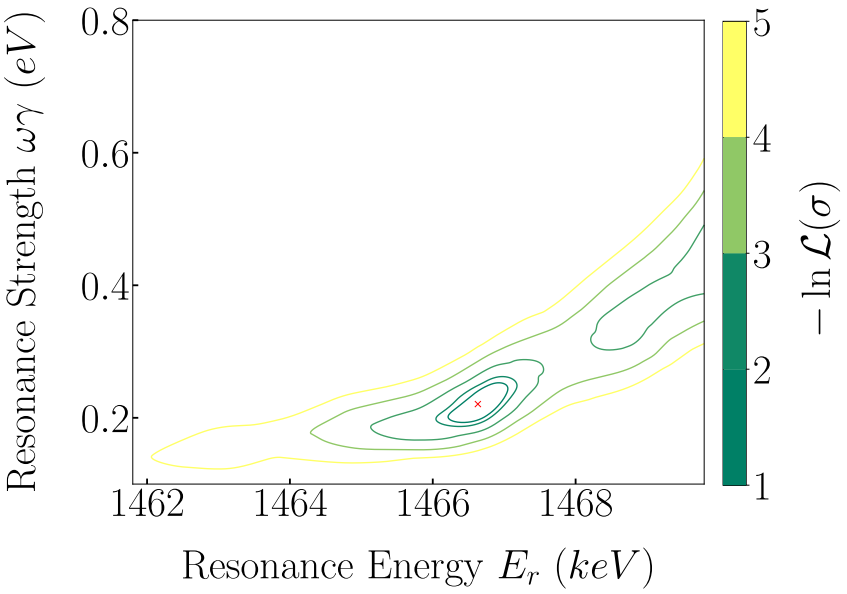

Figure 5.11: Negative Log–likelihood contour plot for the $(\mathrm{E_r}, \omega\gamma)$ space. The red cross shows the global minimum.

5.2.8 Results and Implications

Figure 5.11 shows the results of our simulations with a single minimum for the negative log–likelihood, with energy that corresponds to a location inside the gas target. The global minimum has $-\ln\mathcal{L}_0 = 35.69$ and it is the only point where a 1σ contour can be deduced.

On top of the above analysis, we also performed tests on the `GEANT` by changing the random seed of the Monte Carlo simulation, to ensure that the distribution of events is Poissonian, as in an experimental study. Due to the large number of simulation events (N=5×10^4) the final result does not depend on the random seed.

The results for the resonance energy E_r, and strength $\omega\gamma$, for the global minimum are the following

$$E_r = 1466.6 \ \pm 0.5 \ (\text{stat.}) \pm 2.4 \ (\text{syst.}) \ \text{keV}$$

$$E_x = 5927.8 \ \pm 0.5 \ (\text{stat.}) \pm 2.4 \ (\text{syst.}) \ \text{keV}$$

$$\omega\gamma = 0.225 \ ^{+0.025}_{-0.035} \ (\text{stat.}) \pm 0.030 \ (\text{syst.}) \ \text{eV}$$

Our reported resonance strength has an excellent agreement with the measurement of Forsyth et al. (1966) as shown in Figure 5.12. However, the resonance energy we extracted with DRAGON is higher than the recommended value in nuclear databases, such as NuDat2. A thorough search in the literature (Buccino and Smith, 1965; Kashy et al., 1974; Armitage and Meads, 1964; Gorodetzky et al., 1965; Park et al., 1973; Fife et al., 1967) shows that the excitation energy E_x for the state of interest lies between 5920–5930 keV, which is consistent with our result (see Table 5.5 and Figure 5.13). To obtain an average literature-based excitation energy with a realistic uncertainty, we first excluded the measurement of Buccino and Smith (1965) as an outlier ($E_x = 5900 \pm 80$ keV) applying Peirce's criterion (Peirce, 1852). We then calculated the average using the Rajeval technique (Rajput and Mac Mahon, 1992) for all the remaining measurements with reported uncertainties to be $E_x = (5920.4 \pm 1.2)$ keV. It is worth mentioning that the adopted level energy of $E_x = (5919.5 \pm 0.6)$ keV, which is the weighted average of the same measurements, is mainly determined by the high–precision measurement reported in Kashy et al. (1974) with the same result for the excitation energy. However, this result was extracted using an Enge split–pole spectrograph which usually results in excitation energy uncertainties of approximately ± 5 keV (Marshall et al., 2018). For this reason, we also calculated the Rajeval average with a more realistic uncertainty for the study of Kashy et al. (1974) – $\delta E_x = 5$ keV. The result, $E_x = (5923.0 \pm 2.3)$ keV agrees within 2σ with the energy extracted using the Negative Log–Likelihood analysis $E_x = 5927.8 \pm 0.5$ (stat.) ± 2.4 (syst.) keV (see Figure 5.13).

Our results suggest that DRAGON can measure resonance strengths of reactions with large recoil angular cones. Following that measurement, we shall proceed on the discussion of the measurement of the $^{7}\mathrm{Be}(\alpha,\gamma)^{11}\mathrm{C}$ reaction. It is worth pointing out that more reactions with recoil angular cones larger than the angular acceptance of DRAGON could be studied in the near future, *e.g.*, $^{18}\mathrm{O}(\alpha,\gamma)^{22}\mathrm{Ne}$, $^{20}\mathrm{Ne}(\alpha,\gamma)^{24}\mathrm{Mg}$, $^{22}\mathrm{Ne}(\alpha,\gamma)^{26}\mathrm{Mg}$ and others.

Table 5.5: Summary of reported energies for the E_x= 5920 keV state of ^{10}B from different measurements. See the text for a detailed discussion.

Reaction	$\mathbf{E_x}$ **(keV)**	$\delta\mathbf{E_x}$ **(keV)**	**Reference**
^{9}Be$(d,n)^{10}$B	5900	80	Buccino and Smith (1965)
^{10}B$(p,p')^{10}$B	5919.5	0.6	Kashy et al. (1974)
^{10}B$(d,d')^{10}$B	5920	10	Armitage and Meads (1964)
^{10}B$(p,p')^{10}$B	5920	10	Armitage and Meads (1964)
^{11}B$(^{3}$He$,\alpha)^{10}$B	5923	5	Gorodetzky et al. (1965)
N/A	5924	4	Reported at Kashy et al. (1974)
^{9}Be$(d,n)^{10}$B	5930	10	Park et al. (1973)
^{9}Be$(d,n)^{10}$B	5930	10	Fife et al. (1967)
Average	5920.4	1.2	
Average with $\delta\mathbf{E_x}$ =5 keV on Kashy et al. (1974)	5923.0	2.3	
$\mathbf{^{6}Li(\alpha,\gamma)^{10}B}$	5927.8	$\pm$0.5 (stat.) $\pm$2.4 (syst.)	DRAGON

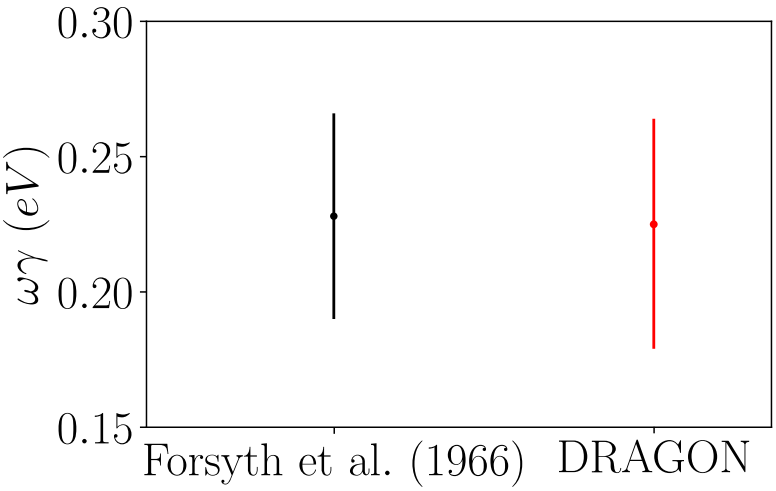

Figure 5.12: Comparison between the result of Forsyth et al. (1966) and the present work for the resonance strength of the E_r= 1458.5 keV resonance.

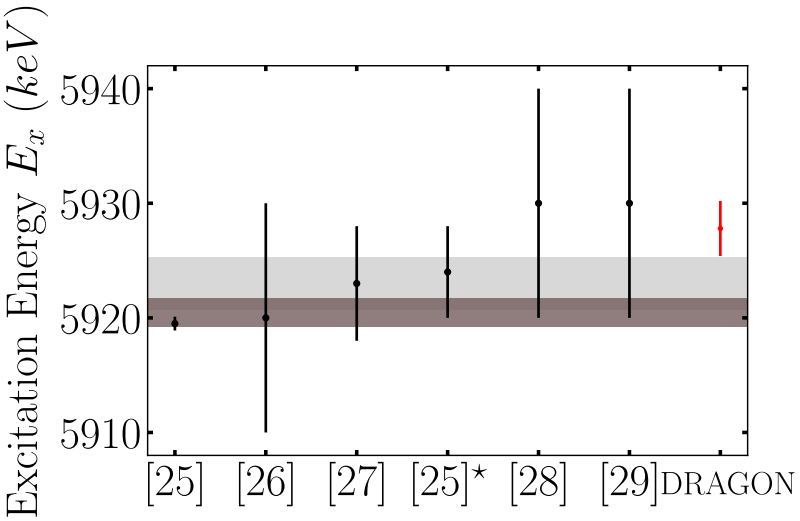

Figure 5.13: Excitation energies for the E_x= 5919.5 keV state of ^{10}B from literature values (Table 5.5) compared with the present work. The two bands correspond to the Rajeval average (dark grey) and the Rajeval average with 5 keV uncertainty for the measurement of Kashy et al. (1974).

5.2.9 Uncertainties

The uncertainties for DRAGON experiments can be separated into statistical, which arise from the statistical nature of the measurements, and systematic, which reflect the intrinsic limitations of the experimental setup. In the case of the ^{6}Li$(\alpha,\gamma)^{10}$B reaction, the statistical uncertainties are extracted from the log–likelihood analysis. Table 5.6 shows the systematic uncertainties for this measurement. It is evident that the most important contributors to the systematic uncertainty is the BGO efficiency, and the reason is that this result rely on the `GEANT` simulations. In any case the total systematic uncertainty of 13.43% is typical for DRAGON experiments using stable ion beams.

Table 5.6: Relative systematic uncertainties used to calculate the resonance strength of the E_r =1458.5 keV resonance.

Quantity	**Measured Value**	**Relative Uncertainty**
Charge state fraction, f_q	0.523 ± 0.008	1.5%
Beam particles, $N_{\rm beam}$	$(3.252 \pm 0.034) \times 10^{14}$	1.1%
BGO efficiency, η_{BGO}	(0.332 ± 0.038)	11.4%
Separator transmission, $\eta_{separator}$	0.122 ± 0.005	4.1%
Stopping power, ϵ (eV cm^2)	$(24.63 \pm 1.36) \times 10^{15}$	5.5%
Live time, $\eta_{\rm live}$	0.91573 ± 0.00008	0.009%
Beam energy, $E_{\rm beam}$ (A MeV)	0.612 ± 0.001	0.16%
Total systematic uncertainty	13.43%	

5.3 Main experiment: ^{7}Be$(\alpha,\gamma)^{11}$C

For the main experiment of this thesis, an intense beam of ^{7}Be^{+} was produced using the ISOL technique (see Section 4.1), by bombarding a thick ZrC target with 55 μA 500 MeV protons from the TRIUMF cyclotron. The A= 7 isobars were extracted from the target using the TRIUMF Resonant Ionization Laser Ion Source (TRILIS) (Lassen et al., 2005). The radioactive beam was then accelerated through the ISAC–I Radio–Frequency Quadrupole (RFQ) and Drift–Tube Linac (DTL) to average energies of 441.7 A keV ($E_{\rm lab}$= 3.098(7) MeV, $E_{\rm c.m.}$= 1.126(3) MeV) and 464.2 A keV ($E_{\rm lab}$=

3.256(7) MeV, $E_{c.m.}$= 1.181(3) MeV), so that each resonance was centered in the gas target. Both beam energies were chosen in order to cover a center–of–mass window of 1103 ± 23 and 1158 ± 38 keV respectively across the gas target volume. To ensure a high purity of the RIB, an additional carbon stripping foil of 20 $\mu g/cm^2$ was placed upstream of the DTL to select a specific charge state (4^+) which eliminates the main isobaric contaminant ^{7}Li. Finally, $^7Be^{4+}$ was delivered to the helium–filled DRAGON windowless gas target at 5.05(7) Torr and 7.9(1) Torr for 25.5 h and 25.4 h respectively.

5.3.1 Particle Identification

For the $^7Be(\alpha,\gamma)^{11}C$ reaction, due to the use of the MCP detector close to the DRAGON focal point (MCP0), we performed both singles and coincidence analysis. One of the main particle identification plots we employed for both resonances was the 2D local time–of–flight (MCP/DSSSD) versus the deposited energy in the DSSSD detector. Using that plot we can simultaneously identify the events of interest in each mode, since both detectors have their own singles and coincidence counterpart in the DRAGON DAQ (see Section 4.2.6).

Figures 5.14 and 5.15 show the particle identification plots for both resonances, E_r= 1110 and 1155 keV, for each analysis mode. For the E_r= 1155 keV resonance, we detect a clear signal of 33 ± 6 and 49 ± 7 events in the coincidence and singles mode, respectively. The uncertainty we report here is statistical and refers to the Poissonian nature of the measurement (see also Section 5.21). The recoil signal for the E_r= 1110 keV resonance is relatively weaker, despite the absence of background. For this reason, we used the prescription of Feldman and Cousins (1998) to calculate the statistical uncertainty of this measurement. The coincidences and singles event we recorded for this resonance are $7^{+3.3}_{-2.8}$ and $12^{+4.3}_{-3.2}$, respectively.

5.3.2 Beam Normalization

Unlike the case of the $^6Li(\alpha,\gamma)^{10}B$ reaction, during the ^{7}Be beamtime the rate of scattered ions on the Silicon Surface Barrier detectors was too low to calculate the $\mathcal{R}$ factor by taking measurements for $\Delta t \sim 240$ s before and after each run. Instead, we first ensured that the beam current during each run was stable by checking the current on the charge slits after the first magnetic dipole (see Figure 4.6) and used the total

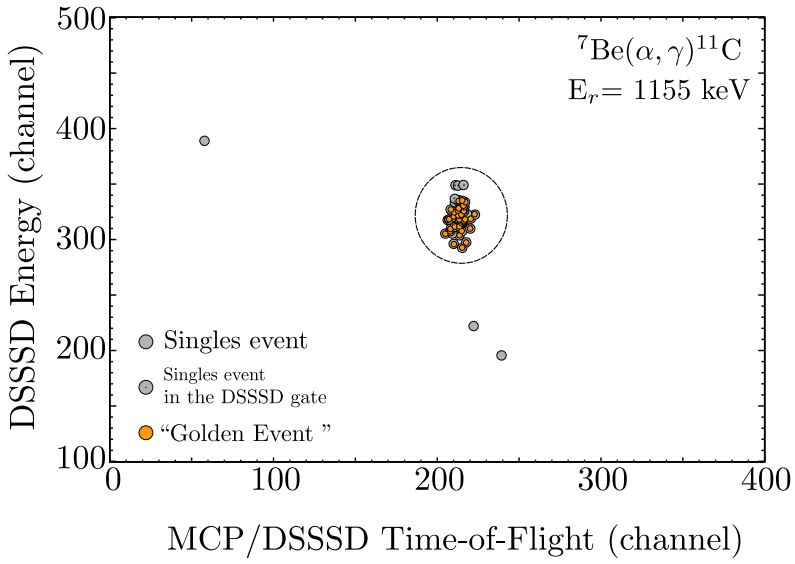

Figure 5.14: Particle identification plots for the E$_r$= 1155 keV resonance. The local time–of–flight (MCP/DSSSD) is plotted against the energy deposited in the DSSSD detector.

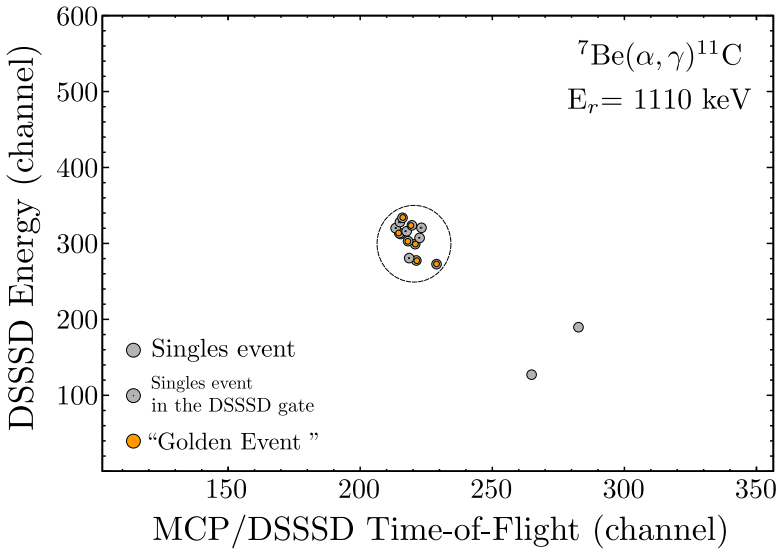

Figure 5.15: Particle identification plots for the E$_r$= 1110 keV resonance. The local time–of–flight (MCP/DSSSD) is plotted against the energy deposited in the DSSSD detector.

integrated counts per run to calculate the $\mathcal{R}$ factor. Figure 5.17 shows the results, which are consistent with the current measurements in the upstream Faraday Cup FC4. Using the $\mathcal{R}$ normalization method we find that the total integrated beam flux was $1.82(5) \times 10^{13}$ and $1.07(2) \times 10^{13}$ ions for the 1110 keV and 1155 keV resonance respectively. For the 1110 keV resonance, we calculate two $\mathcal{R}$ coefficients due to an increase in the beam intensity after Run Number 8695.

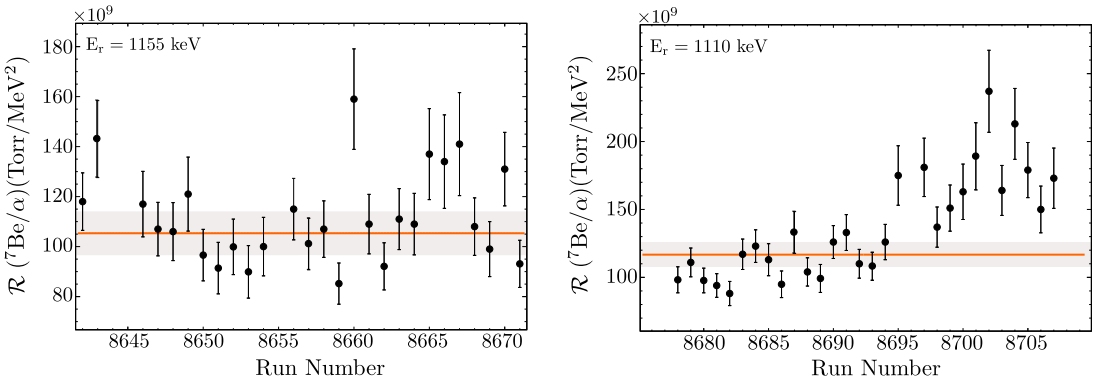

Figure 5.16: Beam normalization coefficient $\mathcal{R}$ results for the two resonances of the $^{7}\mathrm{Be}(\alpha,\gamma)^{11}\mathrm{C}$ reaction. The orange line shows the line of best fit and the grey band the 95% confidence level. See the text for details.

5.3.3 Carbon–in–Helium Charge State Distribution

To determine the carbon–in–helium charge state distribution, we followed a similar approach to the one described in Section 5.2.5. Figure 5.17 shows the results for the important 2^+ charge state to which we tuned DRAGON for the measurement of the $^{7}\mathrm{Be}(\alpha,\gamma)^{11}\mathrm{C}$ resonance strengths. Table 5.7 shows the results for four different energies, corresponding to important resonances of the $^{7}\mathrm{Be}(\alpha,\gamma)^{11}\mathrm{C}$ reaction for three charge states, $2^+, 3^+$ and 4^+. DRAGON cannot bend the 1^+ and so we cannot have a complete charge state distribution measurement. Nevertheless, we were able to measure the charge state of interest, 2^+. For this measurement, since the recoil nucleus, $^{11}\mathrm{C}$, is unstable, we used the abundant and stable isotope $^{12}\mathrm{C}$ from the microwave ion source (MWIS) of OLIS (see Section 4.1.2).

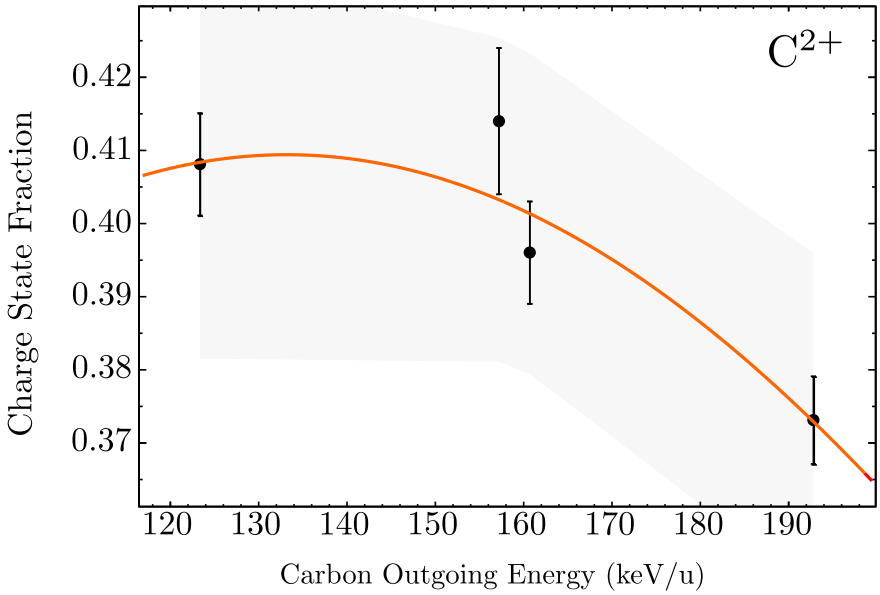

Figure 5.17: C^{2+} in He CSD for different energies. The orange line shows the line of best fit (Gaussian) and the grey band the 95% confidence level. See the text for details.

Table 5.7: Summary of the carbon–in–helium gas charge state distribution (CSD) measurement. The incoming ^{12}C beam charge state was $q_{in} = 4^+$. see the text for details.

$\mathbf{E_r}$ (keV)	$\mathbf{E_{beam}}$ (keV/u)	$\mathbf{P_{target}}$ (Torr)	$\boldsymbol{\eta_{target}}$	$\bar{q}$	$\mathbf{2^+}$	$\mathbf{3^+}$	$\mathbf{4^+}$
876	148.5	8.0(1)	0.92(1)	1.41(2)	0.408(7)	0.124(2)	0.007(1)
1110	168.8	5.0(1)	0.92(1)	1.86(4)	0.414(10)	0.194(4)	0.019(1)
1155	172.6	5.0(1)	0.92(1)	1.85(3)	0.396(7)	0.196(3)	0.020(1)
1356	205.5	5.0(1)	0.92(1)	2.19(3)	0.373(6)	0.282(5)	0.011(1)

5.3.4 ^{7}Be Stopping Power in ^{4}He and Energy Loss

Stopping power was measured for the two beam energies, 441.7 and 464.2 A keV, and the gas target pressure of P= 7.9(1) and 5.05(7) Torr, respectively at a similar approach as in the ^{6}Li$(\alpha,\gamma)^{10}$B experiment. Figure 5.18 and Table 5.8 show the summary of these measurements. The $y-$intercept for the beam energy versus gas target pressure plot gives us the incoming beam energy and the slope of the beam energy ,versus gas target density plot gives us the gas stopping power. Our results obtained using DRAGON are in very good agreement with the calculations of SRIM (Ziegler et al., 2010).

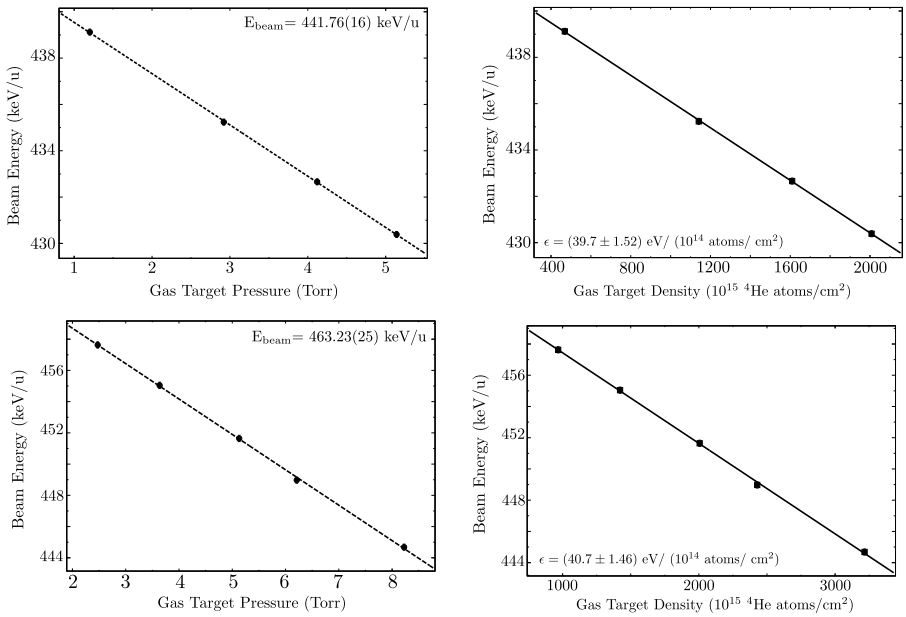

Figure 5.18: Beam energy (left panels) and stopping power (right panels) results for two resonances (E$_r$= 1110 keV, upper panels and E$_r$= 1155 keV, lower panels) of the ^{7}Be$(\alpha,\gamma)^{11}$C reaction. see the text for details.

5.3.5 Resonance Energy Determination

The DRAGON facility is able to measure resonance energies E$_r$ by analyzing the position centroid along the beamline of the γ ray hits in the BGO array. As the beam ions traverse the gas target, they lose energy due to interactions with the target

Table 5.8: Summary of the ^{7}Be in ^{4}He stopping power measurements. The experimental results are compared with the calculations of SRIM (Ziegler et al., 2010).

$\mathbf{E_{beam}}$ (keV/u)	$\epsilon_{\mathbf{DRAGON}}$ eV/ (10^{14} atoms/ cm^2)	$\epsilon_{\mathbf{SRIM}}$ eV/ (10^{14} atoms/ cm^2)
441.8(2)	39.7(15)	38.2
463.2(3)	40.7(15)	38.5

material. Using the measured energy loss through the target and the hit distribution in the BGO array it is possible to calculate the resonance energy E_r. In Figure 5.19 the centroid of the distribution is at $z_r = +0.47$ cm, indicating that this resonance is well centered in the gas target and the measured energy will be very close to the literature value of 1155(2) keV.

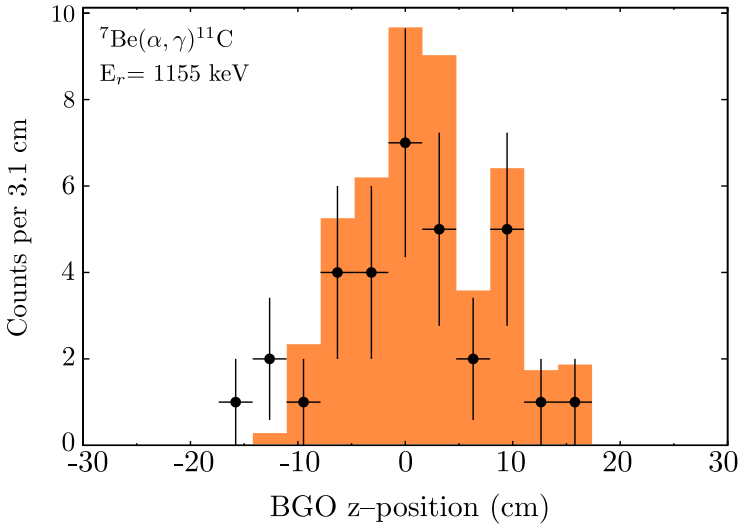

Figure 5.19: BGO position profile spectrum for the E_r=1155 keV resonance. The black points indicate the experimental data and the orange histogram a GEANT simulation. The centroid of the experimental peak is at z_r= +0.47 cm. see the text for details.

Using the prescription of Hutcheon et al. (2012), the beam energy where the resonance is excited in the laboratory frame can be calculated as follows

$$E_f = (1-f)E_{in} + fE_{out} - f(1-f)\frac{(E_{in}-E_{out})^2}{E_{in}+E_{out}}\mathcal{R} \tag{5.11}$$

where E_{in}, E_{out} are the in–going and outgoing beam energy,

$$f = 0.5 + \frac{z_r}{L_{eff}} \tag{5.12}$$

is the fraction of the total thickness of the target that has been traversed by the beam until it stops at position z_r and $\mathcal{R}$=(E/S)(ΔE/ΔS)[5] shows the energy dependence of the stopping power and in most cases is of order unity. L_{eff} = 12.3(5) cm is the effective length of the gas target (recall Section 4.2). A further correction for geometric and kinematic effects is given in Hutcheon et al. (2012), where z_{BGO}= (0.79 z_{true} + 0.57) cm.

The uncertainty of the resonance energy measurement is given by

$$\delta E_{res} = \Delta E \ \frac{\Delta z_{BGO}}{L_{eff}} \ \frac{dz_{true}}{dz_{BGO}} \approx \Delta E \frac{0.6}{\sqrt{N}} \tag{5.13}$$

where the last approximation is valid for cases where there is no (or negligible) background, as in our experiment. N is the total number of counts in the BGO position profile spectrum (Hutcheon et al., 2012).

For the E_r= 1155 keV resonance, the DRAGON measurement gives the following result

$$E_r = (1154.99 \pm 4.84) \text{ keV}$$

which agrees very well with the literature value of 1155(2) keV.

For the E_r= 1110 keV resonance, even though we have very low statistics (see Figure 5.20), it is still possible to make a crude estimate of the energy, using Equations 5.11 and 5.13. The result,

$$E_r = (1111.26 \pm 10.52) \text{ keV}$$

agrees within 1σ with the literature value of 1110(4) keV.

5.3.6 Resonance Strength Calculation

In Section 2.4 we introduced the experimental reaction yield (Equation 2.26). Let us now explain it using statistics. Before any measurement, our knowledge of the

[5]Should not be confused with the beam normalization factor $\mathcal{R}$.

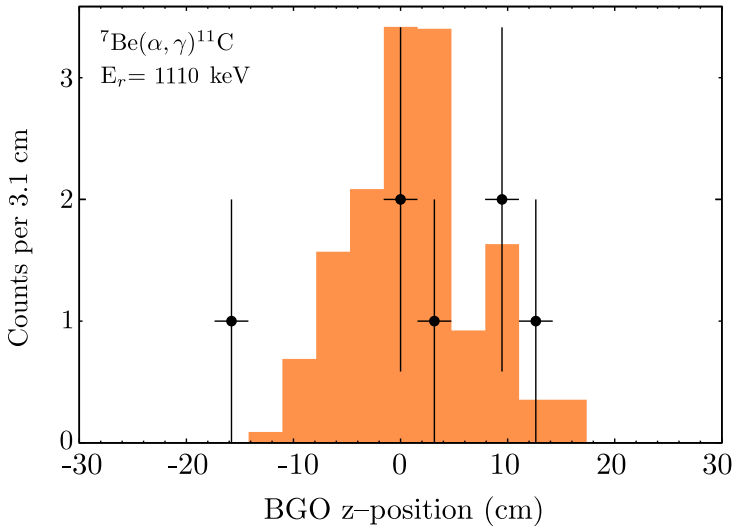

Figure 5.20: BGO position profile spectrum for the E_r=1110 keV resonance. The black points indicate the experimental data and the orange histogram a `GEANT` simulation. see the text for details.

reaction yield Y is almost zero; we can just assume that it must be a positive real number. After the first measurement, let us call it Y_1, our knowledge of the reaction yield is improving. Continuing with more measurements, Y_i, we finally have a set $S = Y_1, \cdots, Y_N$ of N total measurements. Each of them has an individual probability distribution and since they are independent, the total probability distribution will be their product. The peak of the joint probability distribution will be our best estimate of the reaction yield.

Let us first define the probability for reactions occurring inside the DRAGON gas target; that would be a Poissonian distribution

$$P(\mathcal{N}_\mathcal{B}|\mathcal{N}_\mathcal{R}, Y) = \frac{(\mathcal{N}_\mathcal{B}Y)^{N_R}}{\mathcal{N}_\mathcal{R}!} e^{-\mathcal{N}_\mathcal{B}Y} \tag{5.14}$$

where $\mathcal{N}_\mathcal{R}$ is the total number of reactions, $\mathcal{N}_\mathcal{B}$ the number of beam particles and Y the true reaction yield.

However, our experimental setup is comprised of different detectors, *i.e.* BGO, DSSSD and MCP with their respective efficiencies, and also DRAGON can only transmit a single charge state to the focal plane and its recoil transmission can be

less than 100%. Our initial probability distribution then will have to be convoluted with the detection probability for each detector, which follows a binomial distribution; for example the probability that we will detect γ events from the BGO array, with efficiency η_{BGO} will be

$$P(\gamma|\mathcal{N}_{\mathcal{R}}\eta_{BGO}) = \binom{\mathcal{N}_{\mathcal{R}}}{\gamma}\eta_{BGO}^{\gamma}(1-\eta_{BGO})^{\mathcal{N}_{\mathcal{R}}-\gamma} \tag{5.15}$$

We can now write down the probability distribution for the two analysis modes, coincidences and singles

$$P(N_{coinc}|Y) = \frac{(\eta_{DRAGON}^{coinc}\mathcal{N}_{\mathcal{B}}Y)^{N_{coinc}}}{N_{coinc}!}e^{-\eta_{DRAGON}^{coinc}\mathcal{N}_{\mathcal{B}}Y} \tag{5.16}$$

$$P(N_{sing}|Y) = \frac{(\eta_{DRAGON}^{sing}\mathcal{N}_{\mathcal{B}}Y)^{N_{sing}}}{N_{sing}!}e^{-\eta_{DRAGON}^{sing}\mathcal{N}_{\mathcal{B}}Y} \tag{5.17}$$

N_{coinc}, N_{sing} are the detected coincidences and singles events and η_{DRAGON}^{coinc}, η_{DRAGON}^{sing} the corresponding efficiencies. To calculate our best estimate for the reaction yield, we need to maximize the likelihood $\mathcal{L}$ function of Y, or equivalently the log–likelihood

$$\mathcal{L}(Y) = \prod_{i}^{N} P_i(N_{coinc}|Y) \Rightarrow \ln(\mathcal{L}) = \sum_{i} P_i(N_{coinc}|Y) \tag{5.18}$$

with a similar expression for the singles likelihood function. To maximize it, we need to set its first derivative equal to zero and solve for the maximum yield

$$\frac{\partial}{\partial Y}\sum_{i=1}^{N} N_{coinc}^{i}\ln(\eta_{DRAGON}^{coinc}\mathcal{N}_{\mathcal{B}}Y) - \ln(N_{coinc}^{i}!) - \eta_{DRAGON}^{coinc}\mathcal{N}_{\mathcal{B}}Y = 0 \tag{5.19}$$

$$\sum_{i=1}^{N}\frac{N_{coinc}^{i}}{Y_{max}} - \eta_{DRAGON}^{coinc}\mathcal{N}_{\mathcal{B}} = 0 \tag{5.20}$$

$$\frac{N_{coinc}}{Y_{max}} - \eta_{DRAGON}^{coinc}\mathcal{N}_{\mathcal{B}} = 0 \tag{5.21}$$

$$Y_{max} = \frac{N_{coinc}}{\eta_{DRAGON}^{coinc}\mathcal{N}_{\mathcal{B}}} \tag{5.22}$$

where $\mathrm{N_{coinc}}$ is the total number of detected coincidences events and $\eta_{DRAGON}^{coinc} =$

$\eta_{separator}\ f_q\ \eta_{BGO}\ \eta_{DSSSD}\ \eta_{live}^{coinc}\ \eta_{MCP}$ is the total coincidences detection efficiency. The singles counterpart is $\eta_{DRAGON}^{sing} = \eta_{separator}\ f_q\ \eta_{DSSSD}\ \eta_{live}^{sing}\ \eta_{MCP}$.

Finally, our estimate for the maximum reaction yield Y_{max} enters in equation 2.33, and with the use of the measured stopping power ϵ, the masses of the reactants and the de Broglie wavelength $\lambda_r = 2\pi/(0.219\sqrt{\mu E_r})$ we can calculate the resonance strength $\omega\gamma$. In Table 5.9 and Figure 5.21 we present the final results for the E_r=1110 keV and 1155 keV resonance strengths. The results obtained by singles and coincidences analysis agree well and for this reason we will adopt the singles result as the final, due to its lower uncertainty.

Table 5.9: Final results for $\omega\gamma$ of ^{7}Be$(\alpha,\gamma)^{11}$C reaction. The first two rows show the coincidence analysis mode results and the last two the singles analysis mode results.

$\mathbf{E_r^{lit}(keV)}$	$\mathbf{E_r^{DRA}\ (keV)}$	$\mathcal{N}_\mathcal{B}$	$\mathbf{N_{recoils}}$	$\eta_{\mathbf{DRAGON}}$	$\boldsymbol{\omega\gamma}$ **(eV)**
1110(4)	1111(11)	$1.7(5)\times10^{13}$	$7^{+3.3}_{-2.8}$	$3.5(3)\times10^{-2}$	$0.143^{+0.088}_{-0.093}$
1155(2)	1155(5)	$1.07(2)\times10^{13}$	33 ± 6	$2.3(5)\times10^{-2}$	1.44(39)
1110(4)	1111(11)	$1.7(5)\times10^{13}$	$12^{+4.3}_{-3.2}$	$5.3(4)\times10^{-2}$	$0.111^{+0.052}_{-0.056}$
1155(2)	1155(5)	$1.07(2)\times10^{13}$	49 ± 7	$3.5(7)\times10^{-2}$	1.39(36)

From a nuclear structure standpoint, it is worth noting that our results for the two resonance strengths are in very good agreement with their ^{7}Li$(\alpha,\gamma)^{11}$B analogs (Kelley et al., 2012), namely E_x = 9.182 $(7/2^+)$ and 9.271 MeV $(5/2^+)$, as they are shown in Table 5.10.

Table 5.10: Comparison of resonance strengths $\omega\gamma$ for analog states in ^{7}Be$(\alpha,\gamma)^{11}$C and ^{7}Li$(\alpha,\gamma)^{11}$B reactions.

$\mathbf{J^\pi}$	**Nucleus**	$\mathbf{E_x(MeV)}$	$\boldsymbol{\omega\gamma}$ **(eV)**
$7/2^+$	^{11}B	9.182(2)	0.303(26)
$7/2^+$	^{11}C	8.654(4)	$0.111^{+0.052}_{-0.056}$
$5/2^+$	^{11}B	9.271(2)	1.72(24)
$5/2^+$	^{11}C	8.699(2)	1.39(36)

5.3.7 Uncertainties

Similarly to the ^{6}Li$(\alpha,\gamma)^{10}$B, experiment our final result for the resonance strength has an associated uncertainty. The statistical uncertainty arises from the total number

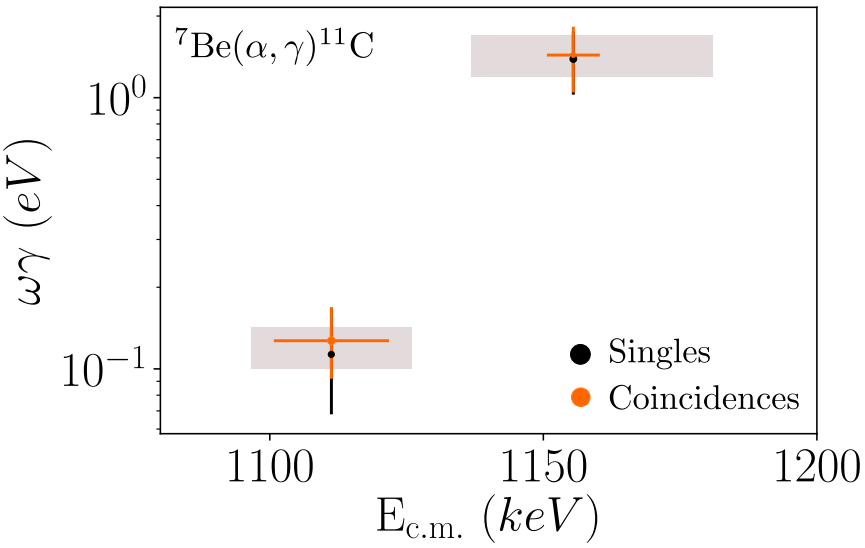

Figure 5.21: Final results for unknown resonance strengths of the ^{7}Be$(\alpha,\gamma)^{11}$C reaction. Results from both singles and coincidences modes are shown. The grey rectangular indicates the thickness of the gas target in the center–of–mass system. See the text for details.

of detected recoils, and in the case of the 1155 keV resonance we used the Poissonian error, $\sigma = 1/\sqrt{\text{N}_{\text{recoils}}}$. As we discussed earlier in this chapter, the faint signal from the 1110 keV resonance recoils does not allow us to use the same approach, and hence we followed the prescription of Feldman and Cousins (1998). More specifically, we calculated the 68.27% (1σ) confidence intervals for a Poisson signal with zero background (as is evident in Figure 5.15).

Tables 5.11 and 5.12 show a summary of the uncertainties for both resonances. For the 1155 keV resonance the largest systematic uncertainty is the separator transmission due to the fact its γ branching ratio has a 24% uncertainty (see Table 3.2). The 1110 keV resonance strength uncertainty is, as expected, dominated by the low recoil yield. In both cases, we added each factor in quadrature to obtain the final result, which includes both statistical and systematic uncertainties.

Table 5.11: Uncertainties in the resonance strength measurement of the E_r = 1155 keV resonance in singles and coincidences modes.

Source	**Measured Value**	**Relative Uncertainty**
Detected recoils, $N_{rec}^{singles}$	49 ± 7	14.3%
Detected recoils, N_{rec}^{coinc}	33 ± 6	17.4%
Charge state fraction, f_q	0.396 ± 0.007	1.8%
Beam particles N_{beam}	$(1.07 \pm 0.02) \times 10^{13}$	2.2%
BGO efficiency, η_{BGO}	0.773 ± 0.010	1.29%
MCP efficiency, η_{MCP}	0.557 ± 0.036	6.46%
Separator transmission, $\eta_{separator}$	0.141 ± 0.028	20%
Live time, η_{live}	0.80389±0.00004	0.005%
Stopping power, ϵ (eV cm^2)	$(4.07 \pm 0.15) \times 10^{14}$	3.59%
Beam energy	463.23 ± 0.25 keV/u	0.05%
Total uncertainty (singles)		25%
Total uncertainty (coincidences)		27%

Table 5.12: Uncertainties in the resonance strength measurement of the E_r = 1110 keV resonance in singles and coincidences modes.

Source	**Measured Value**	**Relative Uncertainty**
Detected recoils, $N_{rec}^{singles}$	$12^{+4.3}_{-3.2}$	$^{+24.8}_{-33.7}$%
Detected recoils, N_{rec}^{coinc}	$7^{+3.3}_{-2.8}$	$^{+31.2}_{-48.8}$%
Charge state fraction, f_q	0.414 ± 0.009	2.17%
Beam particles N_{beam}	$(1.82 \pm 0.05) \times 10^{13}$	2.86%
BGO efficiency, η_{BGO}	0.79 ± 0.01	1.27%
MCP efficiency, η_{MCP}	0.678 ± 0.031	4.57%
Separator transmission, $\eta_{separator}$	0.25 ± 0.01	4%
Live time, η_{live}	0.804338 ± 0.00004	0.005%
Stopping power, ϵ (eV cm^2)	$(3.97 \pm 0.15) \times 10^{14}$	3.83%
Beam energy	441.76 ± 0.16 keV/u	0.04%
Total uncertainty (singles)		$^{+26}_{-34}$%
Total uncertainty (coincidences)		$^{+32}_{-49}$%

5.4 Summary

In this chapter we presented two experimental studies using the DRAGON recoil separator. The first, the $^{6}\mathrm{Li}(\alpha,\gamma)^{10}\mathrm{B}$ reaction, was used as a proof–of–principle for reactions in which the recoils have an angular distribution that exceeds the separator acceptance. Upon the first experiment's success, we measured resonances with unknown strengths of the $^{7}\mathrm{Be}(\alpha,\gamma)^{11}\mathrm{C}$ reaction at energies relevant to the νp–process nucleosynthesis to better constrain its rate. In the next and final chapter of this thesis we shall discuss the results and draw the conclusions of this experimental campaign.

Chapter 6

Conclusions and Discussion

6.1 The Geometric Limitations of DRAGON

The main experimental challenge for this thesis was to demonstrate that DRAGON can study reactions for which the momentum spread of the recoils exceeds its geometric acceptance. We showed that such measurements are possible, first by measuring a known resonance strength of the ^{6}Li$(\alpha,\gamma)^{10}$B reaction, as a proof–of–principle, and then with the astrophysically important ^{7}Be$(\alpha,\gamma)^{11}$C reaction.

It is worth noting that such measurements can provide reliable results only if they are coupled with detailed simulations of the separator, which provide the important information of the recoil transmission and the γ ray detection efficiency. The data analysis is also affected by our knowledge of the γ branching ratios and angular distributions W(θ), as we discussed in Sections 2.5 and 5.1. Accurate measurement of the γ branching ratios using high efficiency detectors (*e.g.* segmented HPGe) are desirable, but even if they are unknown, the γ ray detection efficiency can still be calculated using a combination of the experimental data and simulations, as argued in Ruiz et al. (2014). The final result, however, might suffer from high systematic uncertainty.

Looking ahead, the successful measurements presented in this thesis can be used to motivate studies of astrophysically important reactions previously thought inaccessible with DRAGON due to recoil acceptance constraints, such as ^{18}O$(\alpha,\gamma)^{22}$Ne, ^{20}Ne$(\alpha,\gamma)^{24}$Mg, ^{22}Ne$(\alpha,\gamma)^{26}$Mg, and others.

6.2 Reaction Rate Calculation with `RatesMC`

The new $^7\mathrm{Be}(\alpha,\gamma)^{11}\mathrm{C}$ reaction rate was calculated using the `RatesMC` code (Longland et al., 2010)[1]. In the following, we shall discuss how thermonuclear reaction rates are calculated using Monte Carlo methods with underlying statistical distributions for the nuclear physics input.

Recalling Figure 3.2, there are two versions of the $^7\mathrm{Be}(\alpha,\gamma)^{11}\mathrm{C}$ reaction rate, the compilation by Caughlan and Fowler (1988) and the one by NACRE–II (Xu et al., 2013). The first rate does not include any uncertainty, while the second provides an "upper" and a "lower" limit which nevertheless are not derived by rigorous methods and their statistical meaning is not explained. This has also implications in nucleosynthesis and stellar evolution calculations which, as we have discussed in this thesis, heavily rely on thermonuclear reaction rates.

In the `RatesMC` framework, each nuclear physics input quantity (*e.g.* resonance energy and resonance strength) has an assigned probability density function (PDF). The code samples these functions randomly many times using a Monte Carlo algorithm and outputs reaction rates and associated rate probability densities. According to the central limit theorem a random variable that is determined by the product of many factors will be distributed according to a lognormal density function (Longland et al., 2010; Iliadis et al., 2015), which is given by:

$$f(x) = \frac{1}{\sigma\sqrt{2\pi}}\frac{1}{x}e^{-(\ln x-\mu)^2/(2\sigma^2)} \tag{6.1}$$

and is defined by two parameters, μ and σ which determine the location and the width of the distribution respectively. From these values we can also find the expected value and variance of the distribution:

$$E[x] = e^{(2\mu+\sigma^2)/2},\ V[x] = e^{(2\mu+\sigma^2)}\left[e^{\sigma^2}-1\right] \tag{6.2}$$

Using a lognormal density function to describe a thermonuclear reaction rate, the median value is given by e^{μ} while for a 68.27% probability coverage the upper and lower bounds are given by $e^{\mu-\sigma}$ and $e^{\mu+\sigma}$ respectively[2]. Equivalently, we can define

[1] The code is available online at `http://starlib.physics.unc.edu/RateCalc.php` and the input file used for this study can be found in Appendix A.4.

[2] It can be proved that e^{μ} and e^{σ} are respectively the geometric mean and geometric standard

the "low", "recommended", and "high" Monte Carlo rates as the 16$^{\text{th}}$, 50$^{\text{th}}$, and 84$^{\text{th}}$ percentile respectively of the cumulative reaction rate distribution (see Figure 6.1). In addition, an Anderson–Darling (A–D) test is used to show how well the reaction rate is described by a lognormal distribution. Empirically Iliadis et al. (2010) argue that numerical A–D values between 1–30 show that the lognormal approximation is adequate for reaction network calculations.

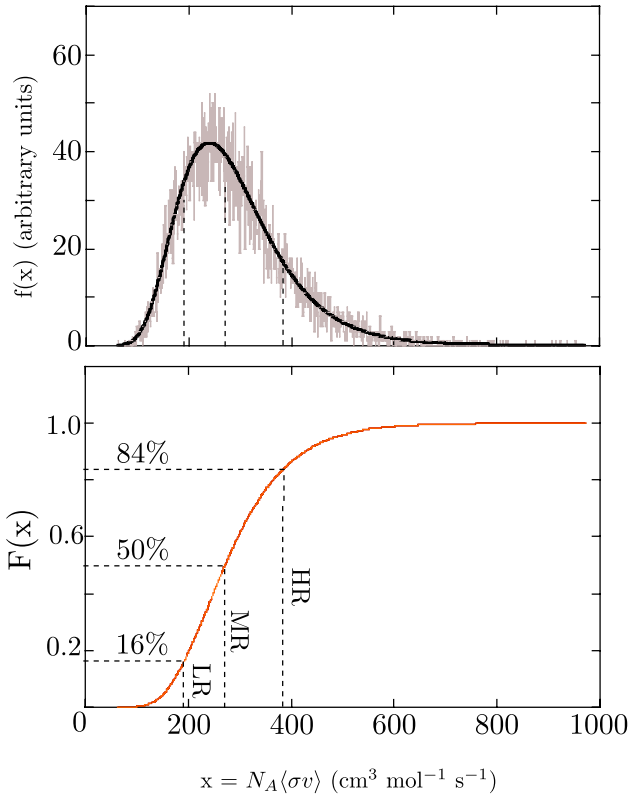

Figure 6.1: (Upper panel) Reaction rate probability density function for a fictitious resonance in the ^{22}Ne$(\alpha,\gamma)^{26}$Mg reaction ($\omega\gamma = 4.1 \pm 0.2$ eV and $E_r = 300 \pm 15$ keV). (Lower panel) Cumulative reaction rate distribution. The dotted lines show the low, median and high Monte Carlo rates. This figure was adapted from Longland et al. (2010).

deviation of a lognormally distributed sample of data.

6.3 The new ^{7}Be$(\alpha,\gamma)^{11}$C reaction rate

Taking into account the results of the present experiment, we can calculate the new ^{7}Be$(\alpha,\gamma)^{11}$C reaction rate using the `RatesMC` code. In Appendix A.5 we present a tabulated version of the new thermonuclear reaction rate, and in Figure 6.2 the new rate is compared to the recommended rate from NACRE–II (Xu et al., 2013). In the present calculation we included the contribution from resonances with previously unknown strengths that now have been measured using DRAGON.

In the bottom panel of Figure 6.2 we present the rate ratio between NACRE–II and the rate obtained from this work. The biggest difference is for $T_9 < 0.3$, which does not affect νp–process nucleosynthesis. In the relevant temperature region the new rate is lower than the NACRE–II rate by 10–50% and shows a similar trend to the Caughlan and Fowler (1988) rate.

Figure 6.3 shows the individual resonant contributions to the total ^{7}Be$(\alpha,\gamma)^{11}$C reaction rate. For temperatures $T_9 < 0.5$, the 877 keV resonance dominates the rate, as we expected from the discussion in Section 2.2.2, since it is the lowest–lying resonance. At the temperature region relevant to the νp–process, $T_9 < 1.5-3$, the 877 and 560 keV resonances have the highest contribution, with the 1155 keV resonance contributing $\approx$10% to the total rate and the 1110 keV $\ll$ 5%.

It is worth noting that in the present calculation we did not include the contribution of the sub–threshold resonance at -44 keV. As it has been argued by Descouvemont (1995), this resonance is expected to dominate the reaction rate at low temperatures, $T_9 < 0.1$, but it does not affect νp–process nucleosynthesis. However, this resonance could affect two different astrophysical scenarios: the evolution of Population III stars via the hot pp–chains (Wiescher et al., 1989) and classical novae, which are binary systems of a main sequence star and a white dwarf, where it can affect the production of ^{7}Be and subsequently ^{7}Li (Hernanz et al., 1996).

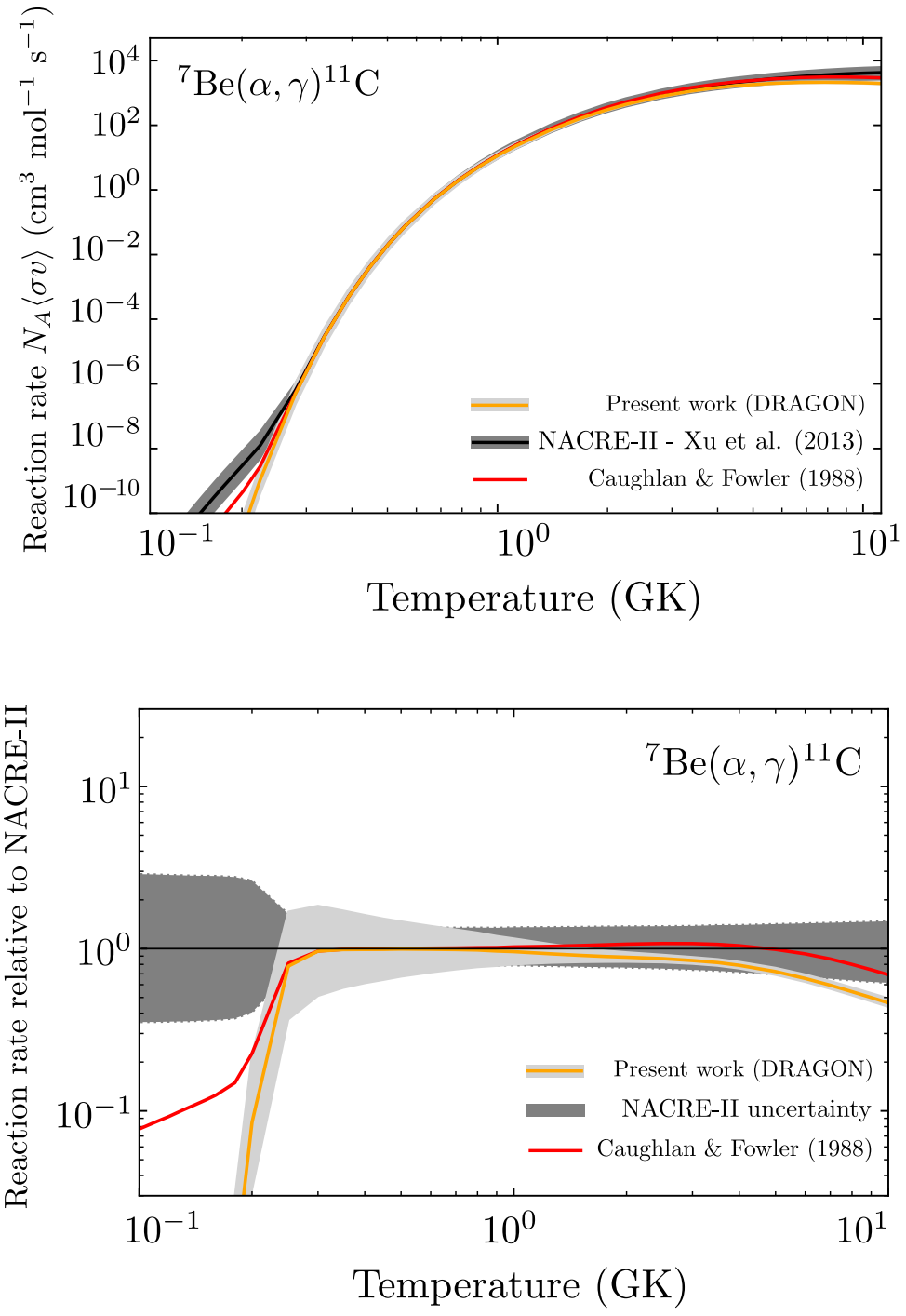

Figure 6.2: (Upper panel) The new ^{7}Be$(\alpha,\gamma)^{11}$C reaction rate for T= 0.1–10 GK. The rates by Xu et al. (2013) and Caughlan and Fowler (1988) are also shown. (Lower panel) Comparison between the NACRE–II ^{7}Be$(\alpha,\gamma)^{11}$C reaction rate (Xu et al., 2013) and that of Caughlan and Fowler (1988) and the present work for the same temperature region.

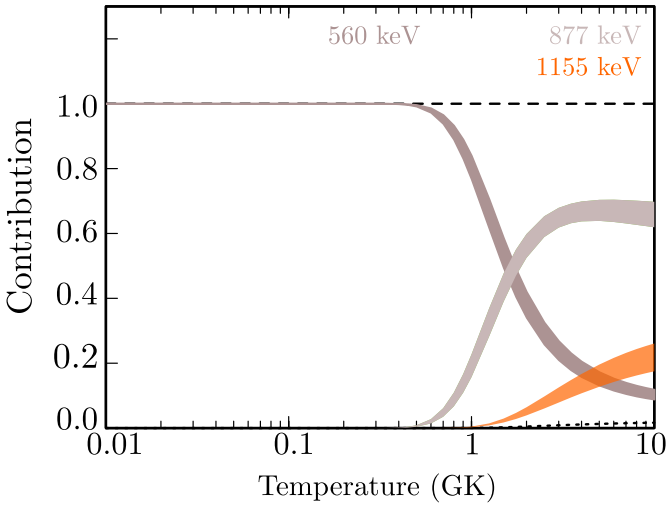

Figure 6.3: Resonant contribution to the $^{7}\mathrm{Be}(\alpha,\gamma)^{11}\mathrm{C}$ reaction rate. The dotted line at the bottom right corner shows the contribution of the 1110 keV resonance. The figure is courtesy of Prof. Richard Longland (TUNL, NCSU).

6.4 Nucleosynthesis Calculations with `NuPPN`

The last part of a nuclear astrophysics experiment is to perform nucleosynthesis calculations using the new reaction rate and study its effect on the astrophysical scenario. For this we used the NuGrid Post–Processing Nucleosynthesis (`NuPPN`) code (Pignatari and Herwig, 2012). `NuPPN` is a nuclear reaction network code (see Section 2.3) and it has three frames, which are used interdependently in different nucleosynthesis scenarios:

1. `PPN` one–dimensional, single zone profile trajectory $(\mathrm{T(t)}, \rho(\mathrm{t}))$,
2. the multi–zone post–processing network parallel, `MPPNP`, which is used for novae or low–mass ABG stars, where mixing is very important but also computational–expensive and,
3. the trajectory post-processing network/parallel frame, `TPPNP`, which is designed for post–processing of trajectories from multidimensional supernova simulations, using the tracer particle technique (*e.g.* see Nishimura et al. (2015)).

For the purpose of the present thesis we used PPN to study νp–process nucleosynthesis from a 1D core–collapse supernova model.

Each of the three NuPPN frames uses two main packages, the physics and the solver. The NuPPN physics package contains nuclear data for over 5,000 species between hydrogen and bismuth, and 50,000 nuclear reactions. It employs all the reaction rate libraries and compilations, such as JINA REACLIB (Cyburt et al., 2010), NACRE I-II (Angulo et al., 1999; Xu et al., 2013), KADoNIS (Dillmann et al., 2006), Caughlan and Fowler (1988) and Iliadis et al. (2001). For some reactions the physics package selects a reaction rate from specific experimental data, such as the $^{12}C(\alpha,\gamma)^{16}O$ (Kunz et al., 2002). The network solver package is a fully implicit Newton–Raphson linear algebra solver with adaptive and automatic sub–time stepping (Pignatari and Herwig, 2012).

The NuPPN code relies on the physics and solver packages to advance the nucleosynthesis network with each time step. The physics package provides the nuclear physics input and the solver package provides the numerical solution for the network at each time step.

Until very recently, NuPPN was unable to perform network calculations for the νp–process, because it did not include the important neutrino interactions that we discussed in Chapter 1. For this reason, the author joined the NuGrid collaboration and worked with Samuel Jones from Los Alamos National Lab on NuPPN code development. The goal of this project was to study νp–process within the NuPPN framework and perform a sensitivity study, similar to Wanajo et al. (2011), using the experimental data from the DRAGON experiment.

The new version of the NuPPN code includes all the neutrino reactions from Woosley et al. (1990) and the neutrino capture rates on free nucleons from McLaughlin et al. (1996), and it can perform the nucleosynthesis calculation by reading an input file which includes temperature, density, radius, neutrino/anti–neutrino luminosity and energy of the simulation particle (see for example Figures 1.11 and 1.12). An example of the input file can be found in Appendix A.6.

In the following we shall present the nucleosynthesis results with the updated NuPPN code and the new $^{7}Be(\alpha,\gamma)^{11}C$ reaction rate. For the following calculations we used the same neutrino–driven wind trajectory from Wanajo et al. (2011) as in Section 1.5.1 and changed only the $^{7}Be(\alpha,\gamma)^{11}C$ reaction rate. Figure 6.4 shows the

relative abundances for two different ^{7}Be$(\alpha,\gamma)^{11}$C reaction rates: the standard by NACRE-II (Xu et al., 2013), and the recommended `RateMC` from the present study. The current rate uncertainty ("upper" and "lower") produce minute differences in the final abundances ($\ll 1\%$) and for this reason is not presented in Figure 6.4.

We can clearly see that the new ^{7}Be$(\alpha,\gamma)^{11}$C reaction rate does not affect the production of light p–nuclei (A= 90–110) in this calculation. The only notable abundance changes are in the light and intermediate mass region (A $>$ 40). Figure 6.5 shows an elemental breakdown of our nucleosynthesis calculations. In the bottom panel, we see a clear increase in the production of boron, carbon and nitrogen, by factors of up to an order of magnitude, and a decrease in the production of lithium, since the ^{7}Be electron capture is the main production channel. Nevertheless, there is no difference in the production of light p–nuclei.

6.5 Conclusions and Future Work

To summarize, in this chapter we presented the main conclusions of this thesis: the DRAGON recoil separator can measure resonance strengths of reactions with recoil angular cones larger than its nominal acceptance, using its sophisticated simulation toolkit and that a more constrained ^{7}Be$(\alpha,\gamma)^{11}$C reaction rate does not affect the production of light p–nuclei via the νp–process.

We measured two resonances with unknown strengths of the ^{7}Be$(\alpha,\gamma)^{11}$C reaction in energies relevant to nucleosynthesis in neutrino–driven winds of ccSNe using DRAGON. The new reaction rate is more constrained than its previous version by NACRE at $T_9 > 1$ (5–10% uncertainty) and using nucleosynthesis calculations we showed that it does not affect the production of light p–nuclei with 90 $<$A$<$ 110. Nevertheless, new studies should be undertaken to explore the contribution of the sub–threshold resonance at -44 keV, which can influence the evolution of Population–III stars in the early Universe via the hot pp–chains and the production of ^{7}Li and ^{7}Be in classical novae.

In the light of these measurements, we plan to re–measure the 876 keV resonance and explore the existence of the 1356 keV resonance using DRAGON, which will further improve our knowledge of the ^{7}Be$(\alpha,\gamma)^{11}$C reaction rate at $T_9 > 1$.

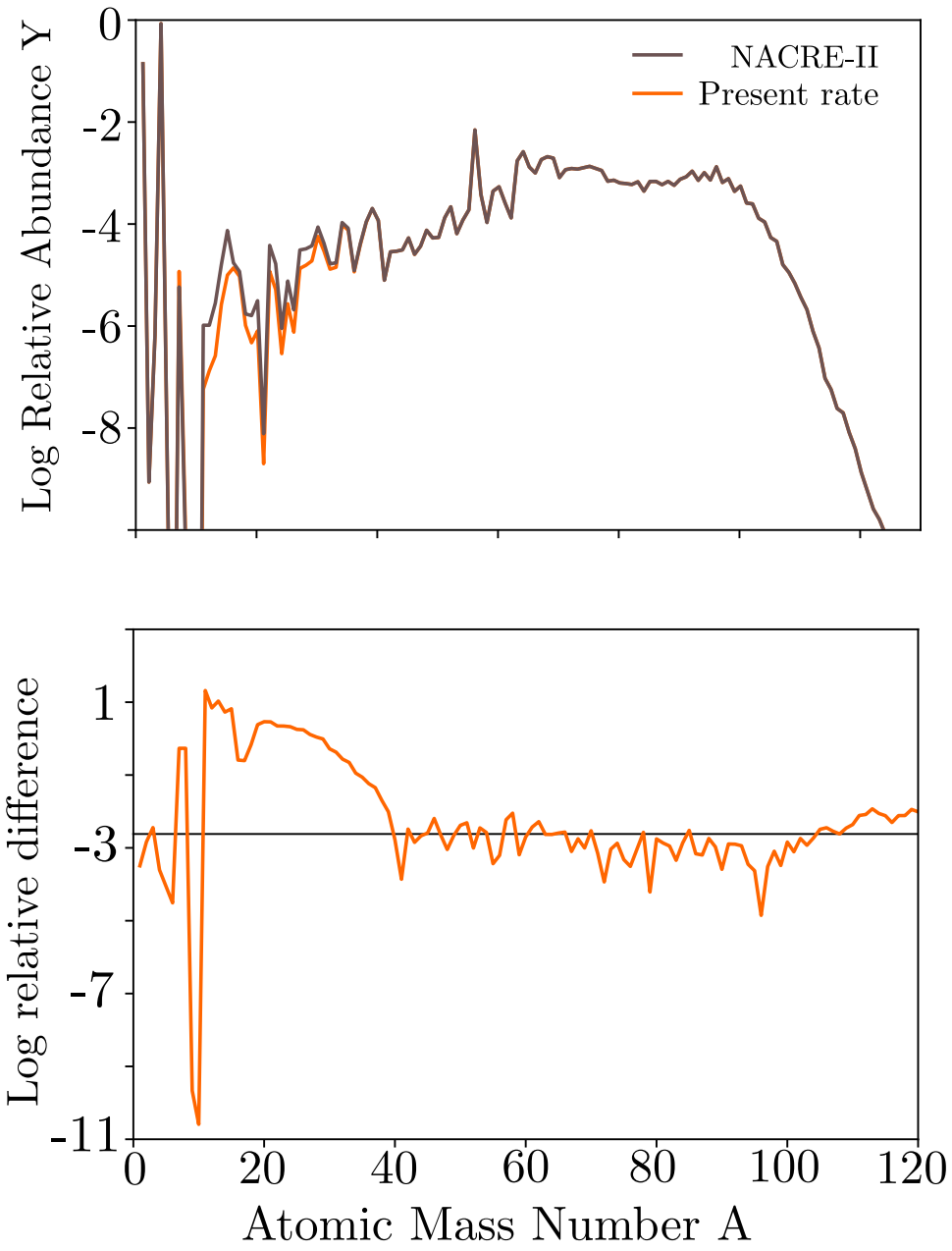

Figure 6.4: Reaction network calculation results with the new $^{7}\mathrm{Be}(\alpha,\gamma)^{11}\mathrm{C}$ reaction rate. (Upper panel) Relative abundance versus atomic mass number for two different $^{7}\mathrm{Be}(\alpha,\gamma)^{11}\mathrm{C}$ reaction rates using the same hydrodynamical trajectory (Wanajo et al., 2011). (Bottom panel) Relative abundance differences between the two calculations. The black horizontal line is used to guide the eye.

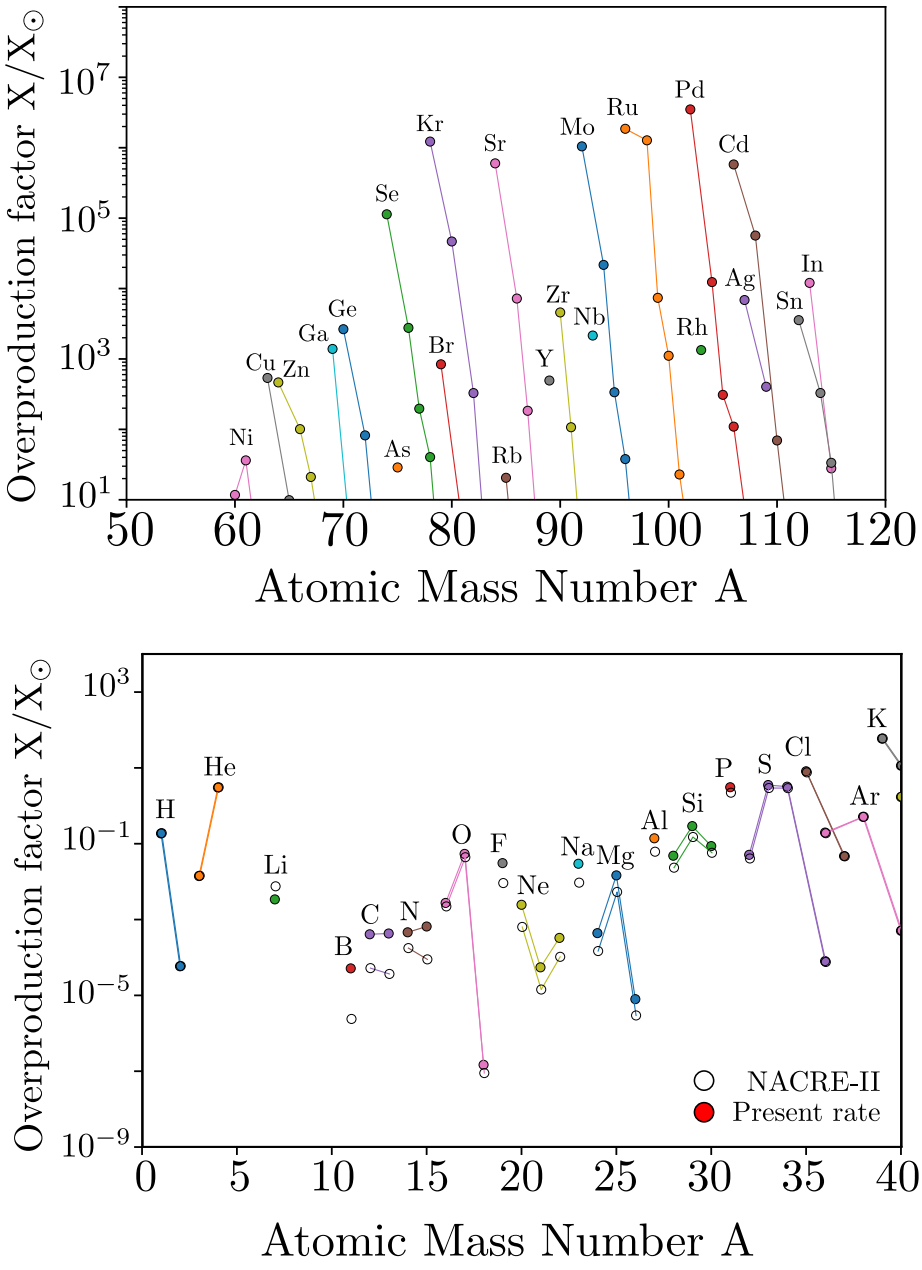

Figure 6.5: Elemental abundances using the new $^{7}\mathrm{Be}(\alpha,\gamma)^{11}\mathrm{C}$ reaction rate. (Upper panel) The light p–nuclei region. No change is shown between the two rates (Bottom panel) $A < 40$ mass region. The filled dots represent the results with the present rate and the unfilled dots the results with the NACRE–II rate.

Appendix A

Software Input Files

A.1 DRAGON GEANT3 Input File

```
# Input namelist for 6Li(a,g)10B reaction
# A. Psaltis 07.06.2016
# Note: All mass excesses in GeV
#       All widths in MeV
#       All energy levels in MeV
# beam_mass_excess and recoil_mass_excess is energy difference
# from (abeam or atarg)*(GeV/amu) to real value
#
# Resonant particles mass/energy/level defined by resenerg,
# not level(rstate)
#
# Resonant mass = Beam mass + Target mass + resenergy
# level(rstate) value only "names" resonant state
#
# part_width/gam_width/spin_stat_fac/ell,
# define resonance width of rstate
#
# rstate is the energy level that GEANT
# creates resonant particles at
#
```

```
# level(x), specifies energy of energy level x
# life(x), specifies lifetime of level(x)
#
# Branching ratios:
# br(x,z), sets branching ratio of level(x) decay mode z
# md(x,z) = y, sets decay mode z, for level(x), to level(y)
#
# example
# br(2,1) = 100
# md(2,1) = 0
# sets braching ratio from level(2) to level index 1 to 100%
# sets level index 1, for level(2), to level(0)
# or, sets branching ratio from level(2) to level(0) to 100%
#
# Q-value= 4.461 MeV
 $params
  life = 15*1000.
  level = 15*0.
  beamtyp = '6Li'
  rectyp = '10B'
  zbeam = 3.
  abeam = 6.
  atarg = 4.
  ztarg = 2.
  zprod = 5.
  beamlifetime = 1000.
  beam_mass_excess = 14086.8E-06
  recoil_mass_excess = 12050.7E-06
  resenerg = 1.459
  part_width = 0.005
  gam_width = 0.000001
  spin_stat_fac = 0.136
  ell = 1.
  rstate = 9
  level( 0) = 0.0
  level( 1) = 0.718
```

```
level( 2) = 1.740
level( 3) = 2.154
level( 4) = 3.587
level( 5) = 4.774
level( 6) = 5.110
level( 7) = 5.164
level( 8) = 5.182
level( 9) = 5.920
level(10) = 6.025
life( 0) = 1000.
life( 1) = 0.707E-9
life( 2) = 4.9E-15
life( 3) = 1.48E-12
life( 4) = 102.0E-15
life( 5) = 5.85E-17
life( 6) = 4.665E-19
life( 7) = 2.549E-16
life( 8) = 4.148E-21
life( 9) = 7.8391E-20
life(10) = 8.77E-18
br(1,1) = 100.
md(1,1) = 0
br(2,1) = 100.
md(2,1) = 0
br(3,1) = 21.1
md(3,1) = 0
br(3,2) = 27.3
md(3,2) = 1
br(3,3) = 51.6
md(3,3) = 2
br(4,1) = 19.
md(4,1) = 0
br(4,2) = 67.
md(4,2) = 2
br(4,3) = 14.
md(4,3) = 3
```

```
  br(5,1) = 0.5
  md(5,1) = 0
  br(5,2) = 99.5
  md(5,2) = 1
  br(6,1) = 64.
  md(6,1) = 0
  br(6,2) = 31.
  md(6,2) = 1
  br(6,3) = 5.
  md(6,3) = 2
  br(7,1) = 4.4
  md(7,1) = 0
  br(7,2) = 22.6
  md(7,2) = 1
  br(7,3) = 65.3
  md(7,3) = 3
  br(7,4) = 7.8
  md(7,4) = 4
  br(8,1) = 100.
  md(8,1) = 0
  br(9,1) = 82.
  md(9,1) = 0
  br(9,2) = 18.
  md(9,2) = 1
  br(10,1) = 100.
  md(10,1) = 0
$[end]
```

A.2 ROOT script to plot the BGO γ_0 z–coordinate spectrum

```
// Convert the BGO Hit pattern into a z-coordinate from GEANT
void zmaskg(){
    TFile *f=new TFile(""); // Input the file name
    TTree *h1000 = (TTree*)f->Get("h1000");
```

```
    TTree *h1001 = (TTree*)f->Get("h1001");

    Float_t coords[30][3] = {   {   0, -4.8,-15.3},
                                {   0,-10.1,-12.2},     //1
                                {   0,  5.0,-12.2},
                                {   0,  9.9, -9.2},     //3
                                {   0,  8.0, -3.1},
                                {   0,  8.0,  3.1},     //5
                                {   0,  9.9,  9.2},
                                {   0,-10.1, 12.2},     //7
                                {   0,  5.0, 12.2},
                                {   0, -4.8, 15.3},     //9
                                {  -4, -2.6, -9.2},
                                {   4, -2.6, -9.2},     //11
                                {  -4, -7.9, -6.1},
                                {   4, -7.9, -6.1},     //13
                                {  -4,  2.7, -6.1},
                                {   4,  2.7, -6.1},     //15
                                {  -4, -2.6, -3.1},
                                {   4, -2.6, -3.1},     //17
                                {  -4, -7.9,    0},
                                {   4, -7.9,    0},     //19
                                {  -4,  2.7,    0},
                                {   4,  2.7,    0},     //21
                                {  -4, -2.6,  3.1},
                                {   4, -2.6,  3.1},     //23
                                {  -4, -7.9,  6.1},
                                {   4, -7.9,  6.1},     //25
                                {  -4,  2.7,  6.1},
                                {   4,  2.7,  6.1},     //27
                                {  -4, -2.6,  9.2},
                                {   4, -2.6,  9.2}      //29

    };
//
// Create a new file and tree to store new parameters,
```

```
// the convoluted energy and z-position
    TFile *fNew = new TFile("", "recreate");
    TTree *tNew = new TTree("tNew", "Convoluted e_bgo_first and
                                    real z-position coordinates");
    Float_t e_bgo_first_conv, z_bgo_first;
    tNew->Branch("e_bgo_first_conv", &e_bgo_first_conv,
                                        "e_bgo_first_conv/F");
    tNew->Branch("z_bgo_first", &z_bgo_first, "z_bgo_first/F");

//
// Fill it with convoluted energy and real BGO z-position
Float_t e_bgo_first;
Int_t num_bgo_first;
h1001->SetBranchAddress("e_bgo_first", &e_bgo_first);
h1001->SetBranchAddress("num_bgo_first", &num_bgo_first);

Long64_t nentries = h1001->GetEntries();
for (Long64_t i = 0; i < nentries; i++) {
    h1001->GetEntry(i);
    if(e_bgo_first>0){
      e_bgo_first_conv = e_bgo_first +
      gRandom->Gaus(0,0.1733*TMath::Sqrt(e_bgo_first)/
                        (TMath::Log(2)*TMath::Sqrt(8)));
    } else {
        e_bgo_first_conv = e_bgo_first;
        }

        assert(num_bgo_first > 0 && num_bgo_first < 30);
        z_bgo_first = coords[num_bgo_first][2];
        tNew->Fill();
    }
    tNew->Write();
// Now add the new tree as a "friend" to h1001
    h1001->AddFriend(tNew, "tNew", kTRUE);

// Now we can just draw the z-coordinate
```

```
    h1001->Draw("z_bgo_first>>zcoord(19,-30,30)",
    "num_bgo_first !=0 && recoil_hit_endv==1 &&
                    e_bgo_first_conv >= 0.5", "");

// And get an explicit pointer to it
    TH1F *zcoord = (TH1F*)gDirectory->Get("zcoord");
    zcoord->SetTitle("z-coordinate of BGO g0 hit");
    zcoord->Draw();
}
```

A.3 Python script for log–likelihood contours

```
import numpy as np
import matplotlib.pyplot as plt
import scipy.interpolate

N = 2000 #number of points for plotting/interpolation

#Read data from data file, where x is the Er, y the wg and z the -ln(L)
x, y, z = np.genfromtxt(r'#your data file', unpack=True)

xi = np.linspace(x.min(), x.max(), N)
yi = np.linspace(y.min(), y.max(), N)
zi = scipy.interpolate.griddata((x, y), z, (xi[None,:],
                            yi[:,None]), method='cubic')

contours = []
#For large N, the likelihood distribution tend to normal distribution,
#hence the i*sigma variance will be the
#i^2/2 change from the minimum value
maxcontour =10 #Number of contours (sigma)
for i in range(0 , maxcontour ):
        contours.append(z.min() + 0.5*i*i )

cs =plt.contourf(xi, yi, zi, levels= contours, cmap='RdGy')
cbar = fig.colorbar(cs)
```

```
cbar.ax.set_yticklabels(['1','2','3','4','5','6','7','8','9','10'])
plt.xlabel("$E_r$ (keV)")
plt.ylabel("$\omega \gamma$ (eV)")
plt.show()
```

A.4 RatesMC Input File

```
7Be(a,g)11C
**********************************************************************
4               ! Ztarget
0               ! Zexitparticle (=0 when only 2 channels open)
4.002602        ! Aproj
7.01692983      ! Atarget
0               ! Aexitparticle (=0 when only 2 channels open)
0.0             ! Jproj
1.5             ! Jtarget
0.0             ! Jexitparticle (=0 when only 2 channels open)
7544.52         ! projectile separation energy
0.0             ! exit particle separation energy
0.70            ! Radius parameter R0 (fm)
2               ! Gamma-ray channel number (=2 if ejectile is a g-ray)
**********************************************************************
1.0             ! Minimum energy for numerical integration (keV)
5000            ! Number of random samples (>5000 for better statistics)
0               ! =0 for rate output at all temperatures;
**********************************************************************
Non-resonant contribution
S(keVb) S'(b)   S''(b/keV)      fracErr Cutoff Energy (keV)
1.2e3   0.0     0.0             0.4     1000.0
0.0     0.0     0.0             0.0     0.0
0.0     0.0     0.0             0.0     0.0
**********************************************************************
Resonant Contribution
Note: G1 = entrance channel, G2 = exit channel, G3 = spectator channel !!
Ecm, Exf in (keV); wg, Gx in (eV) !!
Note: if Er<0, theta^2=C2S*theta_sp^2 must be entered instead
```

```
of entrance channel partial width
Ecm       DEcm      wg        Dwg       Jr        G1        DG1       L1        G2
DG2       L2        G3        DG3       L3        Exf       Int
560.0     17.0      0         0         1.5       6         3         2         0.350
0.056     1         0         0         0         0.0       0
877.0     2.0       3         0         2.5       12.6      3.8       2         3.1
1.3       1         0         0         0         0.0       0
1110.0    4.0       0.131     0.112     3.5       0         0         2         0
0         1         0         0         0         0.0       0
1155.0    2.0       1.39      0.36      2.5       0         0         2         0
0         1         0         0         0         0.0       0
*****************************************************************
Upper Limits of Resonances
Note: enter partial width upper limit by chosing non-zero value for PT,
where PT=<theta^2> for particles and...
Note: PT=<B> for g-rays [enter: 'upper_limit 0.0']; for each resonance:
# upper limits < # open channels!
Ecm  DEcm  Jr  G1  DG1  L1  PT  G2  DG2 L2  PT
G3   DG3   L3  PT  Exf  Int
*****************************************************************
Interference between Resonances [numerical integration only]
Note: + for positive, - for negative interference;
+- if interference sign is unknown
Ecm  DEcm  Jr  G1  DG1  L1  PT  G2  DG2  L2  PT
G3   DG3   L3  PT  Exf
!+-
0.0      0.0      0.0   0.0    0.0  0    0      0.0   0.0    0   0
0.0      0.0      0.0   0.0    0.0
0.0      0.0      0.0   0.0    0.0  0    0      0.0   0.0    0   0
0.0      0.0      0.0   0.0    0.0
*****************************************************************
Input file and PDF at NT selected temperatures only
Note: default values are used for Input file range if Min=Max=0.0
T9        Min       Max
0.01      0.0       0.0
0.1       0.0       0.0
```

****
Comments:
1. Radius parameter R0 and non-resonant contribution from NACRE-II

A.5 Tabulated $^{7}\mathrm{Be}(\alpha,\gamma)^{11}\mathrm{C}$ reaction rate

T_9	Low rate	Median rate	High rate	Log–norm μ	Log–norm σ	A-D
0.030	2.77×10^{-91}	1.66×10^{-88}	1.30×10^{-85}	-2.020×10^{2}	6.52×10^{0}	3.00×10^{-1}
0.040	3.12×10^{-67}	3.76×10^{-65}	5.50×10^{-63}	-1.483×10^{2}	4.89×10^{0}	2.92×10^{-1}
0.050	7.61×10^{-53}	3.57×10^{-51}	1.94×10^{-49}	-1.161×10^{2}	3.91×10^{0}	2.87×10^{-1}
0.060	2.85×10^{-43}	7.11×10^{-42}	1.96×10^{-40}	-9.472×10^{1}	3.25×10^{0}	2.83×10^{-1}
0.070	1.90×10^{-36}	2.96×10^{-35}	5.14×10^{-34}	-7.948×10^{1}	2.79×10^{0}	2.77×10^{-1}
0.080	2.43×10^{-31}	2.67×10^{-30}	3.26×10^{-29}	-6.807×10^{1}	2.44×10^{0}	2.73×10^{-1}
0.090	2.22×10^{-27}	1.89×10^{-26}	1.72×10^{-25}	-5.921×10^{1}	2.16×10^{0}	2.70×10^{-1}
0.100	3.23×10^{-24}	2.23×10^{-23}	1.61×10^{-22}	-5.215×10^{1}	1.95×10^{0}	2.67×10^{-1}
0.110	1.23×10^{-21}	7.12×10^{-21}	4.26×10^{-20}	-4.638×10^{1}	1.77×10^{0}	2.63×10^{-1}
0.120	1.73×10^{-19}	8.61×10^{-19}	4.44×10^{-18}	-4.159×10^{1}	1.62×10^{0}	2.61×10^{-1}
0.130	1.11×10^{-17}	4.94×10^{-17}	2.22×10^{-16}	-3.754×10^{1}	1.50×10^{0}	2.59×10^{-1}
0.140	3.93×10^{-16}	1.58×10^{-15}	6.38×10^{-15}	-3.408×10^{1}	1.39×10^{0}	2.56×10^{-1}
0.150	8.61×10^{-15}	3.14×10^{-14}	1.16×10^{-13}	-3.109×10^{1}	1.29×10^{0}	2.53×10^{-1}
0.160	1.27×10^{-13}	4.29×10^{-13}	1.45×10^{-12}	-2.848×10^{1}	1.21×10^{0}	2.51×10^{-1}
0.180	1.11×10^{-11}	3.30×10^{-11}	9.71×10^{-11}	-2.414×10^{1}	1.08×10^{0}	2.48×10^{-1}
0.200	3.91×10^{-10}	1.04×10^{-9}	2.75×10^{-9}	-2.068×10^{1}	9.71×10^{-1}	2.36×10^{-1}
0.250	2.26×10^{-7}	4.95×10^{-7}	1.08×10^{-6}	-1.452×10^{1}	7.77×10^{-1}	2.19×10^{-1}
0.300	1.49×10^{-05}	2.88×10^{-05}	5.49×10^{-05}	-1.046×10^{1}	6.49×10^{-1}	2.50×10^{-1}
0.350	2.87×10^{-4}	5.06×10^{-4}	8.77×10^{-4}	-7.593×10^{0}	5.59×10^{-1}	3.13×10^{-1}
0.400	2.55×10^{-3}	4.23×10^{-3}	6.84×10^{-3}	-5.471×10^{0}	4.91×10^{-1}	3.55×10^{-1}
0.450	1.38×10^{-2}	2.16×10^{-2}	3.32×10^{-2}	-3.840×10^{0}	4.39×10^{-1}	3.84×10^{-1}
0.500	5.22×10^{-2}	7.83×10^{-2}	1.16×10^{-1}	-2.550×10^{0}	3.97×10^{-1}	3.69×10^{-1}
0.600	3.75×10^{-1}	5.28×10^{-1}	7.37×10^{-1}	-6.417×10^{-1}	3.33×10^{-1}	3.12×10^{-1}
0.700	1.52×10^{0}	2.03×10^{0}	2.70×10^{0}	7.036×10^{-1}	2.85×10^{-1}	2.59×10^{-1}
0.800	4.31×10^{0}	5.53×10^{0}	7.08×10^{0}	1.708×10^{0}	2.45×10^{-1}	2.50×10^{-1}
0.900	9.77×10^{0}	1.21×10^{1}	1.50×10^{1}	2.492×10^{0}	2.13×10^{-1}	2.70×10^{-1}
1.000	1.89×10^{1}	2.27×10^{1}	2.74×10^{1}	3.125×10^{0}	1.85×10^{-1}	4.07×10^{-1}

1.250	6.37×10^{1}	7.26×10^{1}	8.33×10^{1}	4.289×10^{0}	1.34×10^{-1}	1.22×10^{0}
1.500	1.46×10^{2}	1.61×10^{2}	1.78×10^{2}	5.085×10^{0}	1.01×10^{-1}	2.25×10^{0}
1.750	2.65×10^{2}	2.86×10^{2}	3.11×10^{2}	5.660×10^{0}	8.03×10^{-2}	3.07×10^{0}
2.000	4.13×10^{2}	4.39×10^{2}	4.71×10^{2}	6.089×10^{0}	6.67×10^{-2}	3.69×10^{0}
2.500	7.50×10^{2}	7.88×10^{2}	8.31×10^{2}	6.672×10^{0}	5.22×10^{-2}	3.80×10^{0}
3.000	1.08×10^{3}	1.13×10^{3}	1.19×10^{3}	7.033×10^{0}	4.67×10^{-2}	4.11×10^{0}
3.500	1.37×10^{3}	1.43×10^{3}	1.50×10^{3}	7.266×10^{0}	4.52×10^{-2}	5.26×10^{0}
4.000	1.60×10^{3}	1.67×10^{3}	1.75×10^{3}	7.420×10^{0}	4.55×10^{-2}	6.83×10^{0}
5.000	1.89×10^{3}	1.97×10^{3}	2.07×10^{3}	7.590×10^{0}	4.79×10^{-2}	1.01×10^{1}
6.000	2.02×10^{3}	2.11×10^{3}	2.23×10^{3}	7.658×10^{0}	5.06×10^{-2}	1.25×10^{1}
7.000	2.04×10^{3}	2.14×10^{3}	2.26×10^{3}	7.674×10^{0}	5.30×10^{-2}	1.41×10^{1}
8.000	2.01×10^{3}	2.11×10^{3}	2.24×10^{3}	7.660×10^{0}	5.50×10^{-2}	1.51×10^{1}
9.000	1.95×10^{3}	2.04×10^{3}	2.17×10^{3}	7.629×10^{0}	5.67×10^{-2}	1.57×10^{1}
10.000	1.87×10^{3}	1.96×10^{3}	2.09×10^{3}	7.588×10^{0}	5.82×10^{-2}	1.61×10^{1}

Table A.1: Total thermonuclear reaction rates for $^{7}\mathrm{Be}(\alpha,\gamma)^{11}\mathrm{C}$. The rate below $\mathrm{T}_9 < 0.03$ is zero.

A.6 PPN Trajectory File (Partial)

```
# time T rho r lnue lnuebar lnux tnue tnuebar tnux
# YRS/SEC T8K/T9K CGS/LOG
# FORMAT: '(10x A3)'
AGEUNIT = SEC
TUNIT = KKK
RHOUNIT = CGS
  6.34E-02 9.81E+09 5.96E+06 4.98E+06 1.00E+52 1.00E+52 1.00E+52 12 14 14
  6.35E-02 9.75E+09 5.86E+06 5.01E+06 1.00E+52 1.00E+52 1.00E+52 12 14 14
  6.36E-02 9.72E+09 5.80E+06 5.03E+06 1.00E+52 1.00E+52 1.00E+52 12 14 14
  6.37E-02 9.67E+09 5.70E+06 5.06E+06 1.00E+52 1.00E+52 1.00E+52 12 14 14
  6.38E-02 9.61E+09 5.59E+06 5.09E+06 1.00E+52 1.00E+52 1.00E+52 12 14 14
  6.39E-02 9.58E+09 5.54E+06 5.10E+06 1.00E+52 1.00E+52 1.00E+52 12 14 14
  6.40E-02 9.53E+09 5.44E+06 5.14E+06 1.00E+52 1.00E+52 1.00E+52 12 14 14
  6.40E-02 9.50E+09 5.39E+06 5.15E+06 1.00E+52 1.00E+52 1.00E+52 12 14 14
  6.41E-02 9.45E+09 5.30E+06 5.18E+06 1.00E+52 1.00E+52 1.00E+52 12 14 14
```

6.42E−02	9.39E+09	5.20E+06	5.22E+06	1.00E+52	1.00E+52	1.00E+52	12	14	14
6.43E−02	9.36E+09	5.15E+06	5.23E+06	1.00E+52	1.00E+52	1.00E+52	12	14	14
6.44E−02	9.31E+09	5.06E+06	5.27E+06	1.00E+52	1.00E+52	1.00E+52	12	14	14
6.45E−02	9.28E+09	5.01E+06	5.28E+06	1.00E+52	1.00E+52	1.00E+52	12	14	14
6.46E−02	9.23E+09	4.92E+06	5.32E+06	1.00E+52	1.00E+52	1.00E+52	12	14	14
6.47E−02	9.17E+09	4.83E+06	5.35E+06	1.00E+52	1.00E+52	1.00E+52	12	14	14
6.47E−02	9.15E+09	4.79E+06	5.37E+06	1.00E+52	1.00E+52	1.00E+52	12	14	14
6.48E−02	9.09E+09	4.70E+06	5.40E+06	1.00E+52	1.00E+52	1.00E+52	12	14	14
6.49E−02	9.07E+09	4.65E+06	5.42E+06	1.00E+52	1.00E+52	1.00E+52	12	14	14
6.50E−02	9.01E+09	4.57E+06	5.45E+06	1.00E+52	1.00E+52	1.00E+52	12	14	14
6.51E−02	8.99E+09	4.53E+06	5.47E+06	1.00E+52	1.00E+52	1.00E+52	12	14	14
6.52E−02	8.93E+09	4.44E+06	5.50E+06	1.00E+52	1.00E+52	1.00E+52	12	14	14
6.53E−02	8.88E+09	4.36E+06	5.54E+06	1.00E+52	1.00E+52	1.00E+52	12	14	14
6.53E−02	8.85E+09	4.32E+06	5.56E+06	1.00E+52	1.00E+52	1.00E+52	12	14	14
6.54E−02	8.80E+09	4.24E+06	5.59E+06	1.00E+52	1.00E+52	1.00E+52	12	14	14
6.55E−02	8.77E+09	4.20E+06	5.61E+06	1.00E+52	1.00E+52	1.00E+52	12	14	14
6.56E−02	8.72E+09	4.12E+06	5.65E+06	1.00E+52	1.00E+52	1.00E+52	12	14	14
6.57E−02	8.69E+09	4.08E+06	5.66E+06	1.00E+52	1.00E+52	1.00E+52	12	14	14
6.58E−02	8.64E+09	4.01E+06	5.70E+06	1.00E+52	1.00E+52	1.00E+52	12	14	14
6.58E−02	8.62E+09	3.97E+06	5.72E+06	1.00E+52	1.00E+52	1.00E+52	12	14	14
6.59E−02	8.56E+09	3.90E+06	5.76E+06	1.00E+52	1.00E+52	1.00E+52	12	14	14

Bibliography

Abbott, B. P., Abbott, R., Abbott, T., Acernese, F., Ackley, K., Adams, C., Adams, T., Addesso, P., Adhikari, R., Adya, V., et al. (2017). GW170817: Observation of Gravitational Waves from a Binary Neutron Star Inspiral. *Physical Review Letters*, 119(16):161101.

Agostinelli, S., Allison, J., Amako, K., Apostolakis, J., Araujo, H., Arce, P., Asai, M., Axen, D., Banerjee, S., Barrand, G., et al. (2003). GEANT4-a simulation toolkit. *Nuclear instruments and methods in physics research section A: Accelerators, Spectrometers, Detectors and Associated Equipment*, 506(3):250–303.

Ajzenberg-Selove, F. and Busch, C. (1980). Energy levels of light nuclei A= 11–12. *Nuclear Physics A*, 336(1):1 – 154.

Angulo, C., Arnould, M., Rayet, M., Descouvemont, P., Baye, D., Leclercq-Willain, C., Coc, A., Barhoumi, S., Aguer, P., Rolfs, C., et al. (1999). A compilation of charged-particle induced thermonuclear reaction rates. *Nuclear Physics A*, 656(1):3–183.

Antcheva, I., Ballintijn, M., Bellenot, B., Biskup, M., Brun, R., Buncic, N., Canal, P., Casadei, D., Couet, O., Fine, V., et al. (2009). ROOT-A C++ framework for petabyte data storage, statistical analysis and visualization. *Computer Physics Communications*, 180(12):2499–2512.

Arcones, A., Fröhlich, C., and Martínez-Pinedo, G. (2012). Impact of supernova dynamics on the νp-process. *The Astrophysical Journal*, 750(1):18.

Arcones, A., Janka, H.-T., and Scheck, L. (2007). Nucleosynthesis-relevant conditions

in neutrino-driven supernova outflows-I. spherically symmetric hydrodynamic simulations. *Astronomy & Astrophysics*, 467(3):1227–1248.

Arcones, A. and Montes, F. (2011). Production of light-element primary process nuclei in neutrino-driven winds. *The Astrophysical Journal*, 731(1):5.

Armitage, B. and Meads, R. (1964). Levels in ^{10}B above 5.16 MeV observed by proton and deuteron inelastic scattering. *Physics Letters*, 8(5):346–349.

Arnett, W. D. (1966). Gravitational collapse and weak interactions. *Canadian Journal of Physics*, 44(11):2553–2594.

Arnould, M. (1976). Possibility of synthesis of proton-rich nuclei in highly evolved stars. II. *Astronomy and Astrophysics*, 46:117–125.

Arnould, M. and Goriely, S. (2003). The p-process of stellar nucleosynthesis: astrophysics and nuclear physics status. *Physics Reports*, 384(1-2):1–84.

Arnould, M. and Goriely, S. (2006). Microscopic nuclear models for astrophysics: The Brussels BRUSLIB nuclear library and beyond. *Nuclear Physics A*, 777:157–187.

Arnould, M., Goriely, S., and Takahashi, K. (2007). The r-process of stellar nucleosynthesis: Astrophysics and nuclear physics achievements and mysteries. *Physics Reports*, 450(4-6):97–213.

Audi, G., Wapstra, A., and Thibault, C. (2003). The AME2003 atomic mass evaluation:(II). Tables, graphs and references. *Nuclear physics A*, 729(1):337–676.

Baade, W. and Zwicky, F. (1934). On super-novae. *Proceedings of the National Academy of Sciences*, 20(5):254–259.

Bader, G. and Deuflhard, P. (1983). A semi-implicit mid-point rule for stiff systems of ordinary differential equations. *Numerische Mathematik*, 41(3):373–398.

Bethe, H. (1950). The range-energy relation for slow alpha-particles and protons in air. *Reviews of Modern Physics*, 22(2):213.

Bethe, H. A. and Wilson, J. R. (1985). Revival of a stalled supernova shock by neutrino heating. *The Astrophysical Journal*, 295:14–23.

Betz, H.-D. (1972). Charge states and charge-changing cross sections of fast heavy ions penetrating through gaseous and solid media. *Reviews of Modern Physics*, 44(3):465.

Bionta, R., Blewitt, G., Bratton, C., Casper, D., Ciocio, A., Claus, R., Cortez, B., Crouch, M., Dye, S., Errede, S., et al. (1991). Observation of a neutrino burst in coincidence with supernova 1987A in the large magellanic cloud. In *Neutrinos And Other Matters: Selected Works of Frederick Reines*, pages 340–342. World Scientific.

Blackmon, J., Angulo, C., and Shotter, A. (2006). Experimental approaches to nuclear reactions involved in explosive stellar binaries. *Nuclear Physics A*, 777:531–549.

Bliss, J., Arcones, A., Montes, F., and Pereira, J. (2017). Impact of (α, n) reactions on weak r-process in neutrino-driven winds. *Journal of Physics G: Nuclear and Particle Physics*, 44(5):054003.

Blondin, J. M. and Mezzacappa, A. (2007). Pulsar spins from an instability in the accretion shock of supernovae. *Nature*, 445(7123):58–60.

Briesmeister, J. F. (1986). MCNP-a general Monte Carlo code for neutron and photon transport. *LA-7396-M*.

Brun, R., McPherson, A., Zanarini, P., Maire, M., and Bruyant, F. (1987). GEANT 3: user's guide Geant 3.10, Geant 3.11. Technical report, CERN.

Buccino, S. and Smith, A. (1965). Levels in ^{10}B excited by the ^{9}Be(d, n) reaction. *Physics Letters (Netherlands) Divided into Phys. Lett. A and Phys. Lett. B*, 19.

Buras, R., Rampp, M., Janka, H.-T., and Kifonidis, K. (2006). Two-dimensional hydrodynamic core-collapse supernova simulations with spectral neutrino transport-I. Numerical method and results for a 15M$_\odot$ star. *Astronomy & Astrophysics*, 447(3):1049–1092.

Burbidge, E. M., Burbidge, G. R., Fowler, W. A., and Hoyle, F. (1957). Synthesis of the elements in stars. *Reviews of modern physics*, 29(4):547.

Burke, D. (2016). Development of a Hybrid Ionization Chamber/Double-Sided-Silicon-Strip Detector to be Installed at the DRAGON laboratory at TRIUMF. Master's thesis, McMaster University.

Burrows, A. S., Hayes, J., and Fryxell, B. A. (1995). On the nature of core-collapse supernova explosions. *Astrophysical Journal*, 450(2):830–850.

Cameron, A. G. W. (1957). Nuclear reactions in stars and nucleogenesis. *Publications of the Astronomical Society of the Pacific*, 69(408):201–222.

Carmona Gallardo, M. (2014). *Experimental studies of the astrophysical nuclear reaction* ^{3}He$(\alpha,\gamma)^{7}$Be. PhD thesis, Universidad Complutense de Madrid.

Caughlan, G. R. and Fowler, W. A. (1988). Thermonuclear reaction rates V. *Atomic Data and Nuclear Data Tables*, 40(2):283–334.

Chieffi, A. and Limongi, M. (2013). Pre-supernova evolution of rotating solar metallicity stars in the mass range 13-120 $M_{\odot}$ and their explosive yields. *The Astrophysical Journal*, 764(1):21.

Christian, G., Akers, C., Connolly, D., Fallis, J., Hutcheon, D., Olchanski, K., and Ruiz, C. (2014). Design and commissioning of a timestamp-based data acquisition system for the DRAGON recoil mass separator. *The European Physical Journal A*, 50(4):75.

Christian, G., Lotay, G., Ruiz, C., Akers, C., Burke, D., Catford, W., Chen, A., Connolly, D., Davids, B., Fallis, J., et al. (2018). Direct measurement of astrophysically important resonances in ^{38}K(p, γ)^{39}Ca. *Physical Review C*, 97(2):025802.

Colgate, S. A. and White, R. H. (1966). The hydrodynamic behavior of supernovae explosions. *The Astrophysical Journal*, 143:626.

Cyburt, R. H., Amthor, A. M., Ferguson, R., Meisel, Z., Smith, K., Warren, S., Heger, A., Hoffman, R., Rauscher, T., Sakharuk, A., et al. (2010). The JINA REACLIB database: its recent updates and impact on type-I x-ray bursts. *The Astrophysical Journal Supplement Series*, 189(1):240.

Dalesio, L. R., Kozubal, A., and Kraimer, M. (1991). EPCIS architecture. Technical report, Los Alamos National Lab., NM (United States).

Descouvemont, P. (1995). The ^{7}Be(α, γ)^{11}C and ^{7}Li(α, γ)^{11}B reactions in a microscopic three-cluster model. *Nuclear Physics A*, 584(3):532–546.

Dilling, J., Krücken, R., and Merminga, L. (2014). *ISAC and ARIEL: the TRIUMF radioactive beam facilities and the scientific program*. Springer.

Dillmann, I., Heil, M., Käppeler, F., Plag, R., Rauscher, T., and Thielemann, F.-K. (2006). KADoNiS-The Karlsruhe Astrophysical Database of Nucleosynthesis in Stars. In *AIP Conference Proceedings*, volume 819, pages 123–127. AIP.

Dillmann, I., Käppeler, F., Rauscher, T., Thielemann, F., Gallino, R., and Bisterzo, S. (2008). Are there only 30 p-nuclei. *Proceedings of Science*.

Domogatskii, G. and Nadezhin, D. (1978). Neutrino production of bypassed isotopes, and the possible role of neutrinos in nucleosynthesis. *Soviet Astronomy*, 22:297–305.

Drout, M., Piro, A., Shappee, B., Kilpatrick, C., Simon, J., Contreras, C., Coulter, D., Foley, R., Siebert, M., Morrell, N., et al. (2017). Light curves of the neutron star merger GW170817/SSS17a: Implications for r-process nucleosynthesis. *Science*, 358(6370):1570–1574.

DuBois, R. (1985). Charge transfer and ionization of lithium by protons and helium ions. *Physical Review A*, 32(6):3319.

Duncan, R. C., Shapiro, S. L., and Wasserman, I. (1986). Neutrino-driven winds from young, hot neutron stars. *The Astrophysical Journal*, 309:141–160.

Ebisuzaki, T., Hanawa, T., and Sugimoto, D. (1983). Mass loss from the neutron stars associated with x-ray bursts. *Publications of the Astronomical Society of Japan*, 35:17–32.

Erikson, L., Ruiz, C., Ames, F., Bricault, P., Buchmann, L., Chen, A., Chen, J., Dare, H., Davids, B., Davis, C., et al. (2010). First direct measurement of the ^{23}Mg(p, γ)^{24}Al reaction. *Physical Review C*, 81(4):045808.

Evans, M. and Zanolin, M. (2017). Detecting Gravitational Waves from Supernovae with Advanced LIGO. *Handbook of Supernovae*, page 1699.

Fallis, J., Akers, C., Laird, A., Simon, A., Spyrou, A., Christian, G., Connolly, D., Hager, U., Hutcheon, D., Lennarz, A., et al. (2020). First measurement in the gamow window of a reaction for the γ-process in inverse kinematics: ^{76}se(α, γ)^{80}kr. *Physics Letters B*, 807:135575.

Fallis, J., Clark, J., Sharma, K., Savard, G., Buchinger, F., Caldwell, S., Chaudhuri, A., Crawford, J., Deibel, C., Gulick, S., et al. (2011). Mass measurements of isotopes of Nb, Mo, Tc, Ru, and Rh along the νp-and rp-process paths using the Canadian Penning trap mass spectrometer. *Physical Review C*, 84(4):045807.

Feldman, G. J. and Cousins, R. D. (1998). Unified approach to the classical statistical analysis of small signals. *Physical Review D*, 57(7):3873.

Ferguson, A. J. (1965). Angular correlation methods in gamma-ray spectroscopy.

Fife, A., Neilson, G., and Dawson, W. (1967). The excited states of ^{10}B. *Nuclear Physics A*, 91(1):164–176.

Filippone, B., Elwyn, A., Davids, C., and Koetke, D. (1983). Measurement of the ^{7}Be(p, γ)^{8}B reaction cross section at low energies. *Physical Review Letters*, 50(6):412.

Filippone, B. W. and Wahlgren, M. (1986). Preparation of a ^{7}Be target via the molecular plating method. *Nuclear Instruments and Methods in Physics Research Section A: Accelerators, Spectrometers, Detectors and Associated Equipment*, 243(1):41–44.

Fischer, T., Whitehouse, S., Mezzacappa, A., Thielemann, F.-K., and Liebendoerfer, M. (2010). Protoneutron star evolution and the neutrino-driven wind in general relativistic neutrino radiation hydrodynamics simulations. *Astronomy & Astrophysics*, 517:A80.

Forsyth, P., Tu, H., and Hornyak, W. (1966). The ^{6}Li(α, γ)^{10}B reaction and the energy levels of ^{10}B. *Nuclear Physics*, 82(1):33–48.

Fowler, W. A., Lauritsen, C., and Lauritsen, T. (1948). Gamma-radiation from excited states of light nuclei. *Reviews of Modern Physics*, 20(1):236.

Frebel, A., Aoki, W., Christlieb, N., Ando, H., Asplund, M., Barklem, P. S., Beers, T. C., Eriksson, K., Fechner, C., Fujimoto, M. Y., et al. (2005). Nucleosynthetic signatures of the first stars. *Nature*, 434(7035):871–873.

Fröhlich, C., Martinez-Pinedo, G., Liebendörfer, M., Thielemann, F.-K., Bravo, E., Hix, W., Langanke, K., and Zinner, N. T. (2006). Neutrino-induced nucleosynthesis of A>64 nuclei: the νp process. *Physical Review Letters*, 96(14):142502.

Fynbo, H. O., Diget, C. A., Bergmann, U. C., Borge, M. J., Cederkäll, J., Dendooven, P., Fraile, L. M., Franchoo, S., Fedosseev, V. N., Fulton, B. R., et al. (2005). Revised rates for the stellar triple-α process from measurement of ^{12}C nuclear resonances. *Nature*, 433(7022):136–139.

Gamow, G. (1928). Zur quantentheorie des atomkernes. *Zeitschrift für Physik*, 51(3-4):204–212.

Gastis, P., Perdikakis, G., Frohlich, C., Alt, D., Horoi, M., Kontos, A., Liddick, S., Lin, L.-Y., Montes, F., Nikas, S., et al. (2017). Investigating the role of νp-process: Preparations for the measurement of the ^{56}Co(p, n)^{56}Ni reaction. In *Proceedings of the 14th International Symposium on Nuclei in the Cosmos (NIC2016)*, page 020511.

Gear, C. W. (1971). The automatic integration of ordinary differential equations. *Communications of the ACM*, 14(3):176–179.

Gigliotti, D. G. (2004). Efficiency calibration measurement and GEANT simulation of the DRAGON BGO gamma ray array at TRIUMF. Master's thesis, University of Northern British Columbia.

Gigliotti, D. G., Rogers, J. G., and Hussein, A. H. (2003). Calibration and simulation of a gamma array for DRAGON at ISAC. *Nuclear Instruments and Methods in Physics Research Section B: Beam Interactions with Materials and Atoms*, 204:671–677.

Goriely, S., José, J., Hernanz, M., Rayet, M., and Arnould, M. (2002). He-detonation in sub-chandrasekhar co white dwarfs: A new insight into energetics and-process nucleosynthesis. *Astronomy & Astrophysics*, 383(3):L27–L30.

Goriely, S., Samyn, M., Pearson, J., and Onsi, M. (2005). Further explorations of Skyrme–Hartree–Fock–Bogoliubov mass formulas. IV: Neutron-matter constraint. *Nuclear Physics A*, 750(2-4):425–443.

Gorodetzky, S., Gallmann, A., and Rebmeister, R. (1965). Study of the excited states of ^{10}B from 5 to 8 mev by the ^{11}B(^{3}He, α)^{10}B reaction and a note on the ^{11}B(^{3}He, t)^{11}C reaction. *Physical Review*, 137(6B):B1466.

Grebenev, S., Lutovinov, A., Tsygankov, S., and Winkler, C. (2012). Hard-X-ray emission lines from the decay of ^{44}Ti in the remnant of supernova 1987A. *Nature*, 490(7420):373.

Grefenstette, B., Harrison, F., Boggs, S., Reynolds, S., Fryer, C., Madsen, K., Wik, D. R., Zoglauer, A., Ellinger, C., Alexander, D., et al. (2014). Asymmetries in core-collapse supernovae from maps of radioactive ^{44}Ti in Cassiopeia A. *Nature*, 506(7488):339.

Hardie, G., Filippone, B., Elwyn, A., Wiescher, M., and Segel, R. (1984). Resonant alpha capture by ^{7}Be and ^{7}Li. *Physical Review C*, 29(4):1199.

Harrison, F. A., Craig, W. W., Christensen, F. E., Hailey, C. J., Zhang, W. W., Boggs, S. E., Stern, D., Cook, W. R., Forster, K., Giommi, P., et al. (2013). The nuclear spectroscopic telescope array (NuSTAR) high-energy X-ray mission. *The Astrophysical Journal*, 770(2):103.

Hauser, W. and Feshbach, H. (1952). The inelastic scattering of neutrons. *Physical review*, 87(2):366.

Heger, A., Fryer, C., Woosley, S., Langer, N., and Hartmann, D. H. (2003). How massive single stars end their life. *The Astrophysical Journal*, 591(1):288.

Heger, A., Kolbe, E., Haxton, W., Langanke, K., Martinez-Pinedo, G., and Woosley, S. (2005). Neutrino nucleosynthesis. *Physics Letters B*, 606(3-4):258–264.

Hernanz, M., José, J., Coc, A., and Isern, J. (1996). On the synthesis of ^{7}Li and ^{7}Be in novae. *The Astrophysical Journal Letters*, 465(1):L27.

Hirata, K., Kajita, T., Koshiba, M., Nakahata, M., Oyama, Y., Sato, N., Suzuki, A., Takita, M., Totsuka, Y., Kifune, T., et al. (1987). Observation of a neutrino burst from the supernova SN1987A. *Physical Review Letters*, 58(14):1490.

Hix, W. R. and Thielemann, F.-K. (1999). Computational methods for nucleosynthesis and nuclear energy generation. *Journal of Computational and Applied Mathematics*, 109(1-2):321–351.

Horowitz, C. J., Arcones, A., Cote, B., Dillmann, I., Nazarewicz, W., Roederer, I., Schatz, H., Aprahamian, A., Atanasov, D., Bauswein, A., et al. (2019). r-process nucleosynthesis: Connecting rare-isotope beam facilities with the cosmos. *Journal of Physics G: Nuclear and Particle Physics*.

Hou, S., He, J., Parikh, A., Kahl, D., Bertulani, C., Kajino, T., Mathews, G., and Zhao, G. (2017). Non-extensive statistics to the cosmological lithium problem. *The Astrophysical Journal*, 834(2):165.

Hüdepohl, L., Müller, B., Janka, H.-T., Marek, A., and Raffelt, G. G. (2010). Neutrino signal of electron-capture supernovae from core collapse to cooling. *Physical Review Letters*, 104(25):251101.

Hutcheon, D., Bishop, S., Buchmann, L., Chatterjee, M., Chen, A., D'Auria, J., Engel, S., Gigliotti, D., Greife, U., Hunter, D., et al. (2003). The DRAGON facility for nuclear astrophysics at TRIUMF–ISAC: design, construction and operation. *Nuclear Instruments and Methods in Physics Research Section A: Accelerators, Spectrometers, Detectors and Associated Equipment*, 498(1-3):190–210.

Hutcheon, D., Buchmann, L., Chen, A., DAuria, J., Davis, C., Greife, U., Hussein, A., Ottewell, D., Ouellet, C., Parikh, A., et al. (2008). Background suppression by the DRAGON radiative capture facility at TRIUMF/ISAC. *Nuclear Instruments and Methods in Physics Research Section B: Beam Interactions with Materials and Atoms*, 266(19-20):4171–4175.

Hutcheon, D., Ruiz, C., Fallis, J., D'Auria, J., Davids, B., Hager, U., Martin, L., Ottewell, D., Reeve, S., and Rojas, A. (2012). Measurement of radiative capture

resonance energies with an extended gas target. *Nuclear Instruments and Methods in Physics Research Section A: Accelerators, Spectrometers, Detectors and Associated Equipment*, 689:70–74.

Hwang, U., Laming, J. M., Badenes, C., Berendse, F., Blondin, J., Cioffi, D., DeLaney, T., Dewey, D., Fesen, R., Flanagan, K. A., et al. (2004). A million second Chandra view of Cassiopeia A. *The Astrophysical Journal Letters*, 615(2):L117.

Iliadis, C. (2015). *Nuclear physics of stars*. John Wiley & Sons.

Iliadis, C. (2019). Calculation of resonance energies from Q values. *Physical Review C*, 99(6):065809.

Iliadis, C., D'Auria, J. M., Starrfield, S., Thompson, W. J., and Wiescher, M. (2001). Proton-induced thermonuclear reaction rates for A= 20–40 nuclei. *The Astrophysical Journal Supplement Series*, 134(1):151.

Iliadis, C., Longland, R., Champagne, A., Coc, A., and Fitzgerald, R. (2010). Charged-particle thermonuclear reaction rates: II. tables and graphs of reaction rates and probability density functions. *Nuclear Physics A*, 841(1-4):31–250.

Iliadis, C., Longland, R., Coc, A., Timmes, F., and Champagne, A. E. (2015). Statistical methods for thermonuclear reaction rates and nucleosynthesis simulations. *Journal of Physics G: Nuclear and Particle Physics*, 42(3):034007.

Janka, H.-T., Langanke, K., Marek, A., Martínez-Pinedo, G., and Müller, B. (2007). Theory of core-collapse supernovae. *Physics Reports*, 442(1-6):38–74.

Janka, H.-T., Melson, T., and Summa, A. (2016). Physics of core-collapse supernovae in three dimensions: a sneak preview. *Annual Review of Nuclear and Particle Science*, 66:341–375.

Jayamanna, K. (2014). Off line ion source terminal. *Hyperfine Interactions*, 225(1-3):51–62.

José, J. (2016). *Stellar explosions: hydrodynamics and nucleosynthesis*. CRC Press.

José, J. and Iliadis, C. (2011). Nuclear astrophysics: the unfinished quest for the origin of the elements. *Reports on Progress in Physics*, 74(9):096901.

José, J., Moreno, F., Parikh, A., and Iliadis, C. (2010). Hydrodynamic models of type I X-ray bursts: metallicity effects. *The Astrophysical Journal Supplement Series*, 189(1):204.

Käppeler, F., Gallino, R., Bisterzo, S., and Aoki, W. (2011). The s process: Nuclear physics, stellar models, and observations. *Reviews of Modern Physics*, 83(1):157.

Kashy, E., Benenson, W., and Nolen Jr, J. (1974). A= 9 isospin quartet. *Physical Review C*, 9(6):2102.

Kelley, J., Kwan, E., Purcell, J., Sheu, C., and Weller, H. (2012). Energy levels of light nuclei A= 11. *Nuclear Physics A*, 880:88–195.

Köster, U. (2002). Intense radioactive-ion beams produced with the ISOL method. *The European Physical Journal A-Hadrons and Nuclei*, 15(1-2):255–263.

Kroupa, P. (2001). On the variation of the initial mass function. *Monthly Notices of the Royal Astronomical Society*, 322(2):231–246.

Kunz, R., Fey, M., Jaeger, M., Mayer, A., Hammer, J., Staudt, G., Harissopulos, S., and Paradellis, T. (2002). Astrophysical reaction rate of ^{12}C(α, γ)^{16}O. *The Astrophysical Journal*, 567(1):643.

Kurath, D. (1973). Alpha-structure amplitudes for the 1 p shell. *Physical Review C*, 7(4):1390.

Langanke, K., Martinez-Pinedo, G., and Sieverding, A. (2019). Neutrino nucleosynthesis: An overview. *arXiv preprint arXiv:1901.03741*.

Lassen, J., Bricault, P., Dombsky, M., Lavoie, J., Geppert, C., and Wendt, K. (2005). Resonant ionization laser ion source project at TRIUMF. *Hyperfine Interactions*, 162(1-4):69–75.

Laxdal, R. (2003). Acceleration of radioactive ions. *Nuclear Instruments and Methods in Physics Research Section B: Beam Interactions with Materials and Atoms*, 204:400–409.

Laxdal, R., Dutto, G., Fong, K., Mackenzie, G., Pasini, M., Poirier, R., and Ruegg, R. (2001). Beam Commissioning and First Operation of the ISAC DTL at TRIUMF. In *PACS2001. Proceedings of the 2001 Particle Accelerator Conference (Cat. No. 01CH37268)*, volume 5, pages 3942–3944. IEEE.

Laxdal, R. and Marchetto, M. (2014). The ISAC post-accelerator. *Hyperfine Interactions*, 225(1-3):79–97.

Lippuner, J. and Roberts, L. F. (2017). SkyNet: A modular nuclear reaction network library. *Astrophys. J. Suppl.*, 233(arXiv: 1706.06198):18.

Liu, W., Imbriani, G., Buchmann, L., Chen, A., D'Auria, J., D'Onofrio, A., Engel, S., Gialanella, L., Greife, U., Hunter, D., et al. (2003). Charge state studies of low energy heavy ions passing through hydrogen and helium gas. *Nuclear Instruments and Methods in Physics Research Section A: Accelerators, Spectrometers, Detectors and Associated Equipment*, 496(1):198–214.

Lodders, K., Palme, H., and Gail, H.-P. (2009). 4.4 Abundances of the elements in the Solar System. In *Solar system*, pages 712–770. Springer.

Longland, R., Iliadis, C., Champagne, A., Newton, J. R., Ugalde, C., Coc, A., and Fitzgerald, R. (2010). Charged-particle thermonuclear reaction rates: I. Monte Carlo method and statistical distributions. *Nuclear Physics A*, 841(1-4):1–30.

Longland, R., Martin, D., and José, J. (2014). Performance improvements for nuclear reaction network integration. *Astronomy & Astrophysics*, 563:A67.

Marchetto, M. and Laxdal, R. (2013). High energy beam lines. In *ISAC and ARIEL: The TRIUMF Radioactive Beam Facilities and the Scientific Program*, pages 99–109. Springer.

Marshall, C., Setoodehnia, K., Kowal, K., Portillo, F., Champagne, A. E., Hale, S., Dummer, A., and Longland, R. (2018). The Focal-Plane Detector Package on the TUNL Split-Pole Spectrograph. *IEEE Transactions on Instrumentation and Measurement*, 68(2):533–546.

Martínez-Pinedo, G., Fischer, T., Lohs, A., and Huther, L. (2012). Charged-current weak interaction processes in hot and dense matter and its impact on the spectra of neutrinos emitted from protoneutron star cooling. *Physical Review Letters*, 109(25):251104.

Mashonkina, L., Christlieb, N., Barklem, P. S., Hill, V., Beers, T., and Velichko, A. (2010). The Hamburg/ESO R-process enhanced star survey (HERES)-V. detailed abundance analysis of the r-process enhanced star HE 2327-5642. *Astronomy & Astrophysics*, 516:A46.

Matei, C., Buchmann, L., Hannes, W., Hutcheon, D., Ruiz, C., Brune, C., Caggiano, J., Chen, A., DAuria, J., Laird, A., et al. (2006). Measurement of the Cascade Transition via the First Excited State of ^{16}O in the ^{12}C(α, γ)^{16}O reaction, and its S Factor in Stellar Helium Burning. *Physical review letters*, 97(24):242503.

Matz, S., Share, G., Leising, M., Chupp, E., Vestrandt, W., Purcell, W., Strickman, M., and Reppin, C. (1988). Gamma-ray line emission from SN1987A. *Nature*, 331(6155):416.

McLaughlin, G. C., Fuller, G. M., and Wilson, J. R. (1996). The influence of nuclear composition on the electron fraction in the post-core bounce supernova environment. *The Astrophysical Journal*, 472(2):440.

Meyer, B., Howard, W., Mathews, G., Hoffman, R., and Woosley, S. (1992). The r-process in supernovae. *Unstable Nuclei in Astrophysics*, 37.

Meyer-Schützmeister, L. and Hanna, S. (1957). Energy levels in ^{10}B in the reaction ^{6}Li(α, γ)^{10}B. *Physical Review*, 108(6):1506.

Nishimura, N., Rauscher, T., Hirschi, R., Cescutti, G., Murphy, A. S. J., and Fröhlich, C. (2019). Uncertainties in νp-process nucleosynthesis from monte carlo variation of reaction rates. *Monthly Notices of the Royal Astronomical Society*, 489(1):1379–1396.

Nishimura, N., Takiwaki, T., and Thielemann, F.-K. (2015). The r-process nucleosynthesis in the various jet-like explosions of magnetorotational core-collapse supernovae. *The Astrophysical Journal*, 810(2):109.

Olchanski, K. (2012). VME-NIMIO32-General purpose VME FPGA board. Technical report, Technical report, TRIUMF.

Park, Y. S., Niiler, A., and Lindgren, R. (1973). Spectroscopy of ^{10}B levels from the ^{9}Be(d, n)^{10}B reaction. *Physical Review C*, 8(5):1557.

Paxton, B., Bildsten, L., Dotter, A., Herwig, F., Lesaffre, P., and Timmes, F. (2010). Modules for experiments in stellar astrophysics (MESA). *The Astrophysical Journal Supplement Series*, 192(1):3.

Paxton, B., Cantiello, M., Arras, P., Bildsten, L., Brown, E. F., Dotter, A., Mankovich, C., Montgomery, M., Stello, D., Timmes, F., et al. (2013). Modules for experiments in stellar astrophysics (MESA): planets, oscillations, rotation, and massive stars. *The Astrophysical Journal Supplement Series*, 208(1):4.

Paxton, B., Marchant, P., Schwab, J., Bauer, E. B., Bildsten, L., Cantiello, M., Dessart, L., Farmer, R., Hu, H., Langer, N., et al. (2015). Modules for experiments in stellar astrophysics (MESA): binaries, pulsations, and explosions. *The Astrophysical Journal Supplement Series*, 220(1):15.

Paxton, B., Smolec, R., Schwab, J., Gautschy, A., Bildsten, L., Cantiello, M., Dotter, A., Farmer, R., Goldberg, J. A., Jermyn, A. S., et al. (2019). Modules for experiments in stellar astrophysics (MESA): Pulsating variable stars, rotation, convective boundaries, and energy conservation. *The Astrophysical Journal Supplement Series*, 243(1):10.

Peirce, B. (1852). Criterion for the rejection of doubtful observations. *The Astronomical Journal*, 2:161–163.

Pignatari, M., Gallino, R., Heil, M., Wiescher, M., Käppeler, F., Herwig, F., and Bisterzo, S. (2010). The weak s-process in massive stars and its dependence on the neutron capture cross sections. *The Astrophysical Journal*, 710(2):1557.

Pignatari, M., Göbel, K., Reifarth, R., and Travaglio, C. (2016). The production of proton-rich isotopes beyond iron: The γ-process in stars. *International Journal of Modern Physics E*, 25(04):1630003.

Pignatari, M. and Herwig, F. (2012). The NuGrid research platform: A comprehensive simulation approach for nuclear astrophysics. *Nuclear Physics News*, 22(4):18–23.

Poirier, R., Baartman, R., Bricault, P., Fong, K., Koscielniak, S., Laxdal, R., Mitra, A., Root, L., Stanford, G., and Pearce, D. (2000). CW performance of the TRIUMF 8 meter long RFQ for exotic ions. *arXiv preprint physics/0008210*.

Pruet, J., Hoffman, R., Woosley, S., Janka, H.-T., and Buras, R. (2006). Nucleosynthesis in early supernova winds. II. The role of neutrinos. *The Astrophysical Journal*, 644(2):1028.

Qian, Y.-Z. and Woosley, S. (1996). Nucleosynthesis in neutrino-driven winds. I. the physical conditions. *The Astrophysical Journal*, 471(1):331.

Rajput, M. and Mac Mahon, T. (1992). Techniques for evaluating discrepant data. *Nuclear Instruments and Methods in Physics Research Section A: Accelerators, Spectrometers, Detectors and Associated Equipment*, 312(1-2):289–295.

Ramos, J., Stora, T., Senos, A., and Bowen, P. (2018). Thermal stability of nanometric tic-carbon composites: effects of carbon allotropes and zr milling impurities. *Journal of the European Ceramic Society*, 38(15):4882–4891.

Rapp, W., Görres, J., Wiescher, M., Schatz, H., and Käppeler, F. (2006). Sensitivity of p-process Nucleosynthesis to Nuclear Reaction Rates in a 25 $M_{\odot}$ Supernova Model. *The Astrophysical Journal*, 653(1):474.

Rauscher, T., Nishimura, N., Hirschi, R., Cescutti, G., Murphy, A. S. J., and Heger, A. (2016). Uncertainties in the production of p nuclei in massive stars obtained from monte carlo variations. *Monthly Notices of the Royal Astronomical Society*, 463(4):4153–4166.

Ravn, H. L. (1979). Experiments with intense secondary beams of radioactive ions. *Physics Reports*, 54(3):201–259.

Rayet, M., Arnould, M., and Prantzos, N. (1990). The p-process revisited. *Astronomy and Astrophysics*, 227:271–281.

Reed, J. E., Hester, J. J., Fabian, A., and Winkler, P. (1995). The three-dimensional structure of the cassiopeia A supernova remnant. I. The spherical shell. *The Astrophysical Journal*, 440:706.

Reifarth, R., Lederer, C., and Käppeler, F. (2014). Neutron reactions in astrophysics. *Journal of Physics G: Nuclear and Particle Physics*, 41(5):053101.

Ritt, S., Amaudruz, P., and Olchanski, K. (1997). The MIDAS data acquisition system. *Midas online: https://midas. psi.*

Ritter, C., Herwig, F., Jones, S., Pignatari, M., Fryer, C., and Hirschi, R. (2018). NuGrid stellar data set–II. stellar yields from H to Bi for stellar models with M ZAMS= 1–25 $M_{\odot}$ and Z= 0.0001–0.02. *Monthly Notices of the Royal Astronomical Society*, 480(1):538–571.

Rolfs, C. E. and Rodney, W. S. (1988). *Cauldrons in the cosmos: Nuclear astrophysics*. University of Chicago press.

Rose, H. and Brink, D. (1967). Angular distributions of gamma rays in terms of phase-defined reduced matrix elements. *Reviews of Modern Physics*, 39(2):306.

Ruiz, C., Greife, U., and Hager, U. (2014). Recoil separators for radiative capture using radioactive ion beams. *The European Physical Journal A*, 50(6):99.

Sallaska, A. L., Iliadis, C., Champange, A., Goriely, S., Starrfield, S., and Timmes, F. (2013). STARLIB: A next-generation reaction-rate library for nuclear astrophysics. *The Astrophysical Journal Supplement Series*, 207(1):18.

Salpeter, E. E. (1955). The luminosity function and stellar evolution. *The Astrophysical Journal*, 121:161.

Schatz, H. (2006). The importance of nuclear masses in the astrophysical rp-process. *International Journal of Mass Spectrometry*, 251(2-3):293–299.

Schatz, H., Aprahamian, A., Görres, J., Wiescher, M., Rauscher, T., Rembges, J., Thielemann, F.-K., Pfeiffer, B., Möller, P., Kratz, K.-L., et al. (1998). rp-process nucleosynthesis at extreme temperature and density conditions. *Physics reports*, 294(4):167–263.

Schiwietz, G. and Grande, P. (2001). Improved charge-state formulas. *Nuclear Instruments and Methods in Physics Research Section B: Beam Interactions with Materials and Atoms*, 175:125–131.

Schoenfelder, V., Aarts, H., Bennett, K., Boer, H. d., Clear, J., Collmar, W., Connors, A., Deerenberg, A., Diehl, R., Dordrecht, A. v., et al. (1993). Instrument description and performance of the imaging gamma-ray telescope comptel aboard the compton gamma-ray observatory. *Astrophysical Journal Supplement Series*, 86:657.

Sen, A., Ames, F., Bricault, P., Lassen, J., Laxdal, A., and Mjos, A. (2016). Extraction and low energy beam transport from a surface ion source at the TRIUMF-ISAC facility. *Nuclear Instruments and Methods in Physics Research Section B: Beam Interactions with Materials and Atoms*, 376:97–101.

Sjue, S., Singh, B. N., Adsley, P., Buchmann, L., Carmona-Gallardo, M., Davids, B., Fallis, J., Fulton, B., Galinski, N., Hager, U., et al. (2013). Beam suppression of the DRAGON recoil separator for ^{3}He(α, γ) ^{7}Be. *Nuclear Instruments and Methods in Physics Research Section A: Accelerators, Spectrometers, Detectors and Associated Equipment*, 700:179–181.

Skinner, M. A., Dolence, J. C., Burrows, A., Radice, D., and Vartanyan, D. (2019). Fornax: a flexible code for multiphysics astrophysical simulations. *The Astrophysical Journal Supplement Series*, 241(1):7.

Spyrou, A., Liddick, S., Larsen, A.-C., Guttormsen, M., Cooper, K., Dombos, A., Morrissey, D., Naqvi, F., Perdikakis, G., Quinn, S., et al. (2014). Novel technique for constraining r-process (n, γ) reaction rates. *Physical Review Letters*, 113(23):232502.

Surman, R., Mumpower, M., Sinclair, R., Jones, K., Hix, W., and McLaughlin, G. (2014). Sensitivity studies for the weak r process: neutron capture rates. *AIP advances*, 4(4):041008.

Thielemann, F.-K., Nomoto, K., and Hashimoto, M.-A. (1996). Core-collapse supernovae and their ejecta. *The Astrophysical Journal*, 460:408.

Tilley, D., Kelley, J., Godwin, J., Millener, D., Purcell, J., Sheu, C., and Weller, H. (2004). Energy levels of light nuclei A= 8, 9, 10. *Nuclear Physics A*, 745(3-4):155–362.

Timmes, F. (1999). Integration of nuclear reaction networks for stellar hydrodynamics. *The Astrophysical Journal Supplement Series*, 124(1):241.

Travaglio, C., Gallino, R., Rauscher, T., Dauphas, N., Röpke, F., and Hillebrandt, W. (2014). Radiogenic p-isotopes from Type Ia supernova, nuclear physics uncertainties, and galactic chemical evolution compared with values in primitive meteorites. *The Astrophysical Journal*, 795(2):141.

Travaglio, C., Röpke, F., Gallino, R., and Hillebrandt, W. (2011). Type Ia supernovae as sites of the p-process: two-dimensional models coupled to nucleosynthesis. *The Astrophysical Journal*, 739(2):93.

Tueller, J., Barthelmy, S., Gehrels, N., Teegarden, B., Leventhal, M., and MacCallum, C. (1990). Observations of gamma-ray line profiles from SN 1987A. *The Astrophysical Journal*, 351:L41–L44.

Vartanyan, D., Burrows, A., Radice, D., Skinner, M. A., and Dolence, J. (2019). A successful 3D core-collapse supernova explosion model. *Monthly Notices of the Royal Astronomical Society*, 482(1):351–369.

Vockenhuber, C., Buchmann, L., Caggiano, J., Chen, A., DAuria, J., Davis, C., Greife, U., Hussein, A., Hutcheon, D., Ottewell, D., et al. (2008). Improvements of the DRAGON recoil separator at ISAC. *Nuclear Instruments and Methods in Physics Research Section B: Beam Interactions with Materials and Atoms*, 266(19-20):4167–4170.

Vockenhuber, C., Erikson, L., Buchmann, L., Greife, U., Hager, U., Hutcheon, D., Lamey, M., Machule, P., Ottewell, D., Ruiz, C., et al. (2009). A transmission time-of-flight system for particle identification at a recoil mass separator at low energies. *Nuclear Instruments and Methods in Physics Research Section A: Accelerators, Spectrometers, Detectors and Associated Equipment*, 603(3):372–378.

Wagoner, R. V. (1969). Synthesis of the elements within objects exploding from very high temperatures. *The Astrophysical Journal Supplement Series*, 18:247.

Wanajo, S. (2006). The rp-process in neutrino-driven winds. *The Astrophysical Journal*, 647(2):1323.

Wanajo, S. (2013). The r-process in proto-neutron-star wind revisited. *The Astrophysical Journal Letters*, 770(2):L22.

Wanajo, S., Janka, H.-T., and Kubono, S. (2011). Uncertainties in the νp-process: supernova dynamics versus nuclear physics. *The Astrophysical Journal*, 729(1):46.

Wanajo, S., Müller, B., Janka, H.-T., and Heger, A. (2018). Nucleosynthesis in the innermost ejecta of neutrino-driven supernova explosions in two dimensions. *The Astrophysical Journal*, 852(1):40.

Wang, M., Audi, G., Kondev, F., Huang, W., Naimi, S., and Xu, X. (2017). The AME2016 atomic mass evaluation (II). tables, graphs and references. *Chinese Physics C*, 41(3):030003.

Weber, C., Elomaa, V.-V., Ferrer, R., Fröhlich, C., Ackermann, D., Äystö, J., Audi, G., Batist, L., Blaum, K., Block, M., et al. (2008). Mass measurements in the vicinity of the rp–process and the νp–process paths with the penning trap facilities JYFLTRAP and SHIPTRAP. *Physical Review C*, 78(5):054310.

Weisskopf, M. C., Tananbaum, H. D., Van Speybroeck, L. P., and O'Dell, S. L. (2000). Chandra X-ray observatory (CXO): overview. In *X-Ray Optics, Instruments, and Missions III*, volume 4012, pages 2–16. International Society for Optics and Photonics.

Werner, M., Roellig, T., Low, F., Rieke, G. H., Rieke, M., Hoffmann, W., Young, E., Houck, J., Brandl, B., Fazio, G., et al. (2004). The Spitzer space telescope mission. *The Astrophysical Journal Supplement Series*, 154(1):1.

Wiescher, M., Boyd, R., Blatt, S., Rybarcyk, L., Spizuoco, J., Azuma, R., Clifford, E., King, J., Görres, J., Rolfs, C., et al. (1983). ^{11}C level structure via the ^{10}B(p, γ) reaction. *Physical Review C*, 28(4):1431.

Wiescher, M., Gorres, J., Graff, S., Buchmann, L., and Thielemann, F.-K. (1989). The hot proton-proton chains in low-metallicity objects. *The Astrophysical Journal*, 343:352–364.

Winkler, C., Di Cocco, G., Gehrels, N., Giménez, A., Grebenev, S., Hermsen, W., Mas-Hesse, J., Lebrun, F., Lund, N., Palumbo, G., et al. (2003). The integral mission. *Astronomy & Astrophysics*, 411(1):L1–L6.

Wongwathanarat, A., Janka, H.-T., and Müller, E. (2013). Three-dimensional neutrino-driven supernovae: Neutron star kicks, spins, and asymmetric ejection of nucleosynthesis products. *Astronomy & Astrophysics*, 552:A126.

Woosley, S., Hartmann, D., Hoffman, R., and Haxton, W. (1990). The nu-process. *The Astrophysical Journal*, 356:272–301.

Woosley, S. and Weaver, T. A. (1995). The evolution and explosion of massive stars II: Explosive hydrodynamics and nucleosynthesis. Technical report, Lawrence Livermore National Lab., CA (United States).

Woosley, S., Wilson, J., Mathews, G., Hoffman, R., and Meyer, B. (1994). The r-process and neutrino-heated supernova ejecta. *The Astrophysical Journal*, 433:229–246.

Woosley, S. E., Arnett, W. D., and Clayton, D. D. (1973). The explosive burning of oxygen and silicon. *Astrophysical Journal Supplement*.

Woosley, S. E., Heger, A., and Weaver, T. A. (2002). The evolution and explosion of massive stars. *Reviews of modern physics*, 74(4):1015.

Wu, M.-R., Qian, Y.-Z., Martínez-Pinedo, G., Fischer, T., and Huther, L. (2015). Effects of neutrino oscillations on nucleosynthesis and neutrino signals for an 18 $M_\odot$ supernova model. *Physical Review D*, 91(6):065016.

Xing, Y., Li, K., Zhang, Y., Zhou, X., Wang, M., Litvinov, Y. A., Blaum, K., Wanajo, S., Kubono, S., Martínez-Pinedo, G., et al. (2018). Mass measurements of neutron-deficient Y, Zr, and Nb isotopes and their impact on rp and νp nucleosynthesis processes. *Physics Letters B*, 781:358–363.

Xu, Y., Takahashi, K., Goriely, S., Arnould, M., Ohta, M., and Utsunomiya, H. (2013). NACRE II: an update of the NACRE compilation of charged–particle–induced thermonuclear reaction rates for nuclei with mass number A<16. *Nuclear Physics A*, 918:61–169.

Yamaguchi, H., Kahl, D., Wakabayashi, Y., Kubono, S., Hashimoto, T., Hayakawa, S., Kawabata, T., Iwasa, N., Teranishi, T., Kwon, Y., et al. (2013). α-resonance structure in ^{11}C studied via resonant scattering of ^{7}Be + α and with the ^{7}Be(α, p) reaction. *Physical Review C*, 87(3):034303.

Yanagisawa, Y., Kubono, S., Teranishi, T., Ue, K., Michimasa, S., Notani, M., He, J., Ohshiro, Y., Shimoura, S., Watanabe, S., et al. (2005). Low-energy radioisotope beam separator CRIB. *Nuclear Instruments and Methods in Physics Research Section A: Accelerators, Spectrometers, Detectors and Associated Equipment*, 539(1-2):74–83.

Yoshida, T., Kajino, T., Yokomakura, H., Kimura, K., Takamura, A., and Hartmann, D. H. (2006). Supernova neutrino nucleosynthesis of light elements with neutrino oscillations. *Physical Review Letters*, 96(9):091101.

Ziegler, J. F., Ziegler, M. D., and Biersack, J. P. (2010). SRIM–the stopping and range of ions in matter (2010). *Nuclear Instruments and Methods in Physics Research Section B: Beam Interactions with Materials and Atoms*, 268(11-12):1818–1823.